Measurement of polarization observables in the reaction $\gamma p \rightarrow p\pi^0\pi^0$ using linearly polarized photons with the CBELSA/TAPS experiment

Dissertation

zur

Erlangung des Doktorgrades (Dr. rer. nat.)

der

Mathematisch-Naturwissenschaftlichen Fakultät

der

Rheinischen Friedrich-Wilhelms-Universität

Bonn

vorgelegt von

Vahe Sokhoyan

aus

Eriwan, Armenien

Bonn 2012

Angefertigt mit Genehmigung
der Mathematisch-Naturwissenschaftlichen Fakultät der
Rheinischen Friedrich-Wilhelms-Universität Bonn

1. Gutachter: Prof. Dr. U. Thoma

2. Gutachter: Prof. Dr. V. Metag

Tag der Promotion: 27.07.2012

Erscheinungsjahr: 2012

IN DER DISSERTATION EINGEBUNDEN:

Zusammenfassung

Abstract

The spectrum and the properties of baryon resonances can be studied using photons with energies appropriate to excite baryonic states. Double meson photoproduction allows access to cascading resonance decays via other excited states. Also, at higher energies the importance of the double meson photoproduction increases due to higher cross-sections in comparison to single meson photoproduction.
To study baryon resonances, the measurement of polarization observables as well as the measurement of differential cross-sections plays a very important role. In this work the three-body polarization observables I^s, I^c and the respective two-body asymmetry Σ were measured for the reaction $\gamma p \rightarrow p\pi^0\pi^0$ in an incoming photon energy range of $E_\gamma = 970 - 1650\,\mathrm{MeV}$. The data were acquired with the CBELSA/TAPS experiment located at the ELSA accelerator in Bonn, using a linearly polarized photon beam impinging on a liquid hydrogen target.
The observables I^s and I^c which occur in two-meson final states are measured for the first time in the reaction $\gamma p \rightarrow p\pi^0\pi^0$. The corresponding two-body asymmetry Σ is measured in an extended energy range in comparison to already existing data.
A comparison with theoretical models shows that the polarization observables provide valuable input to study resonance contributions and their decay modes. The $D_{33}(1700) \rightarrow \Delta\pi$ decay is studied based on the comparison of the Bonn-Gatchina Partial Wave Analysis (PWA) predictions with the data. Furthermore, a comparison of the data with the Bonn-Gatchina PWA and the Fix isobar model predictions allows to distinguish between these two models.
Additionally, band-like structures and peaks are observed in the mass ranges of $\Delta(1232)$, $D_{13}(1520)$, $F_{15}(1680)$, $f_0(980)$ and $f_2(1270)$ in the according Dalitz plots and invariant mass distributions. The contributions of these states are confirmed by the Bonn-Gatchina PWA. An excellent compatibility with the existing data from the previous CBELSA experiment is observed.

Contents

1. Introduction and motivation

To understand the structure of matter one has to know what its constituents are and how they interact. According to the current knowledge provided by the Standard Model the constituents of matter are 6 leptons and 6 quarks. The particles interact via mediator particles which are the photon for the electromagnetic interaction, $W^{\pm}$ and Z^0 bosons for the weak interaction and the gluons for the strong interaction. The particles which have internal structure and consist of quarks are called hadrons. In this chapter the baryons are presented which are hadrons consisting of three quarks. The role of the reaction $\gamma p \to p\pi^0\pi^0$ for the investigation of the baryon spectrum is discussed. Further, the polarization observables and their importance for the determination of the resonance properties are described. Finally, an overview of the existing theoretical models and experimental data for the reaction $\gamma p \to p\pi^0\pi^0$ is given.

1.1. Baryons

The constituents of hadrons called quarks were introduced by M. Gell-Mann and G. Zweig in 1964. The baryons consist of three quarks, the mesons of quark-antiquark pairs [1]. Within the Standard Model the masses of the 3 lightest quarks called "u", "d" and "s" are $m_u = 1.7 - 3.1\,\mathrm{MeV}$, $m_d = 4.1 - 5.7\,\mathrm{MeV}$ and $m_s = 100^{+30}_{-20}\,\mathrm{MeV}$ [2] [N$^+$10]. The quarks are fermions, with spin of 1/2. The fractional electric charge q of the "u" quark is $q = +\frac{2}{3}$, "d" and "s" quarks have a charge of $q = -\frac{1}{3}$. Since the "u" and "d" quarks are close in mass they can be considered as two different states of the same particle. Also, the proton and the neutron

[1] The difference between constituent and current quarks is discussed further in the text.

[2] After discovery of the three low-mass quarks, three additional quarks called "c", "b" and "t" with significantly higher masses were found.

are very close in mass, are not distinguished by the strong interaction and can be considered as two different states of the nucleon. A quantum number called isospin, with the value of I = 1/2 is assigned to the nucleons, for the proton the third component of the isospin is $I_3 = \frac{1}{2}$, for the neutron $I_3 = -\frac{1}{2}$. The isospin of the "u" and "d" quarks is I = 1/2, forming an isospin doublet with $I_3 = +\frac{1}{2}$ for the "u"-quark and $I_3 = -\frac{1}{2}$ for the "d"-quark, the "s" quark is isosinglet.

When the idea of the quarks was introduced the following question arose. Since the quarks are fermions with the spin of 1/2 they follow the Pauli principle claiming that there can not be more than one identical fermion in the same quantum state, or in other words that the wave function of any system consisting of identical fermions is antisymmetric. The wave function of baryons can be written as

$$\psi = \psi_{space}\psi_{spin}\psi_{flavor}, \tag{1.1}$$

where ψ_{space} describes the spatial wave function of the quarks, ψ_{spin} the spins and ψ_{flavor} the flavors of the quarks building the baryon. However, there are baryons with three identical quarks, e.g. Δ^- consisting of 3 "d" quarks, Δ^{++} of three "u" quarks and Ω^- of three "s" quarks. Taking into account that the space wave function is symmetric because the quarks are in angular orbital momentum L = 0 ground state for the lowest mass baryons [3] and the spin wave function is symmetric for J = 3/2 states, there is a contradiction to the Pauli principle stated above. To resolve this inconsistency a new quantum number called "color" was introduced for quarks. Three colors of the quarks were defined as "red", "green" or "blue". For the antiquarks respectively an anticolor was introduced. In nature only colorless or "white"[4] particles are observed. It means that either a quark of given color and an antiquark with corresponding anticolor or the quarks of all three colors (or anticolors) must be present in the hadron. Quarks or particles with non-white color are never observed as free particles. This phenomenon is called confinement of quarks in hadrons. The wave function of baryons given in 1.1 can be extended to include the color term:

$$\psi = \psi_{space}\psi_{spin}\psi_{flavor}\psi_{color}. \tag{1.2}$$

[3] See more details about octet and decuplet of lightest baryons below in the text.
[4] In analogy with optics where the mixing of light with three main colors turns into white.

Here ψ_{color} has to be antisymmetric, thus leading to the antisymmetric full wave function ψ for baryons. The wave function ψ_{color} for baryons has the following form:

$$\psi_{color} = (RGB - RBG + BRG - BGR + GBR - GRB)/\sqrt{6}. \tag{1.3}$$

Another problem was that the masses of the quarks do not add up to the complete mass of the particles which they form. This inconsistency can be explained by internal structure and interactions within hadrons. The carriers of this (strong) interaction are the gluons. These are massless particles with spin 1, introduced in Quantum Chromodynamics (QCD) which is the theory of the strong interaction. The gluons can produce gluons or quark-antiquark pairs within hadrons, which can further annihilate into gluons. Such processes form a quark-gluon sea which contributes to the mass of a hadron. Thus, two types of the quark masses were introduced: constituent quark masses being the masses of the quarks accounting for the internal interaction within hadrons and current quark masses, defined before, without considering the internal interaction. The constituent quark masses significantly exceed the current masses and are in the order of 350 MeV for "u" and "d" quarks and 500 MeV for "s" quarks. Since the "s" quark is responsible for the strangeness of the particles one can understand the difference in the masses of different states corresponding to the rows of the baryon decuplet (Figure 1.1), the significant change is due to the addition of contributing "s" quarks.

In the Eightfold way classification of particles suggested by Gell-Mann the "u", "d" and "s" quarks which are much lighter than the 3 other quarks can be considered within a special unitary SU(3) group and combined in baryons with the following combinations:

$$3 \otimes 3 \otimes 3 = 10 \oplus 8 \oplus 8 \oplus 1. \tag{1.4}$$

The ten states represent a completely flavour symmetric decuplet, there are two octets with mixed symmetry, the singlet is completely antisymmetric. The total wave function for baryons has to be antisymmetric, thus in nature a completely symmetric flavour decuplet and an octet formed by combinations of the mixed symmetric spin and flavour states occur. Figure 1.1 shows the octet of the lightest baryons with total angular momentum of J = 1/2 and the decuplet of the lightest

baryons with J = 3/2. In the multiplets the particles are ordered according to the third component of the isospin and strangeness [5]. The strangeness (S) in the multiplets varies from one row to another, the isospin in the horizontal direction, the charge (Q) of the particles is defined by the diagonal lines [Gri08] [Per86].

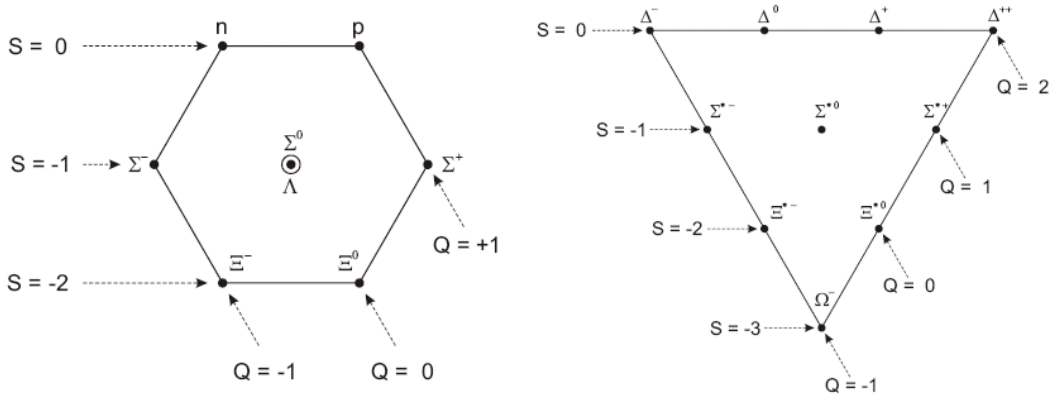

Figure 1.1.: Eight lightest baryons with J = 1/2 (left), ten lightest baryons with J = 3/2 (right).

1.2. Excited baryons

Excited baryonic states can be created by the interactions of baryons with high energetic particles e.g. with photons or pions. Modern quark models, an overview of which is given in [CR00], predict a large number of excited baryonic states, but a large set of the resonance states have not been observed experimentally so far. In particular a serious inconsistency between experimental observations and predictions of symmetric quark models, where all three quark participate in the dynamics, is present in the mass range above 1.9 GeV. A possible explanation for these states not being observed is the fact that until now the most of the data on baryon resonances has been acquired by experiments using pion beams scattering on the nucleons. It might be that the missing states couple weakly to the pion-induced reactions, but couple to other production channels as suggested e.g. by

[5] Historically, when the baryon decuplet of states was constructed the Ω^- was not a known particle. It was predicted by Gell-Mann and later discovered experimentally.

[CR94]. In models using a single quark and a diquark system [Lic69][San05], formed out of two other quarks, the number of states is much smaller.

In the following the problem of the missing states is discussed based on the prediction of the Bonn model [MUMP03] [LMP01] for the nucleon and Δ resonances. They are shown in Figures 1.2 and 1.3, where the blue lines indicate the predicted states, the colored boxes show the experimentally observed states, the bars indicate the uncertainty in the determination of the resonance masses. Many of the predicted states, especially at higher masses were either not found experimentally or the observed states are only one-star (evidence of existence poor [N^+10]) or two-star (evidence of existence is only fair [N^+10]) resonances. Another problem to be investigated is the presence of states which have been found experimentally but are not predicted by the quark models such as $S_{31}(1900)$, $D_{33}(1940)$ and $D_{35}(1930)$. These negative parity resonances were found with less significance compared to their positive parity partners ($P_{31}(1910)$, $P_{33}(1920)$ and $F_{35}(1905)$). The existence of these states is a topic of many discussions, related to restoration of chiral symmetry [Glo00] and quark dynamics [Kle03].

Recent Lattice QCD calculations [EDRW11] predict a number of states similar to the predictions of the Bonn model at low masses (see states marked by the red boxes in Figure 1.4, numbers give the occurring multiplicity of states with a certain quantum number) [6]. The pattern predicted by the Lattice QCD does not show the parity doublets which were also not predicted by the symmetric quark models, but were found experimentally. To resolve the existing questions new experimental input is necessary. In the next section the opportunities for the investigation of the resonance spectrum using double pion photoproduction will be discussed.

[6] The calculation shown in Figure 1.4 was produced with certain approximations, for example the pion mass of 396 MeV was used.

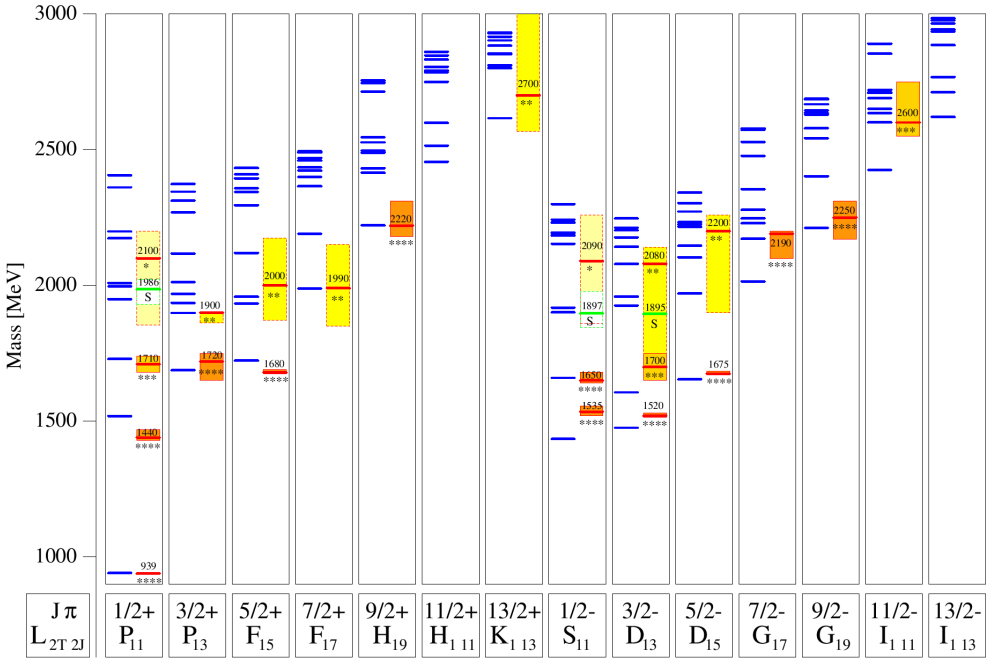

Figure 1.2.: Nucleon resonances predicted by the Bonn model [LMP01], blue: predicted states, colored boxes: experimentally observed states, bars: the error of the measurement, J: spin, π: parity, T: isospin.

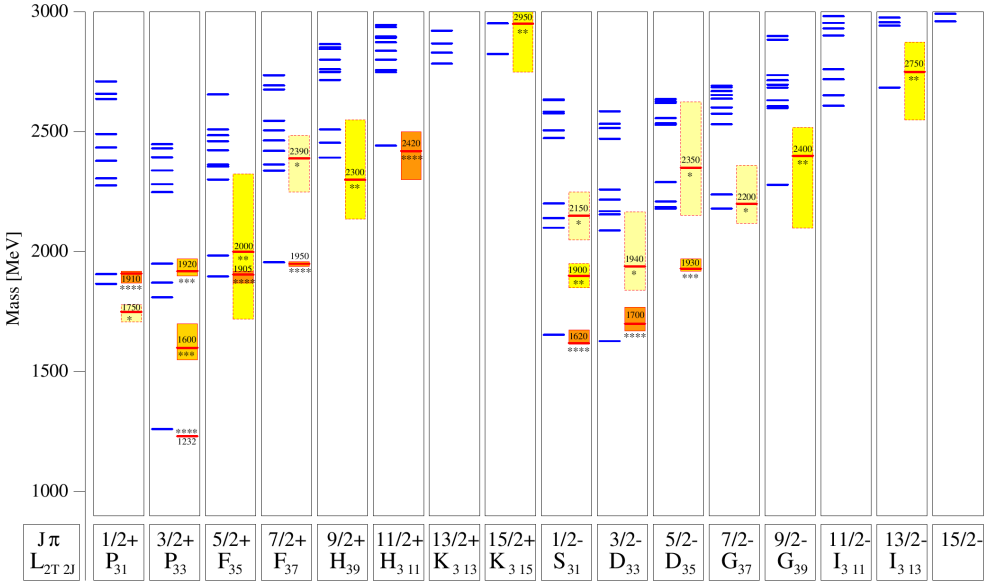

Figure 1.3.: Δ resonances predicted by the Bonn model [LMP01], blue: predicted states, colored boxes: experimentally observed states, bars: the error of the measurement, J: spin, π: parity, T: isospin.

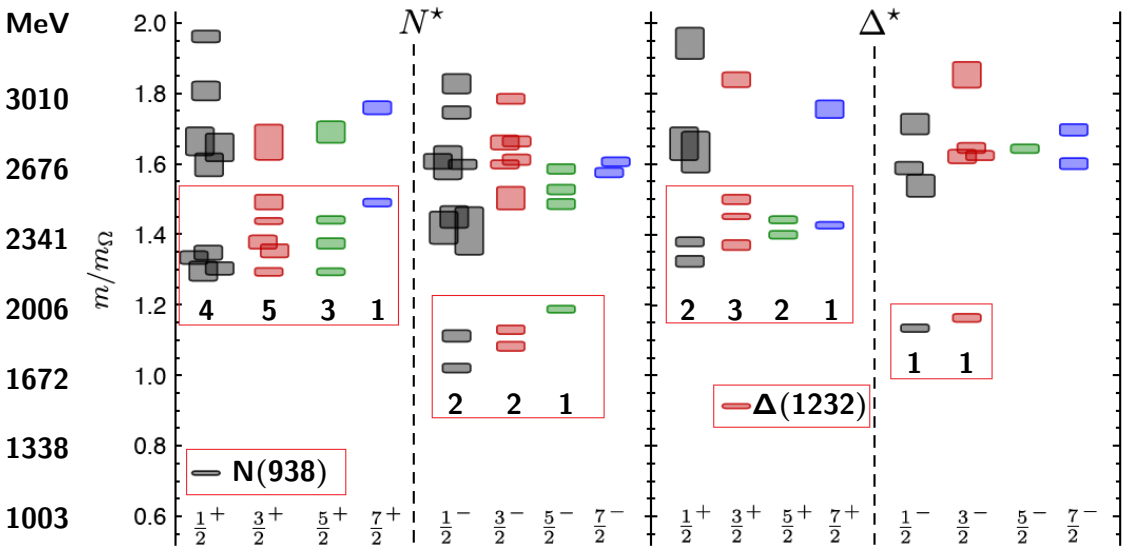

Figure 1.4.: Nucleon and Δ resonances according to the Lattice QCD [EDRW11]. Boxes include patterns with numbers of states compatible with numbers obtained in the Bonn model.

1.3. Double pion photoproduction

Double meson as well as the single meson final states are used to study the properties of baryon resonances in photoproduction experiments. In Figure 1.5 the cross-section of the total photoabsorption, together with the cross-sections of the reactions $\gamma p \to p\pi^0$, $\gamma p \to p\eta$, $\gamma p \to p\pi^0\pi^0$ and $\gamma p \to p\pi^0\eta$ are plotted as a function of the incoming photon energy. For these neutral channels the cross-sections of single meson photoproduction dominate at low energies, whereas the cross-sections of the reactions with two-meson final states are larger at higher energies, where the missing resonance problem occurs (see Section 1.2). The structures seen at different positions in the cross-sections are due to contributions of different resonance states in different reactions. To obtain a complete picture of resonances one has to disentangle their contributions and to understand the interference effects. The resonance properties such as masses, quantum numbers and decay modes can be determined using Partial Wave Analysis (see Section 1.5).

A given resonance or a set of resonances might not contribute to one reaction channel, but have a strong contribution in another. The reaction $\gamma p \to p\pi^0\pi^0$ has the advantage that background terms such as the direct $\Delta\pi$ production, t-channel and Born terms are suppressed [TvPS+05] in comparison e.g. to the channel $\gamma p \to p\pi^+\pi^-$, where the contribution of background terms is significant. Another difference from the reaction $\gamma p \to p\pi^+\pi^-$ is the fact that the contribution of $\rho(770)$ is not present in $\gamma p \to p\pi^0\pi^0$ because its decay into $\pi^0\pi^0$ is forbidden. A relatively low contribution from background terms in the channel $\gamma p \to p\pi^0\pi^0$ leads to a high sensitivity for the investigation of baryon resonances.

Another advantage given by double meson final states is the possibility to access cascading resonance decays via intermediate states e.g. $\gamma p \to N^*/\Delta^* \to \Delta(1232)\pi^0 \to p\pi^0\pi^0$, $\gamma p \to N^*/\Delta^* \to D_{13}(1520)\pi^0 \to p\pi^0\pi^0$ and $\gamma p \to N^*/\Delta^* \to F_{15}(1680)\pi^0 \to p\pi^0\pi^0$. The latter channels were observed for the first time in [Fuc05] and confirmed in this work (see Section 5.5).

Earlier results

There have been a number of experimental and theoretical studies of baryon resonances using the reaction $\gamma p \to p\pi^0\pi^0$. However, there are still many open

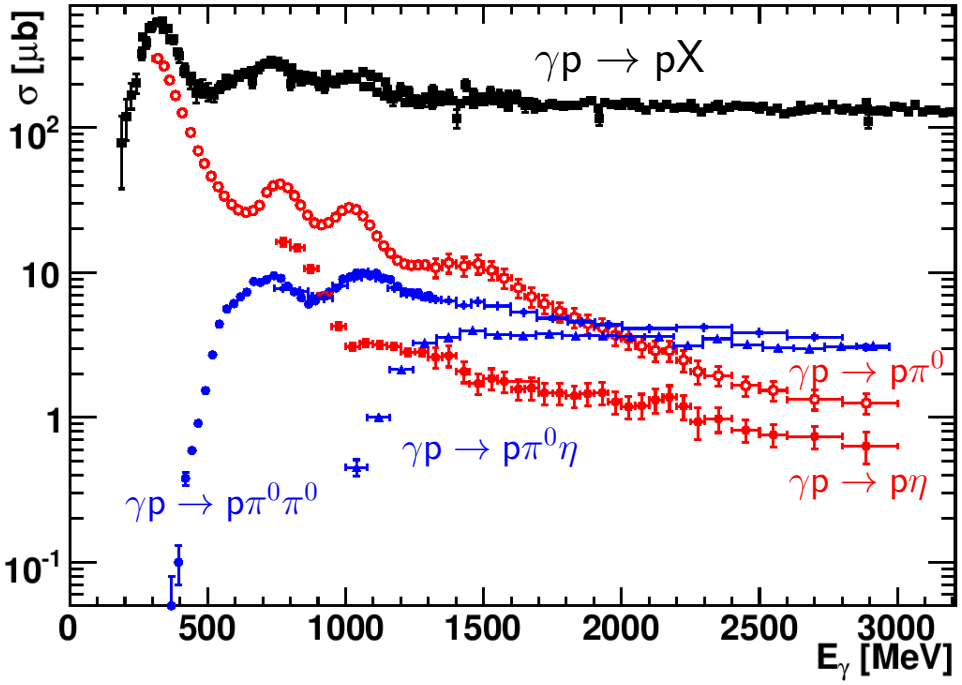

Figure 1.5.: The cross-sections of the photon induced reactions. Black: total photoabsorption cross-section (world data), blue circles the cross-section of $\gamma p \to p\pi^0\pi^0$, blue triangles: $\gamma p \to p\pi^0\eta$, open red circles: $\gamma p \to p\pi^0$, filled red squares: $\gamma p \to p\eta$ (CBELSA data).

questions which can probably be answered based on the new experimental results. In the low energy range the Roper-resonance $P_{11}(1440)$, which contributes to the reaction $\gamma p \rightarrow p\pi^0\pi^0$, is expected according to the quark models to exceed the mass of the lowest mass negative parity state $S_{11}(1535)$ [CR00] [LMP01] [S$^+$08] [TvPS$^+$05], but is observed with significantly lower mass. One heavily debated question (see e.g. [A$^+$03]) was whether the reaction $\gamma p \rightarrow p\pi^0\pi^0$ is dominated by $P_{11}(1440)$ with further $N\sigma$ decay or by $D_{13}(1520)$ decaying into $\Delta\pi$. This question is discussed in detail in Section 1.5. Another issue under investigation is the decay of $D_{13}(1520)$ into $(\Delta\pi)_{D-wave}$ which was found with similar strength as the decay into $(\Delta\pi)_{S-wave}$ [T$^+$08]. For the $D_{13}(1700)$ the D-wave contribution was found to be stronger than the S-wave contribution. These observations contradict the naive expectations expecting suppression of the D-wave due to the orbital angular momentum barrier. In the energy range used in the determination of the polarization observables in this work ($E_\gamma = 970 - 1650\,\mathrm{MeV}$), many resonances such as $D_{13}(1520)$, $F_{15}(1680)$, $D_{33}(1700)$, and $P_{13}(1720)$ contribute to the channel $\gamma p \rightarrow p\pi^0\pi^0$ [T$^+$08] [TvPS$^+$05]. These resonances are predicted with different strengths in different models and new experimental input is necessary to clarify these differences (see Sections 1.5 and 5.6). Also, in this energy range it was not possible to make a decision using Partial Wave Analysis about the decay mode of the $D_{33}(1700)$ - whether it is dominated by S- or D-wave [T$^+$08] [S$^+$08], see Sections 1.6, 5.1 and 5.4.

In the higher energy range [7] ($E_\gamma > 1500\,\mathrm{MeV}$) the missing resonances may contribute. The negative parity Δ-resonances $S_{31}(1900)$, $D_{33}(1940)$ and $D_{35}(1930)$ described in Section 1.2 also can be studied with the double pion photoproduction data. Another question is that, although the states $P_{11}(2100)$, $P_{13}(1900)$, $F_{15}(2000)$ and $F_{17}(1990)$ are observed experimentally, as either one- or two-star resonances [N$^+$10], they are not reproduced by the quark model with one frozen diquark. The confirmation of existence of these states may pose a problem for the quark-diquark models.

Many of the existing results were obtained using cross-section data. However, for the unambiguous identification of resonances and the determination of their

[7] Partly overlapping with the range used for the measurement of the polarization observables in this work.

properties the measurement of only unpolarized cross-sections is not enough. The knowledge about polarization observables provides new constraints for the Partial Wave Analysis and allows us to make a step towards the full description of the reaction and determination of the properties of contributing states.

1.4. Polarization observables

If a well defined set of observables, for a so called "complete experiment" is known, the amplitudes and their relative phases, defined for the reaction under investigation can be unambiguously determined [RO05] [BDS75]. In reactions with the photoproduction of two pseudoscalar mesons, 64 polarization observables from single, double and triple polarization measurements can be extracted. Due to the relations between contributing helicity or transversity amplitudes and their phases that number can be reduced to 15 observables [RO05]. If one considers only the option of a polarized beam, the differential cross-section for the double meson photoproduction can be written in the form [RO05] :

$$\frac{\mathrm{d}\,\sigma}{\mathrm{d}\,\mathrm{x_i}} = \left(\frac{\mathrm{d}\,\sigma}{\mathrm{d}\,\mathrm{x_i}}\right)_0 (1 + \delta_\odot\ I^\odot + \ \delta_l\,(\,\mathbf{I^c}\cos 2\varphi + \ \mathbf{I^s}\sin 2\varphi)), \tag{1.5}$$

where $\left(\frac{\mathrm{d}\,\sigma}{\mathrm{d}\,\mathrm{x_i}}\right)_0$ is the unpolarized cross-section, δ_l is the degree of linear polarization of the beam, $\delta_\odot$ - the degree of circular polarization of the beam. φ is the azimuthal angle, x_i corresponds to the 5 independent variables, the reaction $\gamma\mathrm{p} \rightarrow \mathrm{p}\pi^0\pi^0$ depends on. I^c, I^s and $I^\odot$ are the polarization observables. The angle $\varphi - 90^\circ$ shown in Figure 1.6 is the angle between the polarization plane, formed by the electric field vector and momentum of the incoming photon and the production plane formed by the momentum of the incoming photon and of the recoiling particle. The angle ϕ^* is the angle between the production plane and the decay plane formed by the particles in the final state [8].

This thesis focuses on the measurement of the polarization observables I^c and I^s occurring if the beam is linearly polarized. These observables can be determined as function of the angle ϕ^*. In Section 5.4 it will be shown in detail that the

[8] For the two-body final state the production and decay planes are identical.

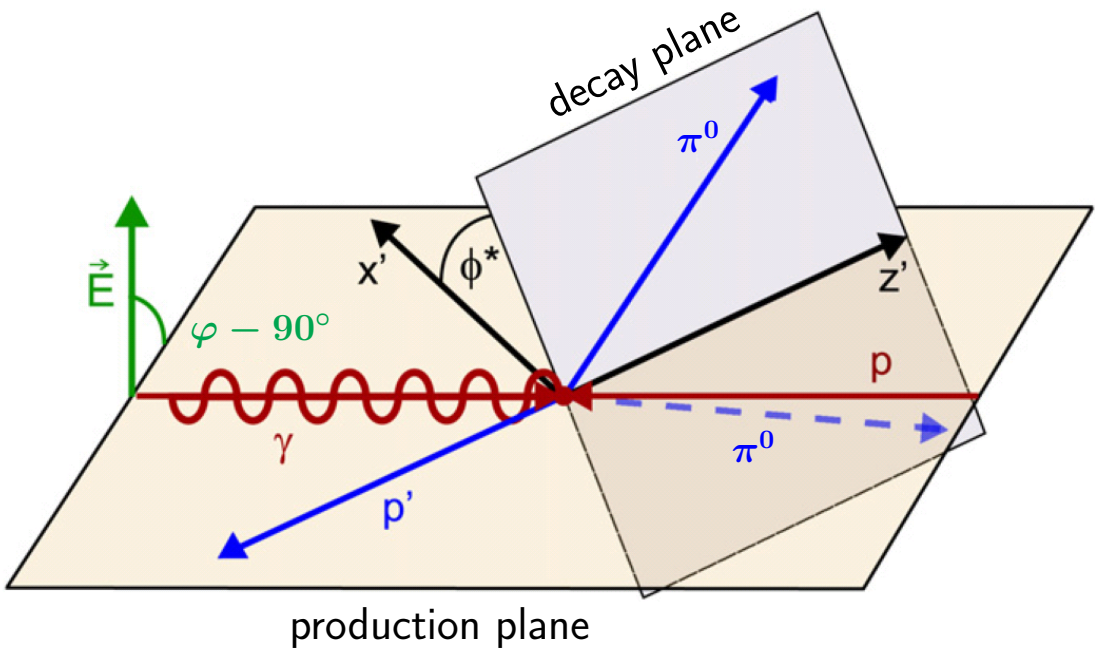

Figure 1.6.: Three-body kinematics and definition of angles, figure taken from [GSvP+10]. For the description see text.

polarization observable Σ, typical for the two-body final state (Section 5.1), is only a special case defined for the observable I^c in a quasi-two body consideration if one integrates over the angle ϕ^* [9]. It means that Σ, which was the only polarization observable measured so far with linearly polarized photons and unpolarized target in the reaction $\gamma p \to p\pi^0\pi^0$ [A+03], still provides a valuable input for the complete experiment, but the comprehensive measurement can be achieved only in a full consideration of the three-body kinematics. Until now the observables I^s and I^c, taking into the account special kinematics of the three-body final state, were only measured for the reaction $\gamma p \to p\pi^0\eta$ [GSvP+10]. In this work the first measurement of I^s and I^c in the reaction $\gamma p \to p\pi^0\pi^0$ is presented.

[9] In a quasi two-body approach $I^s = 0$ by definition (see Section 5.4).

1.5. Interpretation of the data

Most of the baryon resonances being broad and overlapping cannot be observed directly by the consideration of the cross-sections. The information obtained from the experimental data can be transferred into the terms of resonance contributions using Partial Wave Analysis and isobar models. In this section a short overview of the existing models is given. The main contributions of the resonances in the models are discussed as well as the outcome related to the topic of this work. More information about the formalism of the models can be found in the corresponding references.

Bonn-Gatchina Partial Wave Analysis

The Bonn-Gatchina Partial Wave Analysis (BnGa-PWA) in the case of double meson photoproduction is an event-based maximum likelihood fit, which allows us to determine the properties of resonances such as masses, widths, quantum numbers and decay modes. The techniques used in the BnGa-PWA can be found in [AS06] [ASB$^+$05] [AKST05] [ABK$^+$12]. The BnGa-PWA uses a wide database obtained at experiments using photoproduction and pion-nucleon scattering. Single and double pseudoscalar meson production reactions, and also data on the strangeness production are included. The database consists of both cross-section data and data on the polarization observables [ABK$^+$12]. A combined fit using the complete data base is performed. The fit to the included reactions fixes the parameters such as masses and total widths which must be the same in all the reactions. When some of the parameters are fixed (e.g. masses in a given set of resonances) the determination of the others is performed with less available freedom. For example less freedom is present in the fit performed for the reaction $\gamma p \rightarrow p\pi^0\pi^0$, because the previously included data on the single meson photoproduction influence the determination of resonance properties. An important feature of the BnGa-PWA is that the analysis is event based and the 4-vectors of the particles are considered. This allows to take all correlations between kinematic variables in the phase space into account. It is an important advantage in comparison to the methods which use projections only (e.g. on the investigated kinematic variable) because in that case the information about correlations is lost. The results of the BnGa-PWA in regard to the reaction $\gamma p \rightarrow p\pi^0\pi^0$ can be found

in [S$^+$08] [T$^+$08] and [Fuc05]. In the sections 5.1 and 5.4 the predictions based on the Partial Wave Analysis published in [T$^+$08] are compared to the data on the polarization observables Σ, I^c and I^s. Presently the data on the polarization observables measured in this work are also included in the BnGa-PWA.

Laget model

The extension of the Murphy and the Laget model [ML95], called Laget model and discussed in [A$^+$03] is based on the contributions of the states $P_{11}(1440)$, $P_{11}(1710)$, $D_{13}(1520)$, $D_{13}(1700)$, $D_{33}(1700)$. It was found within this model that the state $P_{11}(1440)$ decaying into σp and $\Delta\pi$ is the most important for the reaction $\gamma p \to p\pi^0\pi^0$. The data on the cross-sections and polarization observable Σ have been published in [A$^+$03], for the observable Σ, see also Figure 1.10. In the same paper the authors mention the necessity of the Partial Wave Analysis with a large database.

Valencia Model

The model, developed by Oset [TO96] takes into account large number of possible processes, but the main contributions are $P_{11}(1440)$, $D_{13}(1520)$ and $D_{33}(1700)$. The resonance $D_{13}(1520)$ with further decay into $\Delta\pi$ is taken as the most important ingredient of the model. The model is valid in the photon energy range up to 800 MeV for the reaction $\gamma p \to p\pi^0\pi^0$ and does not overlap with the energy range used for the extraction of the polarization observables in this work. The predictions for the observable Σ in the energy range up to 780 MeV can be found in [NO02] (see also Figure 1.10). The differences between Laget and Valencia models are discussed in Section 1.6.

Fix Isobar model

In the isobar model, developed by Fix et al. for the reaction $\gamma p \to p\pi^0\pi^0$ [Fix05], the four star resonances in the mass region lower than 1.8 GeV are included; exceptions are the resonances $S_{11}(1650)$ and $P_{11}(1710)$ which were not included assuming that the corresponding cross-sections are almost negligibly low. The resonance parameter were not fitted to the experimentally obtained cross-sections. The decay widths used to fit the hadronic coupling constants were taken from PDG, see [Fix05] for more details. The contribution of $D_{13}(1520)$ dominates in the

second resonance region, also significant contributions are provided by $P_{11}(1440)$, $F_{15}(1680)$ and $S_{11}(1535)$. The prediction of the model for the observable Σ are shown in Figure 1.7 together with GRAAL data [A$^+$03][10]. In the low energy range where the amplitude of Σ both for GRAAL data and model predictions is close to 0 the differences are not large, whereas at high energies the sign and the structure of the model and data are different. A comparison of the polarization observables obtained from experimental data, Fix model and BnGa-PWA is shown in Section 5.6.

1.6. Existing data

Cross-sections

The total cross-section of the reaction $\gamma p \to p\pi^0\pi^0$ in the photon energy range starting from threshold up to 820 MeV was measured by the TAPS experiment and published in [H$^+$97] [W$^+$00] [S$^+$08]. There are 2 later articles [Kot04] and [K$^+$04] with results on the total and differential cross-sections. The GRAAL experiment also measured the total cross-section and invariant mass spectra [A$^+$03]. During the first running period the CBELSA experiment was focusing at the measurement of the total and differential cross-sections, which were published for the reaction $\gamma p \to p\pi^0\pi^0$ in [T$^+$08] [S$^+$08] and [Fuc05].

Figure 1.8 shows the total cross-section measured by the CBELSA experiment together with TAPS and GRAAL data compared to a BnGa-PWA fit [S$^+$08] [T$^+$08]. According to the BnGa-PWA, the two-peak structure in the total cross-sections is produced due to the interference between D_{33} and D_{13} partial waves. The BnGa-PWA predicts strong contribution of the $D_{33}(1700)$ resonance (see Figure 1.8), the second strong contribution in the region of the first peak in the total cross-section is due to the $D_{13}(1520)$. The contribution of the P_{11} partial wave is smaller and increases around 1700 MeV due to the contribution of the $P_{11}(1710)$. In the Fix isobar model the contribution of the $D_{33}(1700)$ is relatively low. The strongest contribution in the second resonance region is due to $D_{13}(1520)$, the second peak

[10] For more information about GRAAL data see Section 1.6.

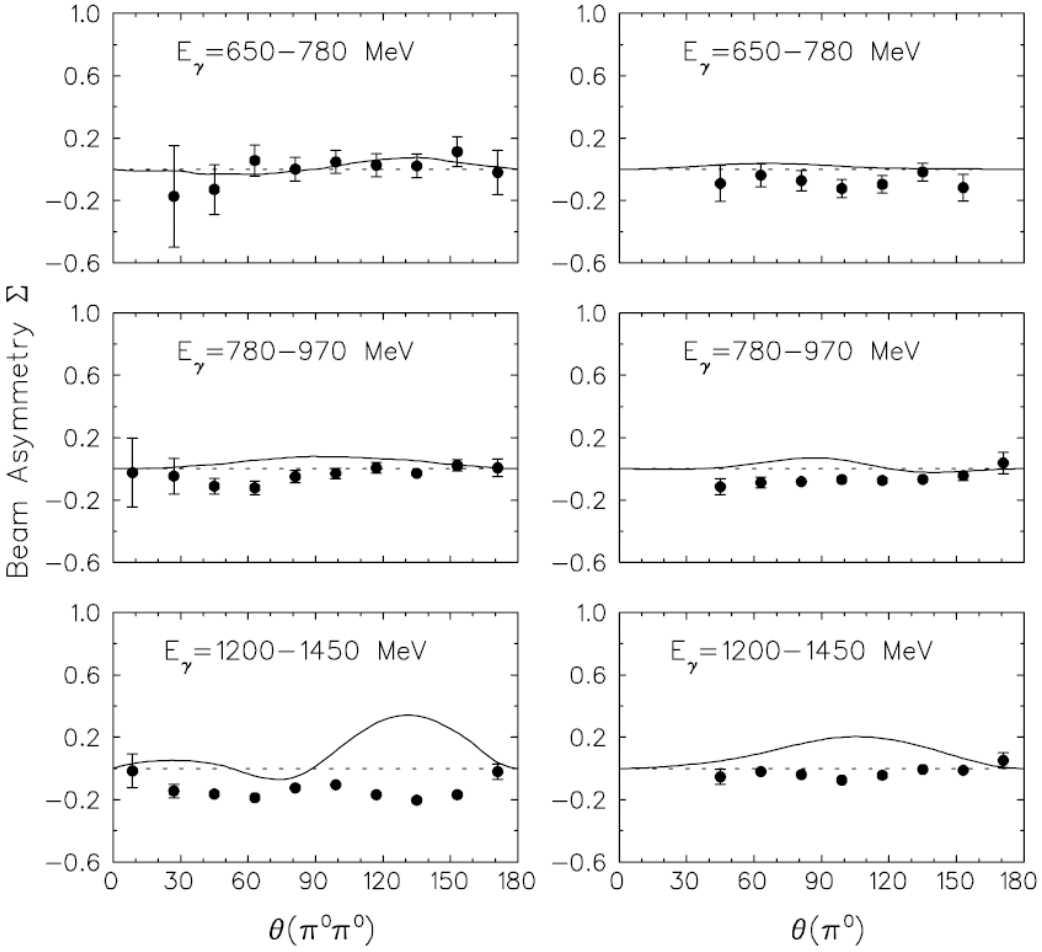

Figure 1.7.: The solid curves show Σ predicted by the isobar model [Fix05], dashed lines indicate the zero line. Left column: Σ is shown as function of polar angle of the $\pi^0\pi^0$ system (proton recoiling), on the right as function of polar angle of one of the pions (the other pion recoiling). The data points are from [A$^+$03].

in the total cross-section of $\gamma p \to p\pi^0\pi^0$ is explained mostly by the contribution of $F_{15}(1680)$ [11].

The two very different scenarios in the Laget model predicting the dominance of $P_{11}(1440) \to N\sigma$ mode in the reaction $\gamma p \to p\pi^0\pi^0$ and Valencia model predicting dominant contribution of $D_{13}(1520)$ with further $\Delta\pi$ decay, were compared in the energy range up to 800 MeV (see Figure 1.9). Both models describe the experimentally measured total cross-section with the same quality, but the resonance strengths are very different. The measurement of the polarization observable Σ (see discussion below and Figure 1.10) and of the invariant masses did not lead to a clear answer of the question about dominant resonance contribution in the reaction $\gamma p \to p\pi^0\pi^0$ [A$^+$03]. This issue was also studied based on the data obtained with circularly polarized photon beam impinging on the longitudinally polarized target at the MAMI facility in Mainz [A$^+$05]. The measurement has shown that the $\sigma_{3/2}$ cross-section obtained with parallel configuration of the photon-nucleon spin significantly exceeds the $\sigma_{1/2}$ cross-section obtained with antiparallel photon-nucleon spin configuration. This observation indicates that the helicity 3/2 contribution and respectively according to the Valencia model the $D_{13}(1520)$ resonance, is preferred in the reaction $\gamma p \to p\pi^0\pi^0$. The BnGa-PWA confirms this observation, predicting also strong contribution of the $D_{33}(1700)$ resonance. Also, as mentioned above according to the Fix model the $D_{13}(1520)$ resonance has the strongest contribution in the second resonance region.

[11] Resonance contributions in the BnGa-PWA and in the Fix model are discussed in more detail in Section 5.6.

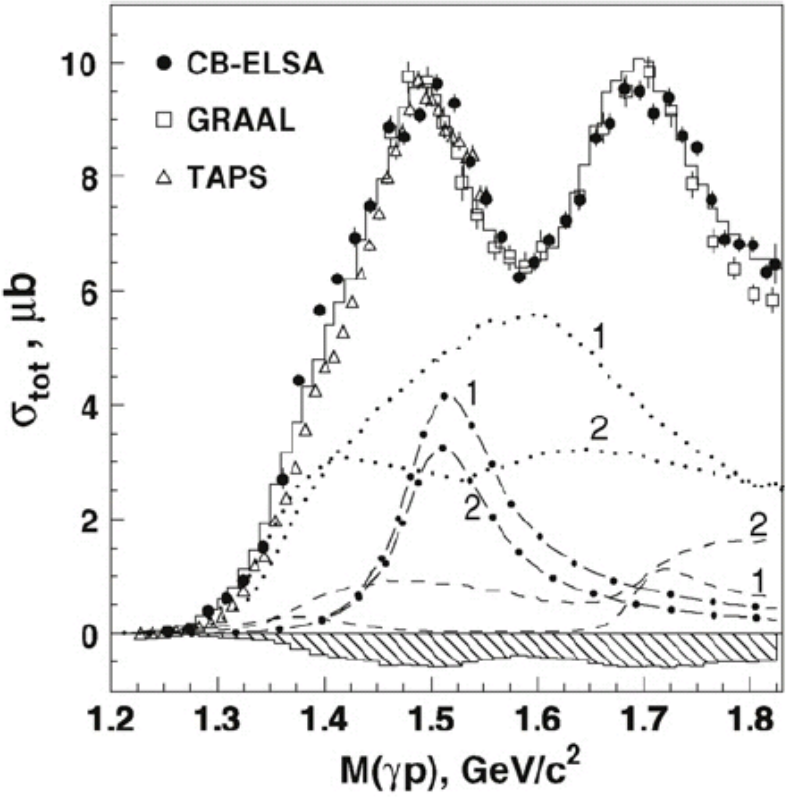

Figure 1.8.: The total cross-section of the reaction $\gamma p \to p\pi^0\pi^0$ [S$^+$08] measured by the CBELSA, GRAAL and TAPS experiments. The solid curve represents result of the BnGa-PWA fit, the shaded area shows the systematic error of the measurement of the CBELSA data. Solution 1 (BnGa-PWA) corresponds to the $D_{33}(1700) \to \Delta\pi$ decay with S-wave dominance, solution 2 with D-wave dominance. Dotted line: contribution of the D_{33} partial wave, dashed-dotted line: D_{13} and dashed line: P_{11}.

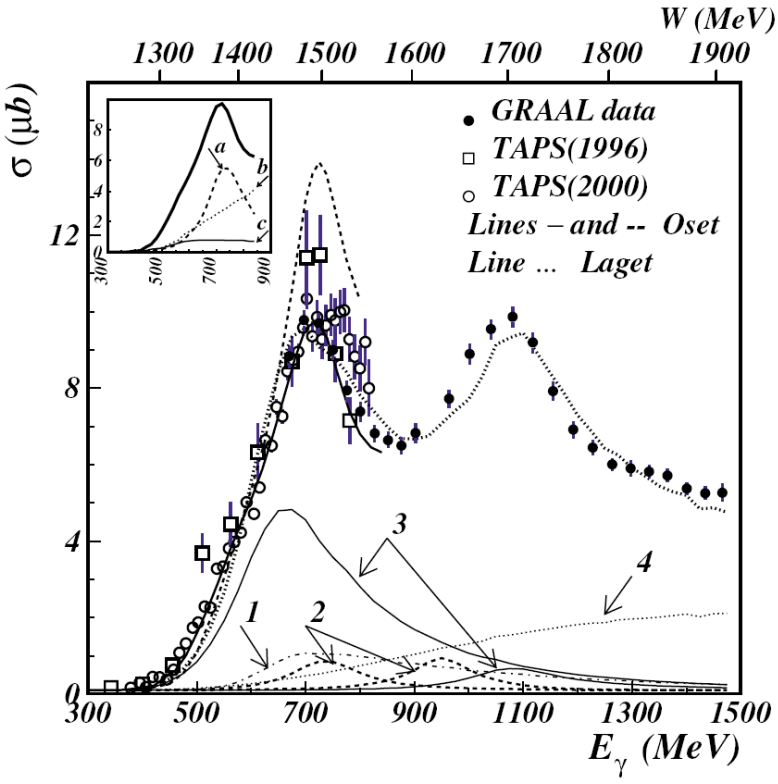

Figure 1.9.: The total cross-section of the reaction $\gamma p \to p\pi^0\pi^0$ measured by the GRAAL [A$^+$03] and TAPS [H$^+$97] [W$^+$00] experiments compared to the calculations of Valencia and Laget models. The contributions of resonances according to the Laget model are shown in the lower part of the figure. Label 1 (dashed-dotted line) shows the contribution of $\gamma p \to P_{11}(1440) \to \Delta(1232)\pi^0$, label 2 (dashed) $\gamma p \to D_{13}(1520), D_{13}(1700) \to \Delta(1232)\pi^0$, label 3 (solid) $\gamma p \to P_{11}(1440), P_{11}(1710) \to \sigma p$, label 4 (dotted) $\gamma p \to \sigma p$. The main contributions of the resonances included in the Valencia model are shown in the inset, the lines (a), (b), (c) correspond respectively to the $D_{13}(1520)$, $\Delta(1232)$ and $P_{11}(1440)$ [A$^+$03].

Polarization observables

Presently the only published data on the polarization observables measured in the reaction $\gamma p \rightarrow p\pi^0\pi^0$ with linearly polarized photons have been obtained with the GRAAL experiment [A$^+$03]. The linearly polarized photon beam was produced via the laser-backscattering method. Polar angles from 25° up to 155° were covered by the bismuth germanate (BGO) calorimeter. Forward angles below 25° were covered by a shower wall and a double wall of scintillators. In the analysis two classes of events with distinct geometrical signature were considered. The first class includes events with four photons detected in the BGO calorimeter, the second class with three photons in the BGO and one photon in the forward shower wall. This signature becomes relevant in the comparison of the GRAAL and the CBELSA/TAPS data and is discussed in detail in Section 5.3.

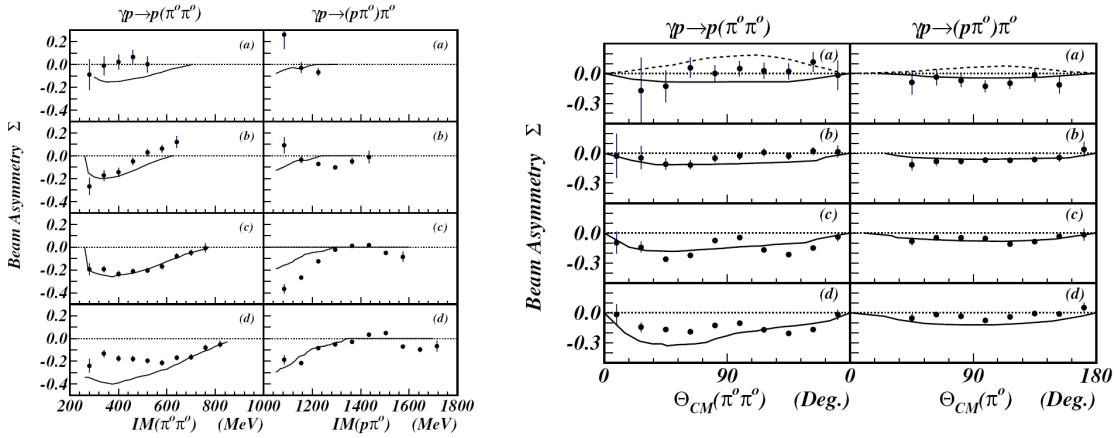

Figure 1.10.: Four incoming photon energy ranges are shown [A$^+$03]: (a) 650-780 MeV, (b) 780-970 MeV, (c) 970-1200 MeV, (d) 1200-1450 MeV. On the left: Σ as a function of the invariant masses $m_{\pi^0\pi^0}$ (proton recoiling) and $m_{p\pi^0}$ (pion recoiling), on the right as function of the angles $\Theta_{\pi^0\pi^0}$ (proton recoiling) and Θ_{π^0} (pion recoiling). Solid curve: Laget model, dashed curve: Valencia model (covers up to 780 MeV).

The quasi two-body beam asymmetry Σ was measured in the energy range of the incoming photon up to 1450 MeV. The results are presented in Figure 1.10, where various structures in Σ can be seen as a function of angles and invariant masses. The data are compared with the predictions of Valencia (up to 780 MeV) and

Laget models. In the lowest energy range (650-780 MeV) the data show amplitudes close to 0. Both Valencia and Laget models do not show good agreement with the experimental data in this energy range. At higher energies significant amplitudes occur in the data and Laget model in general predicts correctly the sign of Σ and in some cases the shapes seen in the data. However noticeable differences are present between the data and Laget model predictions, for example in the energy range 1200-1450 MeV in the $m_{\pi^0\pi^0}$ and in the $\theta_{CMS}(\pi^0\pi^0)$. In this work the data on the polarization observable Σ is presented in Section 5.1 where the photon energy range is extended up to 1650 MeV. In the region where CBELSA/TAPS and GRAAL data sets overlap in some of the cases noticeable differences have been obtained. The acceptance effects [12] and compatibility of the existing data sets are discussed in Section 5.3.

There are also measurements of polarization observables performed at MAMI in Mainz with circularly polarized photons impinging on the unpolarized target [KZF$^+$09] where the observable $I^\odot$ was measured. Double polarization measurements at MAMI [A$^+$05] were important to make a conclusion about the strengths of resonance contributions in the reaction $\gamma p \to p\pi^0\pi^0$ (see discussion above).

Even though some of the open questions have been clarified experimentally and using the PWA, many problems still exist. The significant differences between model predictions for the reaction $\gamma p \to p\pi^0\pi^0$ have to be understood. BnGa-PWA and Fix model predict a similar set of resonances produced in the reaction $\gamma p \to p\pi^0\pi^0$, but there are differences in the decay modes and strengths of the resonance contributions. In Section 5.6 is shown that the data on the polarization observables obtained in this work allows to distinguish between these two models (see Section 5.6). Also, there are ambiguities within models which have to be clarified, such as the open question about S- or D-wave dominance in the $D_{33}(1700) \to \Delta\pi$ decay. This issue is rather important, due to the dominant contribution (according to the BnGa-PWA) of this resonance in the reaction $\gamma p \to p\pi^0\pi^0$. In this work the data on the polarization observables is compared with two predictions of the BnGa-PWA produced with these two scenarios (see Sections 5.1 and 5.4). Besides being used for direct comparison with model predictions the data obtained in

[12] Note e.g. limited coverage in $\Theta_{CM}(\pi^0)$ in Figure 1.10.

this work provide new information for the PWA, which allows to access resonance properties.

2. Experimental setup

In this chapter the experimental setup, used to take the data analyzed in this work, is presented. The accelerator ELSA [1] and the production of linearly polarized photons via coherent bremsstrahlung are described. Further the detector components used in the measurement are discussed. In the last section a description of the applied trigger conditions is given.

2.1. ELSA accelerator facility

The electrons with energies up to 3.5 GeV are produced at the three-stage accelerator ELSA [Hil06] located in Bonn, see Figure 2.1. It consists of two LINear ACcelerators (LINAC), one of which, called LINAC2, has been used while data taking for the CBELSA/TAPS experiment in March and May 2003 in the production of the data used in this work. LINAC2 accelerates the electrons up to an energy of 26 MeV, before they are injected into the booster synchrotron which has an opportunity of acceleration up to 1.6 GeV. After acceleration in the booster synchrotron typically to an energy of 1.2 GeV, the electrons are injected into the stretcher ring and can be accelerated up to the maximum energy of 3.5 GeV. The stretcher ring can operate in the three modes: the stretcher mode, the post-accelerator mode and the storage mode. In the stretcher mode the electrons are not further accelerated in the stretcher ring and the energy maximum corresponds to 1.6 GeV [2]. In this mode the electrons are accumulated during several cycles and can be extracted with constant intensity [Hof01]. In the post-accelerator (booster) mode, used in the production of the data investigated in this work, the electrons

[1] ELectron Stretcher Accelerator.
[2] Defined by the acceleration in the booster synchrotron.

can be accelerated in the stretcher ring up to energies of 3.5 GeV [3]. In the storage mode the electron beam is kept at a constant energy within several hours. This mode is used for the solid state physics experiments using synchrotron radiation.

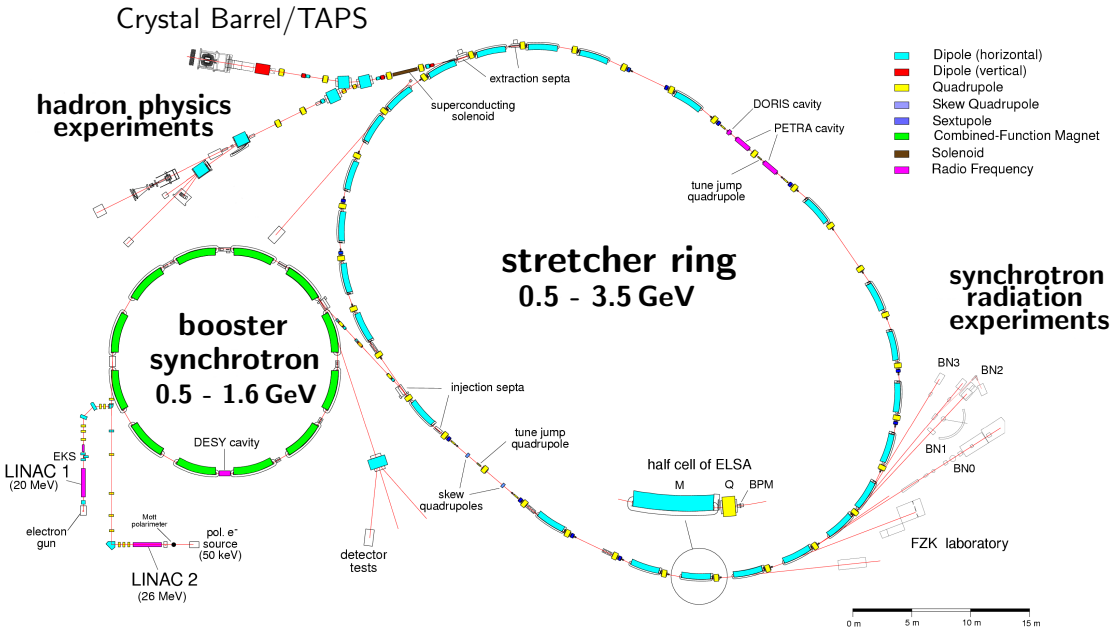

Figure 2.1.: Schematic picture of the ELSA accelerator.

2.2. Production of linearly polarized photons

For the CBELSA/TAPS experiment the electrons accelerated in ELSA were used to produce bremsstrahlung photons on a diamond radiator. The bremsstrahlung photons are emitted due to the deceleration of the electrons in the electric field of the nucleus. If the electron in the amorphous radiator interacts with single atoms there are no preferred directions in the space and respectively no preference for the electric field vector of the emitted photons is obtained. If the recoil momentum is transfered not to the single atom but to the crystal grid, the energy spectrum of the emitted bremsstrahlung photons is modified. The recoil momentum $\vec{q}$ can be transferred to the lattice if it coincides with a vector of the reciprocal lattice

[3] The energy of the electrons used in the beamtimes analyzed in this work was 3.2 GeV.

[Tim69], [E+09] and the condition

$$\vec{q} = n \cdot \vec{g} \tag{2.1}$$

is fulfilled, where $\vec{g}$ is the reciprocal lattice vector defined as $\vec{g} = \sum_{i=1}^{3} h_i \vec{b}_i$, b_i are the basis vectors and h_i the Miller indices of the reciprocal lattice.

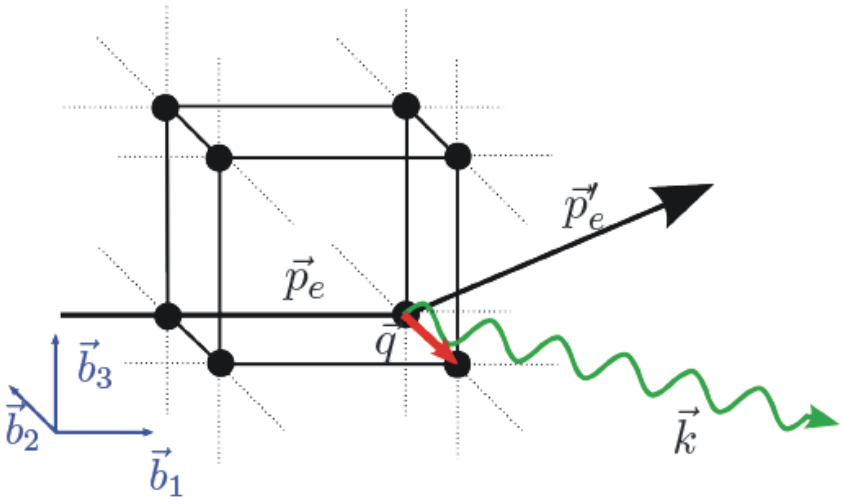

Figure 2.2.: Kinematics of the coherent bremsstrahlung, $\vec{q}$ is the recoil momentum transferred to the lattice, $\vec{p_e}$ the incoming electron momentum, $\vec{p_e'}$ the outgoing electron momentum and $\vec{k}$ momentum of the emitted photon.

In Figure 2.2, the transfer of the recoil momentum to the lattice of the crystal is shown. If the crystal is properly positioned, due to the periodic structure of the crystal and respectively discrete transfer of the momentum, preferred planes occur leading to the preferred directions for the electric field vector, thus producing linearly polarized photons. For the determination of the degree of linear polarization of the photon beam the measurement with diamond crystal only is not enough. The total cross-section of the bremsstrahlung is formed by the sum of the incoherent and coherent contributions. Even if the recoil momentum corresponds to the reciprocal lattice vector, there is a contribution of incoherent bremsstrahlung due to the thermal motion of the atoms. To correct on the effects

mentioned above a measurement with amorphous copper radiator is performed and used for the extraction of the coherent part and respectively of the linear polarization of the photons. The linear polarization of the photons can be calculated by normalization of the coherent contribution with the incoherent contribution, using Analytical Bremsstrahlung Calculation, for more details see [FN03] [E$^+$09] [Gut10].

2.3. The experimental setup

The schematic picture of the CBELSA/TAPS experiment is shown in Figure 2.3. The detectors included in the setup are described in the next sections.

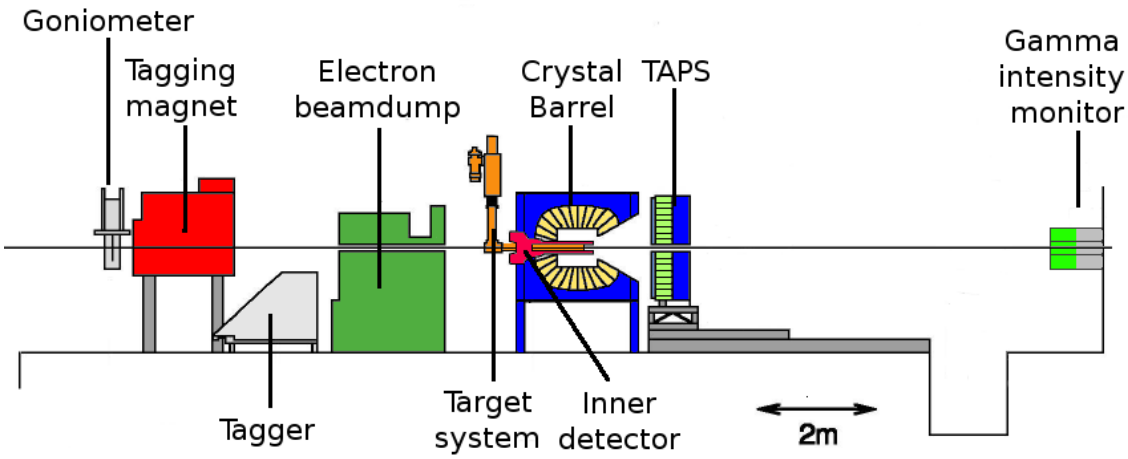

Figure 2.3.: Schematic picture of the CBELSA/TAPS experiment. The figure is taken from [Gut10].

2.4. Tagging system

The energy of the photons emitted via bremsstrahlung can be calculated as

$$E_\gamma = E_0 - E, \tag{2.2}$$

where E_0 is the primary energy of the electrons, E the energy of the electrons after bremsstrahlung. The primary energy E_0 is known with a precision in order of 1 MeV [Fro11]. To measure the electron energy E after bremsstrahlung the electron beam which passes through the dipole magnet, is bent by the magnetic field and thus electrons with different energies [4] are analysed using their position in the tagger (see Figure 2.4).

The tagging system has three parts. The first part consists of 14 scintillator bars with widths varying from 30.5 mm for the uppermost one to 208.3 mm for the lowermost bar, taking into account the rates expected in the experiment. The scintillator bars cover from 22% to 92% of the energy of the electrons delivered by ELSA with an energy resolution of 0.5 MeV at low energies up to 30 MeV at higher energies [Gut10] . The second part of the tagging system is a detector consisting of 480 scintillator fibers with a diameter of 2 mm each. The scintillator fiber detector covers from 18% to 80% of the incoming electron energy. The better granularity of the fiber detector allows to improve the energy resolution of the tagging system, it varies between 2 MeV and 13 MeV. The third component of the tagger is a Multi Wire Proportional Chamber (208 wires) covering from 80% to 92% of the incoming electron energy range [5].

The electrons which were not deflected enough to be detected in the tagger were absorbed in the beam dump (Figure 2.4), which consisted of layers of lead and iron, combined with polyethylene and boron carbide. The beam dump has been built in a way to provide shielding of the detector system against possible background produced by the electrons. Nevertheless, the offline analysis described in the Chapter 4 has shown that there are background contributions in the calorimeters from the beam dump.

2.5. Target

The target in the center of the Crystal Barrel consisted of a cylinder made of kapton foil with the length of 52.75 mm, and had a radius of 15 mm. On both of

[4] According to the bremsstrahlung probability.

[5] Was not used due to energy coverage $E_\gamma > 2500\,\text{MeV}$ which is out of the focus of this work.

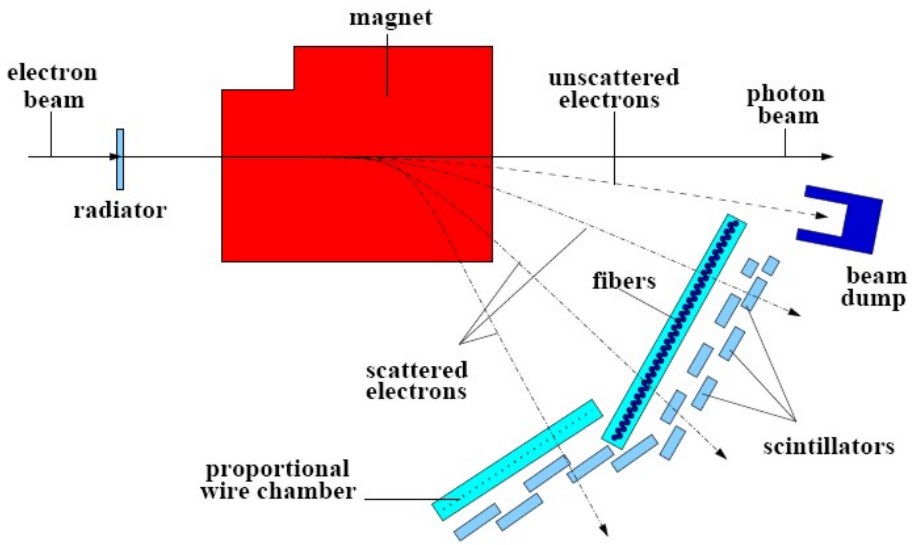

Figure 2.4.: Schematic picture of the tagger.

the sides the kapton thickness was 80 μm, in the cylindrical part 125 μm [Kop02]. The target was positioned in an aluminum beam-pipe, which had a thickness of 1 mm. During the March and May 2003 beam times the target was filled with liquid hydrogen. There is also an opportunity to fill the target cell with liquid deuterium. The target is filled from a reservoir and is cooled down by separately functioning liquid hydrogen circulation system.

2.6. Inner detector

The inner detector placed around the target is used to provide an intersection point of a charged particle trajectory with the detector [S$^+$05], [Fös01]. The detector is 400 mm long, has a diameter of 130 mm and covers the polar angle range of $28° < \vartheta < 72°$. It consists of 513 scintillating fibers with diameter of 2 mm, which are organized in three layers (see Figure 2.5). For the detection of the charged particles an overlap between two or three layers of the detector is used. The outer layer (191 fibers) is positioned parallel to the beam axis, the

middle layer (165 fibers) is bent with an angle of $+25.7°$, the innermost (157 fibers) with an angle of $-24.5°$ with regard to the beam axis. The angles are resulting from the requirement for the bent fibers to cover exactly half round of the detector. This arrangement allows unambiguous identification of the position of the hits if only two of the fibers are fired. The readout is organized via 16-channel photomultipliers connected to the fibers via lightguides. The efficiency of the detection in case of the hits with two overlapping layers is 98.4%, in the case of three overlapping layers 77.6%. The position resolution for the pointlike target in X and Y coordinates is 0.5 mm and in Z coordinate 1.6 mm, the angular resolution is $\Delta\varphi = 0.4°$ and $\Delta\Theta = 0.1°$ [S$^+$05].

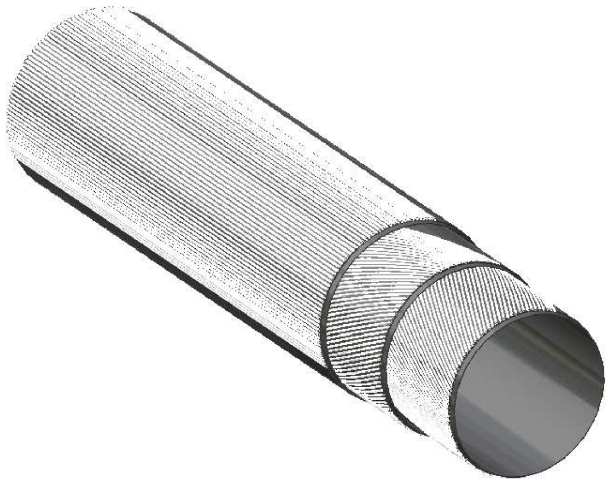

Figure 2.5.: Schematic picture of the inner detector.

2.7. The Crystal Barrel calorimeter

The Crystal Barrel (see Figure 2.6) is an electromagnetic calorimeter particularly well-suited for the measurement of the energy and coordinates of photons. It consists of 1290 CsI(Tl) crystals arranged in 23 rings and covers the angular range from 30° to 168° in polar angle ϑ and the complete range in azimuthal angle φ.

Each crystal has a length of 30 cm corresponding to 16.1 radiation lengths [A$^+$92] and covers 6° both in polar and azimuthal angles. An exception are the crystals

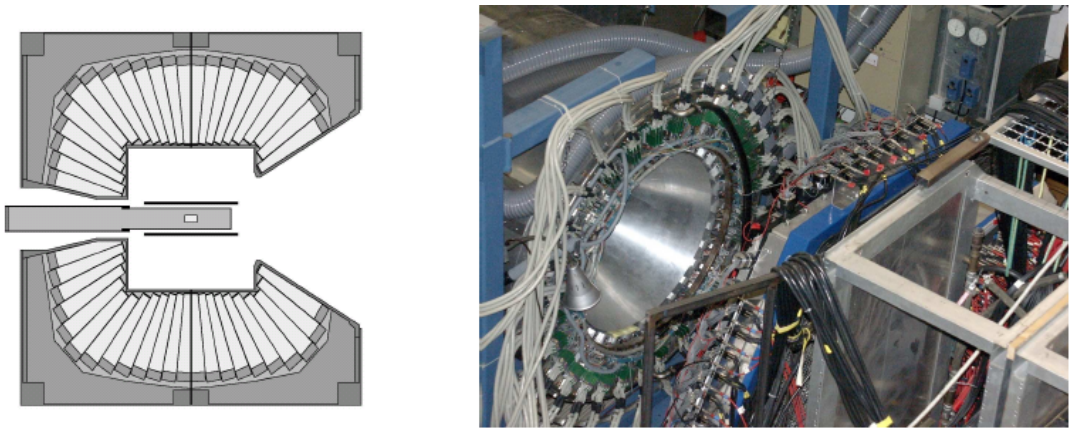

Figure 2.6.: Schematic picture (left) and photograph (right) of the Crystal Barrel.

in the three backward rings which cover 6° in ϑ and 12° in φ. The energy of the photons inducing electromagnetic showers in the Crystal Barrel is determined via identification of the clusters and summing up the energy deposits in the set of the crystals, for more details see Section 3.2.2. The energy resolution of the Crystal Barrel depends on the energy of the photons as [A$^+$92]:

$$\frac{\sigma(E)}{E} = \frac{2.5\%}{\sqrt[4]{E[\mathrm{GeV}]}}. \tag{2.3}$$

The spacial resolution of the Crystal Barrel is related to the energy and varies in the range $1 - 1.5°$ (see also Sections 3.2.2). The energy deposits in the crystals of the Crystal Barrel are measured via detection of the scintillation light produced with a wavelength of 550 nm in CsI(Tl) crystals. To improve the detection of the scintillation light its wavelength is moved to longer wavelengths in the range of the sensitivity of the photodiode using a wavelength shifter. After detection by the photodiode the signal is processed via a preamplifier and a shaper and is read out by 12-bit dual-range ADCs. To control the functionality of the readout and for calibration purposes the light pulser system has been used. The light pulses were directly fed to the wavelength shifter, for more details see [Bar00], [Bös06].

2.8. TAPS

The TAPS electromagnetic calorimeter consists of 528 BaF_2 crystals and is as well as the Crystal Barrel well-suited for the detection of the photons. TAPS covers a polar angular range $5.8° < \vartheta < 30°$ and the complete azimuthal range. The schematic picture of TAPS is shown in Figure 2.7, where the crystal assembly in the hexagonal shape can be seen. The forward opening of TAPS is used as an escape for the photon beam. The energy resolution of TAPS is related to the energy of the photons as

$$\frac{\sigma(E)}{E} = \frac{0.59\%}{\sqrt{E_\gamma}} + 1.91\% \tag{2.4}$$

for the total light output, for more details see [G+94].

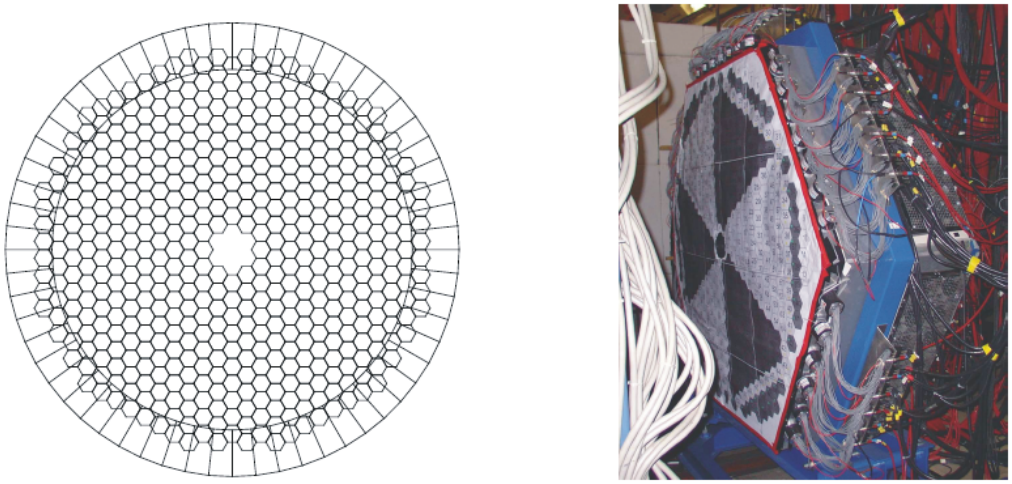

Figure 2.7.: Schematic picture (left) and photograph (right) of the TAPS calorimeter [Trn06].

The crystals of the TAPS have a length of 250 mm, corresponding to 12 radiation lengths and a height of 59 mm. The readout of the TAPS crystals is performed

with photomultipliers, connected to the crystal with an oil of high viscosity and is equipped with both energy and timing readout [Trn06], [Jae09]. The signals from the TAPS modules are processed by the constant-fraction discriminators (CFD) used to set the thresholds for the energy readout (Sections 3.1.1 and 3.2.1) and by the leading-edge discriminators (LED) to form the trigger (see Section 2.10). To distinguish between charged and neutral particles plastic Veto scintillators with thickness of 5 mm have been placed in front of the BaF_2 crystals.

2.9. Photon Intensity Monitor

The number of interactions of the photons with target can be neglected in comparison to the total flux due to the low cross-section. The Photon Intensity Monitor, which consists of a 3x3 matrix of PbF_2 crystals with photomultiplier readout was mounted at the end of the beam line to measure the photon flux. The Photon Intensity Monitor used in coincidence with the tagger allows the determination of the flux.

2.10. Trigger

To suppress strong background contributions such as e.g. hits produced due to the e^+e^- conversion of the photons and to select the particle hits which potentially can correspond to the desired hadronic reactions a two-level trigger system was set for the CBELSA/TAPS experiment. In the trigger the multiplicity of the hits in the calorimeters has been used as a criterion for the selection of the event candidates. Two levels of the trigger were used. At the first step one has to decide whether the digitization of the hits in the calorimeters is necessary. For that purpose a simple algorithm was implemented. Since the signal from the photodiodes of CB crystals has a relatively large rise-time due to the readout electronics, only TAPS equipped with fast photomultiplier readout, has been used in the formation of the first-level trigger. The time needed for the event readout is in order of 1 ms which allows to use the signals from CB to make a decision about either storage or cancellation of the event in the second-level trigger. The trigger conditions are presented below.

First-level trigger

The signals from TAPS are processed through delay lines within 300 ns and respectively the trigger has to be formed within that time. The TAPS crystals are read out with two LED settings, one set at higher thresholds (LED high) and another at lower thresholds (LED low).

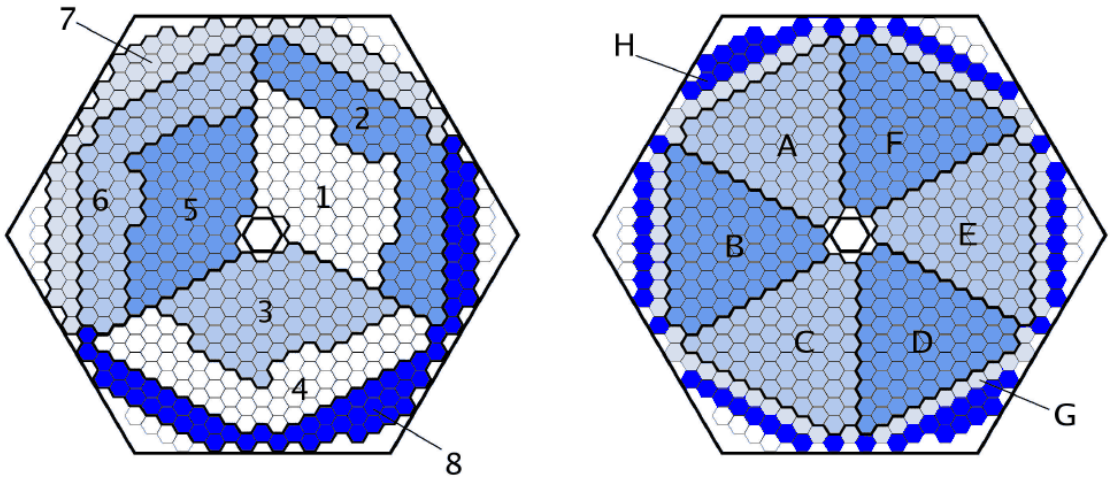

Figure 2.8.: TAPS LED thresholds, on the left: segmentation used for sets of the LED low trigger, on the right: the sectors used in the formation of the LED high trigger. Figure taken from [Gut10].

To reduce the possible contribution from electromagnetic background due to e^+e^- conversion of the photons TAPS LED low readout was split in segments consisting of 64 crystals as shown in Figure 2.8. If two of the LED low thresholds from different segments have been overcome the event is digitized and stored. In this case the decision of the second level trigger is not required anymore. The first level trigger is formed also if at least one of the TAPS crystals provides a signal higher than the corresponding LED high threshold. In this case the event is digitized but the decision about its final storage is not yet made.

Second-level trigger

For the second level trigger the relatively slow signals originating in the Crystal Barrel are used in combination with 1 LED high hit in TAPS. So, the second level trigger is applied only when one hit above the LED high threshold is present and

there were no two hits above LED low threshold. The event is retained if two clusters [6] have been identified by the clusterfinder algorithms [7] implemented in Fast Cluster Encoder (FACE).

[6] As a cluster is defined a group of neighboring crystals in which a particle produces an electromagnetic shower, see Section 3.2.1.

[7] The time needed for the identification of the clusters with FACE varies between 6 μs and 10 μs dependent on the size of the clusters.

3. Calibration and Reconstruction

The signals measured by the readout electronics of the detectors have to be translated to energy, position and time units for further analysis. That transformation is performed via calibration procedures described in this chapter. Further, the particles are identified and their kinematic parameters are determined via corresponding reconstruction procedures.

3.1. Calibration

3.1.1. TAPS calibration

Time calibration

Two steps are done for the time calibration of TAPS: a calibration of the gain and a calibration of the time offsets of the TAPS TDC modules. To calibrate the gain, pulses with different, known frequencies were fed to the TDC modules. The determination of the relative time intervals between the peaks which occur in the time spectra allows the calibration of the gain. The time offsets of the TDCs originating from different cable lengths are calibrated using the time differences between neutral hits detected in TAPS. For that, events with two or more neutral hits were selected and the difference between the times of the clusters was calculated. The time of the cluster is defined by the time of its central crystal [1]. Further, the offsets of the TDCs were shifted so that the differences between the times of the neutral hits all peak at 0. Figure 3.1 shows the sum of all those differences after calibration, from where the time resolution of 0.35 ns was determined [Cas06].

[1] The central crystal is the crystal with maximum energy deposit in the cluster.

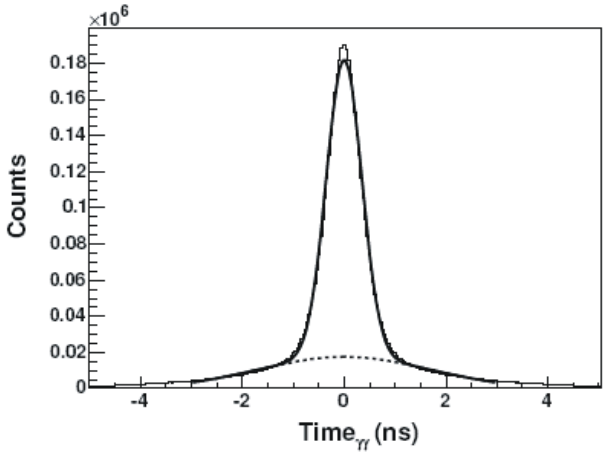

Figure 3.1.: The sum of the all photon time differences (see text) in TAPS [Cas06].

Energy calibration

For the energy calibration of TAPS, three steps were done: a cosmic calibration, a calibration based on the known π^0 mass using photons from π^0 decays, and a correction using the invariant mass of the photons from η decays. The first step of the calibration was done using the known energy deposit of cosmic muons in the TAPS crystals. Since all TAPS crystals are positioned in the same way, have the same geometry and material content, the same energy - on average 38.5 MeV [Cas06] is deposited in each of the crystals by the cosmic muons. To determine the point where the energy is zero a pedestal pulser was used. A typical spectrum obtained in the cosmic calibration is shown in Figure 3.2. The peak at the right side of the spectrum is produced by minimum ionizing muons. The pedestal pulser produces the sharp peak on the left side, the gap seen between the pedestal pulser peak and the other part of the spectrum is due to the CFD threshold, set for the TAPS readout. Using the positions of the minimum ionizing peak and of the pedestal pulser peak a first calibration of the QDCs can be performed using a linear function.

The energy deposit mechanisms in the TAPS crystals are different for the photons and muons. Also, for some of the crystals participating in the electromagnetic shower the energy deposit is below CFD thresholds, which leads to the reduction

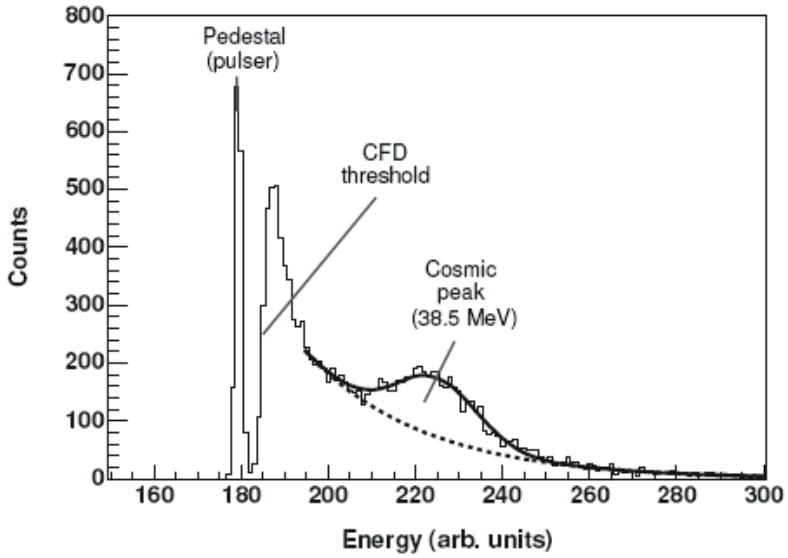

Figure 3.2.: Energy calibration of TAPS with cosmic muons, energy spectrum in arbitrary units, taken from [Cas06].

of the overall measured energy. To account for these effects and to perform the calibration using events from the full energy range, the invariant mass of the two photons [2] originating from π^0 decays was compared to the nominal π^0 mass. The energy deposited in the central crystals of the clusters produced by photons from π^0 decays was corrected so that the invariant mass of the two photons was at the correct position. The sum of the energies measured in the crystals participating in the cluster was taken as a photon energy. The procedure was performed iteratively, the gains of the QDCs were corrected until the invariant mass of the photon pairs fitted to the nominal mass of π^0. The result of this calibration is shown in Figure 3.3, where the agreement between the calculated invariant mass and the nominal π^0 mass is seen.

Depending on the energy of the photon, electromagnetic showers of different size develop in the crystals of the calorimeter. Thus, the relative amount of the lost energy varies with photon energy and therefore an additional correction is needed. To correct for the effects of different development of the shower in the higher energy

[2] Concerning invariant mass calculation see Section 4.4.

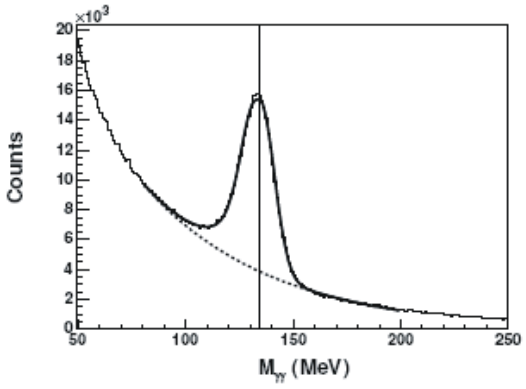

Figure 3.3.: The result of the TAPS energy calibration using π^0 peak, taken from [Cas06]. For more details e.g. concerning function used in the fit see [Cas06][Trn06].

range, compared to the range where the calibration was done using the π^0 peak, the decay photons from the η were in addition used for the calibration. Generally the photons from the η decays have energies higher than the ones from the decays of the π^0. Since the cross-section of the η photoproduction is relatively low and also taking into account the branching ratio and relatively large angle between two decay photons from the η in comparison to the π^0 decay, the statistics of events which can be used for the calibration is relatively low. Therefore an overall correction is used. The correction function was applied in the form:

$$E_{new} = a + b \cdot E_{old} + c \cdot E_{old}^2, \tag{3.1}$$

The coefficient a is zero by definition, b and c were determined referring to the nominal masses of π^0 and η. Typical values for the other coefficients are $b = 1.0165$, $c = -5.6715 \cdot 10^{-5}$ [Gut10]. Figure 3.4 shows the effect of the correction of the invariant mass of two photons with function 3.1.

3.1.2. Crystal Barrel calibration

The calibration of the Crystal Barrel uses the position of the π^0 peak in the invariant mass spectrum. Figure 3.5 shows the invariant mass spectra of the two

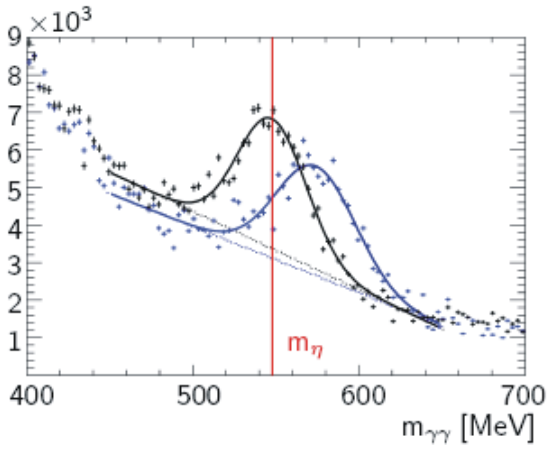

Figure 3.4.: Invariant mass of the $\gamma\gamma$ pair before (blue) and after (black) application of the correction described by function 3.1, taken from [Gut10].

reference photons for different iterations. The calibration using the π^0 mass was sufficient and the correction in regards to the η mass was not required because of the relatively low thresholds of 1 MeV (see Section 3.2.2) set for Crystal Barrel readout and an energy- and ϑ-dependent correction function was applied in the reconstruction procedure (see Section 3.2.2). The readout of the CB crystals uses 12-bit dual-range ADCs. The low ADC range covers the photon energies up to about 130 MeV and is calibrated as described above using the π^0 mass as a reference. The high range of the ADC covers the energies up to about 1100 MeV. The proportionality of the ADC response allowed to extend the calibration performed in respect to the π^0 mass, to the high range using a lightpulser calibration. The lightpulser was directly connected to the wavelength shifter of the CsI(Tl) readout, and produced signals corresponding to the response of the CsI(Tl) crystals to various energy deposits. For more details about the lightpulser calibration see [Bar00], [Bös06]. For more details concerning the calibration of the CB in general see [Jun00].

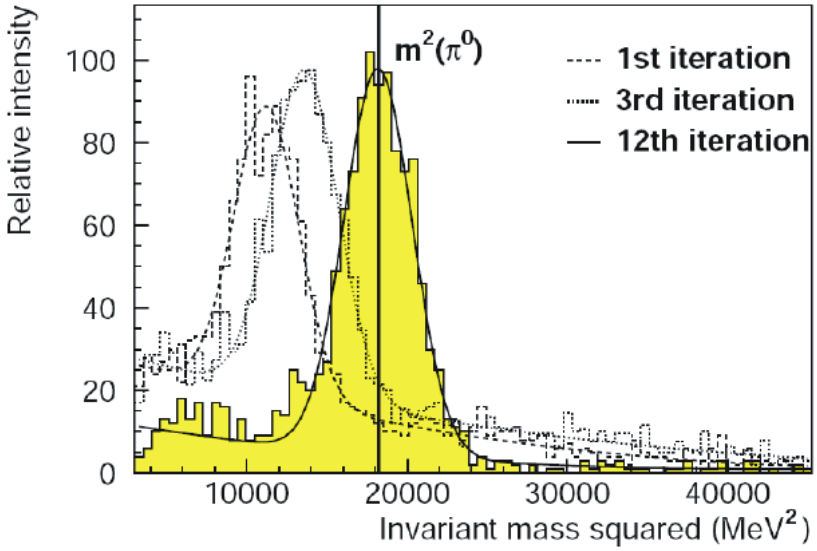

Figure 3.5.: Energy calibration of the CB invariant mass spectra before and after iterative calibration, taken from [Jun00].

3.1.3. Tagger calibration

Time calibration

The calibration of the TDCs of the fiber hodoscope of the tagger was done after the TAPS time calibration, using the same event sample. TAPS with its high timing resolution has been used as a reference, since it is providing the trigger and the time reference for an event. The difference between the times measured by the tagger TDCs and the averaged time of the two photons from π^0 decays detected in TAPS was calculated for all individual fibers of the tagger. The offsets of the tagger TDCs were set such that the calculated difference was consistent with zero. The spectrum resulting from this calibration is shown in Figure 3.6, giving a relative TAPS to tagger time resolution in the order of 1 ns [Cas06].

Energy calibration

For the electrons which are detected in the tagging fiber hodoscope the correlation between measured energy and fiber number in the tagger, when the electrons are bent in the given magnetic field, has to be determined. At first, a polynominal of

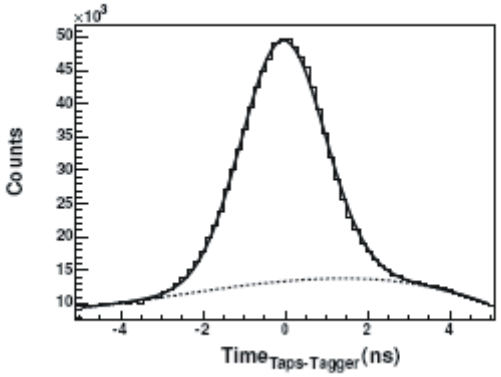

Figure 3.6.: The difference between TAPS and tagger time after calibration [Cas06].

the fifth degree describing the relation between the energy and fiber number was obtained by simulation using the known geometry of the tagger and of the magnetic field [Hor04]. Afterwards, a measurement with direct injection of electrons with four different energies was performed [3]. The results obtained from this measurement were used in the correction of the polynomial derived from simulation. The corrected polynomial used in this work is given as [Els07]:

$$\begin{aligned} E = Pol(x)|_{3.2\,\mathrm{GeV}} &= 2533.81 - 190.67 \cdot 10^{-2}x + 28.86 \cdot 10^{-4}x^2 \\ &- 34.43 \cdot 10^{-6}x^3 + 95.59 \cdot 10^{-9}x^4 - 12.34 \cdot 10^{-11}x^5, \end{aligned} \tag{3.2}$$

E is the photon energy and x is the number of fiber. For more details concerning calibration of the tagger see [FP09].

3.2. Reconstruction

After the calibration an information about energy and time measured by the detector system is available. Further, this information is assigned to the particles and their kinematic parameters are determined. This is done using reconstruction

[3] The electron energies of 680 MeV, 1300 MeV, 1800 MeV and 2500 MeV were used in this work, the strength of the magnetic field was B = 1.413 T [Els07].

routines described in the next sections.

3.2.1. TAPS reconstruction

Electromagnetic showers produced by photons are spread over several TAPS crystals. In the reconstruction the crystals which in the shower development are grouped in clusters. A cluster is defined as a continuous group of crystals with a signal above the CFD threshold. The crystal for which the energy deposit is the largest in the cluster is taken as the central crystal. The hits in the crystals with an energy deposit of higher than 10 MeV are used for the cluster formation. To reduce the contribution of split-offs [4] a threshold of 25 MeV has been used for the total energy of the cluster. The analysis showed that the CFD thresholds on the hardware level were not set not to 10 MeV or lower. They were typically varying between 10 MeV and 20 MeV, in some of the cases reaching 30 MeV [Gut10]. To avoid artificial asymmetries produced due to these variations, the data were recalibrated and thresholds of 30 MeV have been applied for all TAPS crystals on the software level.

To reject contributions from other clusters, which were not correlated in time, the times of the central crystal and other crystals in the cluster have been compared and only hits for which the obtained difference did not exceed 5 ns were selected (see Figure 3.7). If the time information of the central crystal was not available because of readout inefficiencies, the time of crystal with the second highest energy deposit was taken. Further, in the analysis the mean time of the TAPS crystals was set for modules without time information.

The position of the photons is calculated using the coordinates of the crystals which form the cluster with energy-dependent weighting factors [Cas06] :

$$X = \frac{\sum_i w_i x_i}{\sum_i w_i}, \quad Y = \frac{\sum_i w_i y_i}{\sum_i w_i}, \tag{3.3}$$

[4] The split-off is a part of an electromagnetic shower separated from the main cluster produced in the calorimeter.

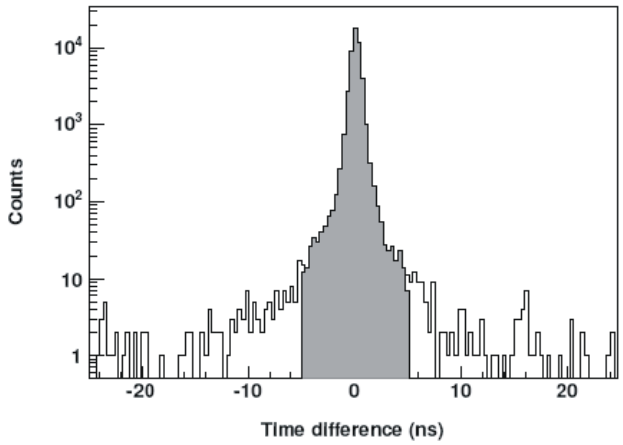

Figure 3.7.: Time difference between hits in the TAPS crystals. The crystals for which the time difference was within the grey area were considered as parts of the same cluster, taken from [Cas06].

where the factors w_i are defined as:

$$w_i = \max\left\{0; W_0 + \ln\frac{E_i}{\sum_i E_i}\right\}. \tag{3.4}$$

The GEANT simulation showed that the offset in the formula 3.4 has a value of $W_0 = 4$ [Cas06]. However, the formulas given in 3.3 and 3.4 were used with the assumption that the development of the shower starts immediately at the point of entrance of the particle in TAPS. In reality due to geometrical effects, such as the entrance particle in TAPS being "askew" (see Figure 3.8), an error in the reconstruction of the position of the photons is introduced [Gut10]. The distance which the photon passes before inducing an electromagnetic shower in the BaF_2 crystals is approximated as [N+10]:

$$Z = X_0\left(\ln\frac{E}{E_c} + C_\gamma\right), \tag{3.5}$$

where X_0 is the radiation length of BaF_2, E is the photon energy and E_c is the critical energy for the BaF_2. Monte Carlo simulations showed that there is a systematic difference between generated and reconstructed proton angles if the

value of $C_\gamma = 0.5$ given in [N+10] is used. The value of $C_\gamma = 2.0$ [Gut10] allowed correction of this difference and was further used in the position reconstruction of TAPS. The resolution in the polar angle was determined to be less than 1.3° [Cas06].

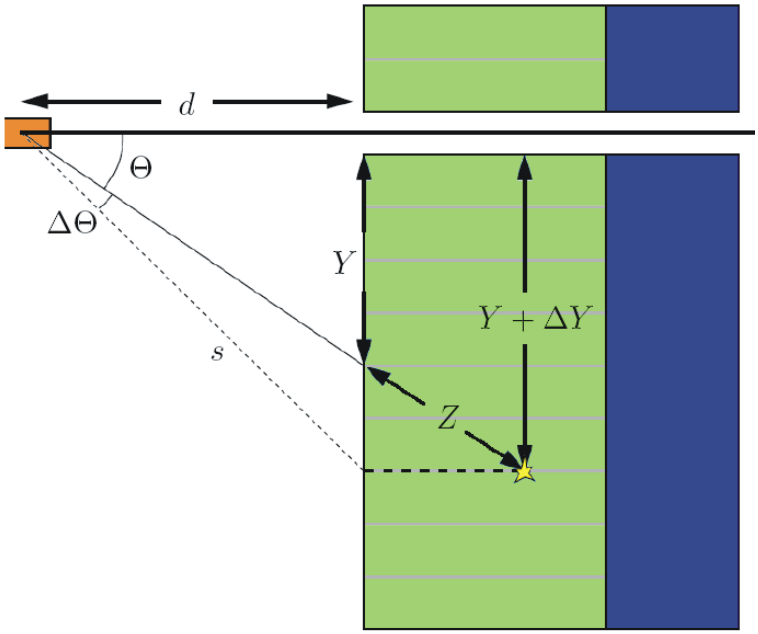

Figure 3.8.: Distortion of the position measurement and its correction, taken from [Gut10].

3.2.2. Crystal Barrel reconstruction

The reconstruction of the Crystal Barrel works in a similar way as the TAPS reconstruction. On the software level a threshold of 1 MeV is set for every individual module, the threshold for the clusters was set to 20 MeV to reduce the contributions from split-offs. If there was only one local maximum in the cluster, the energy measured by the participating crystals was added directly. The principle of the cluster reconstruction in the CB when two local maxima, marked as crystals (A) and (B), is presented in Figure 3.9 and will be shortly discussed in the following.

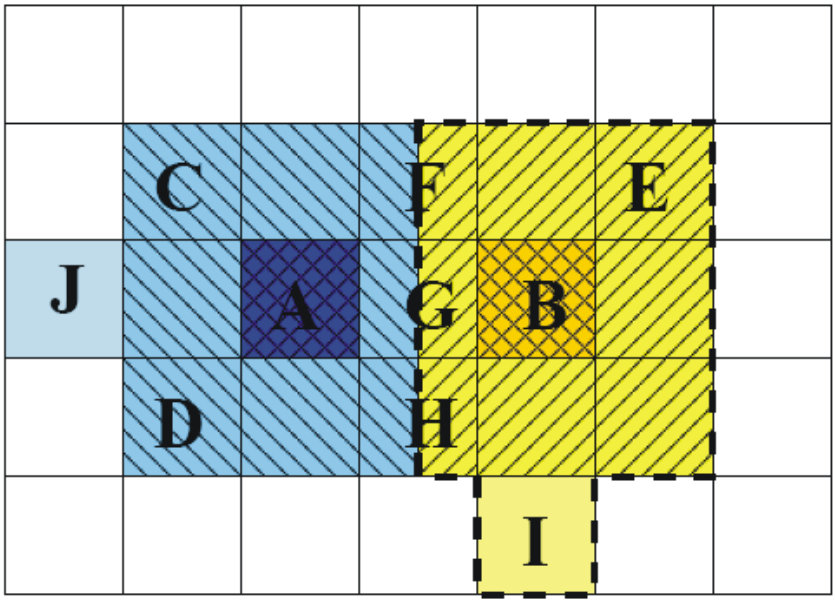

Figure 3.9.: Reconstruction of the clusters in the Crystal Barrel, taken from [Trn06]. See text for more descriptions.

The energy measured in the crystals (C), (D) and (E) was added to the energy measured by the corresponding central crystal. For the crystals (F), (G) and (H) the situation is different: their energy was split between two central crystals (A) and (B) with weights according to the energy deposit in the given central crystal. The energy of the Particle Energy Deposit (PED), already associated with the i-th primary particle producing a shower is calculated as:

$$E^i_{\mathrm{PED}} = \frac{E^i_9}{\sum\limits_k E^k_9} \cdot E_{\mathrm{cl}}, \tag{3.6}$$

where E_{cl} is the cluster energy. E^i_9 is the so-called nine-energy, defined as the sum of the energies of the crystal i and its 8 neighbors:

$$E^i_9 = E^i_{\mathrm{cen}} + \sum_{j=1}^{8} E_j. \tag{3.7}$$

$\sum\limits_k E^k_9$ is the sum of the nine-energies calculated for the k overlapping clusters. If

the crystal i is adjacent to j local maxima, its energy is added to the corresponding nine energy, weighted as:

$$E_{9k}^{i} = \frac{E_{\mathrm{cen}}^{k}}{\sum_{j} E_{\mathrm{cen}}^{j}} \cdot E_{i}. \tag{3.8}$$

The energies of the crystals (I) and (J) in Figure 3.9 which do not have adjacent central crystals, were added to the PED energies so that the PEDs had the same fraction of cluster energy after the addition.

Due to the loss of the energy in certain parts of the calorimeter, because of edge effects, and presence of inactive material, e.g. aluminum holding structure of the CB, the energy summation combined with the weighting procedures mentioned above does not provide the complete sum of the energy of the cluster. To correct for energy losses an energy and ϑ-dependent correction function is applied:

$$E_{\mathrm{PED}}^{\mathrm{corr}} = \left(a(\vartheta) + b(\vartheta) \cdot e^{-c(\vartheta) \cdot E_{\mathrm{PED}}}\right) \cdot E_{\mathrm{PED}}. \tag{3.9}$$

Typical values of the parameters used to correct the data in this work are $a \approx 1.05$, $b \approx 0.05$, $c \approx 0.007$.

The position reconstruction of the particles in the Crystal Barrel is done in a similar way as for TAPS, the main difference is that the polar angle ϑ and azimuthal angle φ were used in the reconstruction. The value of the constant used in 3.4 is at $W_0 = 4.25$. The position resolution of $1^\circ - 1.5^\circ$ is obtained for ϕ and ϑ [Jun05]. The application of the shower depth correction used for TAPS is not necessary for the Crystal Barrel since all crystals are placed so that they all are pointing to the center of the target.

3.2.3. Inner detector reconstruction

The charged particles firing the inner detector are identified dependent on which fiber was hit. If more than one fiber was hit, the group of fibers was identified as a cluster and the fiber number was averaged [S$^+$05]. The position of the hit in the inner detector was determined by intersection of the fibers from different layers. The Cartesian coordinates of the hit were determined by unwinding the

fibers into flat layers as shown in Figure 3.10. The hit is identified as an overlap of the resulting "straight" fibers.

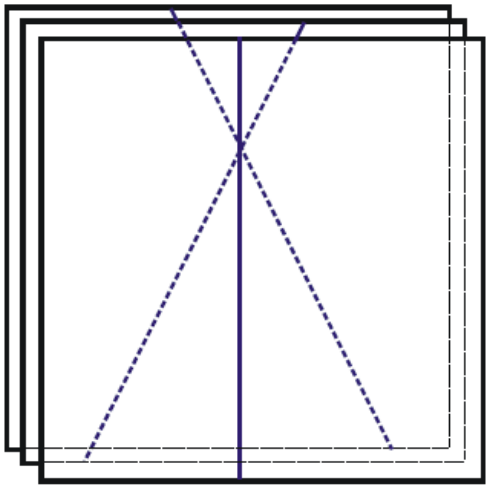

Figure 3.10.: Intersection of the inner detector fibers, taken from [S+05].

3.2.4. Tagger reconstruction

For the determination of the energy of the bent electron and respectively the energy of the primary photon used in the experiment, the fiber which is hit in the tagger must be identified. The electrons can fire one or more fibers in the tagger. To treat these cases with more than one hit, continuous groups of tagger fibers forming clusters were identified. Afterwards the fiber number was averaged, and the central fiber of the cluster was determined and used for the calculation of the electron energy with the tagger polynomial, described in Section 3.1.3. The time of the cluster is taken to be the mean time of the fibers participating in the cluster. To reject hits uncorrelated in time it was required that the fibers which contribute to the cluster had to be coincident within 2 ns. To account for inefficiencies of the measurement, in case one fiber in between two fired fibers was not fired, the group of the fibers was still considered as a cluster.

3.2.5. Timing background

Due to high rates, the number of hits in the tagger, related to the same event, can vary from 1 to 15 before a preselection is applied. Among these, the hit in the tagger which corresponds to the hadronic event has to be found. This is done by using the time-coincidence analysis, based on the fact that the hits in the tagger and in TAPS have to be correlated in time.

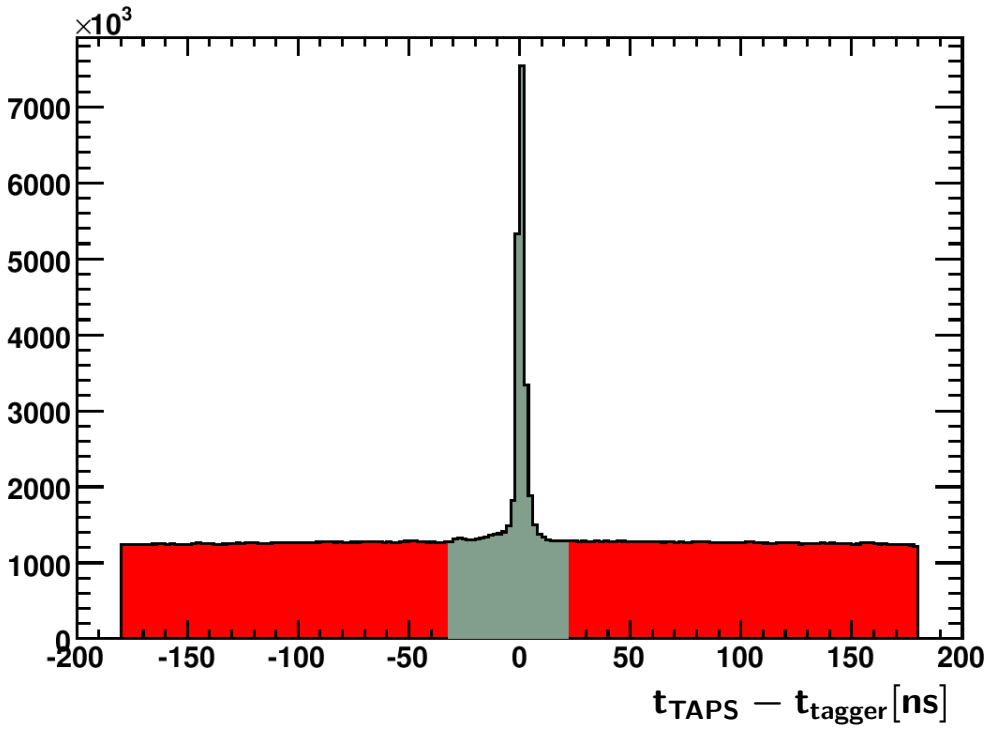

Figure 3.11.: Example spectrum, illustrating the coincident analysis of TAPS and tagger hits. Grey: prompt events in the interval (-30, 20) ns, red: accidental background in the intervals (-180, -30) ns and (20, 180) ns. The sharp cuts on the edges of the spectrum are due to the preselection for timing range used in further analysis.

The difference of the times of the particles in the tagger and TAPS $t_{TAPS} - t_{tagger}$, forming the time window for coincident hits, is shown in Figure 3.11 (example spectrum). The peak around 0 ns corresponds to the coincident hits, the evenly distributed events to the uncorrelated accidental background. The coincidence

region is selected with a (-30, 20) ns wide cut. The cut has been done asymmetrically due to the contribution of events for which slow protons have caused the trigger in TAPS, contributing to the shoulder on the left side from the peak at 0 ns. After application of the (-30, 20) ns cut, there is still a contribution from accidental hits left under the prompt peak. To subtract that background, the events outside of the prompt peak have been taken, with corresponding normalization according to the width of the cut on the prompt events, and events outside of the peak. Afterwards, the accidental background has been subtracted. In this method it is assumed that the accidental hits inside and outside of the prompt peak are evenly distributed in the complete timing range. The effect of the time background subtraction is shown in Sections 4.5 and 4.6.

3.2.6. Charge information and combinatorial analysis

The charged particles (protons) are identified by the TAPS Vetos and by the inner detector. The analysis of the data has shown that the efficiency for the charge identification is not perfect, being relatively low in distinct geometrical regions and leading to a distortion of the acceptance. These effects are illustrated in the two dimensional (ϑ, φ) matrices (Figure 3.12) for the particles which were identified as protons after kinematic cuts in case when five particles have been detected in the calorimeters. The kinematic cuts are described in Section 4.5.

Figure 3.12 shows the data (A) and Monte Carlo (B) [5] (ϑ, φ) matrices with restriction on the number of charged particles less or equal one and with the number of charged particles explicitly required to be one for the data (C) and and Monte Carlo (D) respectively. One can clearly see the effect of the direct charge identification in the data. In particular at low ϑ, and positive φ there is a significant reduction of the charged hits indicating inefficiencies of the TAPS Veto scintillators. About 10% of the whole statistics is lost due to these inefficiencies. Monte Carlo simulation in contrast has shown that there is practically no difference with and without explicit charge detection. In the projections for the region $\vartheta_p < 15^\circ$ the systematic effect is clearly seen (Figure 3.12 (E), (F)). Also a reduction of events at φ angles below -140° in the TAPS region can be seen. The data shows

[5] For the descriptions of the data see Section 4.1, concerning Monte Carlo see Section 4.2.

a noticeable difference over all φ and particularly around 60°, whereas no difference in Monte Carlo has been observed. The modifications of the φ distributions produced due to the polarization effects, seen in the shape of the distributions obtained without explicit charge detection, are described in Chapter 5 [6].

The angular coverage of the detector is extremely important for this work, because it can have a strong influence on the φ distributions and therefore on the polarization observables. To be independent of the observed systematic effects due to the veto inefficiencies, a full combinatorial analysis has been performed and the proton has been identified by kinematic cuts. In case of five hits in the calorimeters each of the particles was considered as a proton candidate. A proton was taken to be the particle which was the proton candidate when the event passed the kinematic cuts (Section 4.5) [7]. In case of four hits in the calorimeters the missing particle is assumed to be a proton, and further analysis has been done using that assumption (Section 4.6).

[6] Note that for example there is no reduction of events due to the detector effects around 0° in φ, but the distribution obtained from the data is modified.

[7] The treatment of events for which more than one proton candidate survives the kinematic cuts is discussed in Section 4.7

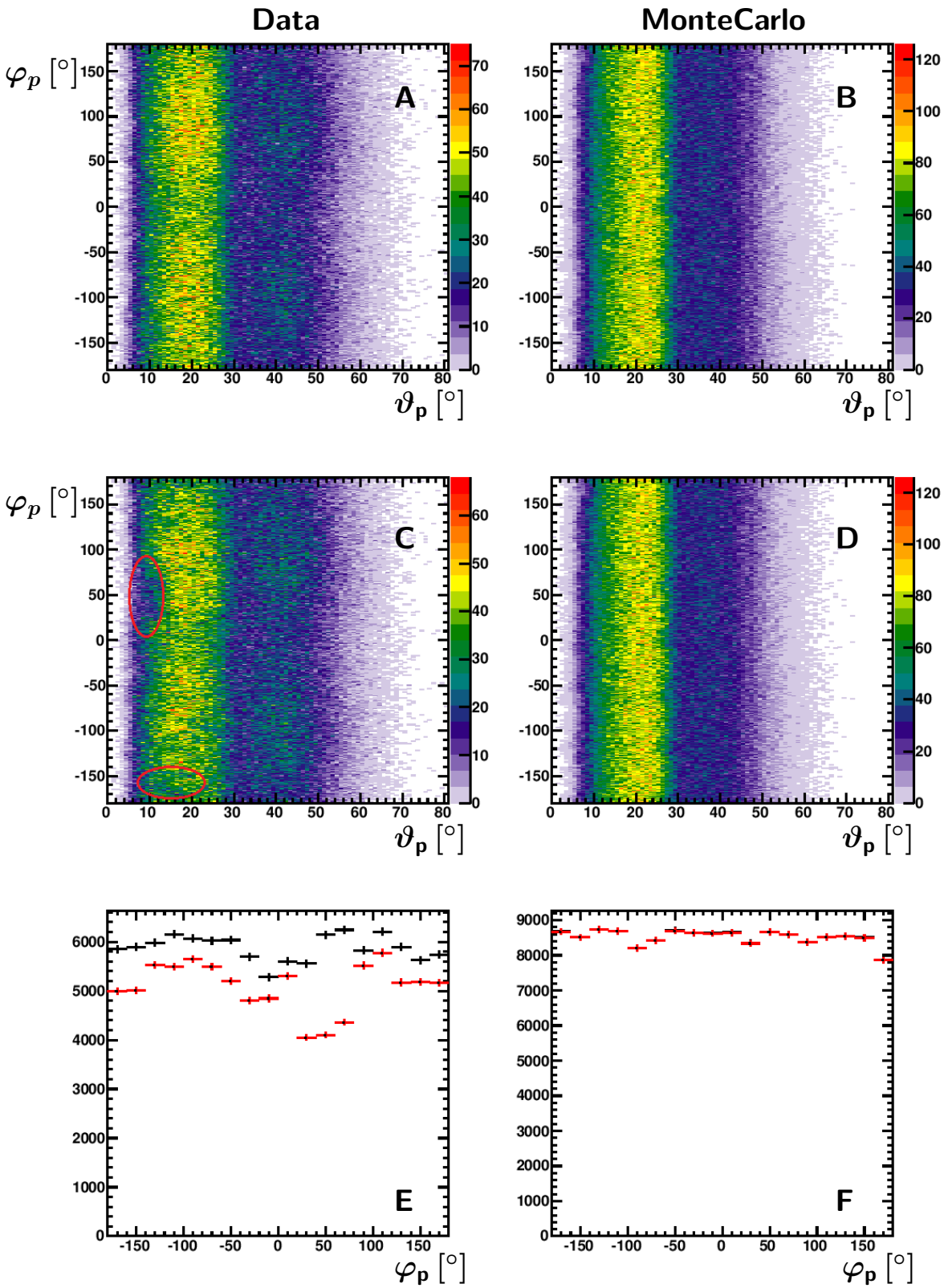

Figure 3.12.: (ϑ, φ) matrices for protons, for the data (A, C) and Monte Carlo (B, D). (A, B): the number of charged particles $N_{ch} \leq 1$, (C, D): the number of charged particles $N_{ch} = 1$, (E, F): comparison of the projections of matrices A and B in the region $\vartheta_p < 15°$, black: $N_{ch} \leq 1$, red: $N_{ch} = 1$.

4. Selection

4.1. Experimental data

The data has been acquired with the CBELSA/TAPS experiment in March and May 2003, using linearly polarized photons, produced via coherent bremsstrahlung at a diamond crystal and impinging on a liquid hydrogen target.

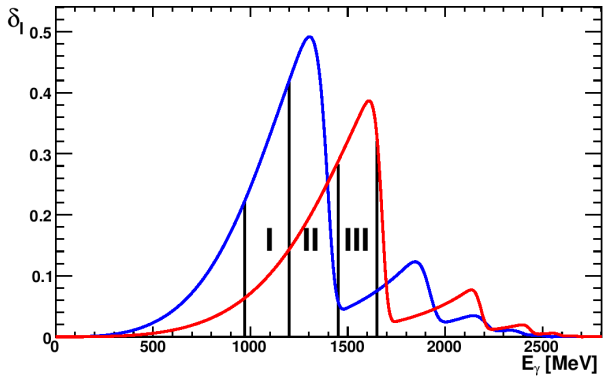

Figure 4.1.: Polarization degree vs. energy of the incoming photons, blue curve: March data, red: May data. The black lines define the energy ranges used for the determination of the polarization observables.

In Figure 4.1 the degree of polarization of the photons versus the incoming photon energy is plotted. The coherent edges for the two cases were set such that for March 2003 data a maximal polarization of 49.2% at 1300 MeV and for May 2003 data a maximal polarization of 38.7% at 1600 MeV were achieved. The polarization observables have been determined in the photon beam energy range $E_\gamma = 970 - 1450\,\mathrm{MeV}$ using March data (intervals I and II in Figure 4.1), and $E_\gamma = 1200 - 1650\,\mathrm{MeV}$ using May data (intervals II and III in Figure 4.1), according to the available ranges with sufficiently high degree of polarization. In the overlap

region $E_\gamma = 1200 - 1450\,\mathrm{MeV}$ (interval II in Figure 4.1) both data sets were added up. The range $E_\gamma = 500 - 2500\,\mathrm{MeV}$, has been used in both data sets for the extraction of Dalitz plots and invariant mass spectra. In this chapter, if not explicitly mentioned, the analysis steps are discussed using the limitation of $E_\gamma = 1200 - 1450\,\mathrm{MeV}$.

4.2. Monte Carlo

For a cross-check of the analysis steps described in the next sections, the Monte Carlo simulation, including the geometry and reconstruction of the CBELSA/-TAPS detector, has been used. The simulation has been performed using the GEANT3-based CBGEANT package [Cre01] where the detector components and also the inactive material present in the setup are included. The tagger is not simulated, the reaction starts in the target and further develops according to the available phase space. The photon beam itself was not simulated, but the interaction in the target was simulated for different photon energies with a flat distribution. Further, the particles are detected taking into account physical effects describing their passage through the matter. The reconstruction was performed in complete analogy to experimental data [1].

Firstly Monte Carlo simulations allowed to have a better control on the background effects comparing the spectra obtained from the data with the background-free spectra obtained with Monte Carlo simulations (see Sections 4.5 and 4.6). Secondly, Monte Carlo simulations were used to account for the detector acceptance and to estimate the effects of present inefficiencies (see e.g. Section 5.2). Monte Carlo simulations have been used also for the attempt of a model-independent 5-dimensional acceptance correction, which was not performed due to disk space and time limitations. The main results of the development of the 5-dimensional correction are summarized in Appendix A.

[1] Including division in two sets, with five and four particles reconstructed in the final state.

4.3. Signature of the reaction $\gamma p \to p\pi^0\pi^0$

The reaction $\gamma p \to p\pi^0\pi^0 \to p4\gamma$ can be reconstructed from the final decay products: four photons and a proton [2]. For that purpose events with five distinct hits (5 PED events) in the calorimeters have been selected. This class of events is described in Section 4.5. The 5 PED events are the statistically dominating contribution in the data sample of $\gamma p \to p\pi^0\pi^0$ events. Nevertheless, due to detector inefficiencies and acceptance effects, particles in the final state can be lost. If four particles, originating from $\gamma p \to p\pi^0\pi^0$ reaction, are detected (4 PED events), and the proton is the lost particle, the reaction can be reconstructed using the information concerning the energy and coordinates of the four detected photons (missing proton analysis). This case is discussed in Section 4.6.

4.4. Kinematic variables

In this section the quantities used in the kinematic cuts for the selection of the reaction $\gamma p \to p\pi^0\pi^0$ based on the energy and momentum conservation (missing mass and coplanarity) and on the masses of the decaying particles (invariant mass) are discussed.

a) Invariant mass

The mass of the particle can be reconstructed out of the energies and momenta of its decay products. In case of the decay into two particles the invariant mass can be calculated as:

$$m_{inv} = \sqrt{(p_1 + p_2)^2} = \sqrt{{m_1}^2 + {m_2}^2 + 2(E_1E_2 - \mathbf{p_1}\mathbf{p_2})}, \qquad (4.1)$$

where p_1 and p_2 are the 4-vectors of decay products, E_1 and E_2 their energies, $\mathbf{p_1}$ and $\mathbf{p_2}$ the 3-vectors. The invariant mass of the photons from π^0 decay

[2] The π^0 decays in photons with branching ratio of 98.8% [N+10], the full branching ratio for both pions decaying in four photons is 97.6%, respectively.

can be written as:

$$m_\pi = \sqrt{2E_{\gamma_1}E_{\gamma_2}(1-\cos\vartheta_{\gamma_1\gamma_2})}, \tag{4.2}$$

E_{γ_1} and E_{γ_2} are the energies of the photons, $\vartheta_{\gamma_1\gamma_2}$ is the angle between the photons.

b) Missing mass

It is possible to calculate the 4-vector of the proton if the information about incoming and four outgoing photons is available, using energy and momentum conservation laws. The mass of the missing particle (the proton) can be calculated as:

$$m_{miss} = \sqrt{(p_{\gamma,i} + p_{p,i} - \Sigma p_{\gamma,f})^2}, \tag{4.3}$$

where $p_{\gamma,i}$ and $p_{p,i}$ are the 4-vectors of the particles before interaction, $p_{\gamma,f}$ are the 4-vectors of the photons in the final state. Events are selected where the missing mass of the proton corresponds to its known mass of 938.272 MeV [N$^+$10].

c) Coplanarity

Momentum conservation forces the three particles in the final state to be situated in one plane. The coplanarity of the particles can be checked by comparison of the azimuthal angles of the three particles.

d) Differences in polar angle ϑ

Additionally, the difference of the polar angle of the proton detected explicitly and calculated out of the photon information, is considered (see Section 4.5). If the proton has not been measured by calorimeters but there is a hit in the inner detector and the momentum of the proton, calculated from photon information, is in the expected range (see Section 4.6) the matching between calculated proton direction and the hit in the inner detector has been required.

4.5. Selection of 5 PED events

To select a sample of $\gamma p \rightarrow p\pi^0\pi^0$ events, kinematic cuts are applied on the variables discussed in the previous section. The widths of the cuts have been determined from the data applying the criterion of collecting maximal amount of $\gamma p \rightarrow p\pi^0\pi^0$ events and in the same time suppressing present background contributions. The widths of the cuts were determined from the obtained distributions so that only the events in the expected ranges were considered. If the events are distributed around a given value, for example if there is a peak in the distribution of the missing mass of the proton at the nominal proton mass, the events outside of the peak in the tails of the spectrum were rejected. In general, to avoid possible reduction of good events, rather wide cuts were used. For the missing mass and invariant mass, it was additionally checked that after application of the kinematic fit, where these two quantities are taken as constraints, the events with high Confidence Level are not affected by the cuts and only low confidence level events are rejected [3]. For the angular differences the widths of the cuts were determined from the spectra as well, with the requirement to reject the background contributions outside of the peaks occurring in the expected regions (see Sections 4.5.2 and 4.5.3).

The following cuts were applied:

a) For the missing mass of the proton: $m_{miss} = 938.272 \pm 100\,\mathrm{MeV/c^2}$.

b) For the invariant mass, simultaneously for both photon combinations : $m_{\gamma\gamma} = 134.9766 \pm 35\,\mathrm{MeV/c^2}$.

c) For the difference $\varphi_p - \varphi_{2\pi^0}$, the ranges $\varphi_p - \varphi_{2\pi^0} = 180 \pm 10^\circ$ and $\varphi_p - \varphi_{2\pi^0} = -180 \pm 10^\circ$, where φ_p is the azimuthal angle of the proton and $\varphi_{2\pi^0}$ the azimuthal angle of the $2\pi^0$ system.

d) For the difference $\vartheta_p^{calc} - \vartheta_p^{meas}$, ϑ_p^{calc} being the polar angle of the proton calculated from the photon information, ϑ_p^{meas} the polar angle measured directly $\vartheta_p^{calc} - \vartheta_p^{meas} = 0 \pm 10^\circ$ if the proton is detected in CB and $\vartheta_p^{calc} - \vartheta_p^{meas} = 0 \pm 5^\circ$ if the proton is detected in TAPS. These cuts were set

[3] The application of the kinematic fit is described in Section 4.7

differently for the proton being detected either in the CB or in TAPS taking into account the different granularity of these detectors.

In the next sections the according spectra are shown, the observed shapes and the effects of the cuts are discussed. Where not explicitly mentioned the effects of the kinematic cuts on the considered spectra are shown after application of the given kinematic cut only (not combined with other cuts).

4.5.1. Invariant mass

In the combinatorial analysis the particle which corresponds to the proton has to be selected out of 5 PEDs (5 proton candidates). It is possible to build 6 different photon pairs out of four photons for each of the 5 proton candidates, thus for each event 30 combinations of photons can be constructed. In Figure 4.2 the invariant masses of each of the photon pairs are plotted against the invariant mass of the other pair (e.g. γ_1, γ_2 vs. γ_3, γ_4). Each pair of photons enters the histogram once, consequently reducing the number of entries twice. Since there are no preferred pairs of photons, the histograms are filled symmetrically, every combination of two photon pairs enters the histogram twice, thus finally 30 entries (before kinematic cuts) are introduced in the histograms. After assuming that a given particle is a proton, the invariant masses of all possible photon pairs are calculated for the prompt events and the timing background alone. The timing background is then subtracted from the prompt events. The data is shown in the first three columns, in the most right column Monte Carlo distributions are shown. The uncut spectra are shown in the first row (A, B, C, D). The enhancement in the region corresponding to the pion mass represents the events for which the invariant masses of two photon pairs are simultaneously in agreement with the π^0 mass. The timing background (B) contains a substantial amount of events for which the invariant mass of the photons is consistent with two pions, because the incoming photon energy has not been used to construct the invariant masses. Further, the effects of individually applied cuts are shown. After the missing mass cut (E, F, G, H) the background is suppressed, especially at very low invariant masses. Also, after the $\Delta\vartheta$ (I, J, K, L) and $\Delta\varphi$ (M, N, O, P) cuts, a significant change in the background situation is made, leading to the better separation of

the enhancement in the π^0 mass region. After kinematic cuts the contribution of the competing $\gamma p \to p\pi^0\eta$ reaction can be seen as two enhancements in the regions around the π^0 and in the same time η masses. After all cuts (Q, R, S, T), the $2\pi^0$ signal is separated and the cut in the invariant mass is indicated with two bands, where the region of their crossing is selected (S, T). It is easier to see and estimate the widths of the peak and the evolution of the signal to background ratio in one-dimensional plots, which are shown in Figure 4.3 with the same sequence of cuts.

4.5.2. Coplanarity

To fulfill the condition of coplanarity, the difference of azimuthal angles of the proton and of the $2\pi^0$ system has to be consistent with $\pm 180°$ ("back to back topology"). The difference $\varphi_p - \varphi_{2\pi^0}$ is plotted in Figure 4.4: grey spectra represent prompt events, red - timing background, blue - prompt after background subtraction, green - Monte Carlo distributions. In the uncut spectrum two peaks, which are expected to be at $\pm 180°$ are observed on top of the background. The third peak at the position $\Delta\varphi = 0 \pm 20°$ can not be explained by kinematics of the reaction. One can clearly recognize significant time background contribution in that peak (A), and its reduction after time-background subtraction (B). Also, that peak is strongly suppressed after each of the kinematic cuts. The origin of that peak is discussed in 4.5.4. The strongest effect of the background reduction makes the $\Delta\vartheta$ cut (J, K, L), the largest reduction of coplanar events is due to the invariant mass cut (D, E, F) because there is a significant amount of events which fulfill the coplanarity condition but are not corresponding to $\gamma p \to p\pi^0\pi^0$ reaction, e.g. due to the $\gamma p \to p\pi^0\eta$ reaction or combinatorics within the given event. After all cuts in combination, the distributions in the data (N) are compatible with Monte Carlo distributions (O) and the peak at $\Delta\varphi = 0 \pm 20°$ is completely eliminated. The cut of $\Delta\varphi = \pm 180 \pm 10°$ is shown with brown lines (N, O).

4.5.3. Differences in polar angle ϑ

In addition to the $\Delta\varphi$ difference, to reduce the background the difference between polar angle ϑ_p^{calc}, calculated out of photon information and ϑ_p^{meas} from explicit

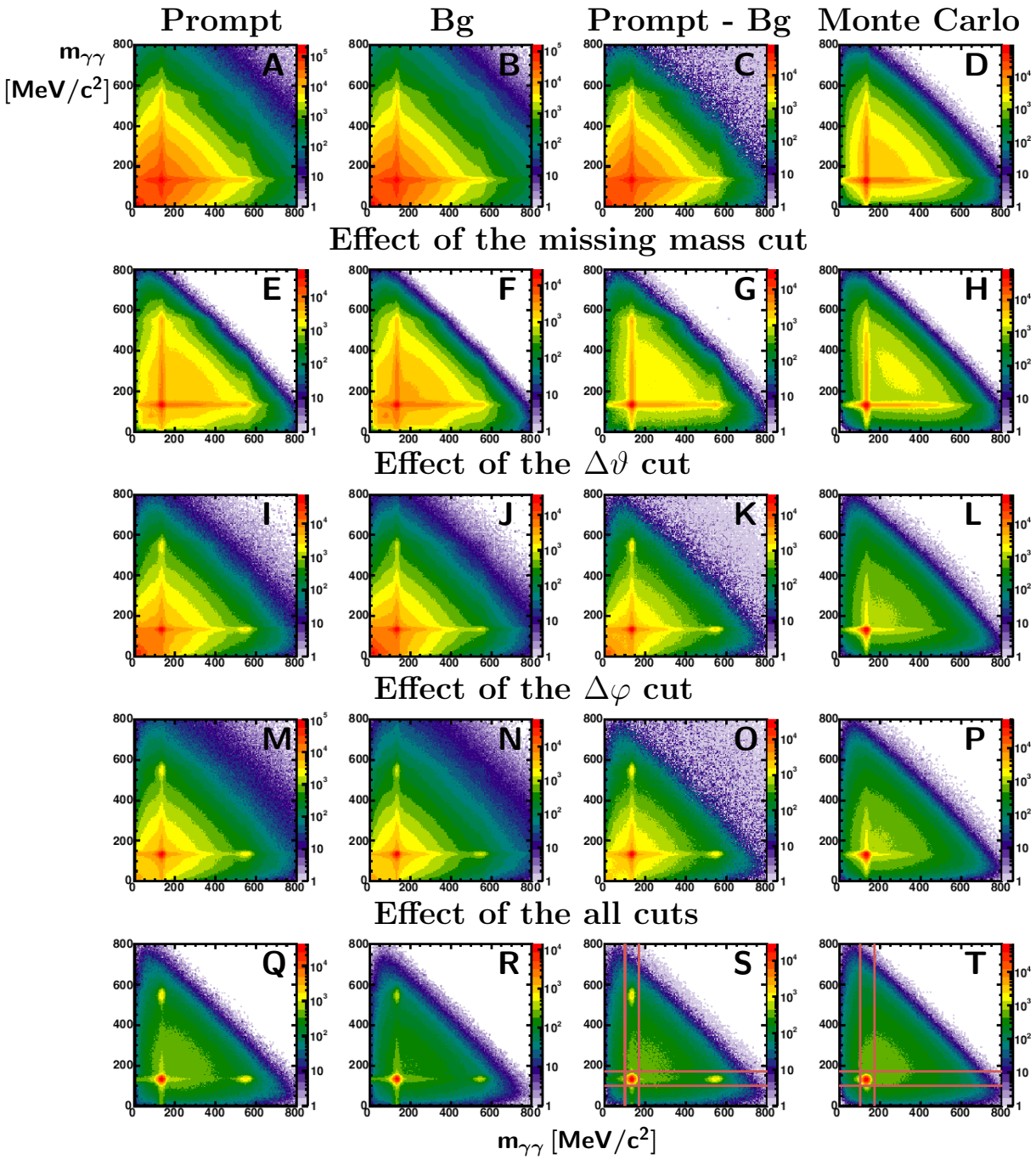

Figure 4.2.: Invariant mass of one $\gamma\gamma$ pair vs. invariant mass of the other $\gamma\gamma$ pair (30 entries per event before cuts). The first column: prompt events, second: normalized timing background, third: prompt events after background subtraction, fourth: Monte Carlo. Shown are the effects of each cut applied separately.

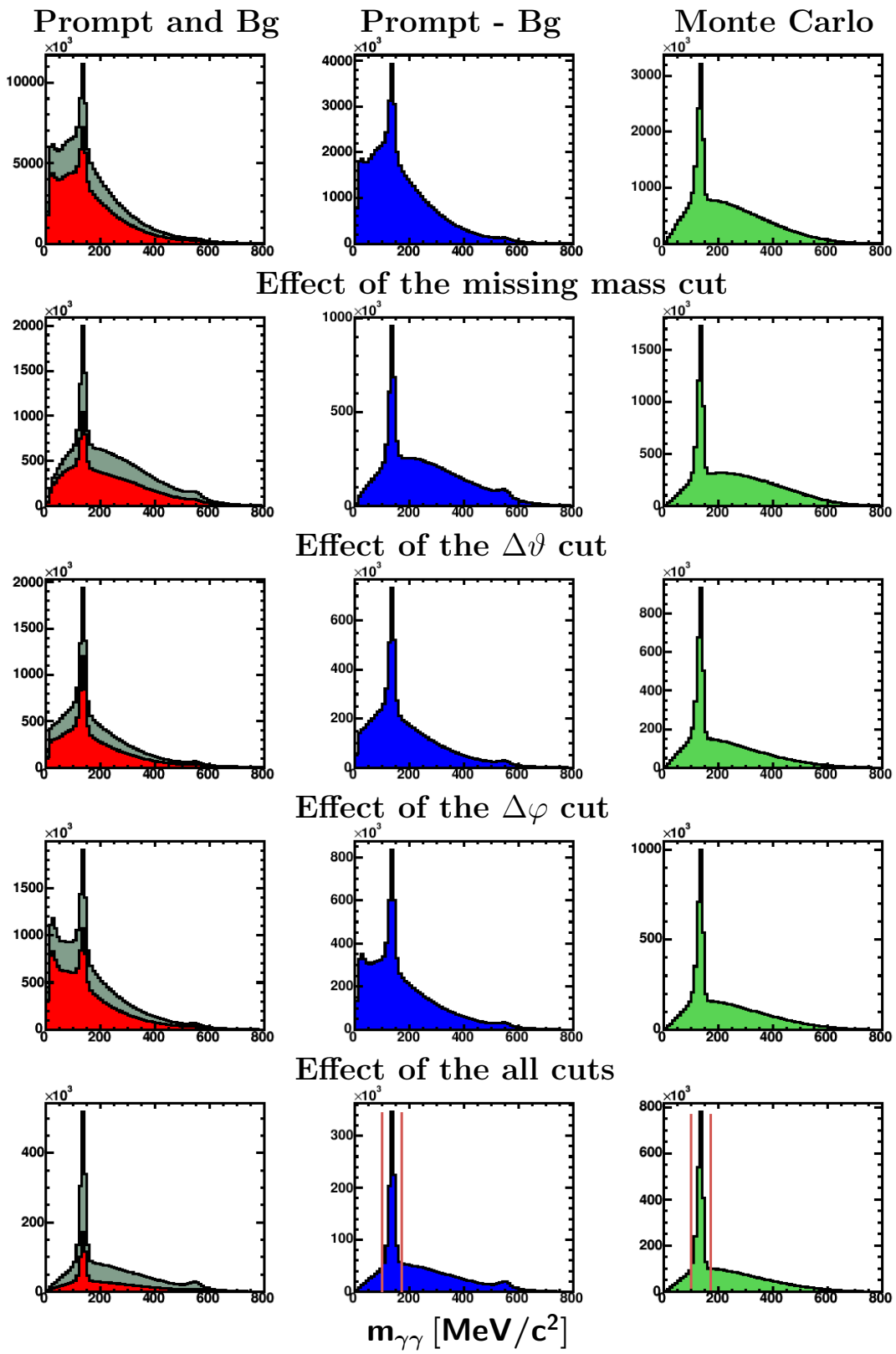

Figure 4.3.: $\gamma\gamma$ invariant mass in 1 dimension (30 entries per event before cuts). Grey: prompt events, red: normalized timing background, blue: prompt events after background subtraction, green: Monte Carlo. Shown are the effects of each cut applied separately.

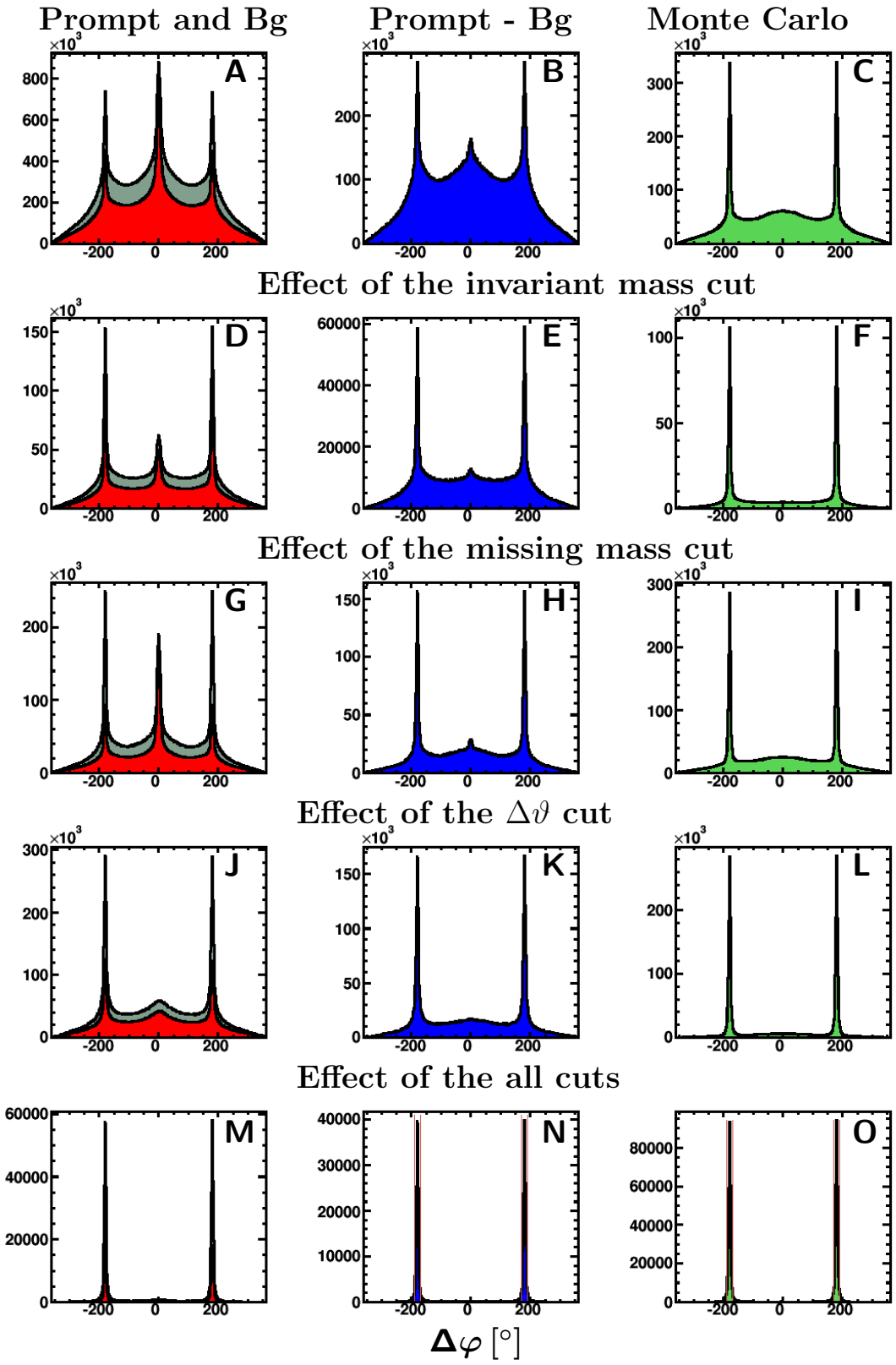

Figure 4.4.: Coplanarity: $\Delta\varphi = \varphi_p - \varphi_{2\pi^0}$ (5 entries per event before cuts), grey: prompt events, red: normalized timing background, blue: prompt events after background subtraction, green: Monte Carlo. The cuts are applied individually. Shown are the effects of each cut applied separately.

detection, is considered. Figure 4.5 shows the difference $\vartheta_p^{calc} - \vartheta_p^{meas}$ before application of kinematic cuts. One can expect that events with correct kinematics would form a peak in $\Delta\vartheta$ around 0°.

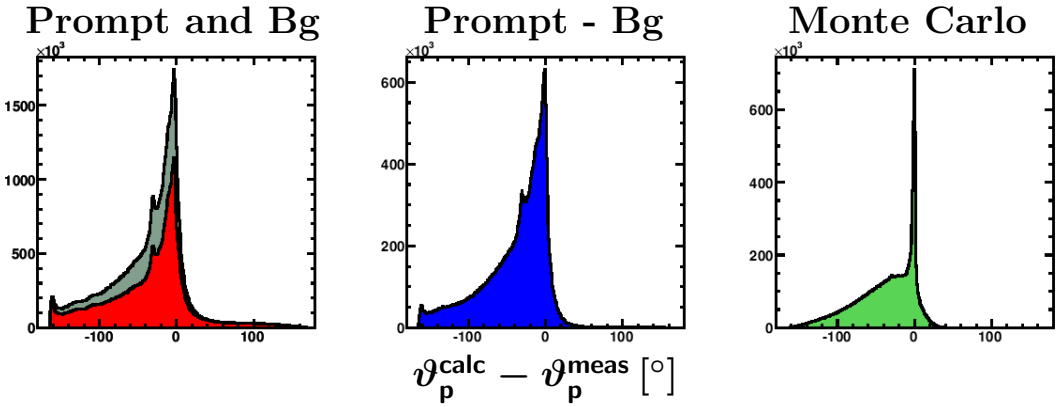

Figure 4.5.: Difference $\vartheta_p^{calc} - \vartheta_p^{meas}$ before application of kinematic cuts (5 entries per event), grey: prompt events, red: normalized timing background, blue: prompt events after background subtraction, green: Monte Carlo.

In the spectra that peak can be seen on top of the background. The background on the right side of the peak (at large positive $\Delta\vartheta$) is practically removed after timing background subtraction. On the left side, in comparison to Monte Carlo distribution, two additional peaks are present around $-30°$ and $-160°$. The origin of the background mechanisms producing these peaks is explained in 4.5.4.

Due to the different granularity, phase space coverage, and background situation of CB and TAPS, the spectra for the cases when the proton is reconstructed in CB and TAPS have been considered separately. The difference $\vartheta_p^{calc} - \vartheta_p^{meas}$ for the proton candidate in the CB is shown in Figure 4.6. In the first row the uncut spectra are shown, where one can see that the spectrum is dominated by background showing a non-significant peak around 0° (A, B). The same is true for the Monte Carlo distribution (C), nevertheless the signal to background ratio is much higher and there are no structures such as the peak at $-160°$. The strongest background suppression is achieved after the $\Delta\varphi$ cut (G, H, I). The cut on $\Delta\vartheta$ with the width of $0 \pm 10°$ is indicated with brown lines in the spectra after all cuts (N, O).

A significant amount of background events is present in $\vartheta_p^{calc} - \vartheta_p^{meas}$ spectra if the

proton was detected in the CB (see Figure 4.6) after each of the kinematic cuts. The effects of various cut combinations showing the subsequent reduction of the background are shown in Figure 4.7. One can see a significant reduction of the background for all cut combinations in comparison to individually applied cuts. The final result after application of all cuts is shown in Figure 4.6 (M, N. O).

The case when the proton candidate is detected in TAPS is shown in Figure 4.8. Already in the uncut spectra (A, B, C) one can recognize that the background contamination is much lower than if the proton was detected in CB. Also, the signal is narrower in comparison to the proton in the CB case. A different signal to background ratio for the candidate to be a proton in the Crystal Barrel and the proton in TAPS can be explained, not only by background contribution (see 4.5.4), but also by the fact that the protons dominantly cover the forward angular range, therefore the probability for the particle to be a proton in the combinatorial analysis is higher if the particle is detected in TAPS. This argument can be confirmed by comparing the background contributions Monte Carlo spectra in Figures 4.6 and 4.8. The width of the cut applied finally is $0 \pm 5^\circ$ and is shown with brown lines (N, O).

4.5.4. Identification of background sources

The events which produce the peak at $\Delta\varphi = 0 \pm 20^\circ$ (see Figure 4.4) have been additionally analyzed to make sure that their contribution is finally excluded. After selection of the peak at $\Delta\varphi = 0 \pm 20^\circ$, $(\vartheta_p \varphi_p)$ matrices for the proton candidate in these events are shown in the Figure 4.9 for prompt events (A), timing background (B) and for the case after background subtraction (C). One can see an enhancement of events at ϑ_p higher than 30° and negative φ_p corresponding to the lower part of the Crystal Barrel. These events, spread over all ϑ and localized in φ mostly contribute to the accidental background (B). The largest part of those is rejected by the time background subtraction (C). It additionally hints towards the assumption that these events originate from a different source and are not related with events produced in the target. The correlation between $\Delta\varphi$ and φ_p of the proton is shown in (D, E, F). The two bands corresponding to coplanar events are obtained at $\Delta\varphi = \pm 180^\circ$, the events corresponding to the

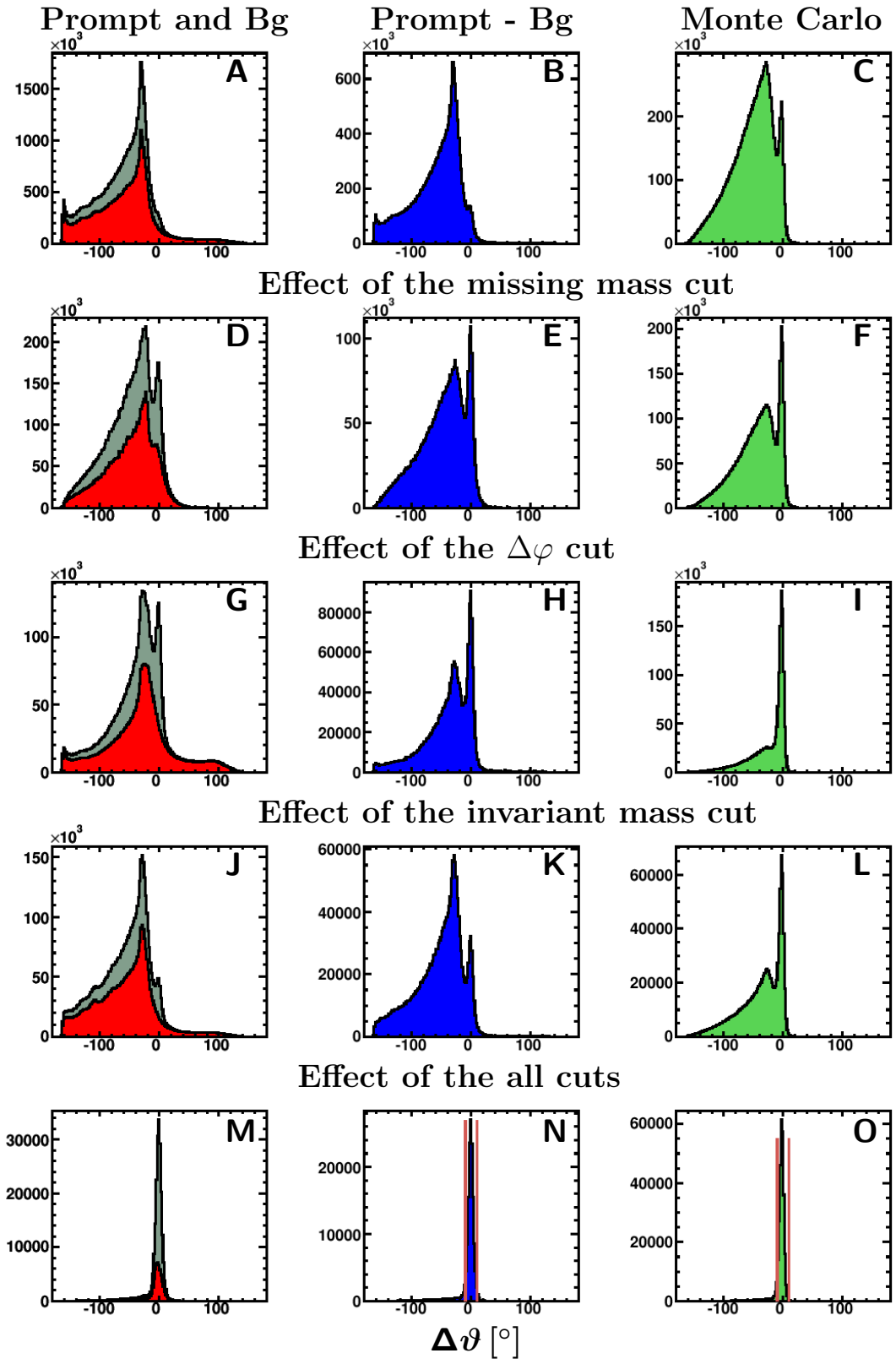

Figure 4.6.: Coplanarity: $\Delta\vartheta = \vartheta_p^{calc} - \vartheta_p^{meas}$ (proton in CB, 5 entries per event before cuts), grey: prompt events, red: normalized timing background, blue: prompt events after background subtraction, green: Monte Carlo. Shown are the effects of each cut applied separately.

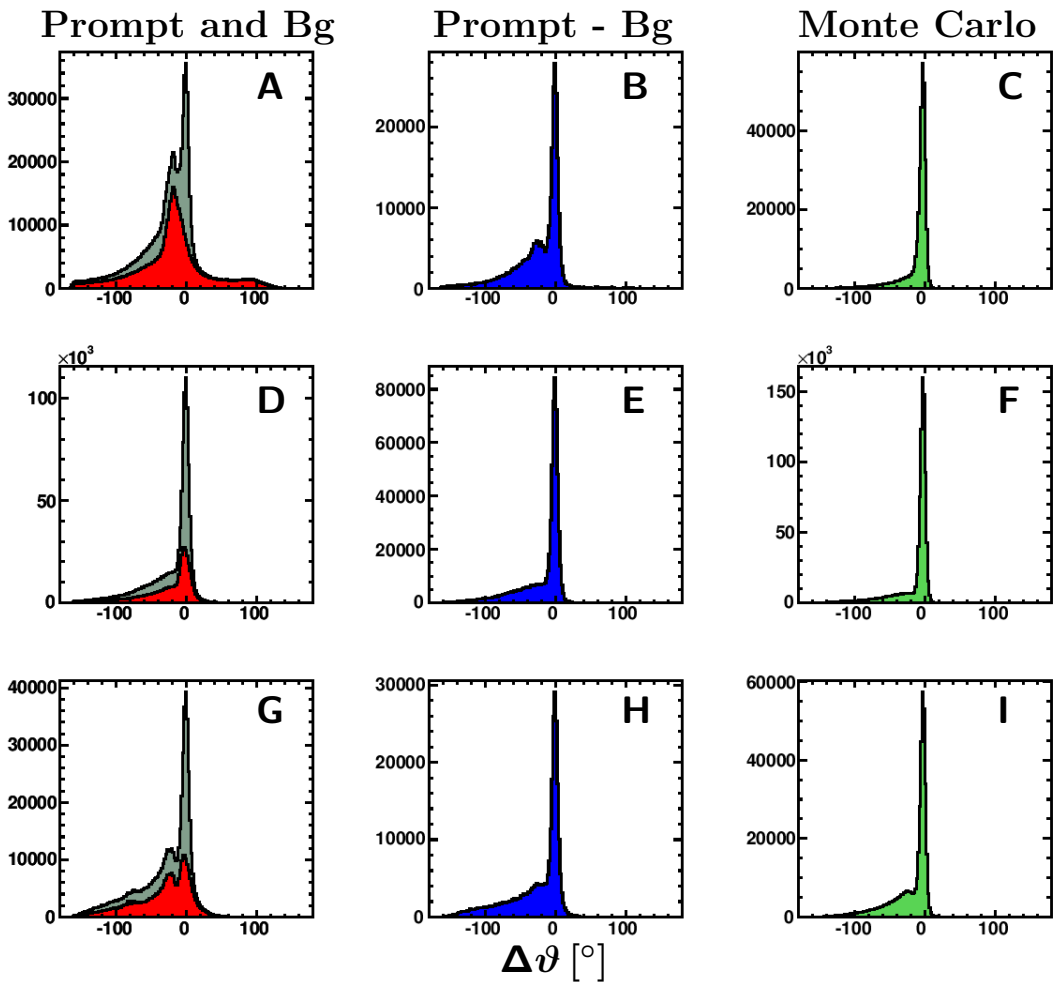

Figure 4.7.: Combinations of cuts: $\Delta\vartheta = \vartheta_p^{calc} - \vartheta_p^{meas}$ (proton in CB), grey: prompt events, red: normalized timing background, blue: prompt events after background subtraction, green: Monte Carlo. (A, B, C): $\Delta\vartheta$ spectra after application of $\Delta\varphi$ and invariant mass cuts, (D, E, F): after application of $\Delta\varphi$ and missing mass cuts, (G, H, I): after application of invariant and missing mass cuts.

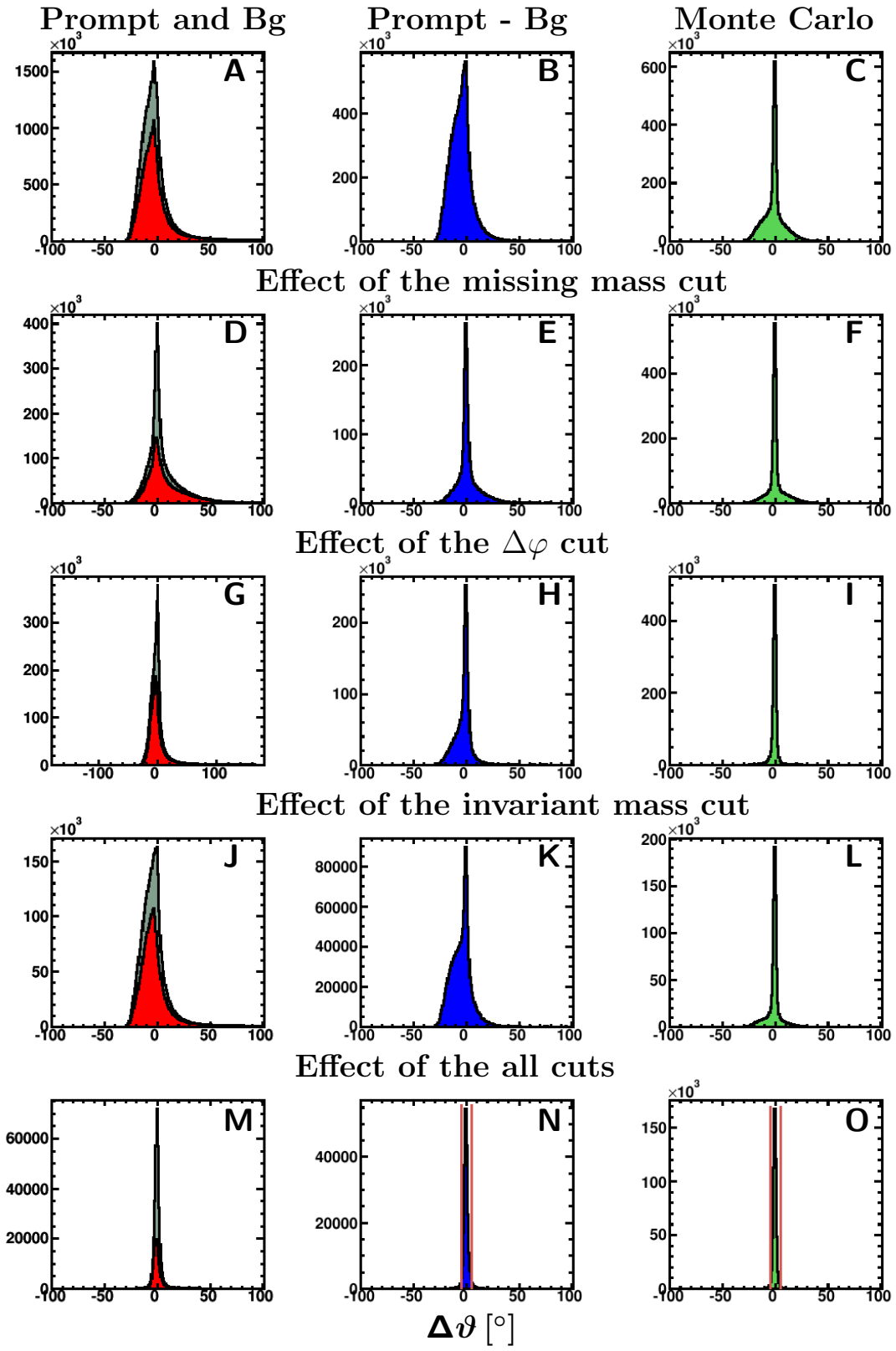

Figure 4.8.: Coplanarity: $\Delta\vartheta = \vartheta_p^{calc} - \vartheta_p^{meas}$ (proton in TAPS, 5 entries per event before cuts), grey: prompt events, red: normalized timing background, blue: prompt events after background subtraction, green: Monte Carlo. Shown are the effects of each cut applied separately.

peak around 0° can be seen, and its location in φ is identified. To find the source of the background the clusters in the Crystal Barrel have been investigated. One can assume that the neutrons escaping from the beam dump penetrate through the CB and produce "long" clusters, containing relatively high number of local maxima along the direction of their flight. To check whether the neutrons from the beam dump can cause the observed structure, the difference $\Delta\varphi$ was plotted vs. number of PEDs in the cluster. In Figure 4.9 (G, H, I) one can see that large number of PEDs in the cluster corresponds to the peak at $\Delta\varphi = 0 \pm 20°$. This is the region in $\Delta\varphi$ where the investigated background contribution is localized and seen in (D, E, F) at negative azimuthal angles. This observation allows the conclusion that the source of these events is the beam dump, emitting neutrons, which penetrate through the lower part of the Crystal Barrel (and further to the lower part of TAPS). As it has been shown above, this background is eliminated after combination of all kinematic cuts.

In addition, the origin of the peaks in the spectrum of $\vartheta_p^{calc} - \vartheta_p^{meas}$ (see e.g. Figure 4.5) has been investigated. As has been shown above, there is a substantial amount of background contributing in the CB due to the beam dump events, which are localized in φ and spread over ϑ. In Figure 4.10 is shown the difference $\Delta\vartheta$ as a function of φ_p of the proton (A, B, C). The enhancement seen at negative $\Delta\vartheta$ is localized in the same region in φ as it was discussed above (Figure 4.9). Another proof that the enhancement in $\vartheta_p^{calc} - \vartheta_p^{meas}$ around 30° originates from the beam dump can be seen in Figure 4.10 (D, E, F), where the number of PEDs in the cluster is plotted as a function of $\Delta\vartheta$ and one can see that the events with high number of PEDs contribute in the region, where the background is enhanced. The peak around -160° is most likely due to e^+e^- pairs produced in the collimators by the incoming photon beam and later split in two parts (in φ) by the sweeping magnet. In Figure 4.10 (A) one can see that effect on the very edge of $\Delta\vartheta$ around $-160°$. This background source due to high rates could always produce signal in the backward crystals of the Crystal Barrel. In the same Figure (G, H, I) the dependence of the deposited energy on the angle ϑ is shown for the particle considered to be the proton in the combinatorial analysis. At the very edge of the Crystal Barrel the enhancement in number of events is present at low deposited energies, which provides additional evidence for these events to have e^+e^- origin.

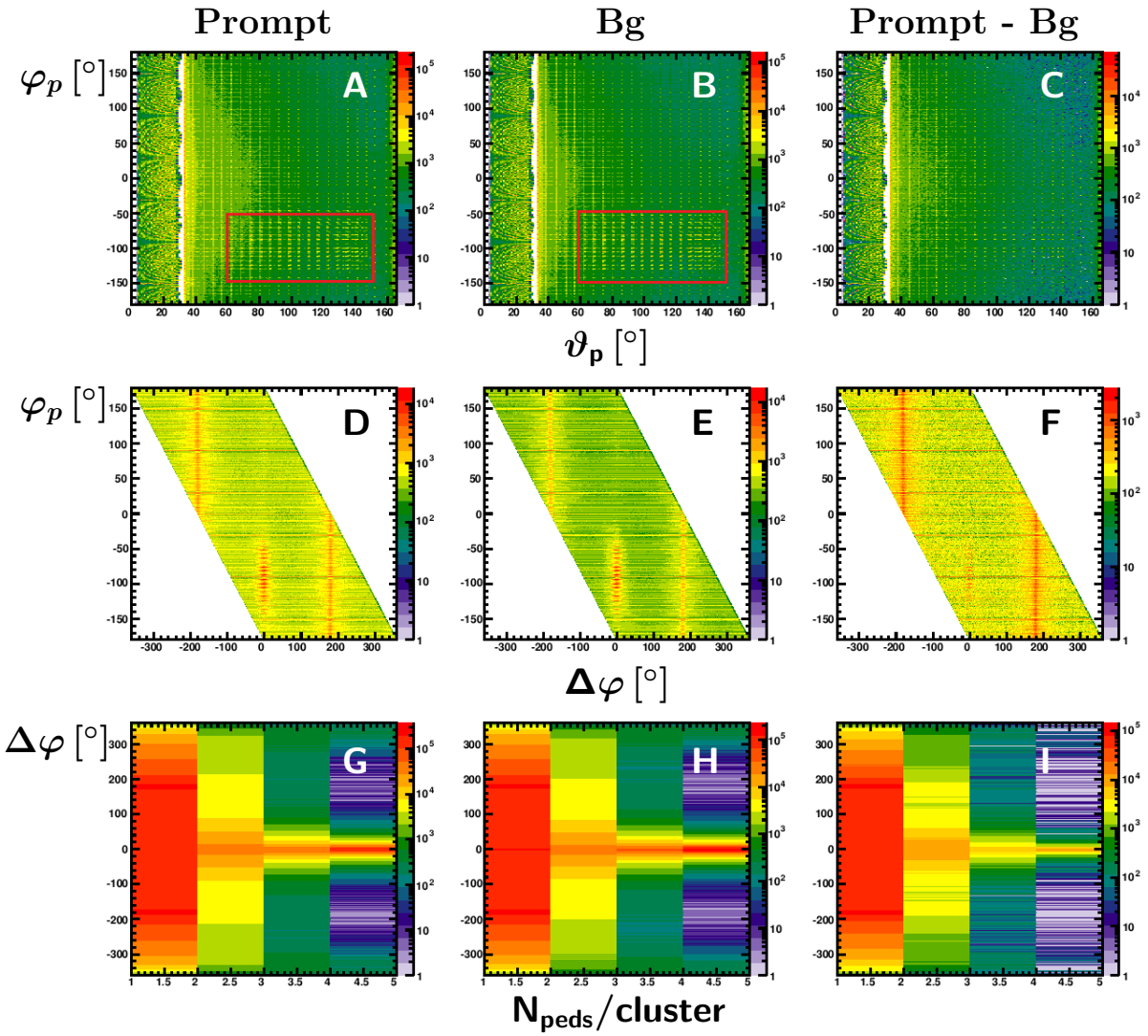

Figure 4.9.: The first column (A, D, G): prompt events, second (B, E, H): normalized timing background, third (C, F, I): prompt events after background subtraction. First row (A, B, C): ($\vartheta_p\varphi_p$) matrices for the proton in case $\Delta\varphi \pm 20°$, Second row (D, E, F): φ_p vs. $\Delta\varphi$, third row (G, H, I): $\Delta\varphi$ vs. N_{peds}/cluster.

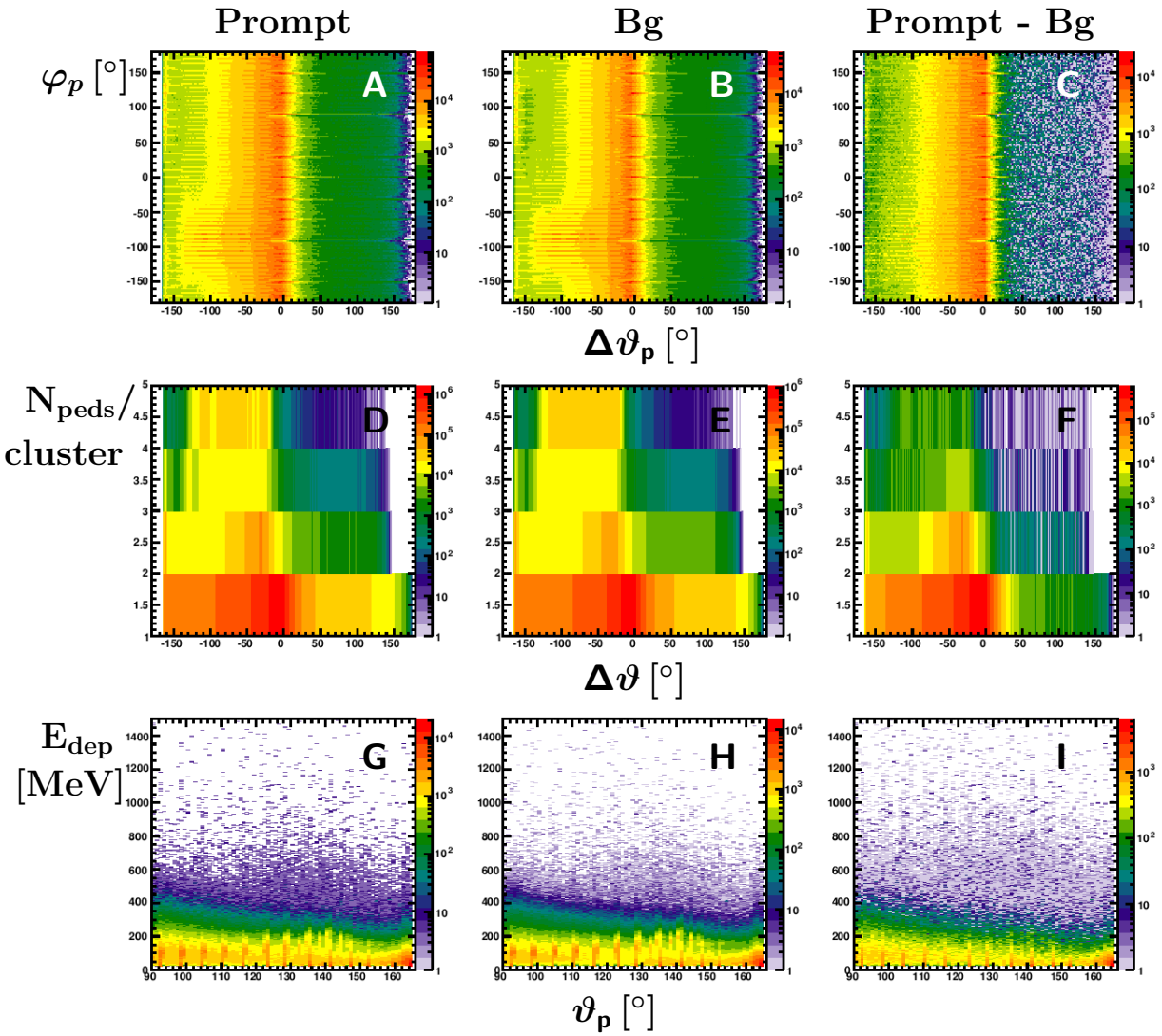

Figure 4.10.: The first column (A, D, G): prompt events, second (B, E, H): normalized timing background, third (C, F, I): prompt events after background subtraction. First row (A, B, C): φ vs. $\Delta\vartheta_p$, Second row (D, E, F): Number of PEDs in the crystals vs. $\Delta\vartheta$, third row (G, H, I): deposited energy E_{dep} vs. ϑ_p.

The investigation of the background described above allows identification of the sources of the background events and to ensure that most of these events are rejected by the kinematic cuts.

4.5.5. Missing mass

The missing mass for each of the combinations of 4 out 5 the 5 PEDs has been calculated taking one PED as a proton candidate. Figure 4.11 shows the missing mass of the proton candidates (5 entries per event).

In the first row (A, B, C) where the uncut spectra are shown, a shoulder in the region of the nominal proton mass can be seen on a high background contribution in the prompt events (grey). After subtraction of the timing background (blue) the peak corresponding to the missing proton can be identified on top of strongly contributing background. On the very right the Monte Carlo spectrum (green) is shown. The proton signal is much more clearly visible here, nevertheless there is a non-negligible background contamination present due to combinatorics introduced in the spectrum. In the second row (D, E, F) the missing mass spectra are shown after cutting on the invariant mass of the two photon pairs. The background is reduced compared to the uncut spectra, and one can recognize significant reduction of the statistics in the histogram due to suppression of the combinatorial background and other sources, such as the competing reaction $\gamma p \to p\pi^0\eta$. After the coplanarity cut (J, K, L) on the difference of $\varphi_p - \varphi_{2\pi^0}$ and the cuts on $\Delta\vartheta$ (G, H, I) the background is strongly suppressed. After all cuts the improvement in the data quality is very obvious and the proton signal is clearly separated. Remaining background is finally rejected after application of the kinematic fit (Sections 4.7 and 4.8). In the fifth row (N, O) the width of the cut $m_{miss} = 938.272 \pm 100\,\mathrm{MeV/c^2}$, applied on the missing mass is indicated.

After all kinematic cuts, in about 94% of the cases one proton candidate is identified for each event, in about 6% two proton candidates are remaining and the number of events with higher number of proton candidates is negligibly low. If there are more than one proton candidates remaining after kinematic cuts, the

kinematic fit has been used to decide which proton candidate to use in the further analysis (see Section 4.7 for details).

4.6. Selection of 4 PED events

Due to inefficiencies and not complete acceptance coverage, the particles in certain parts of the phase space may not be detected, forming an event sample with a distinct geometrical signature. The information about particles can be lost because of having non-sufficient energy to reach the detectors or to overcome the thresholds set for the readout electronics, as is the case for low energetic protons in the region covered by CB, or because the given part of the detector system is not covered by detectors at all, e.g. if the particle escapes through the forward hole of TAPS. If a photon is lost the reaction can not be reconstructed due to the absence of a reliable and complete energy measurement of the protons. If only the proton is not detected there is an opportunity to handle the events by treating the proton as a missing particle. To select the events for which the proton has been lost, the invariant mass and missing mass cuts have been applied. The widths of these two cuts are taken as the same as in 5 PED analysis (see Section 4.5). Afterwards, the data was split in several classes of events and analyzed according to the geometry and performance of the detector system, applying various cuts on polar angle ϑ in combination with the momentum of the missing proton.

a) Invariant mass

At the first look the four detected particles are considered as photon candidates and the missing particle to be the proton. In Figures 4.12 and 4.13 are shown the invariant mass spectra constructed for all possible particle pairs of the four detected particles (6 combinations of photon pairs). The photon combinations have been entered in the histogram symmetrically. The spectra are shown before (the first row) and after the missing mass cut (the second row). One can clearly observe $\gamma p \rightarrow p\pi^0\pi^0$ events and the effect of the background reduction after the missing mass cut.

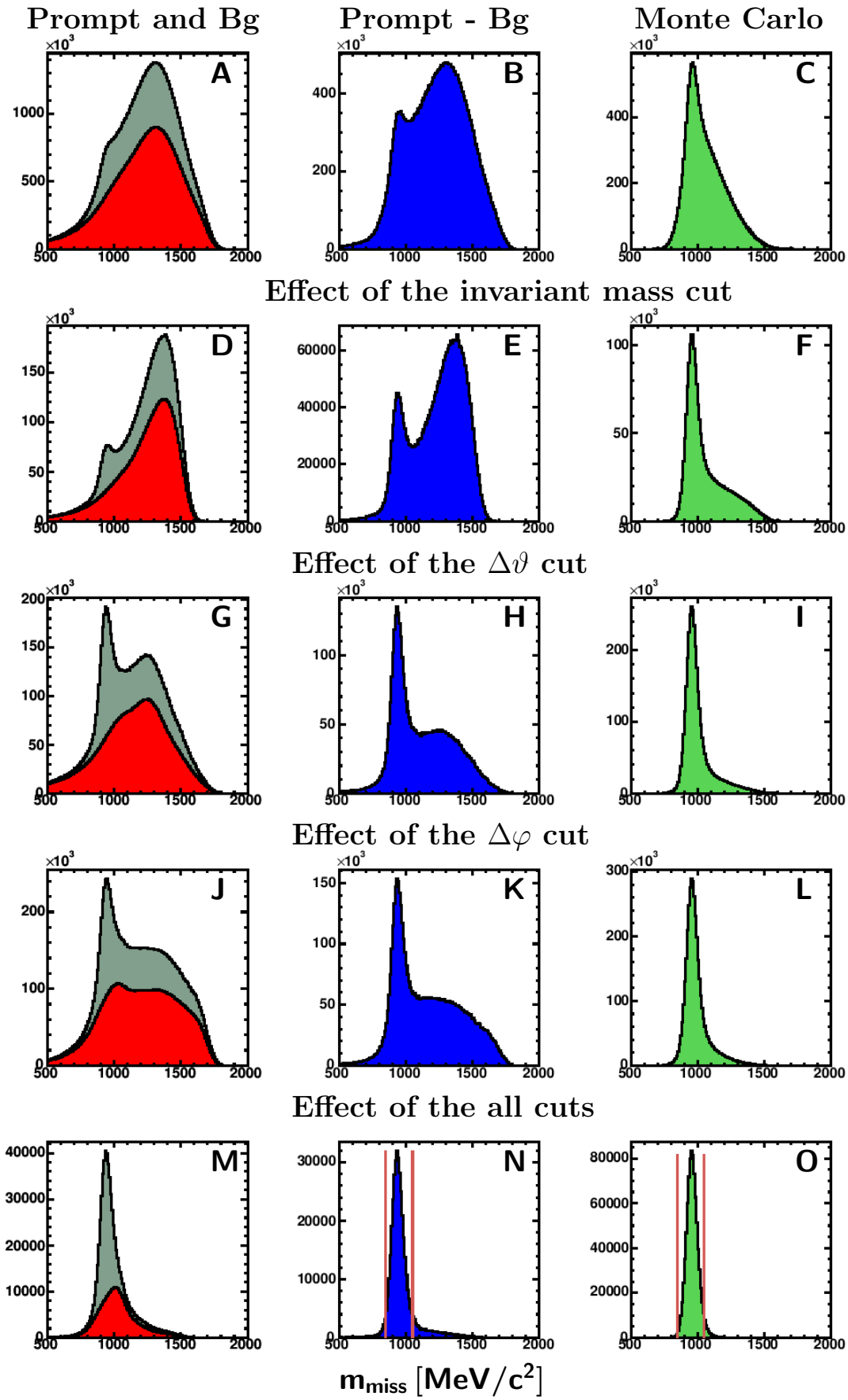

Figure 4.11.: Missing mass spectra (5 entries per event before cuts), grey: prompt events, red: normalized timing background, blue: prompt events after background subtraction, green: Monte Carlo.

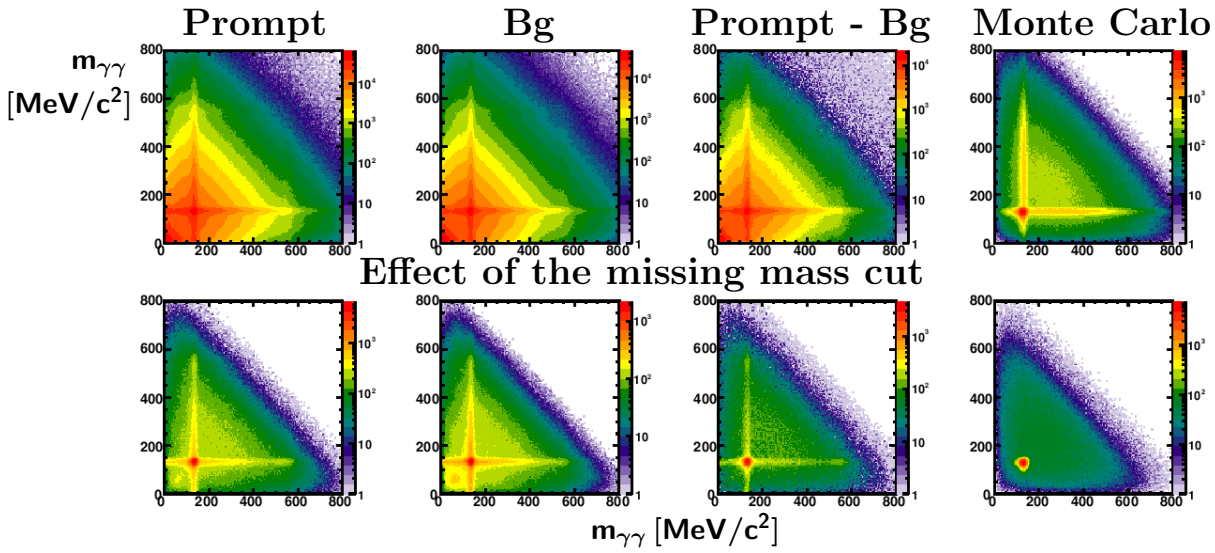

Figure 4.12.: Invariant mass of one $\gamma\gamma$ pair vs. the invariant mass of the other $\gamma\gamma$ pair (6 entries per event before cuts). The columns - first: prompt events, second: normalized timing background, third: prompt events after background subtraction, fourth: Monte Carlo. See text for more details.

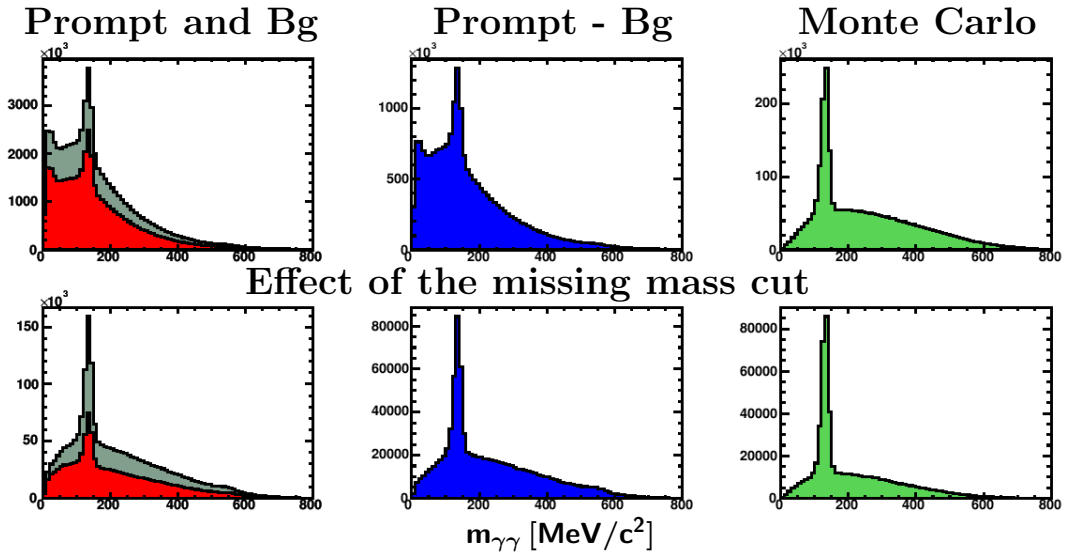

Figure 4.13.: $\gamma\gamma$ invariant mass in 1 dimension (6 entries per event before cuts). Grey: prompt events, red: normalized timing background, blue: prompt events after background subtraction, green: Monte Carlo. See text for more details.

b) Missing mass

The missing mass of the particle assumed to be the proton calculated using four detected particles is shown in Figure 4.14 before the invariant mass cut (the first row) and after (the second row). The background situation is improved and the proton signal is separated after the invariant mass cut, but the spectrum itself and the comparison of the data after time background subtraction with Monte Carlo simulation show that the background contamination is still substantial.

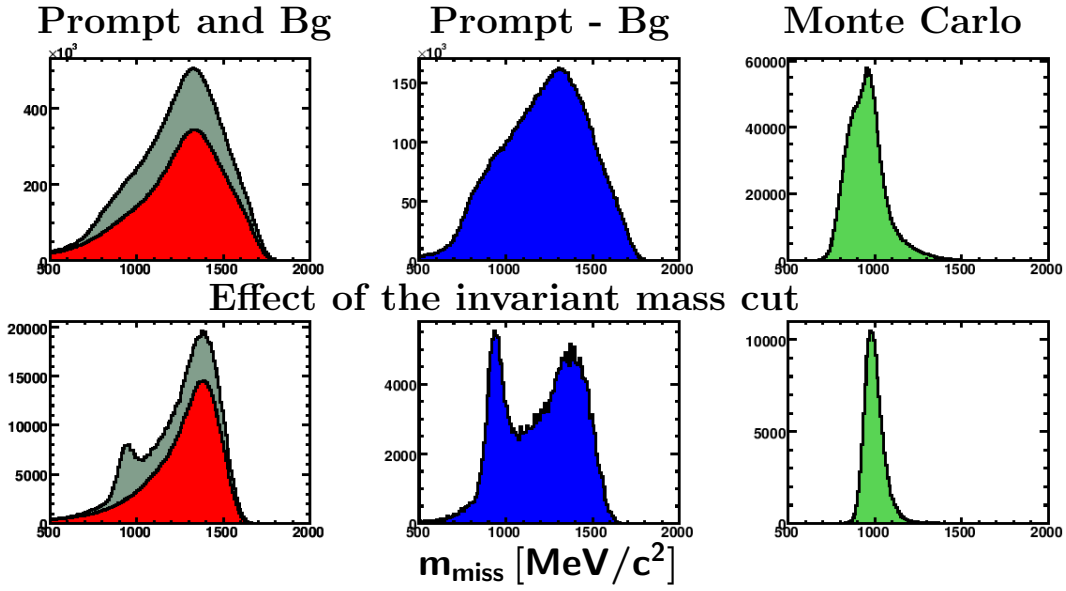

Figure 4.14.: Missing mass of the proton. Grey: prompt events, red: normalized timing background, blue: prompt events after background subtraction, green: Monte Carlo. See text for more details.

One option to further reduce the background is the application of cuts according to the detector performance, using the polar angle and momentum of the missing proton. The dependence of the momentum of the proton on its polar angle ϑ is shown in the Figure 4.15 for data (A, D), reconstructed Monte Carlo events (B, E) and generated Monte Carlo (C, F). In the first row are shown the figures after the invariant mass cut, in the second after the invariant and missing mass cuts. The Monte Carlo spectra have been used for understanding of the detector effects and helped to set the cuts accordingly, e.g. to determine the width of the cuts to separate different structures since the structures in the data are smeared out due to relatively higher background contamination.

The regions covered by 4 PED events correspond to the cases for which one of the particles was lost and so they were not reconstructed as 5 PED events. Rather distinct structure is observed in the reconstructed and generated Monte Carlo spectra. The kinematic cuts (invariant and missing mass cut) applied for Monte Carlo events reduce the contributions of the events in which a photon was lost. However, in the data (see e.g. (A)) there is a contribution of particles with high momenta at low polar angles, which can not be protons [4]. The largest part of these events is rejected after applying the missing mass cut in addition to the invariant mass cut. After these cuts one can see a pattern in the data (D), which is smeared by background contribution. The structures are much better seen in reconstructed (E) and generated Monte Carlo spectra (F) as enhancements in the regions with low detection efficiency. These structures are discussed in the following.

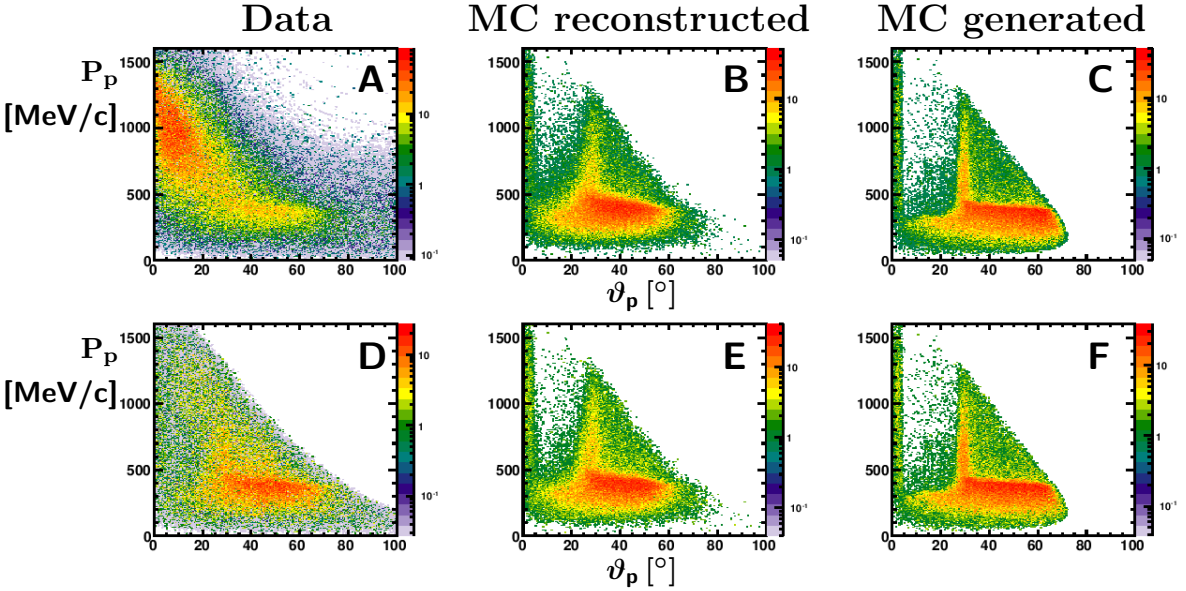

Figure 4.15.: Momentum P_p vs. polar angle ϑ_p of the missing particle (the proton). (A, B, C) after invariant mass cut, (D, E, F) after invariant and missing mass cuts. In the data the timing background is already subtracted.

To further reduce the background, the data was split in several classes of events and corresponding cuts where chosen for each of these classes. As a quality criterion for the applied cuts the minimal reduction of the signal with simultaneous

[4] The cross-check has shown that these events are suppressed after explicit limitation to four neutral hits.

suppression of the background has been used. The missing mass spectrum was taken as a reference.

One can split the data in the region corresponding to TAPS ($0° < \vartheta_p < 30°$) and Crystal Barrel ($30° < \vartheta_p < 80°$) [5]. The cases when the proton is going in the forward direction ($0° < \vartheta_p < 30°$) are the following:

a) The events in the region $0° < \vartheta_p < 5°$ correspond to the cases when the proton escapes through the forward opening of TAPS [6]. These protons have no restriction on their momentum and can be seen in Figure 4.15 as a narrow band at low ϑ_p angles. For these events the cut is set accordingly: no restriction on the momentum is applied. In Figure 4.16 the missing mass of these events is shown. The comparison to the Monte Carlo data shows a high background contribution, but most of the background is separated and can later be eliminated by missing mass cut.

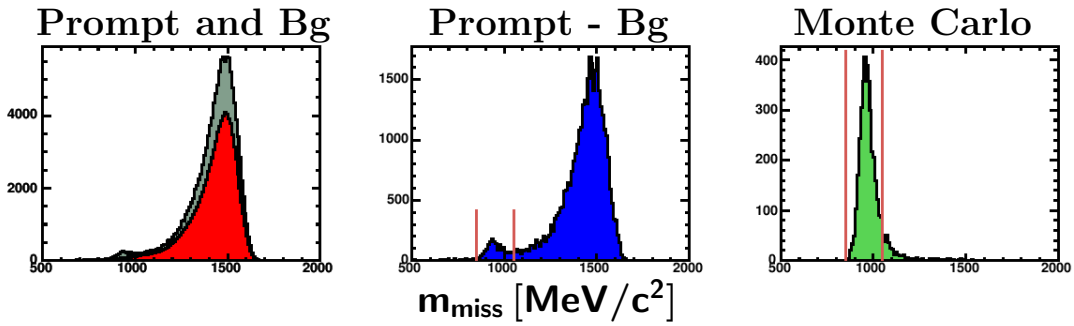

Figure 4.16.: Missing mass of the proton after invariant mass cut in case if $0° < \vartheta_p < 5°$. Grey: prompt events, red: normalized timing background, blue: prompt events after background subtraction, green: Monte Carlo. See text for more details.

b) The region $5° < \vartheta_p < 30°$ is covered by the TAPS. If the energy deposit of the proton exceeds the thresholds of 30 MeV set on the software level for the readout of BaF_2 crystals (see Section 3.2.1), the proton has to be detected and the event in that case would be identified as a 5 PED event. To select the 4 PED events the upper border of possible momentum (with the condition that no proton is detected) has been determined iteratively, using the missing mass

[5] The polar angle of protons does not exceed 70°, 80° in the analysis has been taken as upper border, and can be reduced (not performed).

[6] The limit of 5° was determined from Monte Carlo spectra shown in Figure 4.15.

as a reference and looking at the background to signal ratio. To suppress the background which strongly contributes in the region $P_p > 350\,MeV/c$ only events with a proton momentum smaller than 350 MeV/c have been considered [7]. The generated spectrum (Figure 4.15) confirms the choice of the cut because the value 350 MeV/c is higher than the edge in the spectrum in the region $5° < \vartheta_p < 30°$. Figure 4.17 shows the corresponding missing mass of the proton. The contribution of the background is present, but the significant part of it is later cut by the missing mass cut [8].

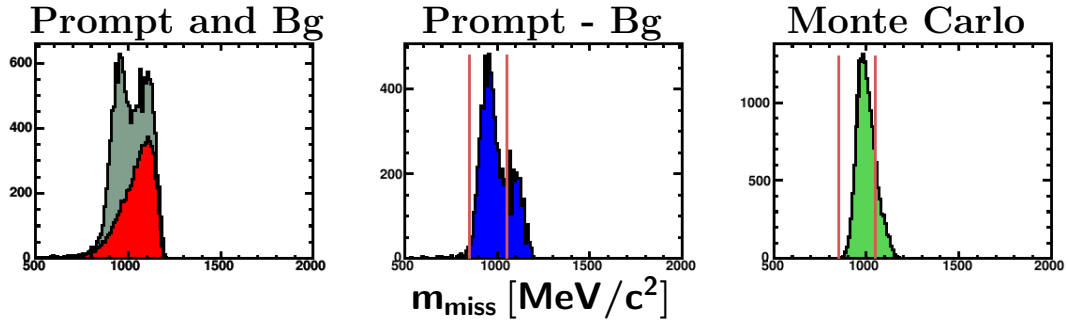

Figure 4.17.: Missing mass of the proton after invariant mass cut in case if $5° < \vartheta_p < 30°$ and $P_p > 350\,MeV/c$. Grey: prompt events, red: normalized timing background, blue: prompt events after background subtraction, green: Monte Carlo. See text for more details.

c) In the overlap region ($28° < \vartheta_p < 32°$) between Crystal Barrel and TAPS protons with different momenta contribute. The protons with momenta higher than 350 MeV/c in the overlap region have been considered. The missing mass of the proton is shown in Figure 4.18. The background contamination is much higher than in the other event classes. Taking into account the fact that these events (signal part) form only a small fraction of the total statistics, it has been decided to leave this class of events out of further analysis.

d) The second part of the data ($30° < \vartheta_p < 80°$) is covered by Crystal Barrel and inner detector. The protons in this case can be selected by their momenta and the

[7] The value of 350 MeV/c is already higher than the threshold value set for the BaF_2 crystals. However, since the effective thresholds are somewhat higher for protons than for photons due to different energy deposit mechanism, the value of 350 MeV/c was used.

[8] In this class of events the cut rejects some of the Monte Carlo events in the high missing mass region. This is a small part of the statistics, however for the accurate extraction of the cross-sections this cut can be applied differently for data and Monte Carlo.

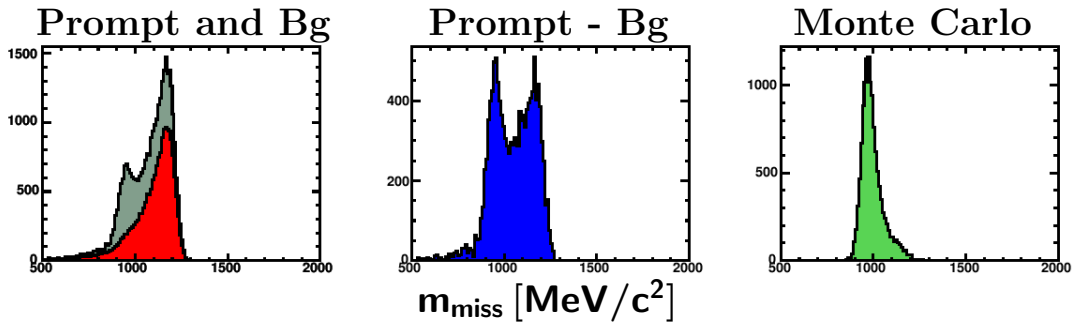

Figure 4.18.: Missing mass of the proton after invariant mass cut in case if $28° < \vartheta_p < 32°$ and $P_p > 350\,MeV/c$. Grey: prompt events, red: normalized timing background, blue: prompt events after background subtraction, green: Monte Carlo. See text for more details.

inner detector information can be used to reduce the background contribution.

d1) The protons with very low momenta do not fire the inner detector. To select this class of events and to reduce the background, the absence of the hit in the inner detector has been required. In Figure 4.19 the dependence of the missing mass of the proton on the proton momentum is shown with and without asking for a hit in the inner detector for Data (A,C) and Monte Carlo (B, D). One can observe a rather clear cut at 250 MeV/c if one hit in the inner detector is required. It means that the protons with momentum below this limit do not produce a signal in the inner detector. The determined number, 250 MeV/c is consistent with [vP$^+$07] (260 MeV/c). In Figure 4.19 one can see that the events which are cut at low missing proton momenta by requiring one hit in the inner detector are in the correct missing mass range. For this type of events the selection criterion for the missing proton momentum is not to exceed 250 MeV/c and in the same time no hit in the inner detector must be present. The missing mass for those events is plotted in Figure 4.20, where a clear proton signal is observed.

d2) An overall reduction of the background is also achieved at higher momenta by requiring a hit in the inner detector. According to simulation (Figure 4.19) and in good agreement with [vP$^+$07] (420 MeV/c) the protons in the momentum range $250 < P_p < 450\,MeV/c$ (Figure 4.19) can cause a signal in the inner detector but do not reach the CB, or the energy of the protons is not high enough to overcome the thresholds of the CsI(Tl) crystal readout. For this type of events the presence

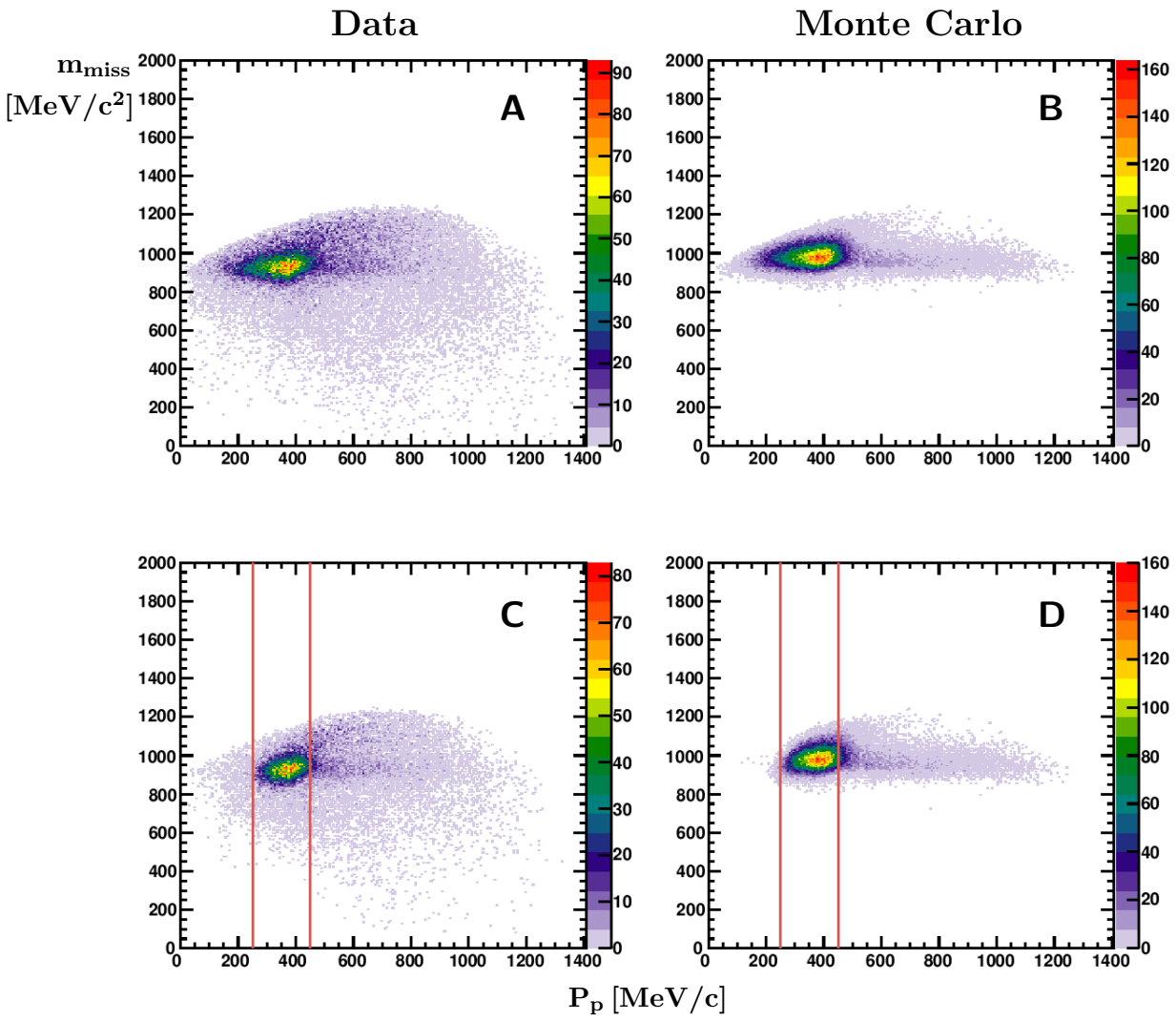

Figure 4.19.: Missing mass of the proton m_{miss} vs. its momentum P_p (after invariant mass cut) without asking for an inner detector hit (A, B) and requiring one hit in the inner detector (C, D). The brown lines at 250 MeV/c and 450 MeV/c show the limits for the momenta used in the cuts. See text for more details.

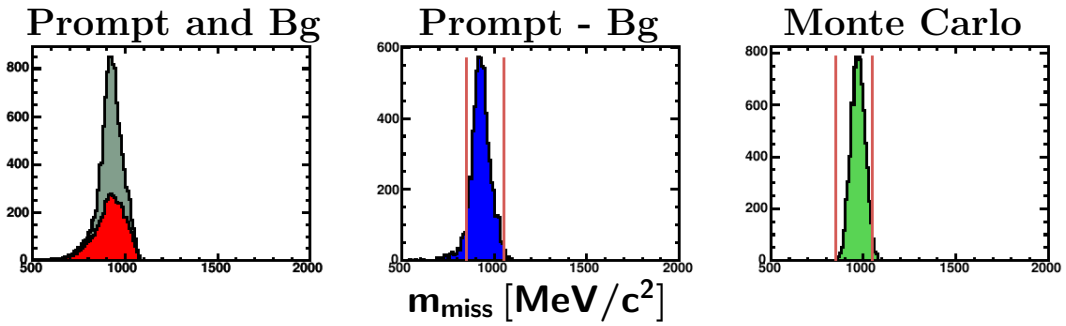

Figure 4.20.: Missing mass of the proton after invariant mass cut in the case $30° < \vartheta_p < 80°$, $P_p < 250\,MeV/c$, requiring no hit in the inner detector. Grey: prompt events, red: normalized timing background, blue: prompt events after background subtraction, green: Monte Carlo. See text for more details.

of one inner detector hit and in the same time the momentum of the missing particle being within $250 < P_p < 450\,MeV/c$ were chosen as a selection criterion. Corresponding missing mass spectra are shown in Figure 4.22 (A, B, C). The background contamination for these events was additionally reduced by requiring a match between the calculated proton direction and the hit in the inner detector. For that the differences between polar and azimuthal angles of the proton and position of the hit in the inner detector are considered (see Figure 4.21). The cuts have been selected to be: $\vartheta_p - \vartheta_{hit}^{inner} = 0 \pm 20°$ and $\varphi_p - \varphi_{hit}^{inner} = 0 \pm 15°$. The asymmetric shape in $\Delta\vartheta$ is due to the contribution of inner detector hits at high ϑ_p, however most of these cases are rejected by the $\vartheta_p - \vartheta_{hit}^{inner} = 0 \pm 20°$ cut [9].

The missing mass of the proton with and without angular matching for this type of events is shown in the Figure 4.22. One can recognize that the change due to the angular matching is relatively small and mostly leads to the reduction of the background, seen in the tails of the missing mass spectra. The events with proton momenta above 450 MeV/c seen in Figure 4.19, partly being in the desired missing mass range were rejected. These events strongly contribute in the region corresponding to the overlap of the Crystal Barrel and TAPS. As was shown above, this class of events has a very high background contamination and were therefore rejected for in further analysis.

[9] Also can be done by restricting the range of ϑ, used in the inner detector.

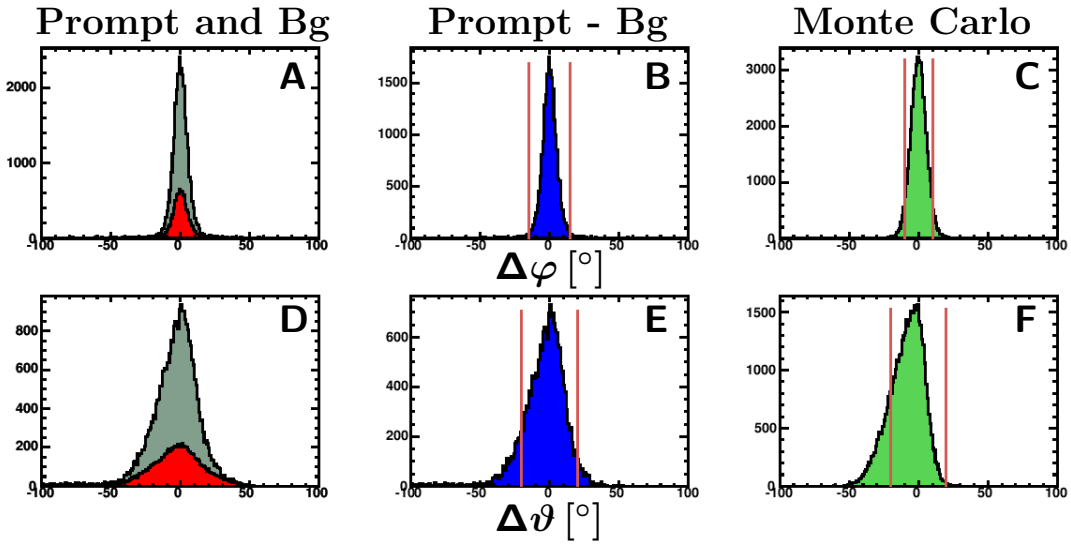

Figure 4.21.: $\Delta\varphi$ (A, B, C) and $\Delta\vartheta$ (D, E, F) of the missing particle and the hit in the inner detector (after invariant mass cut) if $30° < \vartheta_p < 80°$, $250\,\mathrm{MeV/c} < \mathrm{P_p} < 450\,\mathrm{MeV/c}$ and a hit present in the inner detector. Grey: prompt events, red: normalized timing background, blue: prompt events after background subtraction, green: Monte Carlo. See text for more details.

The final missing mass spectrum after invariant mass cut and P and ϑ dependent selection is shown in Figure 4.23. The proton peak is nicely separated from the background and can be selected by the final missing mass cut as it is shown with brown lines.

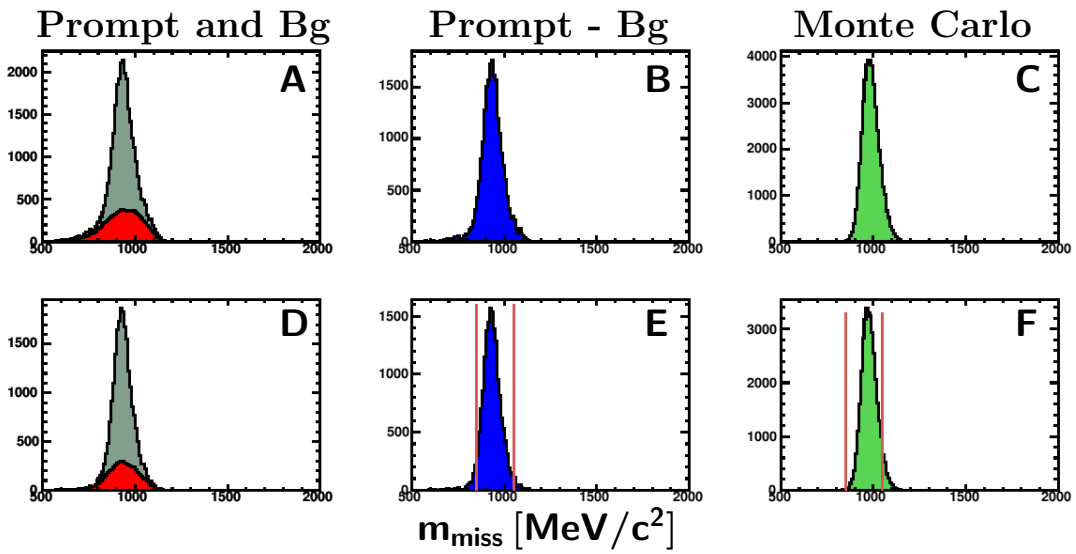

Figure 4.22.: Missing mass of the proton after invariant mass cut in the case $30° < \vartheta_p < 80°$, $250\,\mathrm{MeV/c} < \mathrm{P_p} < 450\,\mathrm{MeV/c}$, requiring a hit in the inner detector, before (A, B, C) and after (D, E, F) matching of the missing proton direction with inner detector hit (after invariant mass cut). A reduction of the tails present in the missing mass before matching, is achieved. Grey: prompt events, red: normalized timing background, blue: prompt events after background subtraction, green: Monte Carlo. See text for more details.

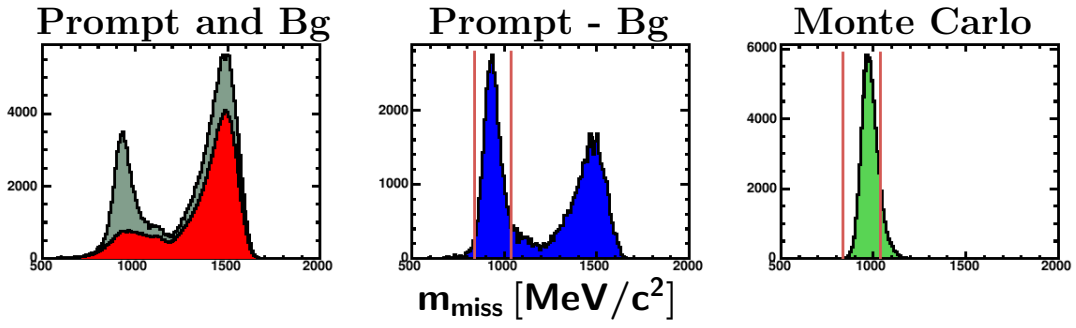

Figure 4.23.: Missing mass of the proton (combined) after all cuts. Grey: prompt events, red: normalized timing background, blue: prompt events after background subtraction, green: Monte Carlo. See text for more details.

4.7. Application of the kinematic fit

The energy and momentum of the particles, determined by the reconstruction, are affected by detector performance and resolution and are not precise. The kinematic fit is a tool, which allows to vary the values of the kinematic parameters within errors, so that the kinematics of the reaction is fulfilled exactly, according to energy and momentum conservation. The masses of the particles can also be used as constraints for the fit. A detailed description of the kinematic fit is given in [vP03]. Here the quantities which are determined from the data and which indicate the quality of the fit are described. If the shifts of the kinematic parameters y_i, by the kinematic fit are defined as δy_i, a quantity which allows to conclude whether the errors of the measurement have a gaussian shape is called pull and defined as:

$$pull_i = \frac{\delta y_i}{\sqrt{\sigma_i^2 - \sigma_i'^2}} \tag{4.4}$$

where σ_i is the error before the fit, $\sigma_i^{'}$ is the error after the fit and is smaller than the primary errors σ_i. If the values y_i extracted from the measurement have a gaussian distribution and there are no systematic effects present, then the pull distribution has to have a gaussian distribution too, with a mean value $\mu = 0$ and variation $\sigma = 1$ (after normalization with errors as in Equation 4.4) [vP$^+$07][vP03]. The pull distributions (data) for variables $\sqrt{E}$, ϑ and φ of the incoming photon, and photons in CB and TAPS separately are shown in Figure 4.24 for the case of the 3C (3-constraint) $\gamma p \rightarrow p\pi^0\pi^0$ fit, which uses a missing proton hypothesis with the constraints on the masses of two π^0s. The mean values μ and the variation σ of the gaussian spectra are compatible with expected values, showing the absence of strong systematic effects in the measurement. The value of χ^2 assuming uncorrelated errors can be calculated as [vP$^+$07]:

$$\chi^2 = \sum_i \left(\frac{\delta y_i}{\sigma_i} \right)^2 \tag{4.5}$$

In the kinematic fit the errors after fitting are correlated and χ^2 can be determined using the covariance matrix. For more details see [vP$^+$07][vP03]. The probability

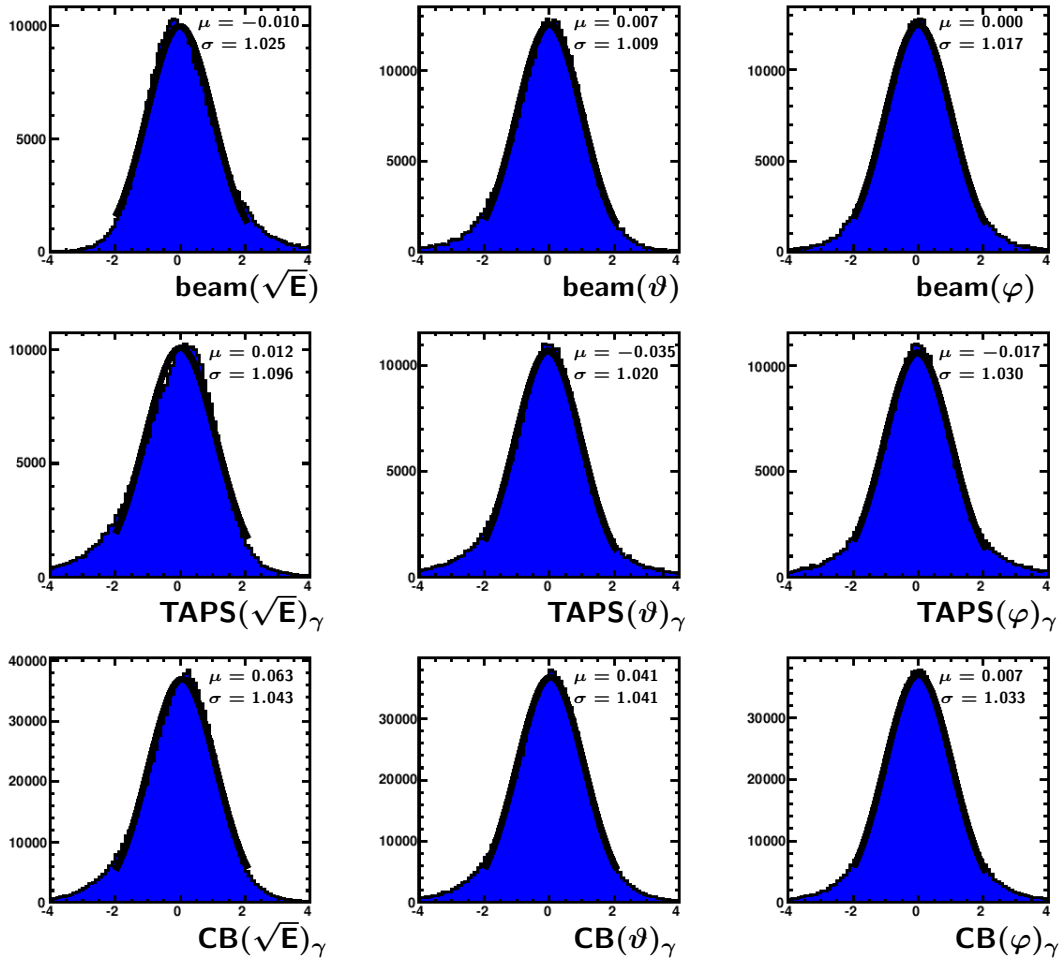

Figure 4.24.: Pull distributions (data) of the photons for the hypothesis $\gamma p \rightarrow p\pi^0\pi^0$.

distribution function is defined as:

$$F(\chi^2) = P(\chi^2 < \chi^2_{theor}) \tag{4.6}$$

and gives the probability for the obtained χ^2 value to be smaller than the theoretical χ^2_{theor} [10]. Using this definition, a quantity which gives a handle on the quality of the events, called Confidence level (Cl) is defined as:

$$Cl = 1 - F(\chi^2) \tag{4.7}$$

The Cl has values in the interval $[0, 1]$ and if no background is present has to have a flat distribution. Figure 4.25 shows the distribution of the Cl for the hypothesis $\gamma p \rightarrow p\pi^0\pi^0$ for data and Monte Carlo events. One can see that at high Cl the distribution is practically flat, the rise towards small Cl values corresponds to the events with bad quality and possibly to the background events (in the case of the experimental data). The cut on these events reduces the background in the data. The kinematic fit is applied as follows. After preselection using kinematic cuts the data has been subjected to the fit using $\gamma p \rightarrow p\pi^0\pi^0$ hypothesis. For the events which have passed the kinematic cuts with more than one proton candidate, the confidence levels of the $\gamma p \rightarrow p\pi^0\pi^0$ hypothesis have been compared, and only the combination with the highest confidence level has been used in the further analysis. The information about type of the particles determined with combinatorial analysis and kinematic cuts was transferred to the kinematic fit. Thus, four photons identified by kinematic cuts were selected to be the photons in the kinematic fit. The events with low confidence level have been rejected with a cut on the Cl of $\gamma p \rightarrow p\pi^0\pi^0$ hypothesis at 10%. In addition an anticut on the competing $\gamma p \rightarrow p\pi^0\eta$ hypothesis is applied. In Figure 4.26 is shown the Cl of the $\gamma p \rightarrow p\pi^0\eta$ vs. Cl of the $\gamma p \rightarrow p\pi^0\pi^0$ for the data and Monte Carlo events. The kinematic cuts are already applied. One can see a red narrow band with high intensity for events with different Cl of $\gamma p \rightarrow p\pi^0\pi^0$ and low Cl of $\gamma p \rightarrow p\pi^0\eta$. There are events present in the region where both confidence levels have high values simultaneously in the data and as well in Monte Carlo (even though the $\gamma p \rightarrow p\pi^0\eta$ was not included in the simulation), but their number

[10] For the definition of χ^2_{theor} see [N$^+$10] [vP03].

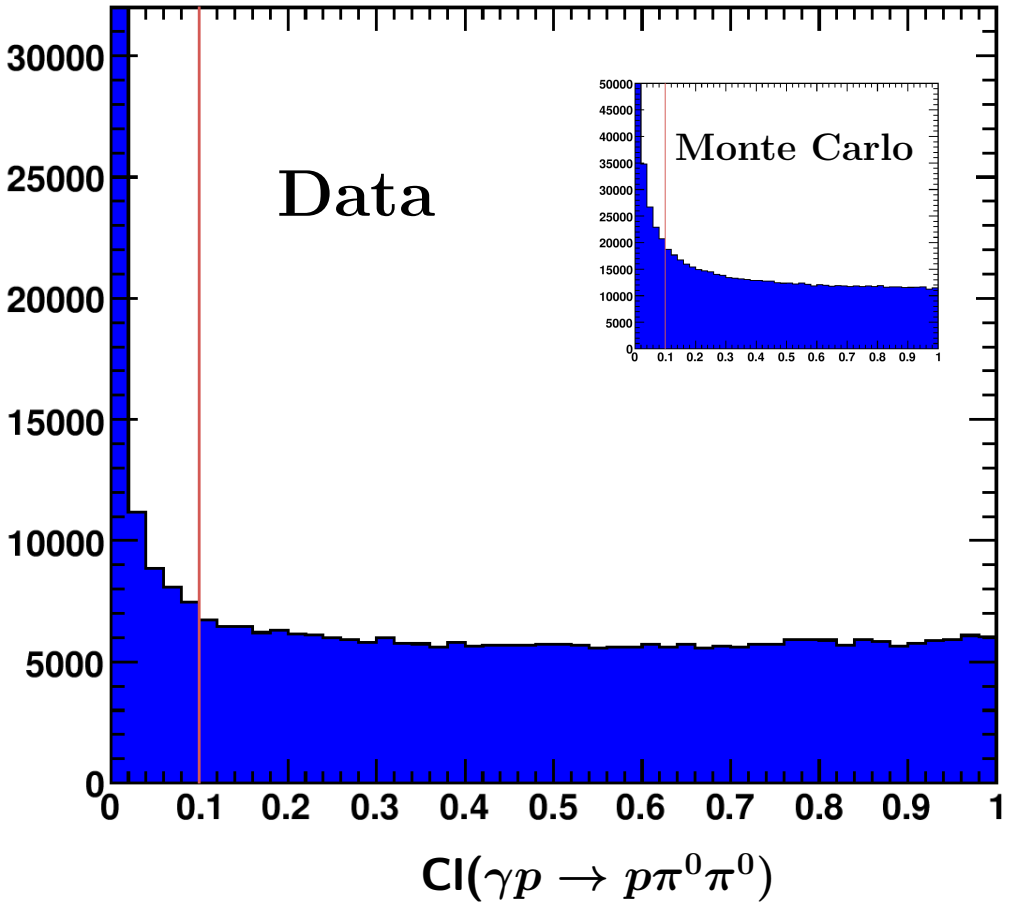

Figure 4.25.: Confidence level of the hypothesis $\gamma p \to p\pi^0\pi^0$ for the data and Monte Carlo events.

is not significant. To reduce the possible contribution of $\gamma p \to p\pi^0\eta$, the events with high $Cl_{\pi\eta}$ and in the same time low $Cl_{\pi\pi}$ have been rejected by requiring $Cl_{\pi\pi} > Cl_{\pi\eta}$. The cut is indicated with diagonal line in Figure 4.26, the events below the line have been retained.

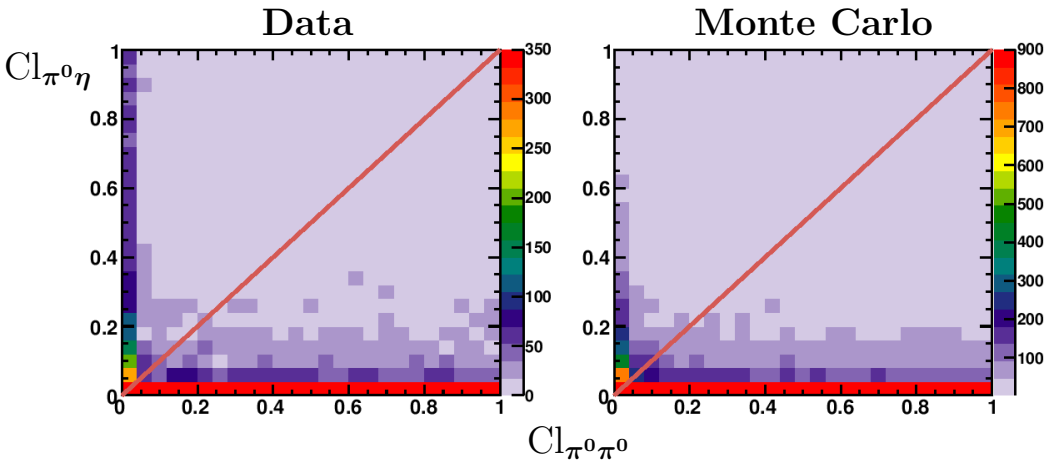

Figure 4.26.: Confidence level of the $\gamma p \to p\pi^0\eta$ hypothesis vs. Confidence level of the $\gamma p \to p\pi^0\pi^0$ hypothesis. On the left: data, on the right Monte Carlo events. The maximum number of events in the plots is suppressed to access the structures which otherwise are not seen due to a large amount of events at very low confidence levels (seen as a rise in Figure 4.25).

Figure 4.27 shows the Cl of the $\gamma p \to p\pi^0\eta$ hypothesis vs. Cl of the $\gamma p \to p\pi^0\pi^0$ for simulated $\gamma p \to p\pi^0\eta$ events after kinematic cuts. One can see that for most of the events the condition $Cl_{\pi^0\eta} < Cl_{\pi^0\pi^0}$ is fulfilled, which means that this cut efficiently eliminates events from the competing $\gamma p \to p\pi^0\eta$ reaction. Additionally, it was determined that only 0.01% of generated $\gamma p \to p\pi^0\eta$ events pass all the cuts applied in the selection of $\gamma p \to p\pi^0\pi^0$ (including cuts on the Cl mentioned above). This number, being already negligible, is further reduced due to the branching ratios and relatively low cross-section of the reaction $\gamma p \to p\pi^0\eta$.

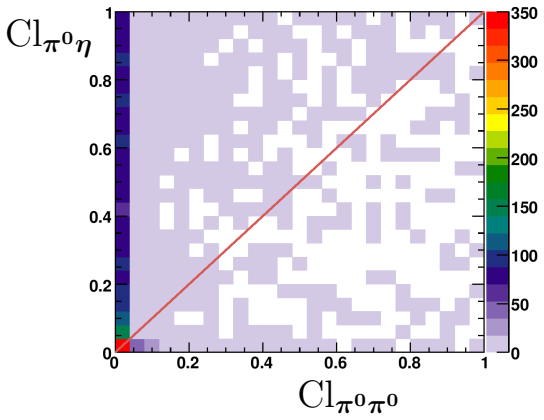

Figure 4.27.: Confidence level of the $\gamma p \to p\pi^0\eta$ hypothesis vs. Confidence level of the $\gamma p \to p\pi^0\pi^0$ hypothesis for simulated $\gamma p \to p\pi^0\eta$ events.

4.8. Compatibility of kinematic fit with kinematic cuts

In case if the proton is detected in one of the calorimeters (5 PED events), its direction is used to check the agreement between the fitted information and the information obtained from reconstruction. The angle φ of the proton determined by the fit had to differ from the φ of the corresponding particle $2\pi^0$ system within $\pm 180 \pm 10°$ (see Figure 4.28). The difference $\Delta\vartheta$ for fitted and reconstructed proton had to be $0 \pm 8°$ if the proton was detected in the Crystal Barrel (A, B, C), and $0 \pm 4°$ if the proton was in TAPS (D, E, F) (see Figure 4.29). The widths of the cuts were determined so that the tails in the spectra outside of the peak would be rejected. The cuts are indicated with brown lines [11].

Using the knowledge about detector performance, three additional cuts are applied. The proton can deposit only a certain amount of energy in the calorimeters. The limits of the energy deposits for protons were determined based on Monte Carlo simulations. Since the protons do not produce electromagnetic showers in the calorimeters, the number of crystals fired in the calorimeters by the proton

[11] Due to the smaller width of spectra the cuts on $\Delta\vartheta$ are chosen to be narrower than for the difference obtained from the reconstructed particles only.

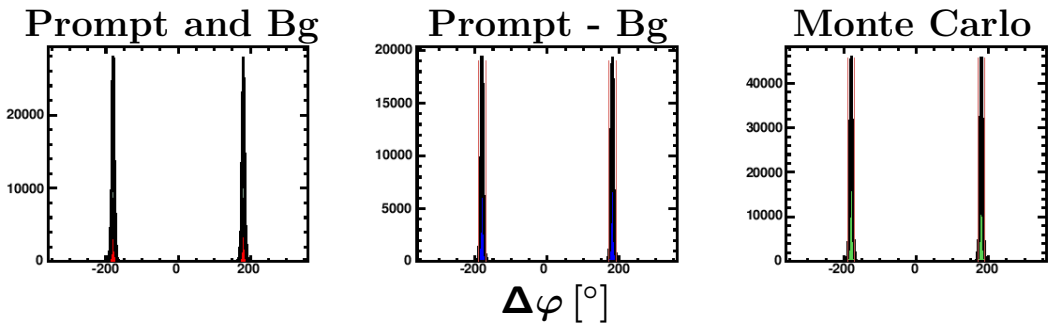

Figure 4.28.: Difference $\Delta\varphi = \varphi_p^{rec} - \varphi_{2\pi^0}^{fit}$, grey: prompt events, red: normalized timing background, blue: prompt events after background subtraction, green: Monte Carlo.

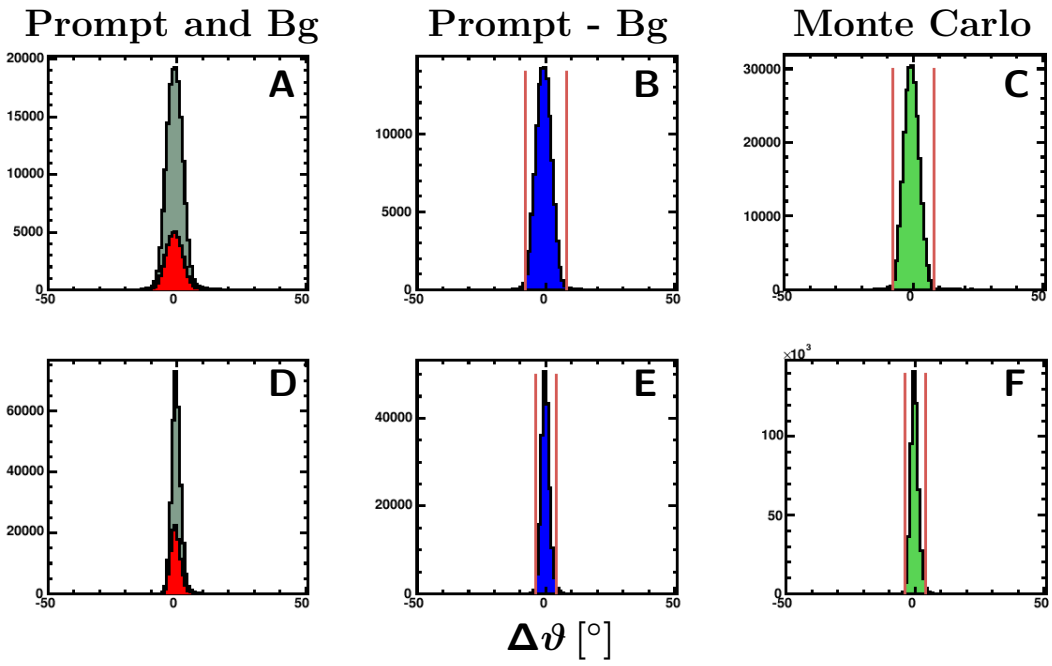

Figure 4.29.: Difference $\Delta\vartheta = \vartheta_p^{rec} - \vartheta_p^{fit}$, grey: prompt events, red: normalized timing background, blue: prompt events after background subtraction, green: Monte Carlo.

is limited due to geometrical reasons. After comparison with simulated distributions, the events with unreasonably high number of crystals fired by protons were rejected. Figure 4.30 shows the correlations between energy deposited by the proton and number of crystals fired in the CB by the proton. The events with a number of crystals larger than five and deposited energy larger than 450 MeV are rejected. The cut on the number of crystals has been chosen to reduce the possible background contamination present at high number of crystals with the tendency of having higher energy deposits than it is observed in Monte Carlo. This cut allows to be on the safe side with the background suppression and does not produce noticeable reduction of good events.

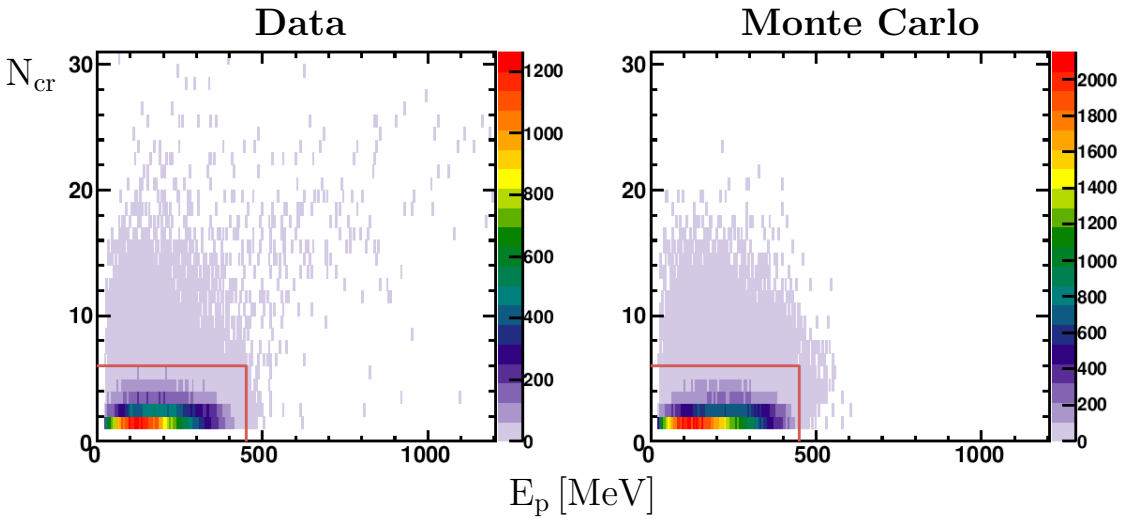

Figure 4.30.: Number of crystals N_{cr} fired in CB vs. E_p energy deposited by the proton in CB. On the left data after timing background subtraction, on the right Monte Carlo.

For protons in TAPS (Figure 4.31) events are retained with a maximum of five crystals fired and the energy deposited by the proton less than 600 MeV. Additionally, it has been required that the polar angle of the proton does not exceed 70° [12].

[12]Kinematic constraint determined from Monte Carlo.

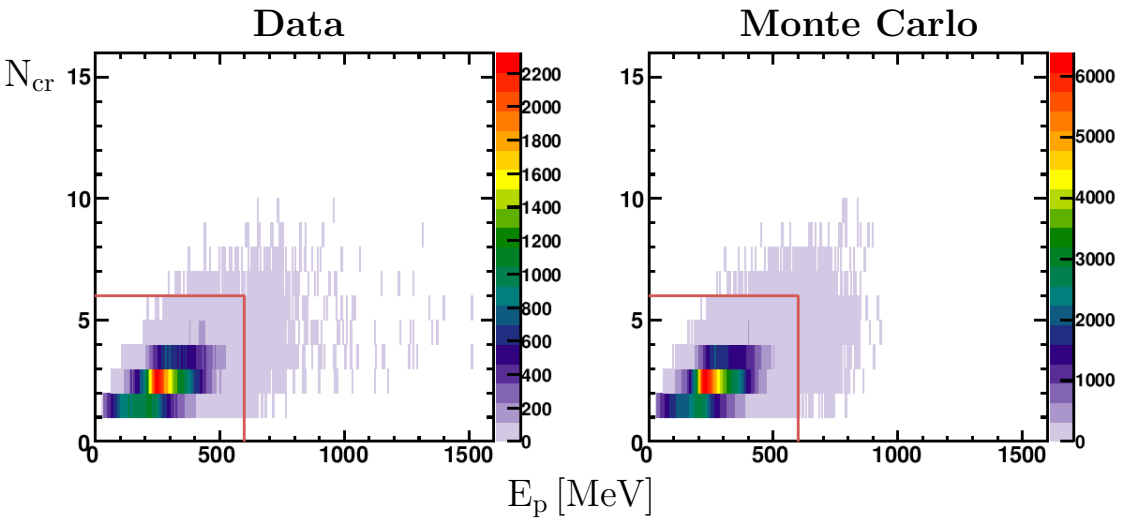

Figure 4.31.: Number of crystals N_{cr} fired in TAPS vs. E_p energy deposited by the proton in TAPS. On the left data after timing background subtraction, on the right Monte Carlo.

4.9. Background estimate

The remaining background contamination has been estimated by using the invariant masses of the photons after application of the preselection and the kinematic fit. The 3-constraint (3C) hypothesis $\gamma p \rightarrow p\pi^0\pi^0$ can not be directly used for the determination of the background because the fit directly imposes strict constraints on the masses of both π^0s. In that case the selection of events with high confidence levels leads to a reduction in the $\gamma\gamma$ invariant mass spectrum far from the pion nominal mass. Then, the estimate of the background contamination under the peak is not possible, because one can not use the events outside of the peak to make an assumption about the background contributing in the peak. In contrast, the 2-constraint (2C) hypothesis $\gamma p \rightarrow p\pi^0\gamma\gamma$ has only one strict constraint on the invariant mass of one of the combinations of the two photons. As a pion is taken the combination of the two photons with the best Cl and the invariant mass of the two "free" photons does not have explicit limits in regards to the known π^0 mass. After the cut on the Cl of $\gamma p \rightarrow p\pi^0\gamma\gamma$ at 10% and the requirement for the Cl of the hypothesis to exceed the one of $\gamma p \rightarrow p\pi^0\eta$ the invariant mass of the "free" $\gamma\gamma$ pairs is plotted, for which one would expect that the photons are

	500-800 MeV	1200-1450 MeV	2000-2500 MeV
Data	1.21%	0.54%	0.13%
Monte Carlo	1.25%	0.36%	0.16%

Table 4.1.: The background contamination in the three energy ranges.

originating from the decay of the other π^0 (Figure 4.32). The two peak structure in the free $\gamma\gamma$ invariant mass spectra occurs because the kinematic fit orders the pairs constructed of the four photons by Cl. The kinematic fit chooses the best combination of photons as π^0, thus some of the good events can be rejected by the Cl cut if the invariant masses of two photon combinations are close to the nominal π^0 mass, producing the two-peak structure in the invariant mass spectrum. The background is determined by fitting the invariant mass spectrum outside of the pion peak with polynomial of the fifth order (red line in Figure 4.32). The background in the energy range $E_\gamma = 1200 - 1450\,\mathrm{MeV}$ has been determined to be 1.48% in the data and 1.12% in Monte Carlo. An additional background reduction is achieved by using the 10% anticut on the Cl of the $\gamma p \to p\pi^0\pi^0$ hypothesis. The parts of the data which are rejected after cut on the Cl of $\gamma p \to p\pi^0\pi^0$ are shown in green in Figure 4.32 on the edge of the invariant mass spectra. After rejecting those events the background has been determined to be ($E_\gamma = 1200 - 1450\,\mathrm{MeV}$) 0.54% in the data and 0.36% in Monte Carlo. Additionally, the background estimate has been performed for relatively low energies ($E_\gamma = 500 - 800\,\mathrm{MeV}$) and for high energies ($E_\gamma = 2000 - 2500\,\mathrm{MeV}$). The corresponding results are shown in Table 4.1.

Additional Monte Carlo simulations using generated Monte Carlo events and comparing them with fitted Monte Carlo events, have shown that the number of wrong photon combinations forming pions is strongly suppressed by using the 3C $\gamma p \to p\pi^0\pi^0$ hypothesis in the fit in comparison to the hypothesis $\gamma p \to p\pi^0\gamma\gamma$. Since the $\gamma p \to p\pi^0\pi^0$ hypothesis has been used for the final analysis of the data, one can conclude that the background level in the final spectra is lower than the estimate using the $\gamma p \to p\pi^0\gamma\gamma$ hypothesis, which can be used as an upper limit for the background estimate. To check how the fit orders the particles, the difference between generated pions and pions in the fit has been investigated. The φ angles of both pions have been consequently compared to the φ of the $\gamma\gamma$ sys-

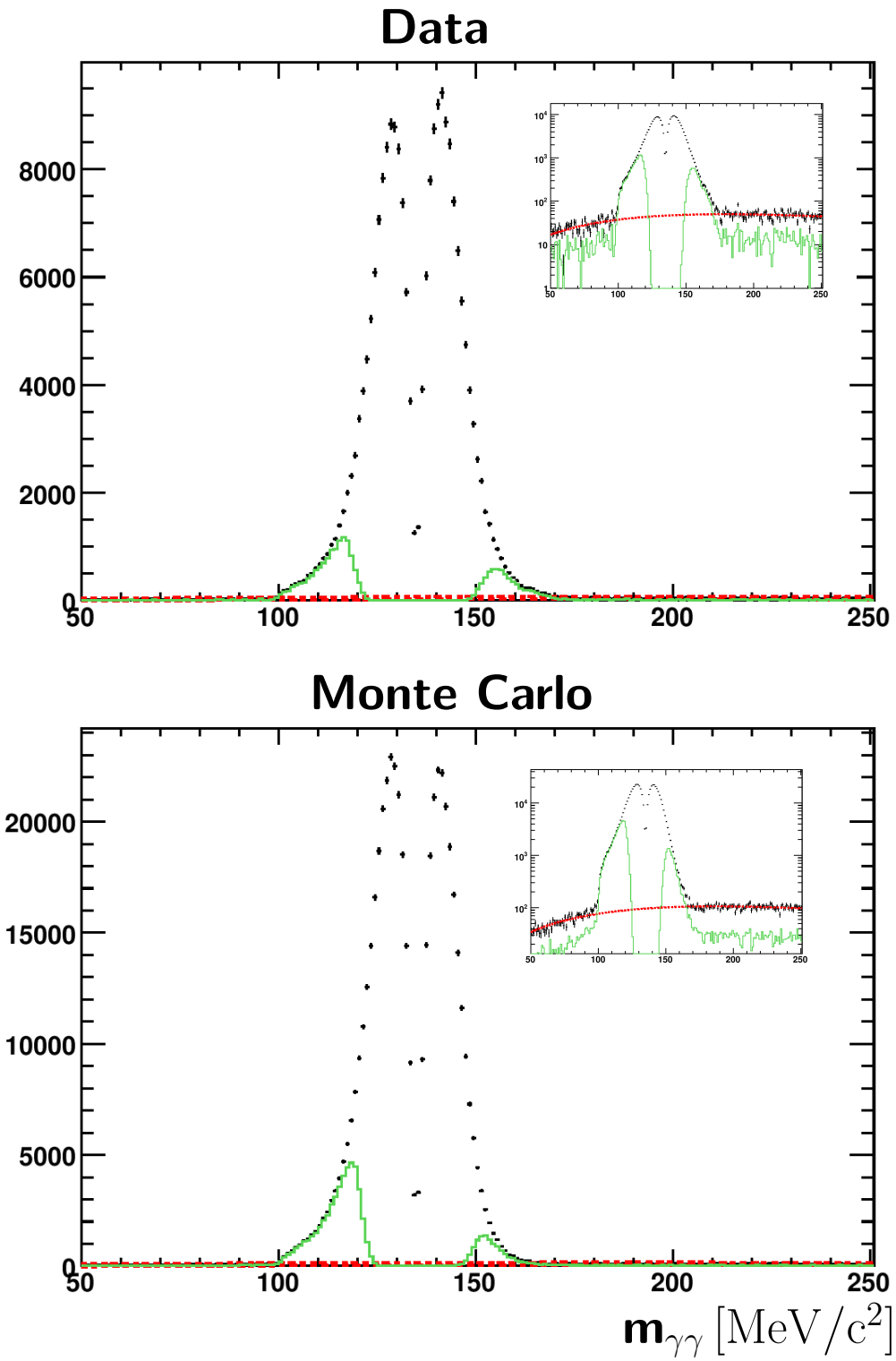

Figure 4.32.: The free $\gamma\gamma$ invariant mass, the data are shown in the upper figure, Monte Carlo in the lower, red: background, green: events rejected by an additional $\gamma p \to p\pi^0\pi^0$ fit with 10% Cl cut.

tem from the $\gamma p \to p\pi^0\gamma\gamma$ fit (the best $\pi^0\gamma\gamma$ combination is considered). The difference is shown in Figure 4.33 (left), where on the x and y axis are plotted the differences of φ of both generated pions and φ of the $\gamma\gamma$ system from the $\gamma p \to p\pi^0\gamma\gamma$ fit. The φ angle of the $\gamma\gamma$ system has to correspond either to the first or the second generated pion, forming a cross-like shape. The events which are presenting the correct combinations (selected by the fit) belong to one of the bands in the cross-like shape. The events outside represent the combinatorial background which is very similar in the data and in the Monte Carlo (see Table 4.1) [13]. One can see that most of the events are concentrated in the cross-like shape, however wrong combinations are also present. On the other hand, if the pions from the $\gamma p \to p\pi^0\pi^0$ fit are used for comparison with generated events (Figure 4.33 (right)), the suppression of the combinatorial background is obvious and is seen as a reduction of the events outside of the cross-like shape. The performed comparison allowed to show qualitatively the difference between 2C and 3C fits, and the improvement in the reduction of the combinatorial background by using the $\gamma p \to p\pi^0\pi^0$ hypothesis.

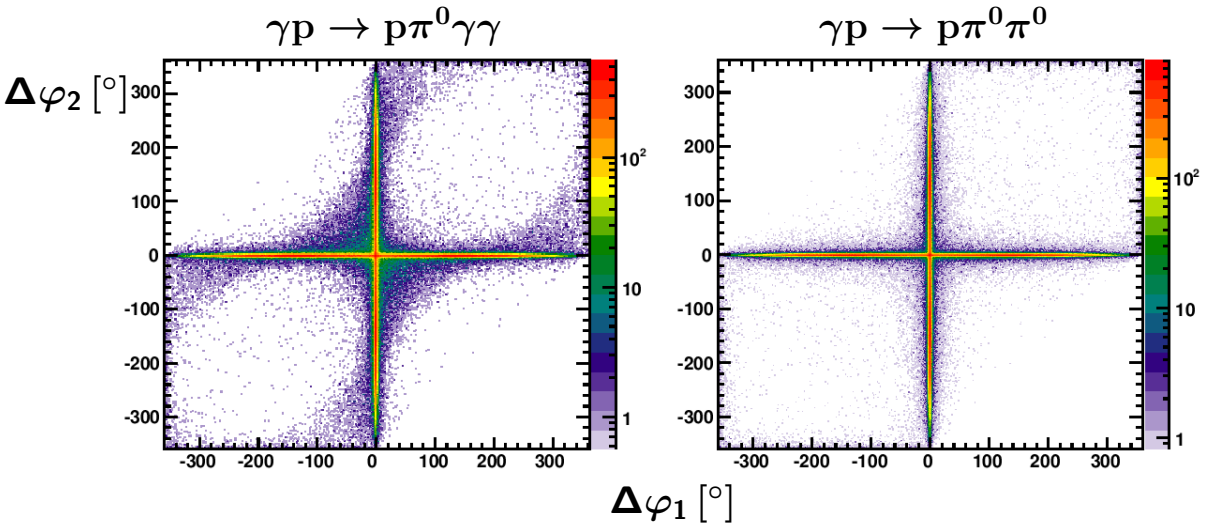

Figure 4.33.: Comparison of the angles of generated and fitted pions, on the left: the pions are taken from the hypothesis $\gamma p \to p\pi^0\gamma\gamma$, on the right from the $\gamma p \to p\pi^0\pi^0$ hypothesis (after all cuts made in the analysis).

After all cuts 561,443 events were selected and used in the determination of po-

[13] Since the background contamination in Monte Carlo is purely combinatorial.

	970-1200 MeV	1200-1450 MeV	1450-1650 MeV	500-2500 MeV
March 2003	227,304	142,250	-	690,382
May 2003	-	116,646	75,243	636,012

Table 4.2.: Number of selected events after all cuts for March 2003 and May 2003 beamtimes.

larization in the energy range $E_\gamma = 970 - 1650\,\mathrm{MeV}$ and 1,326,394 events were selected in the energy range $E_\gamma = 500 - 2500\,\mathrm{MeV}$ for the analysis of the unpolarized observables such as Dalitz plots and invariant masses. The statistics of events for the corresponding beamtimes and energy ranges is summarized in Table 4.2. May 2003 data in the energy range 970-1200 MeV and March 2003 data in the energy range 1450-1650 MeV were not used for the determination of the polarization observables due to the low polarization in these ranges. However, these parts of the data were used in the extraction of the invariant mass distributions and Dalitz plots.

5. Results

This chapter includes the results on the polarization observables Σ, I^c and I^s, invariant mass spectra and Dalitz plots. The polarization observable Σ is extracted in an extended energy range compared to the so far existing data [A$^+$03]. The observables I^c and I^s which occur in the three-body final state in case of a linearly polarized photon beam and unpolarized target are measured for the first time in the reaction $\gamma p \to p\pi^0\pi^0$. It is shown that the extracted data on polarization observables provides important and valuable constraints for the PWA. The reaction mechanisms are discussed using Dalitz plots and invariant mass spectra. Furthermore, a comparison with the predictions of the BnGa-PWA and analysis by Fix et al. shows that the data on the polarization observables allows a clear distinction between these two models.

5.1. Quasi two-body approach: observable Σ

One possible way for the investigation of the three particle state is an analysis within a quasi two-body approach. Such an approach assumes the construction of two systems out of three final state particles. In this case the incoming photon and the two outgoing systems [1] are in the same plane. The kinematics is similar to the case of the two-body final state, which allows us to use the corresponding formalism. For the reaction $\gamma p \to p\pi^0\pi^0$ the two-body systems can be constructed in two ways: from both pions as the first part and a proton as the second part or from the $p\pi^0$ system as the first part and the second pion as the second part. Due to the indistinguishability of the pions, the second case was always symmetrized (2 entries per event, normalized by 1/2).

[1] The two-particle system (e.g. $\pi^0\pi^0$) and one particle (e.g. the proton).

In analogy to a two-body final state in the case of a linearly polarized photon beam and unpolarized target the cross-section can then be written in the form:

$$\frac{\mathrm{d}\sigma}{\mathrm{d}\Omega} = \left(\frac{\mathrm{d}\sigma}{\mathrm{d}\Omega}\right)_0 (1 + \delta_l \Sigma \cos 2\varphi)\,, \tag{5.1}$$

where $\left(\frac{\mathrm{d}\sigma}{\mathrm{d}\Omega}\right)_0$ is the unpolarized differential cross-section and δ_l is the degree of linear polarization of the beam. The polarization observable Σ defines the impact of the term $\cos 2\varphi$ in the cross-section [Wor72].

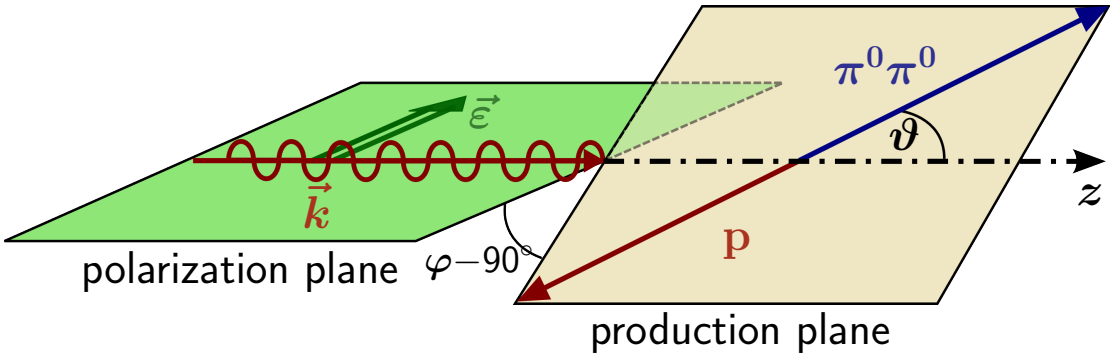

Figure 5.1.: Kinematics of the reaction in a two-body approach (picture from [Gut10]): $\vec{k}$ is the momentum of the incoming photon, $\vec{\varepsilon}$ - electric field vector, polarization plane is shown in green, the production plane defined by the incoming photon and the recoiling particle in yellow. φ is the angle between polarization and production planes with an offset of 90°, ϑ is the polar angle defined with respect to the incoming photon direction z.

Figure 5.1 illustrates the kinematics of the reaction $\gamma p \to p\pi^0\pi^0$ in a quasi two-body approach when the two pions are considered as a two-body system. The angle $\varphi - 90°$ is defined as the angle between the polarization plane, formed by the incoming photon's electric field vector $\vec{\varepsilon}$ and its momentum $\vec{k}$ and the production plane defined by the incoming photon and the recoiling particle. It is important to note that the photon, the two-particle system and the single particle are in the same (production) plane. In case of an unpolarized photon beam there are no preferred directions in φ and the events have a flat distribution over the azimuthal angle. If the photons are linearly polarized, the φ isotropy is broken and following formula 5.1 the flat distribution is modulated by $\cos 2\varphi$ contribution.

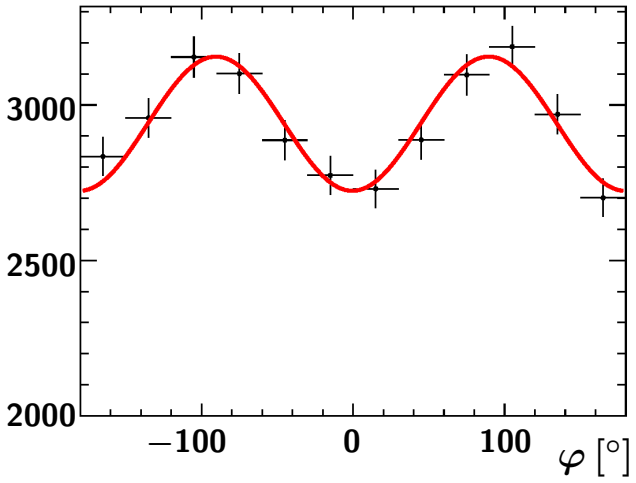

Figure 5.2.: Example of the distribution of the azimuthal angle φ (Y-scale starts at 2000 rather than 0) in the energy range $E_\gamma = 1200 - 1450\,\mathrm{MeV}$ and in the interval $640 < m_{\pi\pi} < 700\,\mathrm{MeV/c^2}$.

The cross-section can be parametrized as:

$$f(\varphi) = A\,(1 + \delta_l B \cos 2\varphi), \tag{5.2}$$

where A corresponds to the unpolarized cross-section and B to Σ. An example of a φ distribution fitted with function 5.2 is shown in Figure 5.2. To extract the observable Σ, the azimuthal angular distributions are investigated in different parts of the phase space dependent on different kinematic variables. The collection of φ distributions as function of various kinematic variables is given in Appendix B. The polarization observable Σ is extracted using parametrization given in 5.2, where the degree of linear polarization δ_l, is at first determined event by event and further averaged for every bin in the kinematic variables used in the measurement. The data has been analyzed in three energy ranges: 970-1200, 1200-1450 and 1450-1650 MeV and was additionally binned in one of four kinematic variables: the angles $\cos\vartheta_{\pi\pi}^{CMS}$, $\cos\vartheta_{\pi}^{CMS}$ and invariant masses $m_{p\pi}$, $m_{\pi\pi}$. Ten bins have been used in each of the variables and for every bin a φ distribution has been considered and was fitted with function 5.2. The results are presented in Figures 5.3 and 5.4. The data exhibits different structures with amplitudes of beam asymmetries

varying from numbers close to 0 up to -0.5. The largest amplitudes have been observed in the energy range 970-1200 MeV, being comparably smaller at higher energies. The systematic errors were determined calculating the difference between the BnGa-PWA solution for the complete and reconstructed phase space and also using two-dimensional phase space correction for the data. The two-dimensional phase space correction was used in the determination of the systematic error only and is not applied on the data shown in Figures 5.3 and 5.4. The determination of the systematic error is in detail described in Section 5.2, here the important information is that the systematic errors in the most of the cases are compatible or smaller than the statistical errors of the measurement (see Figures 5.3 and 5.4).

The CBELSA/TAPS data are plotted together with the data from GRAAL experiment [A$^+$03], which are the only existing data concerning the beam asymmetry Σ in the reaction $\gamma p \to p\pi^0\pi^0$. The both data sets in general show similar structures, however there are also significant differences present. For example in the invariant masses noticeable differences occur between CBELSA/TAPS and GRAAL data at low energies especially in the $m_{\pi\pi}$ invariant mass. These differences are discussed in more detail in Section 5.3 where it is shown that the differences can occur due to different acceptance and phase space coverage of the both experiments. In the energy range higher than 1450 MeV there has been no experimental data available so far and the CBELSA/TAPS experiment provides the very first data for Σ ($\gamma p \to p\pi^0\pi^0$) in the energy interval 1450-1650 MeV. According to [T$^+$08], two distinct solutions of the BnGa-PWA exist for the decay of the state $D_{33}(1700) \to \Delta\pi$ with either D-wave or S-wave as the dominant mode (see also Section 1.6). These solutions of the BnGa-PWA have been also compared to the experimental data. The GRAAL data has been included in the BnGa-PWA [2] for energies up to 1450 MeV and therefore both solutions reasonably describe the GRAAL data in that energy regime. For the energy range 970-1450 MeV the CBELSA/TAPS data provides new information due to different acceptance coverage of the two experiments which is discussed in detail in Section 5.3 [3]. In the energy interval 1450-1650 MeV the difference between the two BnGa-PWA solutions is larger because they are not constrained by any experimental data. The largest differences between two

[2] As well as the unpolarized data from CBELSA [T$^+$08] and TAPS [K$^+$04] experiments.

[3] The generated and reconstructed 4-vectors from Monte Carlo simulations reflecting the acceptance of the CBELSA/TAPS experiment are available for the BnGa-PWA.

solutions have been observed in the $\cos\vartheta_{\pi\pi}^{CMS}$ binning, where both solutions differ from the experimental data.

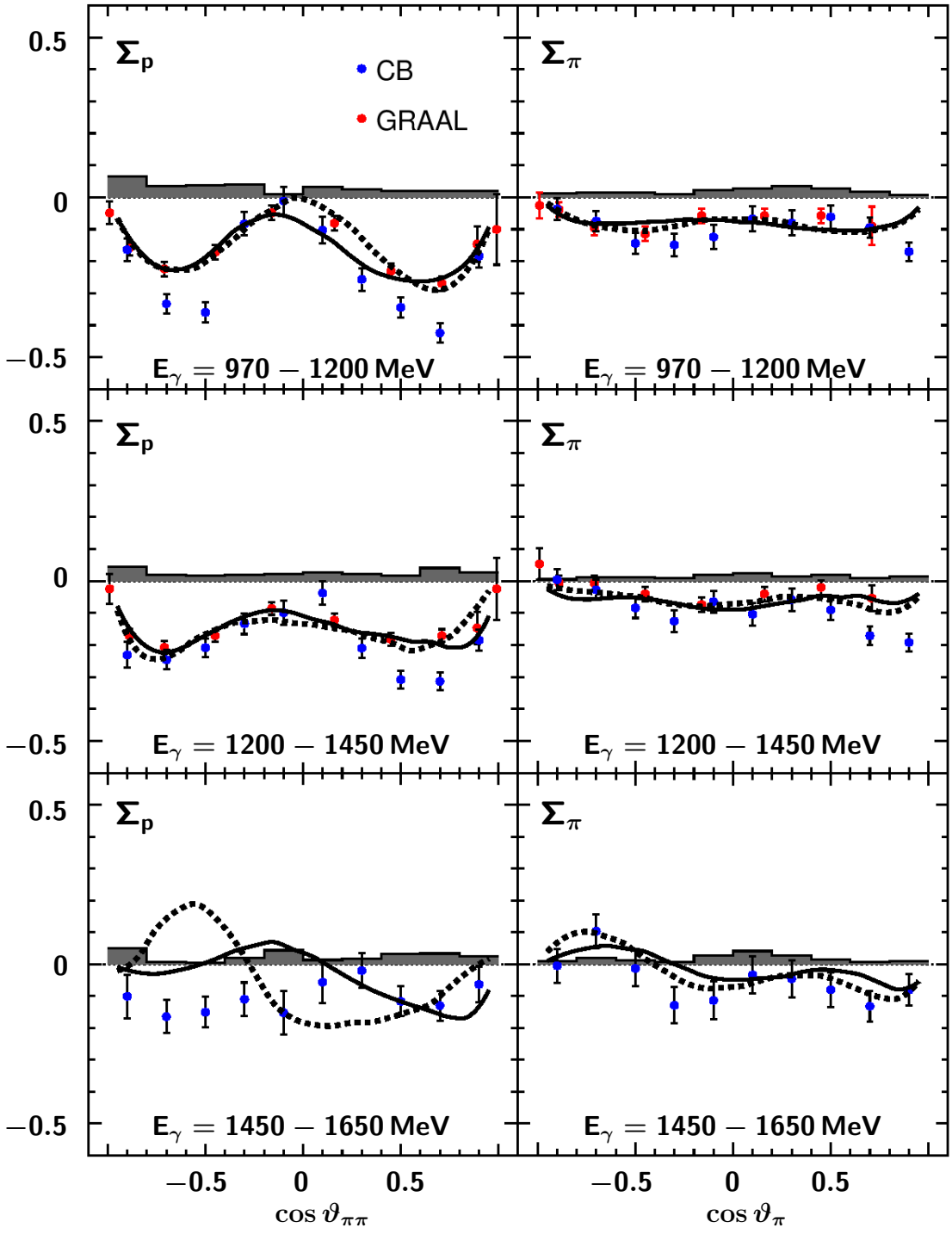

Figure 5.3.: Polarization observable Σ as function of $cos\vartheta_{\pi\pi}$ and $\cos\vartheta_{\pi}$, indices of Σ indicate the recoiling particle. Blue circles: CBELSA/-TAPS, red circles: GRAAL [A^{+}03], solid curve: BnGa-PWA solution $D_{33}(1700) \rightarrow \Delta\pi$ D-wave dominated, dashed curve: BnGa-PWA solution $D_{33}(1700) \rightarrow \Delta\pi$ S-wave dominated. Bars indicate the systematic error.

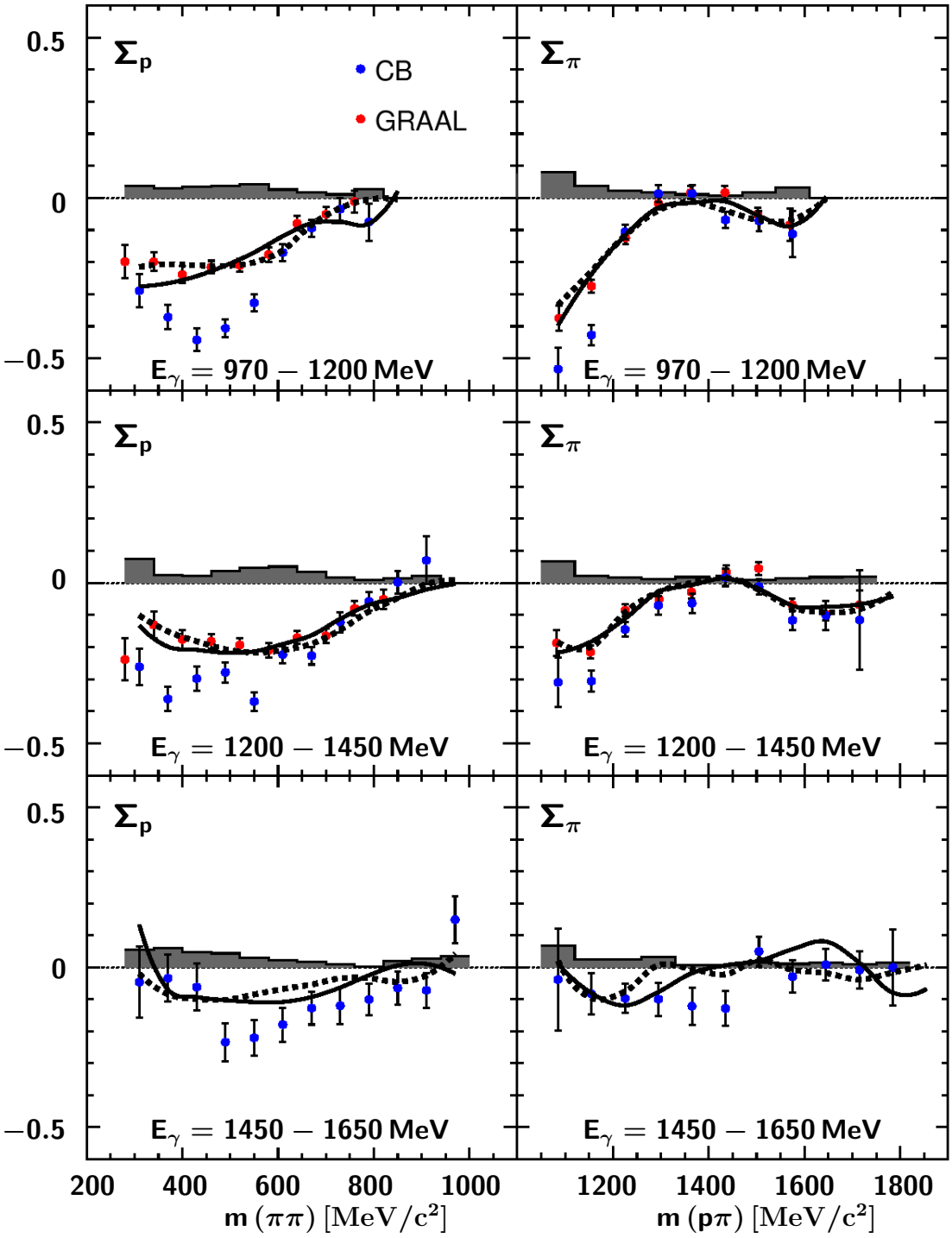

Figure 5.4.: Polarization observable Σ as function of $m_{\pi\pi}$ and $m_{p\pi}$, indices of Σ indicate the recoiling particle. Blue circles: CBELSA/TAPS, red circles: GRAAL [A$^+$03], solid curve: BnGa-PWA solution $D_{33}(1700) \to \Delta\pi$ D-wave dominated, dashed curve: BnGa-PWA solution $D_{33}(1700) \to \Delta\pi$ S-wave dominated. Bars indicate the systematic error.

5.2. Systematic errors

As already mentioned in Section 4.2, a completely model-independent 5-dimensional correction (see Appendix A), which would allow to take into account the influence of the detector system on the complete phase space, was not applied due to time and disk space limitations. To estimate the systematic error for the polarization observables, two other methods were used. In the first method the results on the polarization observables were compared for the complete phase space coverage (using generated Monte Carlo) and for the phase space coverage limited to the detector acceptance (using reconstructed Monte Carlo) based on the BnGa-PWA predictions for the solutions corresponding to $D_{33}(1700) \rightarrow \Delta\pi$ decay with S-wave dominant mode and also to the D-wave dominant mode. BnGa-PWA included unpolarized data on the reaction $\gamma p \rightarrow p\pi^0\pi^0$ and reproduces the corresponding cross-sections. For each of the bins in the 5-dimensional phase space corresponding to the reaction $\gamma p \rightarrow p\pi^0\pi^0$ a factor reflecting the dynamics of the reaction was calculated in the BnGa-PWA. Further, each of the Monte Carlo events was identified according the location in the phase space and the corresponding weight determined in the BnGa-PWA was applied. The complete coverage in the BnGa-PWA was considered using generated Monte Carlo events, the acceptance effects were taken into account by consideration of reconstructed Monte Carlo events. Further, the φ distributions were obtained as function of various kinematic variables, such as invariant masses or angles and the polarization observables were extracted from these distributions. The differences between the BnGa-PWA predictions based on the generated and reconstructed Monte Carlo events represent the influence of the acceptance and efficiency effects on the final result. The largest effect determined by using the solutions with either S- or D-wave dominant mode was taken as the systematic error using this method.

For an additional cross-check of the systematic effects a 2-dimensional acceptance correction was applied using purely phase space distributed Monte Carlo events. The acceptance was determined as the ratio of the number of reconstructed and generated events in two dimensions, using respective kinematic variable and the azimuthal angle φ (see Figure 5.5). Further, the corresponding 2-dimensional histograms obtained from the experimental data have been divided by the acceptance

histograms. The observable Σ was extracted by binning the corrected histograms in the respective angular or mass variable and fitting the φ distributions in these ranges (by analogy with Σ extraction described in Section 5.1). Further, the effect of the acceptance correction was determined as the difference between observable Σ extracted before and after acceptance correction.

For the estimate of the final systematic error the largest error determined from the both BnGa-PWA solutions and the 2-dimensional acceptance correction was taken. The systematic errors of the measurement of the observable Σ determined by this method are shown in Figures 5.3 and 5.4. In most of the cases the systematic errors are smaller or compatible with statistical errors of the measurement. The method described in this section was as well used for the determination of the systematic errors of the polarization observables I^s and I^c (see Section 5.4).

5.3. Compatibility of the data from different experiments

In Section 5.1 (Figures 5.3 and 5.4) the results for the polarization observable Σ measured by CBELSA/TAPS have been compared to GRAAL data. In some cases, for example in the plots showing Σ as function of $m_{p\pi}$ (Figure 5.4) the agreement between both data sets is relatively good, whereas in others, for example for Σ measured as function of $m_{\pi\pi}$ (Figure 5.4), noticeable differences above the systematic error are observed. Since both experiments have a different acceptance and phase space coverage a relevant question arises - whether the data from different experiments are directly comparable or whether acceptance might still play a role in the measurement of the beam asymmetry. In case of asymmetry one would expect that the acceptance does not play a role, but this statement is not entirely true if bins integrated over some of the variables are considered or bins are large.

In Section 5.1 it has been shown that the amplitude of the observable Σ varies as a function of the invariant masses and the angles of the particles. In the five-dimensional phase space, defined for the three-body final state, a limitation in one

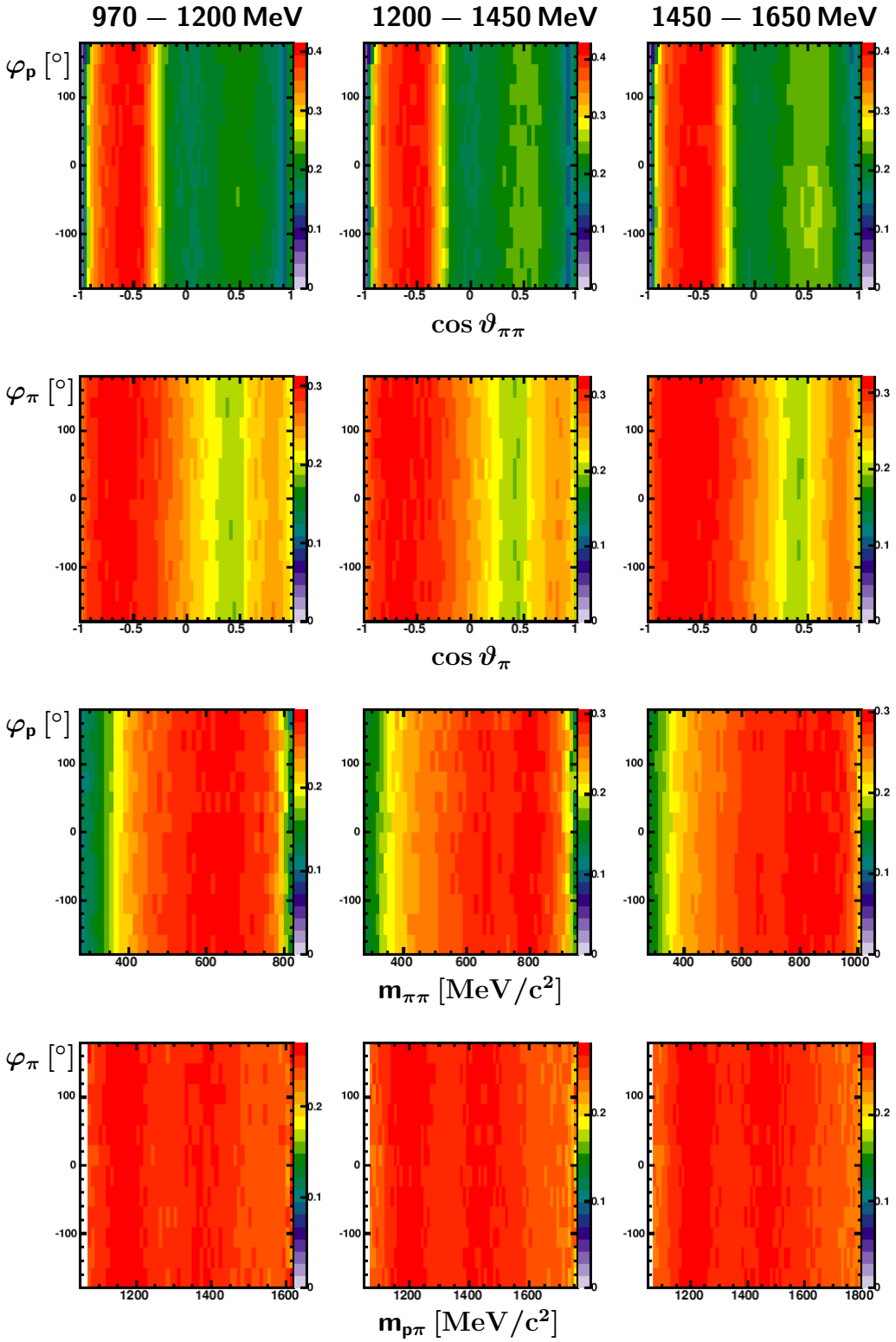

Figure 5.5.: Acceptance histograms used in the determination of the systematic error of Σ for the three energy bins. The first row: φ_p vs. $\cos\vartheta_{\pi\pi}^{CMS}$, the second row: φ_π vs. $\cos\vartheta_\pi^{CMS}$, the third row: φ_p vs. $m_{\pi\pi}$, the fourth row: φ_π vs. $m_{p\pi}$.

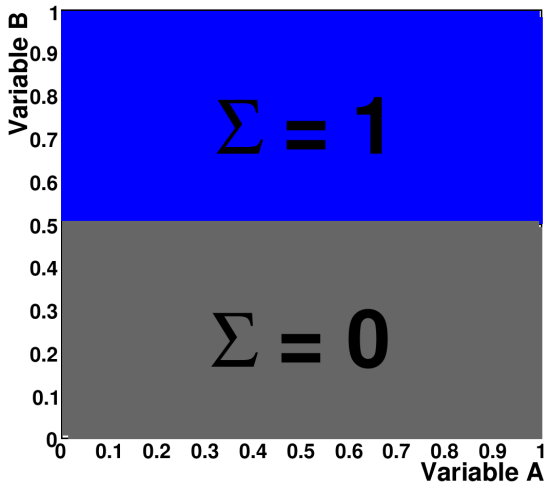

Figure 5.6.: Theoretical example, showing the effect which acceptance coverage can have on Σ.

of kinematic variables can cause changes in the other, thus leading to a reduction of events in the given interval. For example, if the range covered by the detector in $\cos\vartheta_\pi$ is limited (as it is for GRAAL data), it also influences the distribution of variables such as $\cos\vartheta_{\pi\pi}$. Figure 5.6 shows an example how the limitation in one dimension can influence the result in the other. For simplicity the figure is divided in two parts, dependent on the variables A and B. As function of variable B $\Sigma = 1$ above 0.5 and $\Sigma = 0$ below 0.5. If the complete range is used for the variable B then the result would be obtained from the mixture of both areas. Assuming a homogeneous distribution of events over the whole area a beam asymmetry of $\Sigma = 0.5$ would be obtained. However, if there is a restriction on the variable B, the result will be different and can vary in the range between 0 and 1, depending on which range is chosen. Such effects can be taken into account only in the complete consideration of the dimensions describing the phase space. If only the projection on the X axis in Figure 5.6 is considered, it is possible to draw a conclusion about coverage in the variable B. If for example the acceptance in the region B > 0.5 is zero, no acceptance hole would be observed, but one would wrongly determine $\Sigma = 0$.

To investigate these effects and the compatibility of the data sets an attempt to

approximately reproduce the acceptance of the GRAAL experiment was done. The CBELSA/TAPS data have been considered in the topological cases limited to the coverage of the GRAAL detector, namely cases described in [A+03] were selected. Next, the observable Σ has been extracted for each of the two cases and was compared with Σ determined for the full CBELSA/TAPS coverage. To

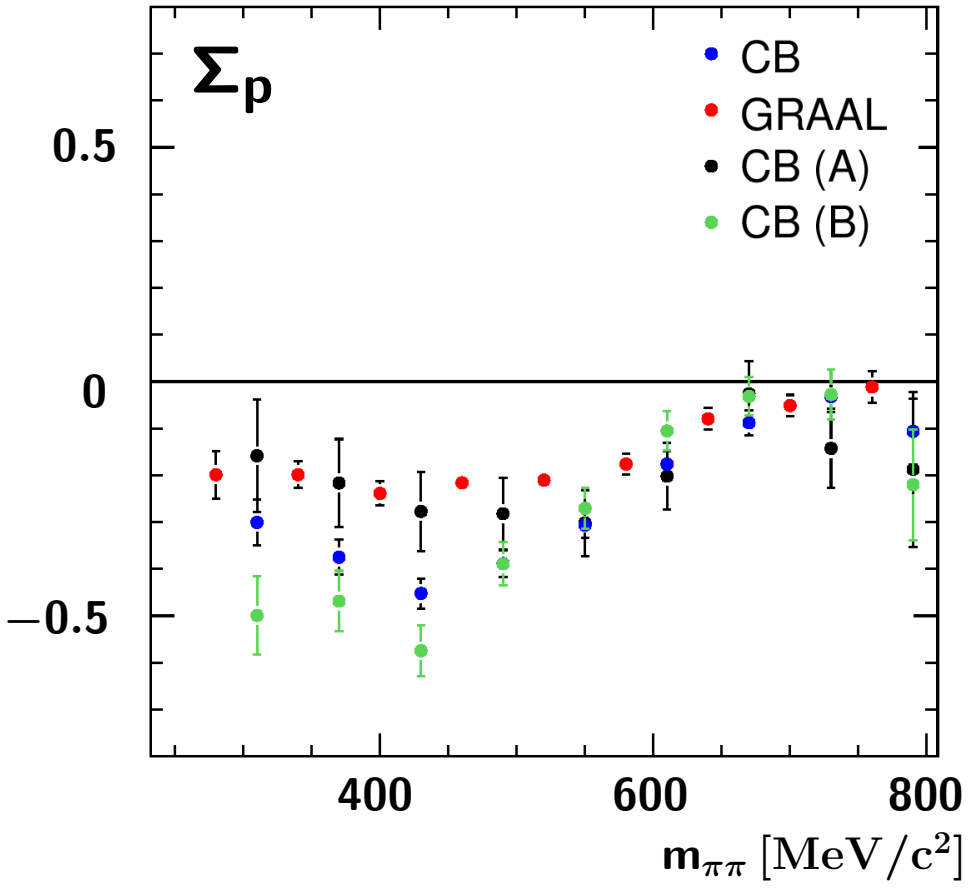

Figure 5.7.: Polarization observable Σ as function of invariant mass $m_{\pi\pi}$ in the energy range 970-1200 MeV: blue circles: CBELSA/TAPS complete data set, red: GRAAL data, black and green: CBELSA/TAPS data limited to classes A and B. The description is given in the text.

approximate the GRAAL analysis two classes of events have been selected. Class A has been determined as four photons in the backward direction for $25° < \vartheta_\gamma < 155°$, class B: three photons in the backward direction for $25° < \vartheta_\gamma < 155°$ and one

photon going forward ($\vartheta_\gamma < 25°$). These classes of events together represent about 70% of the events from the CBELSA/TAPS data obtained without restriction on the number of events. In Figure 5.7 the comparison of different topological cases is shown using the example of the $m_{\pi\pi}$ dependence of Σ in the energy range 970-1200 MeV. Class B in this energy regime shows significantly higher amplitude in comparison to class A and also the shapes of Σ for these two cases are different. Since the final result is obtained by merging all possible topological cases, the proportion in which the events are used has an influence on the result. From the point of view of compatibility of the two detector systems it will lead to differences in Σ due to different efficiencies of the detectors covering the same parts of the phase space. Differences can also occur due to regions not covered by one or the other experiment at all. Following this logic one can conclude that the result of the measurement depends on the detector system and results from different detectors can only be directly compared if the 5-dimensional acceptance is taken into account. It is also important for theoretical models to consider the acceptance of the setup when the experimental data are taken as an input for the model. Using the BnGa-PWA, which considers the CBELSA/TAPS setup we determine the systematic error due to the uncovered phase space which consider the dynamics of the reaction (see Section 5.2).

5.4. The observables I^c and I^s

Five independent variables define the phase space in the case of the three body final state (see Appendix A), compared to the two-body case for which the number of independent variables is limited to two. Figure 5.8 shows the kinematics of the three-body final state. The production plane defined by the incoming photon and one of the particles and the decay plane, defined by the three outgoing particles, are not necessarily the same. The presence of the additional plane leads to additional polarization observables occurring in the polarized cross-section. In case of linearly polarized beam and unpolarized target the polarized cross-section can be

written as:

$$\frac{\mathrm{d}\sigma}{\mathrm{d}\Omega} = \left(\frac{\mathrm{d}\sigma}{\mathrm{d}\Omega}\right)_0 \left(1 + \delta_l \left(I^c \cos 2\varphi + I^s \sin 2\varphi\right)\right), \tag{5.3}$$

where as in 5.1 $\left(\frac{\mathrm{d}\sigma}{\mathrm{d}\Omega}\right)_0$ is the unpolarized differential cross-section and δ_l is the degree of linear polarization of the beam. The polarization observables I^c and I^s define the impact of the $\cos 2\varphi$ and $\sin 2\varphi$ terms in the cross-section [RO05].

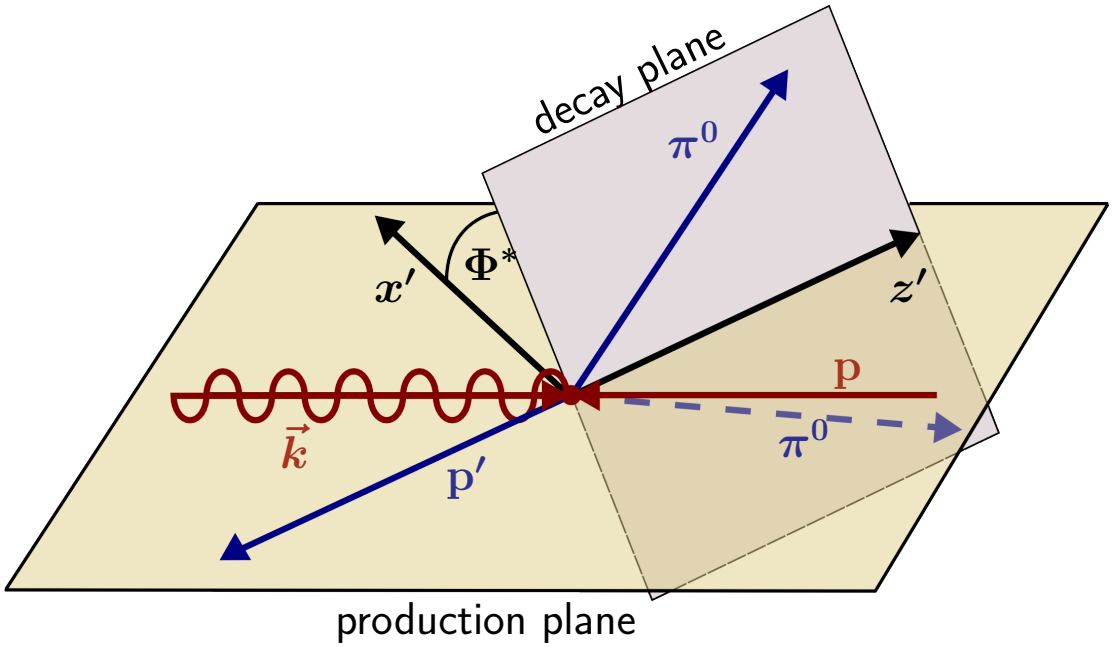

Figure 5.8.: Kinematics of the three-body final state in the CMS frame : incoming photon $\vec{k}$ and outgoing proton p' define the production plane, the decay plane is defined by particles in the final state. Φ^* is defined as an angle between production and decay planes (picture from [Gut10]).

The kinematics of the reaction is shown in Figure 5.8 for the case when the proton is considered to be a recoiling particle. In the CMS frame the production plane is defined by the incoming photon and the recoiling particle (either the proton or one of the pions) and the decay plane is defined by the three particles in the final state. The angle Φ^* between production and decay planes occurs only in a three-body final state (in a two body final state the production and the decay plane are identical) and a determination of the polarization observables as a function of Φ^* allows access to I^c and I^s which are the relevant observables for the description of

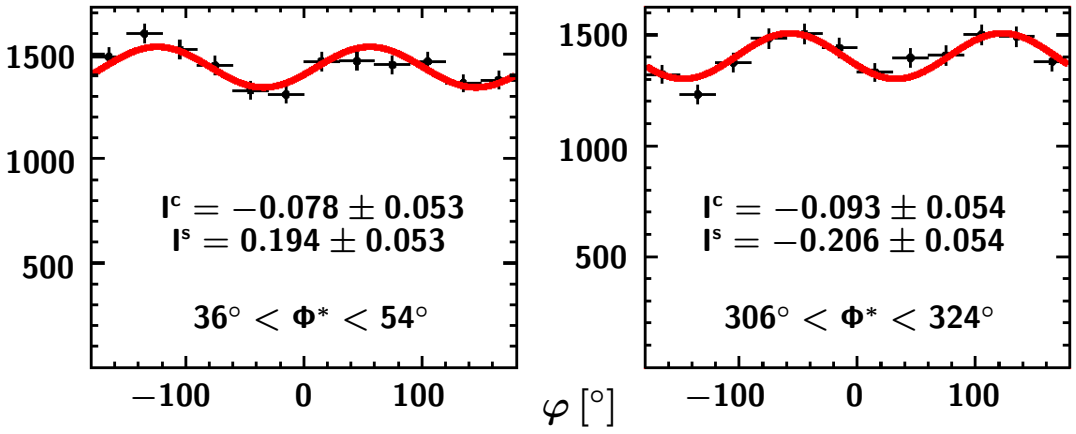

Figure 5.9.: Examples of distributions of azimuthal angle φ, binned in limited ranges of Φ^* in the energy range $E_\gamma = 1200 - 1450\,\text{MeV}$ and in the interval $0.5 < \cos\vartheta_\pi < 1$.

a three body final state. Φ^* can be calculated as the angle between the normals to the production and the decay planes (being the angle between the production and the decay planes) and in the case of the recoiling proton can be calculated out of the three vectors of the photon $\vec{k}$, outgoing proton $\vec{p'}$ and pions $\vec{p}_{\pi^0(1)}$ and $\vec{p}_{\pi^0(2)}$. $\vec{q}$ is defined as a sum of 3-vectors of pions $\vec{q} = \vec{p}_{\pi^0(1)} + \vec{p}_{\pi^0(2)}$. The angle Φ^* is defined ([Roc05], [Gut10], [KZF+09]) as:

$$\begin{aligned} \cos\Phi^* &= \frac{(\vec{k}\times\vec{q})\cdot(\vec{q}\times\vec{p}_{\pi^0(1)})}{|\vec{k}\times\vec{q}|\cdot|\vec{q}\times\vec{p}_{\pi^0(1)}|} \\ &= \frac{(\vec{k}\times\vec{p'})\cdot(\vec{p}_{\pi^0(1)}\times\vec{p}_{\pi^0(2)})}{|\vec{k}\times\vec{p'}|\cdot|\vec{p}_{\pi^0(1)}\times\vec{p}_{\pi^0(2)}|} \end{aligned} \tag{5.4}$$

and

$$\begin{aligned} \sin\Phi^* &= -1\cdot\frac{\Big((\vec{k}\times\vec{q})\times\vec{q}\Big)\cdot(\vec{q}\times\vec{p}_{\pi^0(1)})}{|(\vec{k}\times\vec{q})\times\vec{q}|\cdot|\vec{q}\times\vec{p}_{\pi^0(1)}|} \\ &= \frac{\Big((\vec{k}\times\vec{p'})\times\vec{p'}\Big)\cdot(\vec{p}_{\pi^0(1)}\times\vec{p}_{\pi^0(2)})}{|(\vec{k}\times\vec{p'})\times\vec{p'}|\cdot|\vec{p}_{\pi^0(1)}\times\vec{p}_{\pi^0(2)}|}. \end{aligned} \tag{5.5}$$

From 5.5 and 5.6 Φ^* is calculated as:

$$\Phi^* = \begin{cases} \arccos(\Phi^*) & \text{for} \quad \sin(\Phi^*) > 0 \\ 2\pi - \arccos(\Phi^*) & \text{for all else.} \end{cases} \tag{5.6}$$

Both pions are indistinguishable and therefore are considered symmetric. It means that for each event two Φ^* angles are calculated and later used in the determination of polarization observables. In the case of the recoiling pion the formulas 5.5, 5.6, 5.6 by analogy are constructed in the corresponding order. In this case the angle Φ^* is also defined twice: once as an angle between the plane formed by the proton and one of the pions (the second pion considered as recoiling), and once the pion in the previously defined production plane and the recoiling pion are interchanged.

According to formula 5.3 the cross-section is parametrized as:

$$f(\varphi) = A\,(1 + \delta_l\,(B\cos 2\varphi + C\sin 2\varphi)), \tag{5.7}$$

where A corresponds to the unpolarized cross-section, B to the observables I^c and C to the observable I^s. I^c and I^s are extracted for different Φ^* bins (in other words as a function of Φ^*). Examples of φ distributions corresponding to limited ranges in Φ^* are shown in Figure 5.9. The sine and cosine contributions are clearly seen in the distributions which are fitted with function 5.7. One can also observe different phases if the ϕ distributions are considered in the different ranges of Φ^*. The collection of φ distributions as function of angle Φ^* in different energy ranges is given in Appendix B. Due to the kinematics of the reaction (Figure 5.8) and the definition of angle Φ^*, certain conditions originating from parity and symmetry constraints have to be fulfilled ([GSvP$^+$10], [KZF$^+$09]):

a) When $\Phi^* = 0, \pi, 2\pi$ the kinematics of the reaction becomes coplanar leading to vanishing I^s in these points $I^s(0, \pi, 2\pi) = 0$.

b) The mirror operation, meaning rotation of the decay plane in respect to the production plane $\Phi^* \rightarrow 2\pi - \Phi^*$ corresponds to the sign flip of the Y-axis. In the case of such an operation the polarization plane is also rotated changing the azimuthal angle: $\varphi \rightarrow 2\pi - \varphi$. According to formula 5.3

describing the cross-section 5.3 it would lead to $\sin(2\cdot(2\pi-\varphi)) = -\sin(2\varphi)$ and $\cos(2\cdot(2\pi-\varphi)) = \cos(2\varphi)$ and finally to $I^c(\Phi^*) = I^c(2\pi-\Phi^*)$ and $I^s(\Phi^*) = -I^s(2\pi-\Phi^*)$.

c) Indistinguishability of the pions in the case of the proton in the production plane according to formulas 5.5 and 5.6 leads to: $\Phi_2^* = \Phi_1^* + \pi$ where Φ_1^* and Φ_2^* correspond to the order in which the pions are considered (which pion is taken as the first and which as the second). The sequence in which the pions are considered does not influence azimuthal angle φ used for the measurement of polarization observables and therefore $I^c(\Phi^*) = I^c(\Phi^*+\pi)$ and $I^s(\Phi^*) = I^s(\Phi^*+\pi)$.

According to the kinematics of the reaction and symmetry conditions mentioned above I^c and I^s can be expanded as:

$$I^c(\Phi^*) = \sum_{n=0} a_n \cos(n\Phi^*) \text{ and} \tag{5.8}$$

$$I^s(\Phi^*) = \sum_{n=0} b_n \sin(n\Phi^*). \tag{5.9}$$

In the case of the proton being in the production plane only even terms contribute to the I^s expansion due to $I^s(\Phi^*) = I^s(\Phi^*+\pi)$ (see above). Integration over angle Φ^* leads to a quasi-two body final state consideration. In this case the sine terms vanish in the Fourier expansion of I^s leading to $I^s = 0$ and only the constant term a_0 remains in the Fourier expansion of I^c. Therefore, a_0 corresponds to the observable Σ defined for the quasi two-body final state presented in Section 5.1. The full three-body approach allows access not only to the constant term in I^c expansion but also to the higher terms of I^c and I^s. Examples of fulfillment of the symmetry conditions (a-c) defined above and expansion in sine series are shown in Figure 5.10, where shown on the left is a distribution of I^s when the proton is considered as recoiling particle, on the right: pion taken as recoiling. Blue points correspond to I^s directly extracted out of data, green points are obtained after mirror operation $\Phi^* \to 2\pi - \Phi^*$. The symmetry constraints are fulfilled:

a) The data points cross the 0 line at $0, \pi, 2\pi$. In the case of the proton recoiling also at $\frac{\pi}{2}$ and $\frac{3}{2}\pi$ which can be explained by condition $I^s(\Phi^*) = I^s(\Phi^* + \pi)$ and contribution of even terms only in the expansion 5.9 in this case.

b) Condition $I^s(\Phi^*) = -I^s(2\pi - \Phi^*)$ is checked by comparison of the blue and green points and is reasonably fulfilled. The agreement between these two sets proves the high quality of the data.

c) In the case of the proton recoiling the condition $I^s(\Phi^*) = I^s(\Phi^* + \pi)$ is fulfilled exactly by definition out of 5.5 and 5.6.

The data points in Figure 5.10 are fitted with a sine series up to the fourth order. In the case of the proton recoiling only even terms contribute whereas both even and odd terms are present in the pion recoiling case.

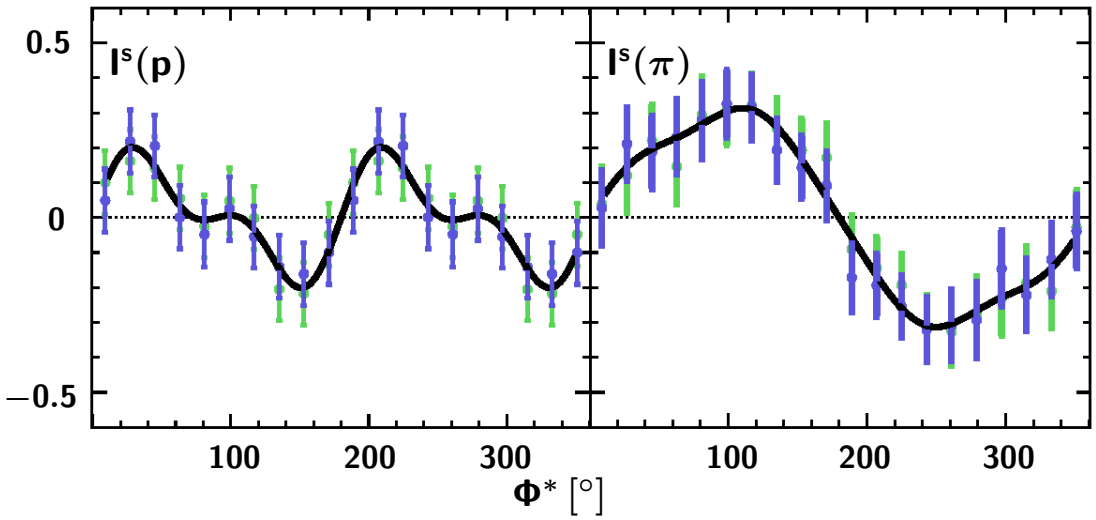

Figure 5.10.: Polarization observable I^s fitted with a sine series up to the fourth order in the case if the proton considered as the recoiling particle on left, and pion as the recoiling particle on the right. Blue circles: I^s directly extracted out of data, green circles: I^s after mirror operation $I^s(\Phi^*) \rightarrow -I^s(2\pi - \Phi^*)$. The energy range used: $E_\gamma = 970 - 1200\,\mathrm{MeV}$ with differential binning - on the left $0.5 < cos\vartheta_p < 1$, on the right: $1250 < m_{p\pi} < 1350\,\mathrm{MeV/c^2}$.

Observables I^c and I^s have been extracted in three energy ranges: 970-1200, 1200-1450 and 1450-1650 MeV, shown in Figures 5.12 - 5.21. In these figures

directly extracted data in blue are plotted together with points after the mirror operation $\Phi^* \to 2\pi - \Phi^*$. The fulfillment of conditions $I^c(\Phi^*) = I^c(2\pi - \Phi^*)$ and $I^s(\Phi^*) = -I^s(2\pi - \Phi^*)$ illustrates the proper quality of the data. The systematic errors have been estimated with the method described in Section 5.2 using BnGa-PWA predictions and a 2-dimensional acceptance correction, in a similar way as in the determination of the systematic errors of the observable Σ. The 2-dimensional acceptance correction in this case was performed using the correlation between the angles Φ^* and Φ [4]. The acceptance histograms for the proton and pion recoiling cases in the three energy ranges are shown in Figure 5.11. The systematic errors are shown in the following figures as red bars.

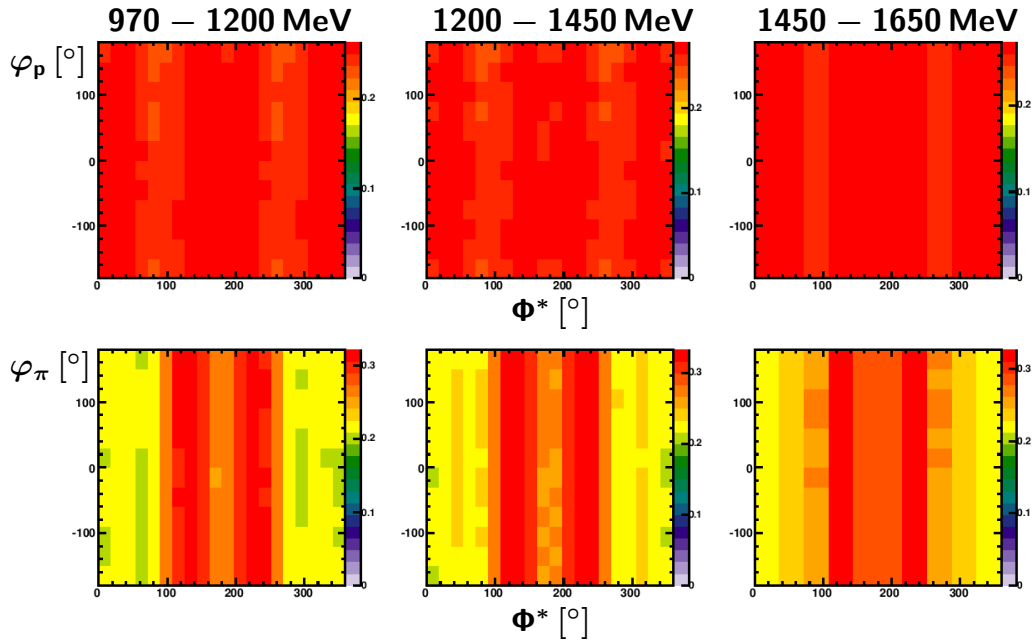

Figure 5.11.: Acceptance histograms used in the correction of I^s and I^c in case for the proton (upper row) and pion (lower row) recoiling cases in the three energy ranges. It is important to note that the angle Φ^* is defined differently for the proton and the pion recoiling cases (for the definitions see the text).

In addition to energy binning only, significant information is provided by determination of observables I^c and I^s in different angular and invariant mass ranges for

[4] It is important to note that the acceptance correction was used only for the determination of the systematic error. The data on the polarization observables are shown without application of the acceptance correction.

each of the three energy bins used in the measurement. Different and rich structures have been observed using $\cos\vartheta_p^{CMS}$, $\cos\vartheta_\pi^{CMS}$, $m_{\pi\pi}$ and $m_{p\pi}$ as secondary binning. As in Section 5.1 the data have been compared with two BnGa-PWA solutions - one with $D_{33}(1700) \to \Delta\pi$ dominantly decaying in D-wave and another in S-wave [T$^+$08]. As an example of such a comparison let us consider the case of additional binning in $\cos\vartheta_p$ (see Figure 5.14). In the energy bin 970-1200 MeV, significant amplitudes for I^s are present when the proton goes forward in the CMS frame ($0.5 < \cos\vartheta_p < 1$) while they are compatible with zero at backward angles (-1 $< \cos\vartheta_p <$ -0.5). It is also interesting to observe the difference between two solutions of BnGa-PWA in the bin $0.5 < \cos\vartheta_p < 1$, where the solution with L = 2 in the $D_{33}(1700) \to \Delta\pi$ decay shows a larger amplitude and has a better agreement than the solution with L = 0, which has a relatively low amplitude and an opposite phase. In the pion recoiling case an interesting pattern is observed in the $m_{p\pi}$ invariant mass binning (see Figure 5.18) where at high invariant masses a dip structure is present in the experimental data and in the both BnGa-PWA solutions in the energy range 970-1200 MeV but this structure remains only in the data and in the solution with L = 0 in the $D_{33}(1700) \to \Delta\pi$ decay in the energy range 1200-1450 MeV. In general, the differences between both BnGa-PWA solutions are already visible in the energy binning only (Figures 5.12 and 5.17) but they are much more pronounced if the data are binned in one of the kinematic variables (such as angles or invariant masses) used in combination with energy binning. Whereas some shapes observed in the data are reproduced by the BnGa-PWA solutions, neither solution fully describes the data. From an overall comparison one can conclude that the measured data set on polarization observables in its completeness will have a significant impact on the BnGa-PWA. Presently the data is included in the BnGa-PWA and its influence on determination of resonance properties is studied.

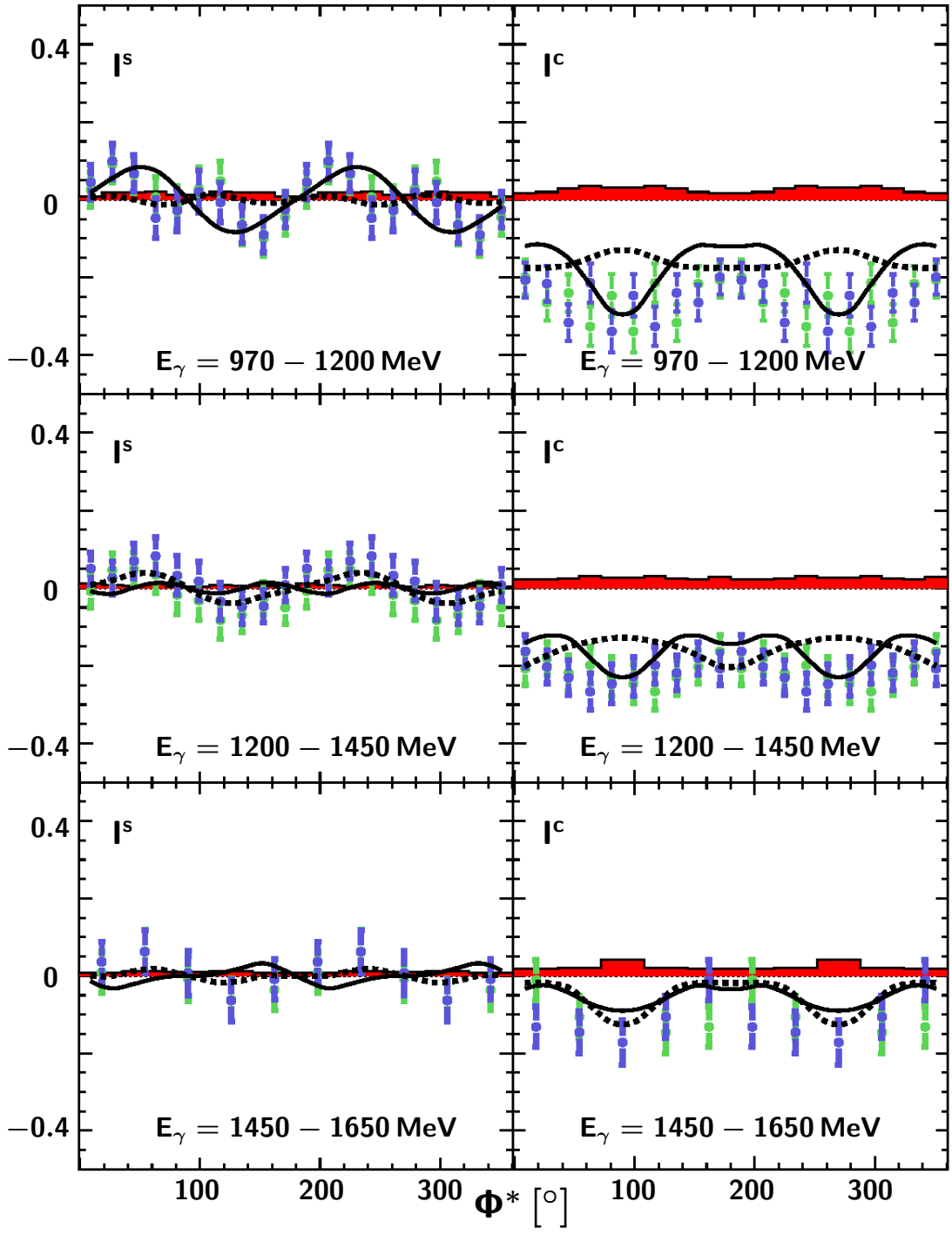

Figure 5.12.: Polarization observable I^s and I^c in the case of the recoiling proton - blue circles: I^s and I^c directly extracted out of data, green circles: I^s and I^c after mirror operations $I^s(\Phi^*) \rightarrow -I^s(2\pi - \Phi^*)$, $I^c(\Phi^*) \rightarrow I^c(2\pi - \Phi^*)$, solid curve: BnGa-PWA solution $D_{33}(1700) \rightarrow \Delta\pi$ D-wave dominated, dashed curve: BnGa-PWA solution $D_{33}(1700) \rightarrow \Delta\pi$ S-wave dominated. Bars indicate the systematic error.

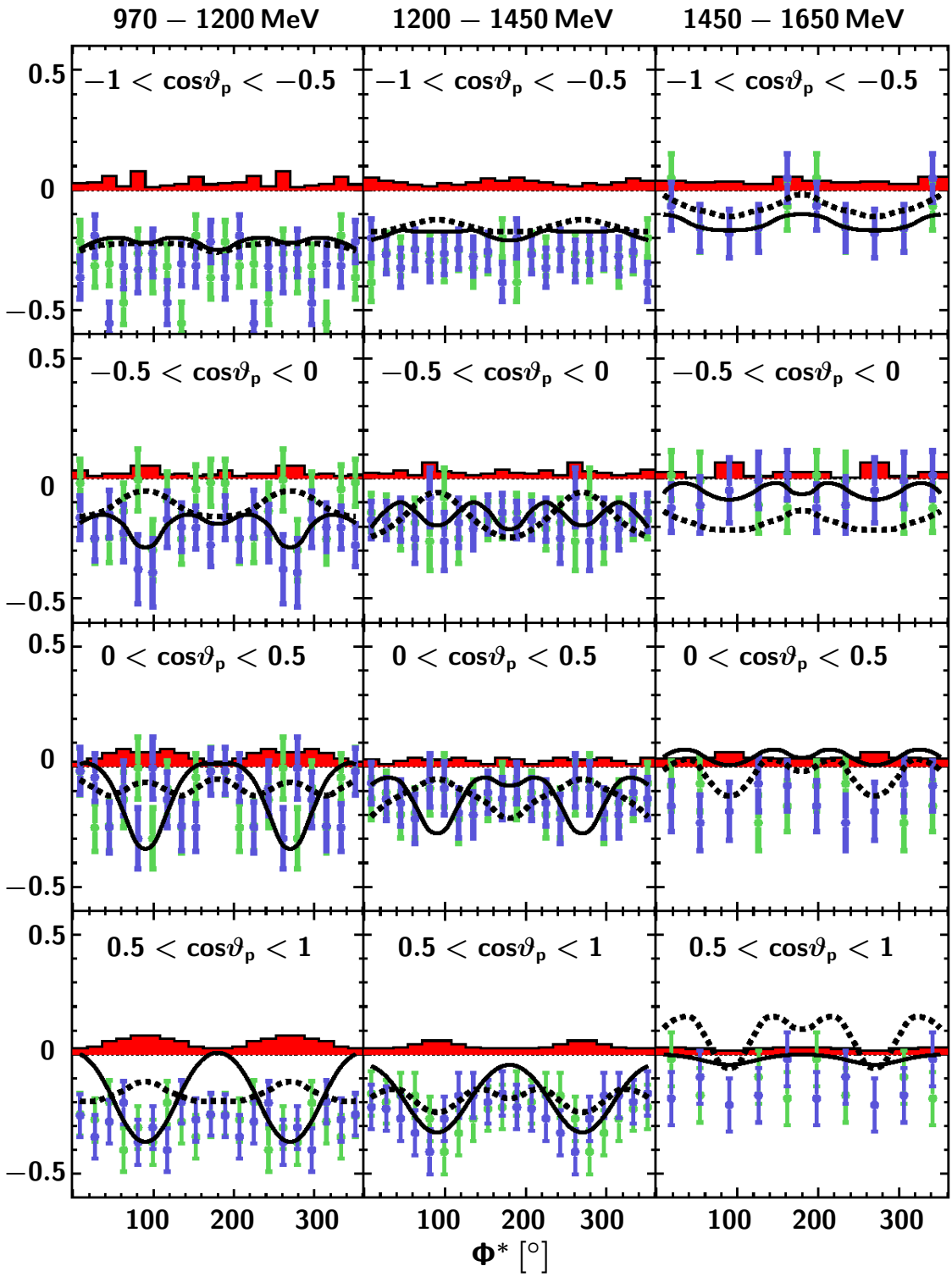

Figure 5.13.: Polarization observable I^c in the case of the recoiling proton binned in $\cos\vartheta_p$ blue circles: I^c directly extracted out of data, green circles: I^c after mirror operation $I^c(\Phi^*) \rightarrow I^c(2\pi - \Phi^*)$, solid curve: BnGa-PWA solution $D_{33}(1700) \rightarrow \Delta\pi$ D-wave dominated, dashed curve: BnGa-PWA solution $D_{33}(1700) \rightarrow \Delta\pi$ S-wave dominated. Bars indicate the systematic error.

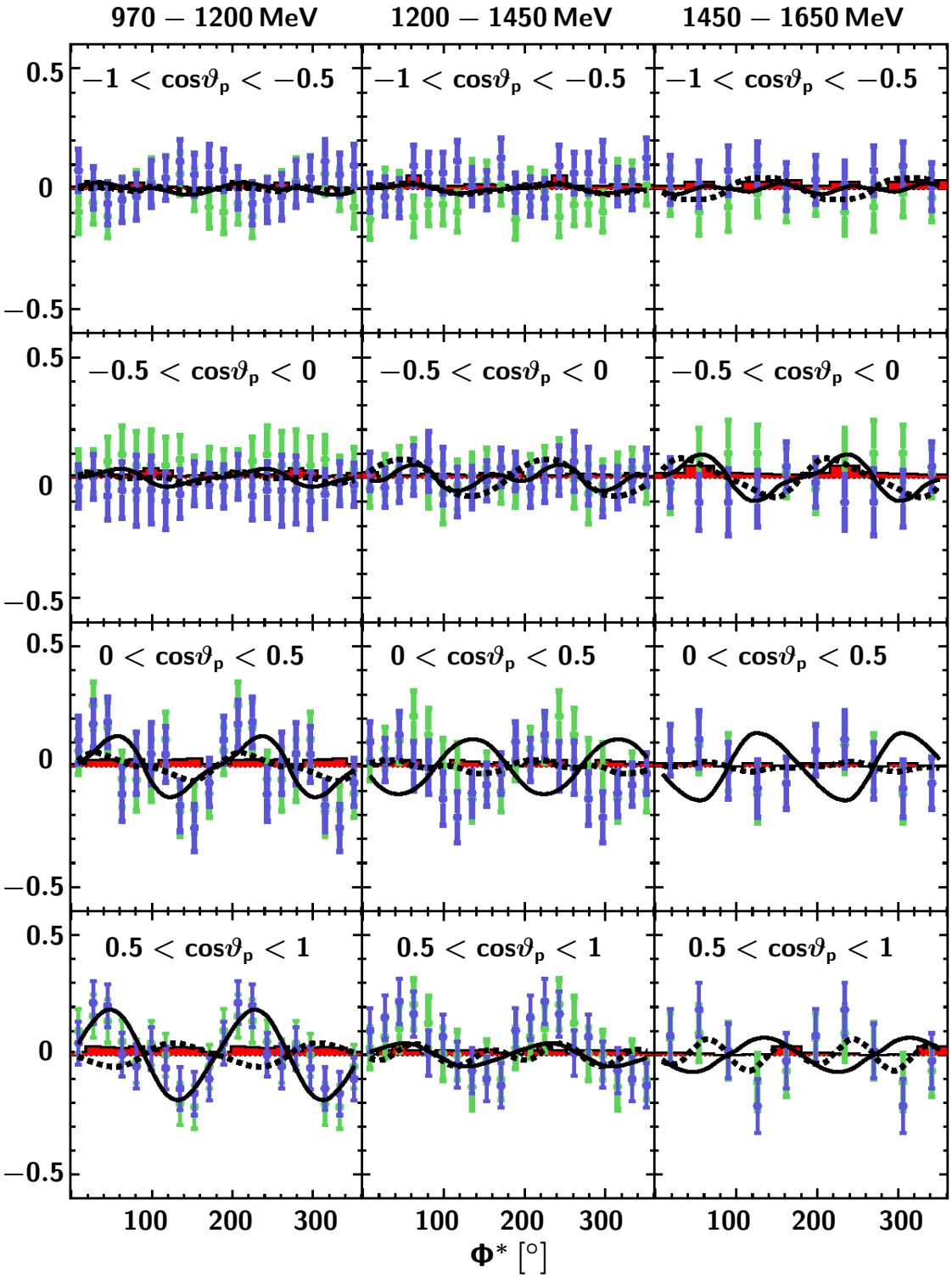

Figure 5.14.: Polarization observable I^s in the case of the recoiling proton binned in $\cos\vartheta_p$ blue circles: I^s directly extracted out of data, green circles: I^s after mirror operation $I^s(\Phi^*) \rightarrow -I^s(2\pi - \Phi^*)$, solid curve: BnGa-PWA solution $D_{33}(1700) \rightarrow \Delta\pi$ D-wave dominated, dashed curve: BnGa-PWA solution $D_{33}(1700) \rightarrow \Delta\pi$ S-wave dominated. Bars indicate the systematic error.

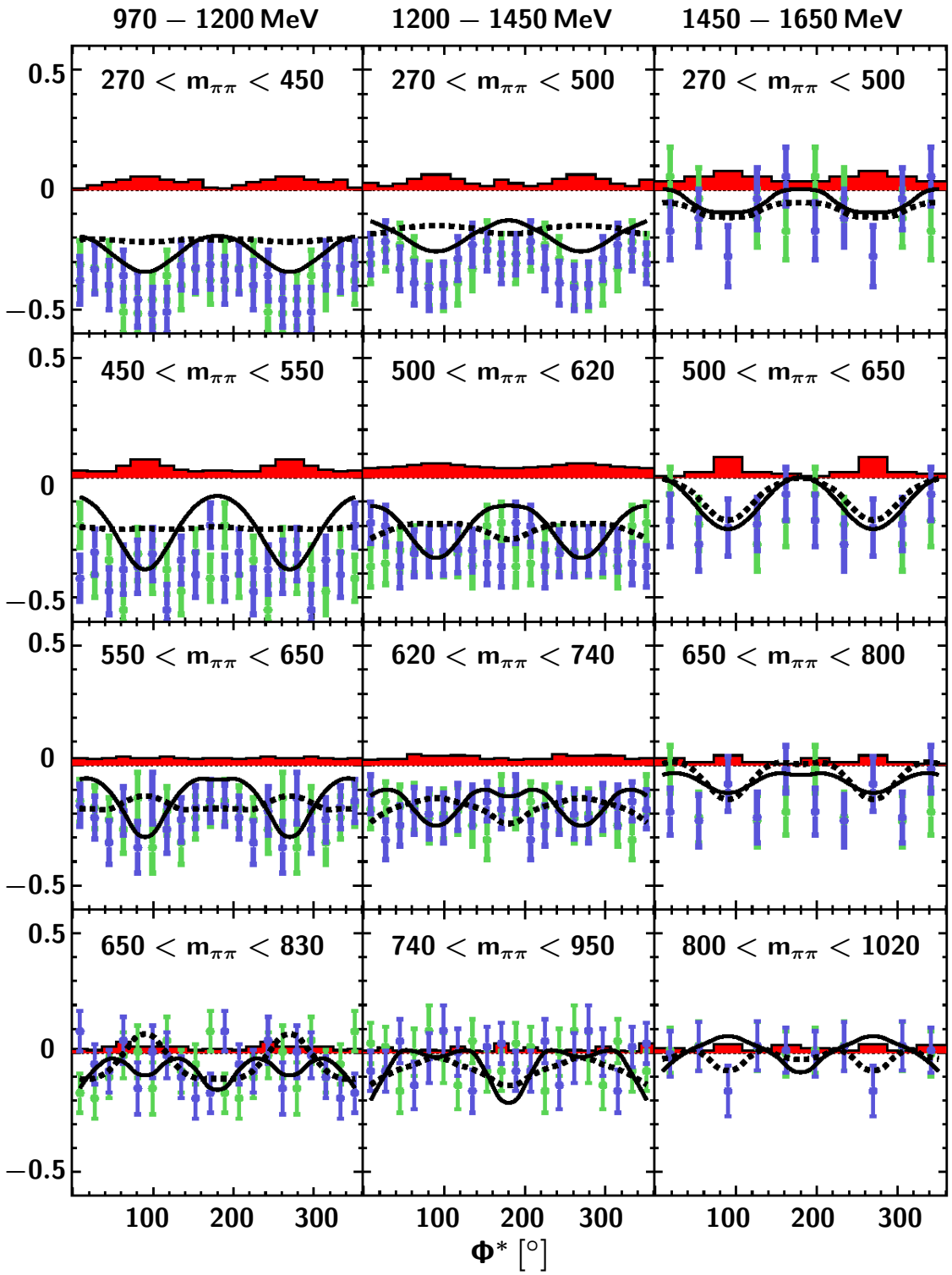

Figure 5.15.: Polarization observable I^c in the case of the recoiling proton binned in $m_{\pi\pi}$ blue circles: I^c directly extracted out of data, green circles: I^c after mirror operation $I^c(\Phi^*) \rightarrow I^c(2\pi - \Phi^*)$, solid curve: BnGa-PWA solution $D_{33}(1700) \rightarrow \Delta\pi$ D-wave dominated, dashed curve: BnGa-PWA solution $D_{33}(1700) \rightarrow \Delta\pi$ S-wave dominated. Bars indicate the systematic error.

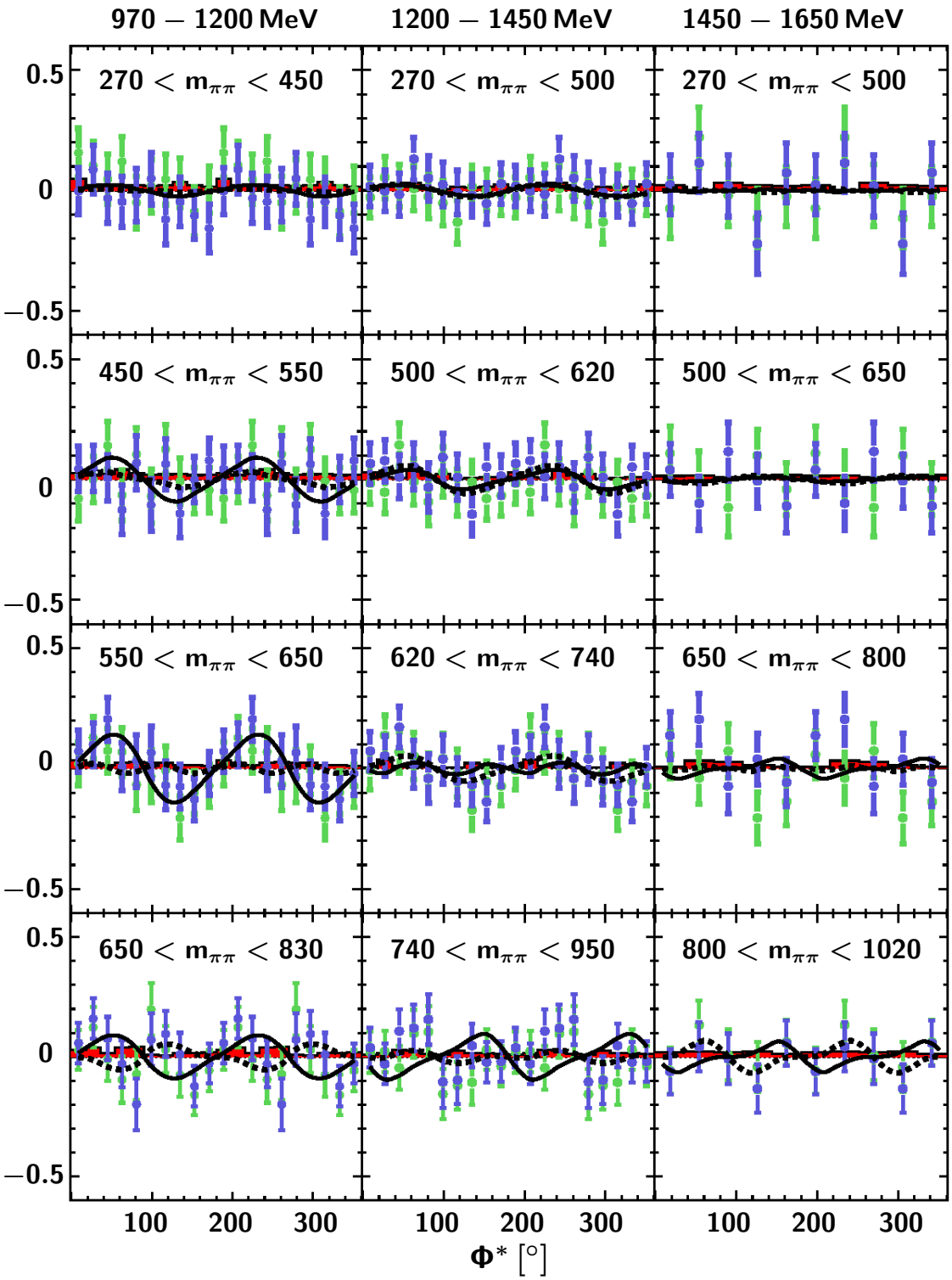

Figure 5.16.: Polarization observable I^s in the case of the recoiling proton binned in $m_{\pi\pi}$ blue circles: I^s directly extracted out of data, green circles: I^s after mirror operation $I^s(\Phi^*) \rightarrow -I^s(2\pi - \Phi^*)$, solid curve: BnGa-PWA solution $D_{33}(1700) \rightarrow \Delta\pi$ D-wave dominated, dashed curve: BnGa-PWA solution $D_{33}(1700) \rightarrow \Delta\pi$ S-wave dominated. Bars indicate the systematic error.

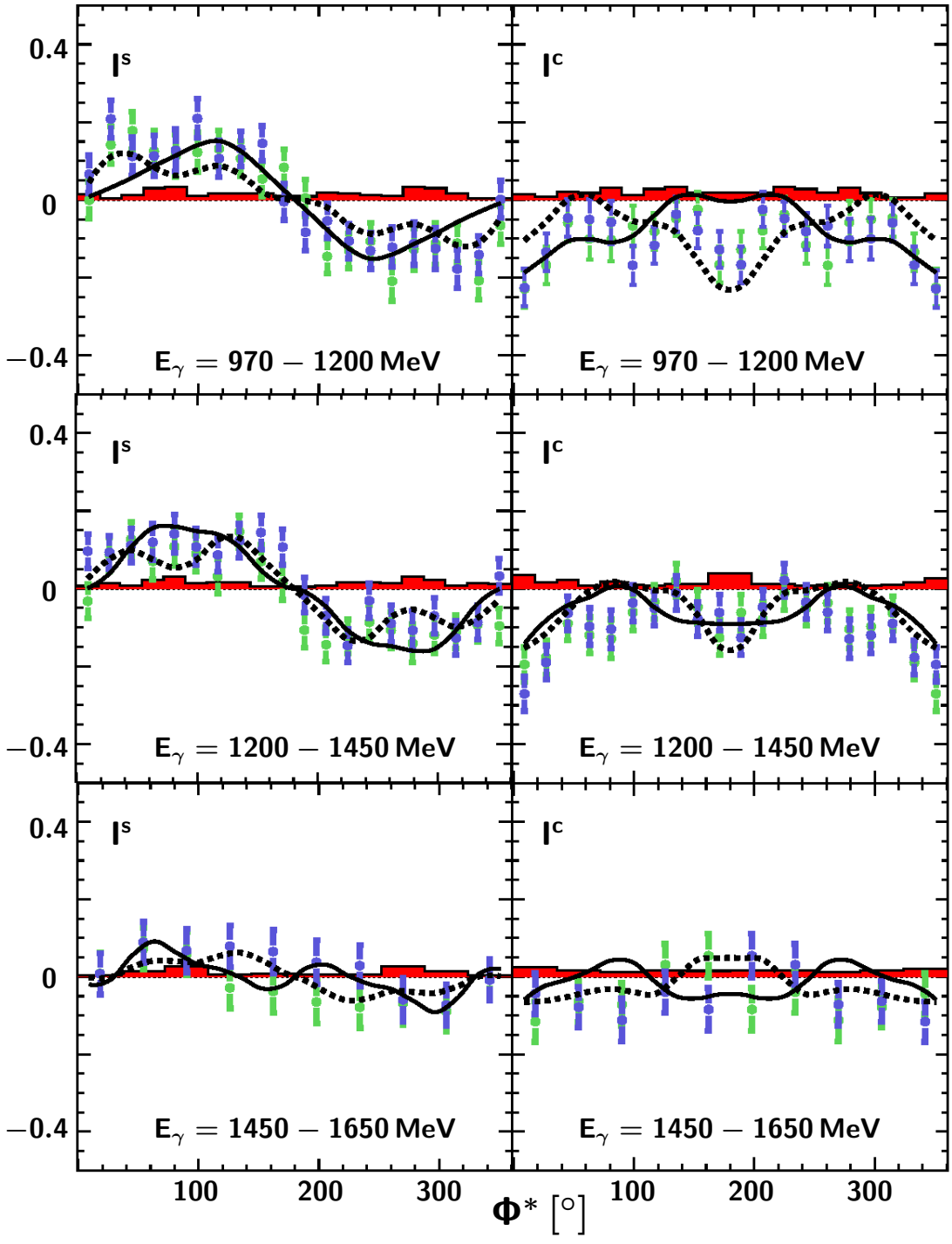

Figure 5.17.: Polarization observable I^s and I^c in the case of the recoiling pion - blue circles: I^s and I^c directly extracted out of data, green circles: I^s and I^c after mirror operations $I^s(\Phi^*) \rightarrow -I^s(2\pi - \Phi^*)$, $I^c(\Phi^*) \rightarrow I^c(2\pi - \Phi^*)$, solid curve: BnGa-PWA solution $D_{33}(1700) \rightarrow \Delta\pi$ D-wave dominated, dashed curve: BnGa-PWA solution $D_{33}(1700) \rightarrow \Delta\pi$ S-wave dominated. Bars indicate the systematic error.

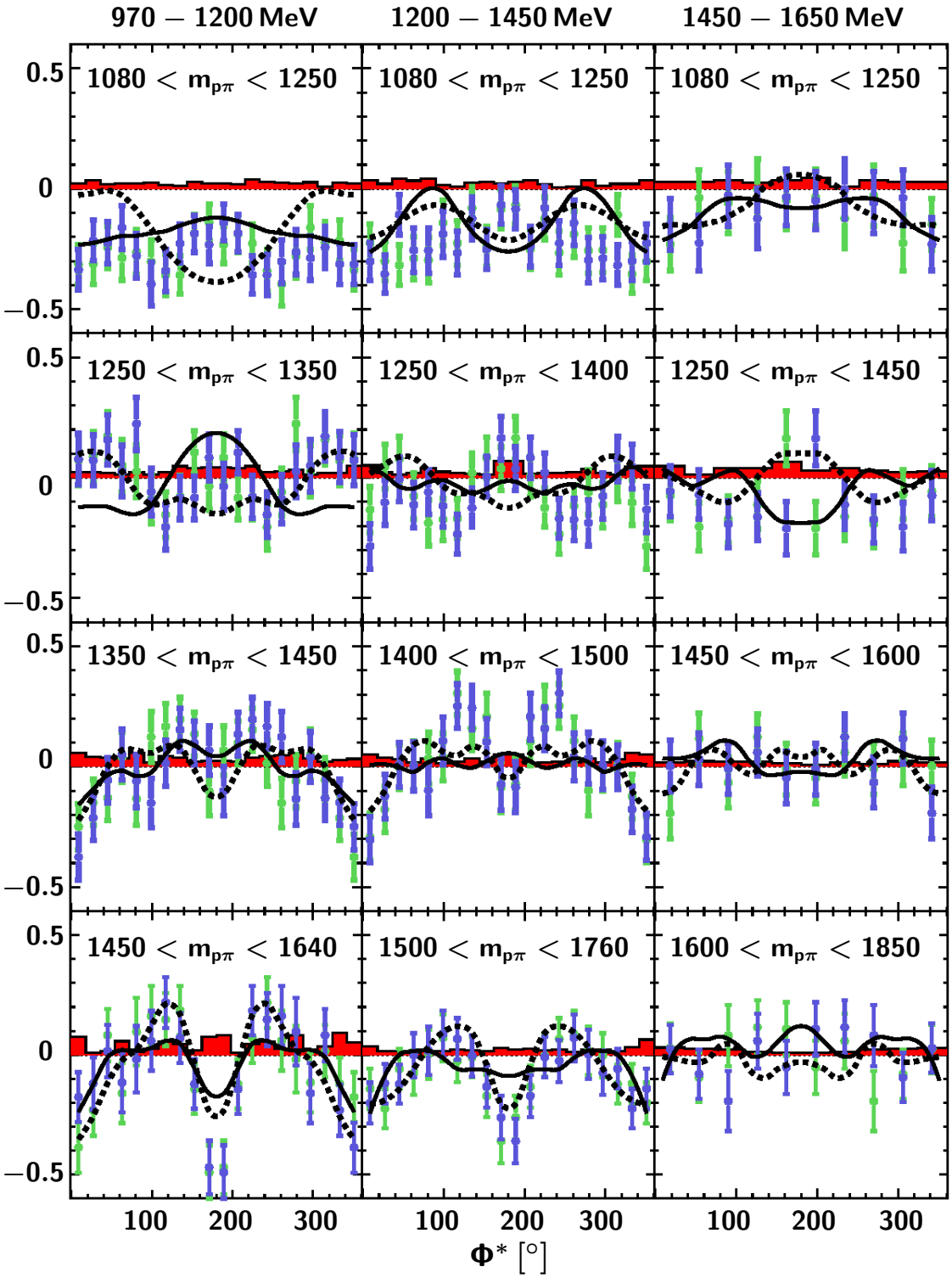

Figure 5.18.: Polarization observable I^c in the case of the recoiling pion binned in $m_{p\pi}$ blue circles: I^c directly extracted out of data, green circles: I^c after mirror operation $I^c(\Phi^*) \to I^c(2\pi - \Phi^*)$, solid curve: BnGa-PWA solution $D_{33}(1700) \to \Delta\pi$ D-wave dominated, dashed curve: BnGa-PWA solution $D_{33}(1700) \to \Delta\pi$ S-wave dominated. Bars indicate the systematic error.

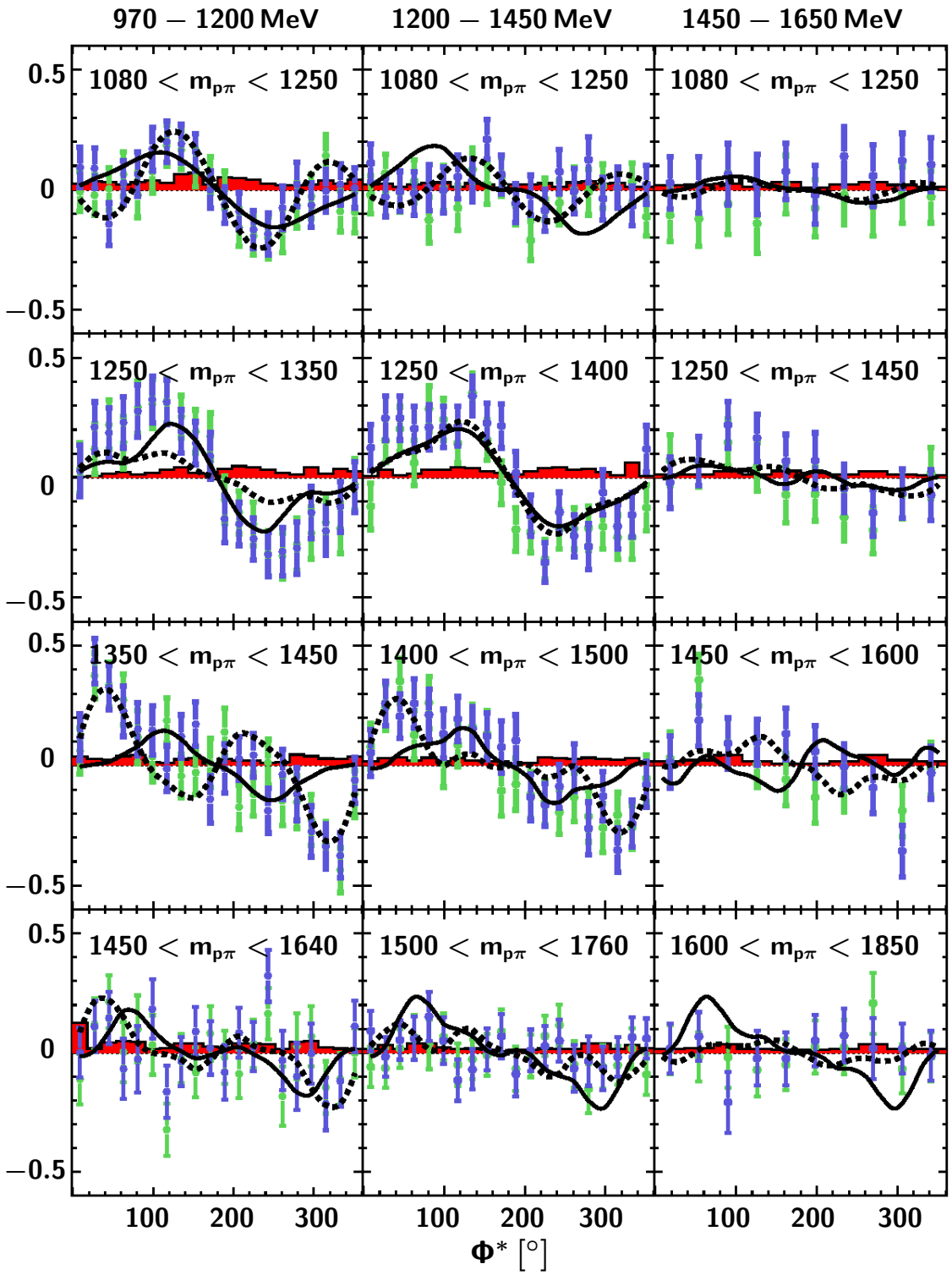

Figure 5.19.: Polarization observable I^s in the case of the recoiling pion binned in $m_{p\pi}$ blue circles: I^s directly extracted out of data, green circles: I^s after mirror operation $I^s(\Phi^*) \rightarrow -I^s(2\pi - \Phi^*)$, solid curve: BnGa-PWA solution $D_{33}(1700) \rightarrow \Delta\pi$ D-wave dominated, dashed curve: BnGa-PWA solution $D_{33}(1700) \rightarrow \Delta\pi$ S-wave dominated. Bars indicate the systematic error.

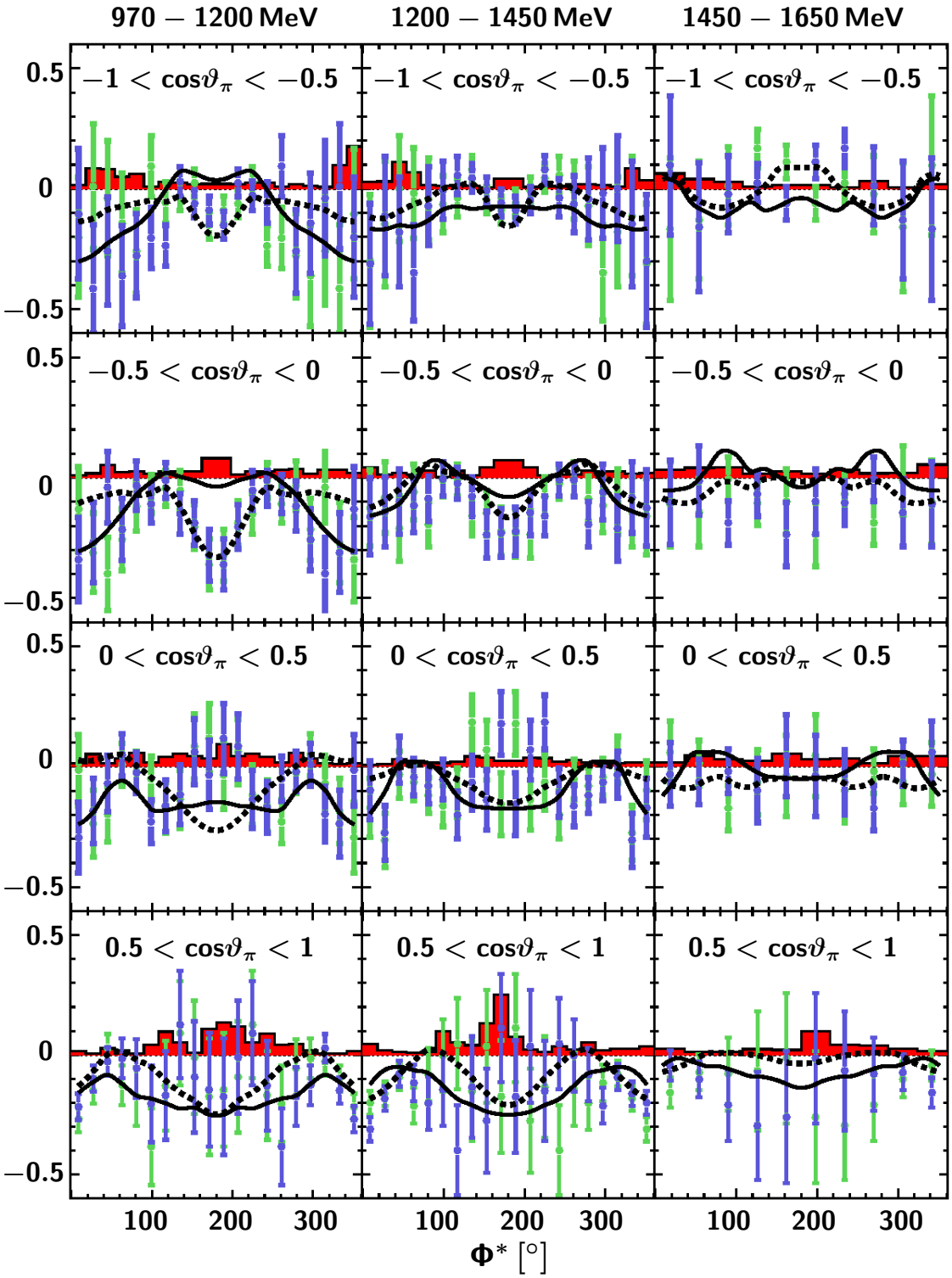

Figure 5.20.: Polarization observable I^c in the case of the recoiling pion binned in $\cos\vartheta_\pi$ blue circles: I^c directly extracted out of data, green circles: I^c after mirror operation $I^c(\Phi^*) \rightarrow I^c(2\pi - \Phi^*)$, solid curve: BnGa-PWA solution $D_{33}(1700) \rightarrow \Delta\pi$ D-wave dominated, dashed curve: BnGa-PWA solution $D_{33}(1700) \rightarrow \Delta\pi$ S-wave dominated. Bars indicate the systematic error.

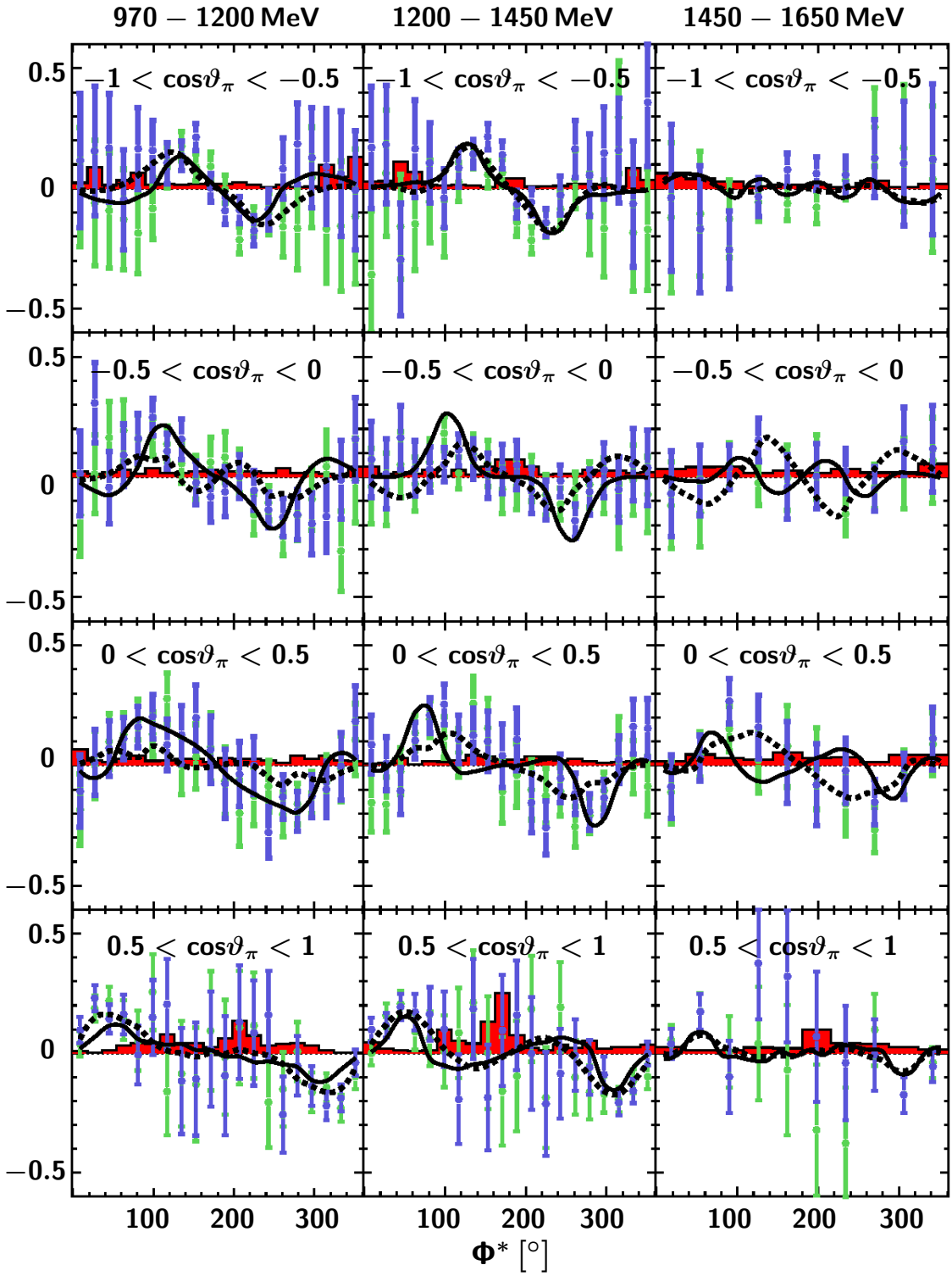

Figure 5.21.: Polarization observable I^s in the case of the recoiling pion binned in $\cos\vartheta_\pi$ blue circles: I^s directly extracted out of data, green circles: I^s after mirror operation $I^s(\Phi^*) \rightarrow -I^s(2\pi - \Phi^*)$, solid curve: BnGa-PWA solution $D_{33}(1700) \rightarrow \Delta\pi$ D-wave dominated, dashed curve: BnGa-PWA solution $D_{33}(1700) \rightarrow \Delta\pi$ S-wave dominated. Bars indicate the systematic error.

5.5. Decay cascades

In addition to the polarization observables the transition from the initial γp state to the final $2\pi^0$ state via possible intermediate resonances has been investigated using invariant mass distributions and Dalitz plots in the photon beam energy range $E_\gamma = 500 - 2500\,\mathrm{MeV}$. Figures 5.23 and 5.24 show selected spectra with pronounced resonance contributions.

The data are corrected for the acceptance of the detector system based on the distributions of generated and reconstructed phase space Monte Carlo events. The acceptance is determined as the ratio of number of reconstructed and generated events for all bins. Then, the histograms extracted from the experimental data are divided by the acceptance histograms. For the Dalitz plots the corrections are performed for the given photon energy range using the corresponding squares of invariant masses (see Figure 5.22). For the invariant masses the correction is performed using incoming photon energy and the plotted invariant mass. After the acceptance correction the invariant mass distributions were normalized to the area covered by the spectrum obtained from the CBELSA data [Fuc05] in the considered energy bin. Figure 5.23 shows the invariant mass spectra of the pπ^0 pair and the $m^2_{\mathrm{p}\pi^0}$ vs. $m^2_{\mathrm{p}\pi^0}$ Dalitz plots after acceptance correction. The data are binned in three selected energy ranges (1500-1600, 2000-2200 and 2200-2400 MeV). The states decaying into pπ^0 are clearly seen as peaks in the invariant mass spectra and as bands in the corresponding Dalitz plots and indicate strong contribution from the $\Delta(1232)$ resonance in the energy range 1500-1600 MeV and a contribution corresponding to the mass of $D_{13}(1520)$. In the energy range 2000-2200 MeV also a peak in the region of $F_{15}(1680)$ is observed. At high energies in the bin 2200-2400 MeV also three peaks can be seen. The CBELSA/TAPS data in addition to already existing CBELSA data [Fuc05] indicate the existence of cascading resonances:
$\gamma\mathrm{p} \rightarrow \mathrm{N}^*/\Delta^* \rightarrow \Delta(1232)\pi^0$
$\gamma\mathrm{p} \rightarrow \mathrm{N}^*/\Delta^* \rightarrow \mathrm{D}_{13}(1520)\pi^0$ and
$\gamma\mathrm{p} \rightarrow \mathrm{N}^*/\Delta^* \rightarrow \mathrm{F}_{15}(1680)\ \pi^0$,

and having the advantage of higher statistics lead to the opportunity to have higher resolution of the spectra with better separation of the structures. The

latest studies using the BnGa-PWA showed that the third peak in the invariant mass of the pπ^0 system can include contributions not only from $F_{15}(1680)$ but also from $P_{11}(1710)$ [Sar12].

In Figure 5.24 Dalitz plots for $m^2(\pi^0\pi^0)$ vs. $m^2(p\pi^0)$ (left) and the corresponding $m(\pi^0\pi^0)$ invariant mass spectra (right) are shown. In the energy regime 1500-1600 MeV there are no structures observed in the $\pi^0\pi^0$ invariant mass. The structures due to the contributions of $\Delta(1232)$ and $D_{13}(1520)$ are seen in the corresponding Dalitz plot. In the energy range 2000-2200 MeV a peak is seen in the region of $f_0(980)$ and in the higher energy ranges, e.g. in the energy range 2200-2400 MeV an enhancement is seen in the region of the $f_2(1270)$ mass in combination with $f_0(980)$. The collection of the Dalitz plots in the energy range $E_\gamma = 500 - 2500\,\mathrm{MeV}$ split in 50 MeV wide energy bins is shown in Appendix C.

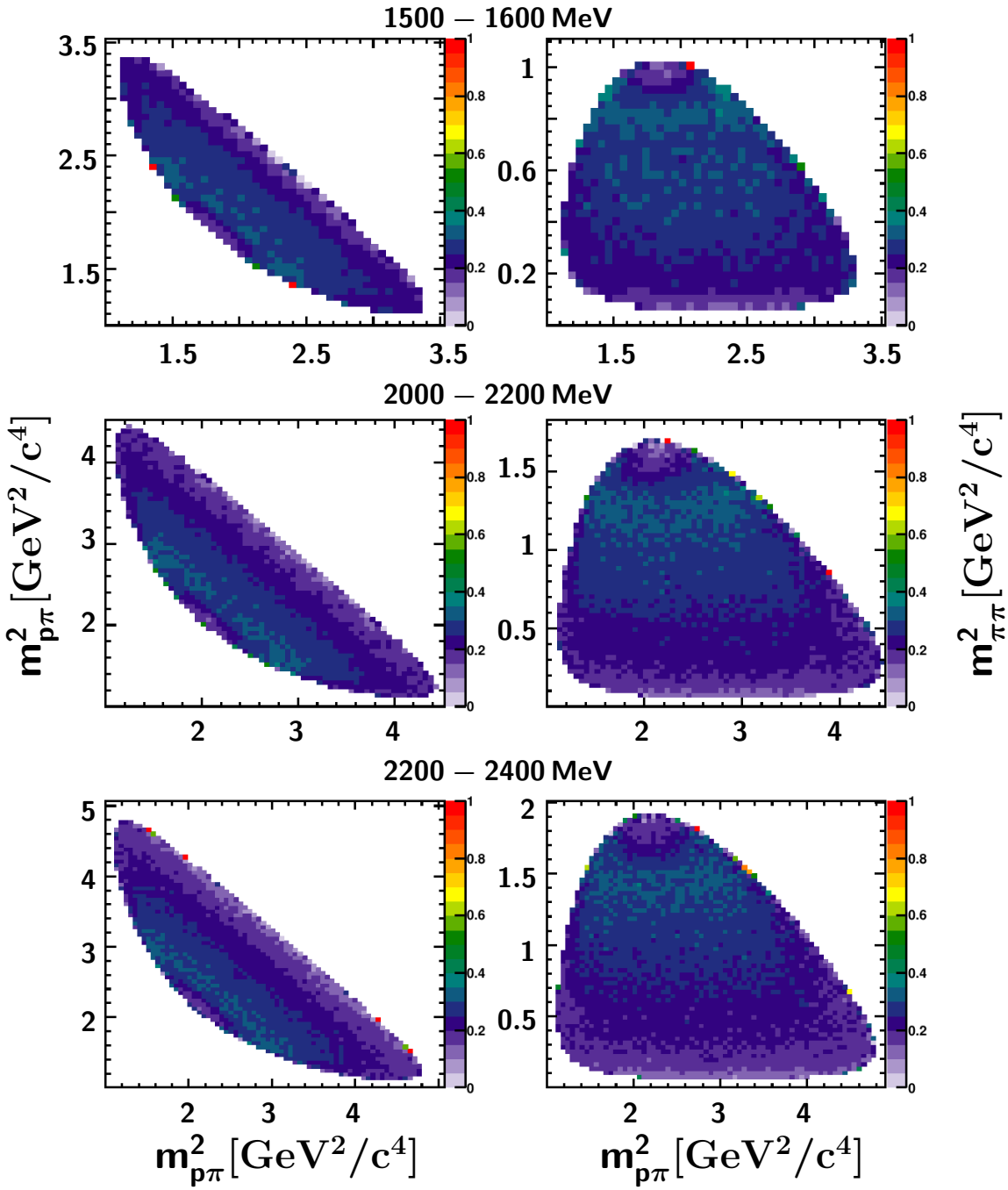

Figure 5.22.: Acceptance histograms used for the correction of the Dalitz plots. Left column: $m^2(p\pi^0)$ vs. $m^2(p\pi^0)$, right column: $m^2(\pi^0\pi^0)$ vs. $m^2(p\pi^0)$.

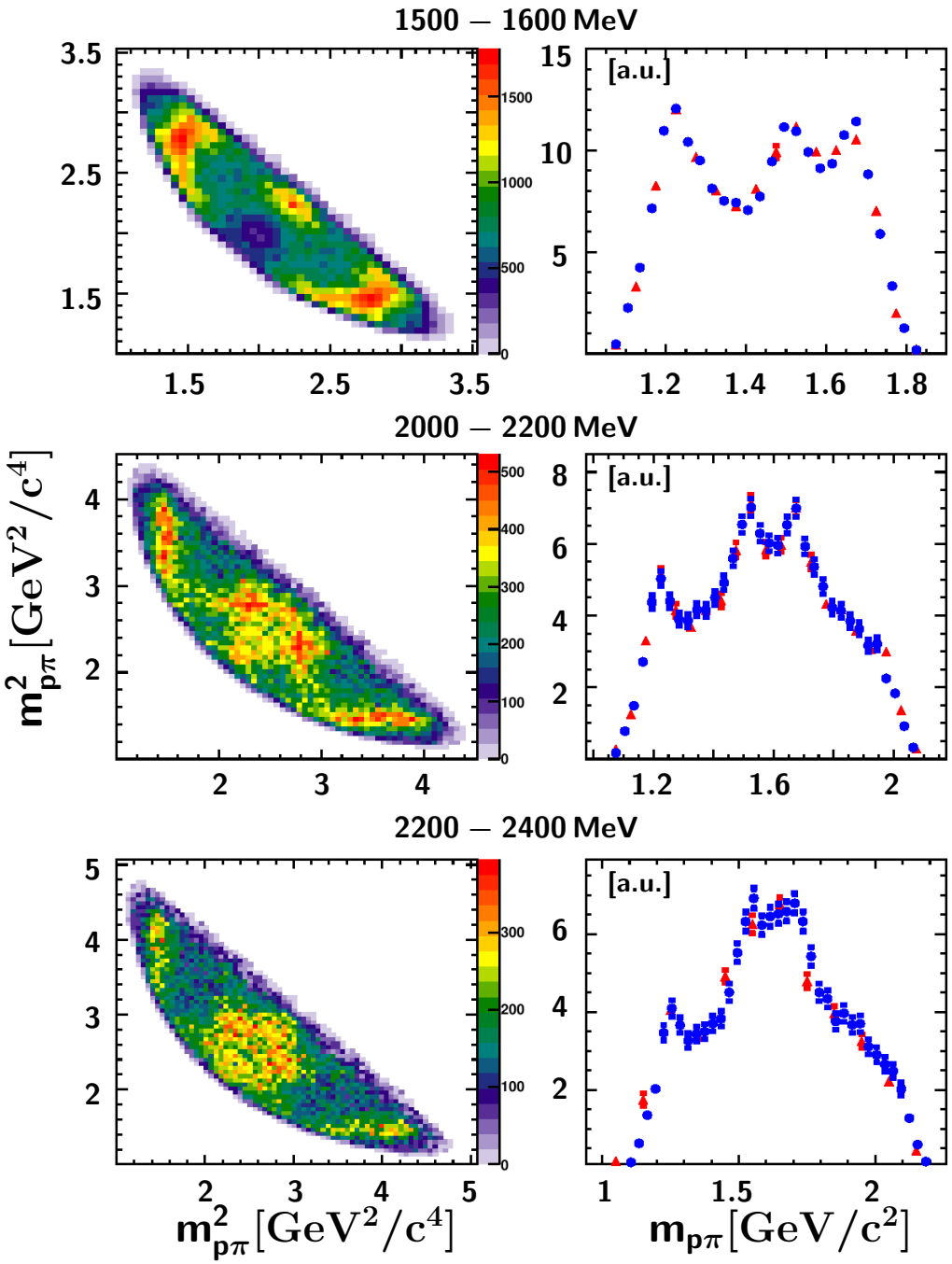

Figure 5.23.: Acceptance corrected Dalitz plots ($m^2(p\pi^0)$ vs. $m^2(p\pi^0)$) and invariant mass spectra of the $p\pi^0$ pair, red: CBELSA data, blue: CBELSA/TAPS data after acceptance correction and normalization to the integral of CBELSA data [Fuc05][T$^+$08].

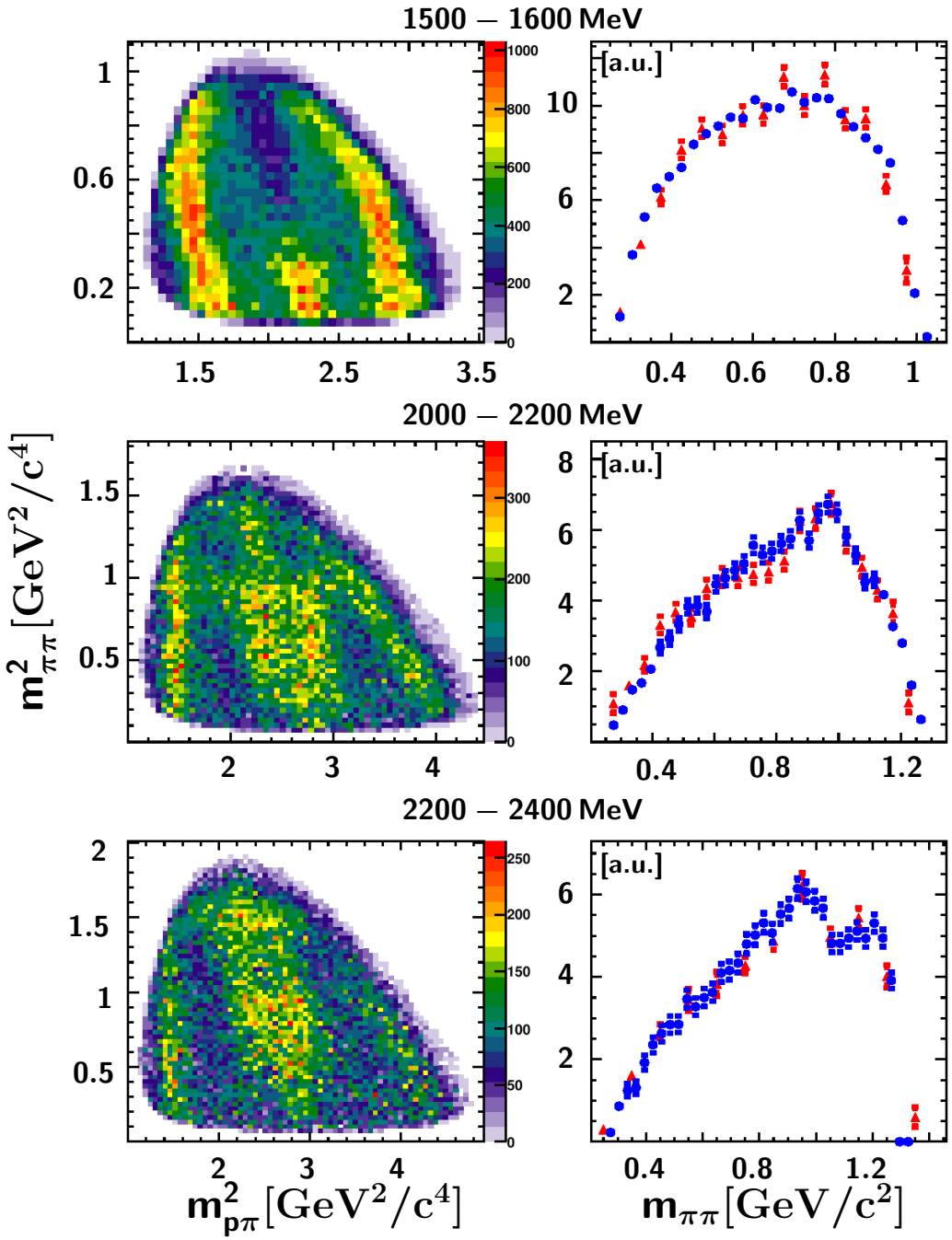

Figure 5.24.: Acceptance corrected Dalitz plots ($m^2(\pi^0\pi^0)$ vs. $m^2(p\pi^0)$) and invariant mass spectra of the $\pi^0\pi^0$ pair, red: CBELSA data, blue: CBELSA/TAPS data after acceptance correction and normalization to the integral of CBELSA data [Fuc05][T+08].

	Resonance	BnGa-PWA	Fix model
	$N(1440)P_{11}$	$N\sigma, \Delta(1232)\pi$	$N\sigma, \Delta(1232)\pi$
	$N(1535)S_{11}$	$\Delta(1232)\pi$	$N\sigma$
	$N(1650)S_{11}$	$\Delta(1232)\pi$	not included
	$N(1520)D_{13}$	$N\sigma, \Delta(1232)\pi, N(1440)P_{11}\pi$	$\Delta(1232)\pi$
	$N(1700)D_{13}$	$N\sigma, \Delta(1232)\pi, N(1440)P_{11}\pi$	not included
	$N(1675)D_{15}$	$N\sigma$, $\Delta(1232)\pi$, $N(1440)P_{11}\pi$	$\Delta(1232)\pi$
	$N(1720)P_{13}$	$N\sigma$, $\Delta(1232)\pi$, $N(1520)D_{13}\pi$	(no $\pi^0\pi^0$ mode)
	$N(1680)F_{15}$	$N\sigma$, $\Delta(1232)\pi$	$N\sigma$, $\Delta(1232)\pi$
	$\Delta(1620)S_{31}$	$\Delta(1232)\pi$, $N(1440)P_{11}\pi$	$\Delta(1232)\pi$
	$\Delta(1700)D_{33}$	$\Delta(1232)\pi$, $N(1440)P_{11}\pi$, $N(1520)D_{13}\pi$	$\Delta(1232)\pi$

Table 5.1.: Main resonance contributions in the reaction $\gamma p \to p\pi^0\pi^0$ in the BnGa-PWA and Fix model. The decay modes which may contribute to the channel $\gamma p \to p\pi^0\pi^0$ are shown. The BnGa-PWA fitted the cross-section data in the energy range for $\gamma p \to p\pi^0\pi^0$ between 400 MeV and 1300 MeV [T$^+$08]. Fix model covers up to 1450 MeV [Fix05], no fit to the experimental cross-section data was performed.

5.6. Comparison with models

In Sections 5.1 and 5.4 it has been shown that the data on the observables measured in this work provide a significant impact for the BnGa-PWA. Noticeable differences were observed between experimental data and BnGa-PWA predictions obtained with $D_{33}(1700) \to \Delta\pi$ decaying dominantly either via S-wave or D-wave. Even though there are differences between BnGa-PWA predictions and experimental data, the description of data with these two predictions has a similar quality and it is difficult to make a statement about preferred decay mode from this comparison. It is likely that both modes contribute notably to the decay of this state.

The data have been also compared with predictions from the model developed by A. Fix [Fix05]. This comparison is particularly interesting because the dominant resonance contributions included in the BnGa-PWA and Fix model are rather different. The resonance contributions are listed in Table 5.1 for the incoming photon energy range up to 1.3 GeV in the BnGa-PWA (fitted energy range of

$\gamma p \to p\pi^0\pi^0$ data) and up to 1.45 GeV in the Fix model [5]. With some exceptions, a similar set of resonances contributes to the reaction $\gamma p \to p\pi^0\pi^0$ in both models, however in some cases decays into different intermediate channels are included. In the BnGa-PWA in addition to the $N\sigma$ and $\Delta(1232)\pi$ decay modes, the cascading decays via $P_{11}(1440)\pi$ and $D_{13}(1520)\pi$ are also allowed for some of the resonances. Background channels have been also considered in these two models. Fix model includes Born terms [Fix05], BnGa-PWA includes Born terms, t-channel and u-channel exchanges [T^+08].

Even though there are similarities in the list of contributing resonances and in their decay modes, the strength of different contributions (see Figure 5.25) is very different between BnGa-PWA and Fix model. In the BnGa-PWA $D_{33}(1700)$ contributes strongly over the whole considered energy range. In the region of the first peak in the cross-section D_{13} partial wave contributes significantly. The two peak structure is explained in the BnGa-PWA by the interference between D_{33} and D_{13} partial waves with a moderate contribution from $F_{15}(1680)$ [S^+08] (see also Section 1.5). A contribution of the P_{11} partial wave is also present and somewhat increases at higher energies. In the Fix model the contributions are different. Although, in the low energy range around 800 MeV a strong contribution of $D_{13}(1520)$ is also present and $P_{11}(1440)$ contributes notably. $F_{15}(1680)$ contributes significantly in the region around 1 GeV and the second peak in the cross-section is explained in the Fix model mostly by the contribution of this resonance. The contribution of $D_{33}(1700)$ is smaller in comparison to the resonances shown in Figure 5.25 (right).

Below it is shown that the data obtained in this work allows to distinguish between these two very different models. In Figure 5.27 the data on beam asymmetry Σ obtained in this work are plotted together with the predictions from the BnGa-PWA and Fix model. The BnGa-PWA predictions for Σ in this range are constrained by GRAAL data (CBELSA/TAPS data were not included) and in general reasonably reproduce the sign and the shapes observed in the CBELSA/TAPS data. In both energy ranges 970-1200 MeV and 1200-1450 MeV the calculations of the Fix

[5] It is worth to mention that there was no fit to the experimental cross-sections performed in the Fix model. The decay widths were taken from the Particle Data Group and hadronic coupling constants were fitted to the corresponding widths. For more details see [Fix05].

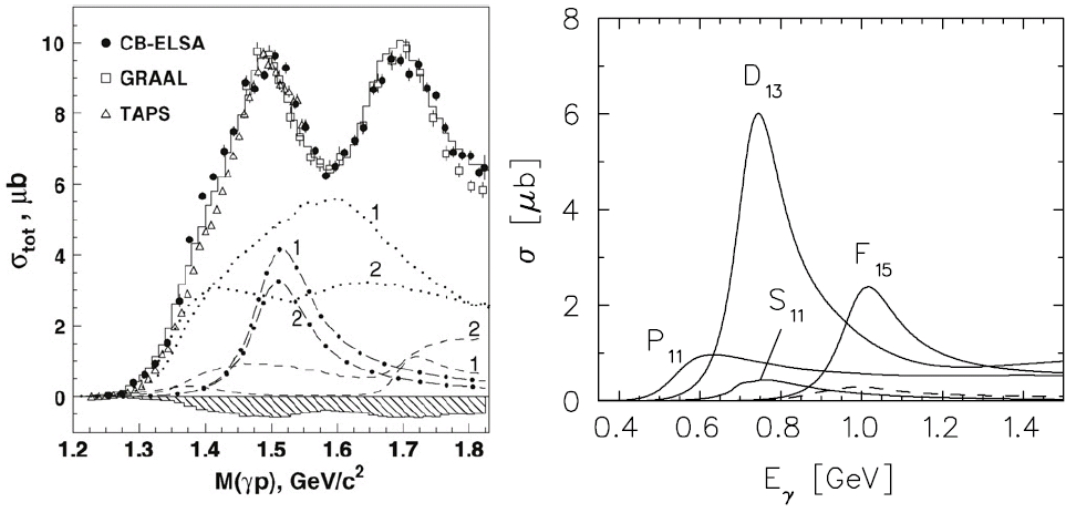

Figure 5.25.: Comparison of the Fix model calculations [Fix05] with the BnGa-PWA predictions [S$^+$08]. On the left: BnGa-PWA, the solid curve represents result of the BnGa-PWA fit, the shaded area shows the systematic error of the measurement of the CBELSA data. Solution 1 (BnGa-PWA) corresponds to the $D_{33}(1700) \rightarrow \Delta\pi$ decay with S-wave dominance, solution 2 with D-wave dominance. Dotted line: contribution of the D_{33} partial wave, dashed-dotted line: D_{13} and dashed line: P_{11} partial wave. On the right: calculation of the Fix model [Fix05], solid curves show contributions of $P_{11}(1440)$, $D_{13}(1520)$, $F_{15}(1680)$ and $S_{11}(1535)$, dashed: sum of the contributions of $S_{31}(1620)$, $P_{13}(1720)$ and $D_{15}(1675)$.

model in general do not reproduce the sign and shape of the asymmetry Σ seen in the experimental data.

Further, a similar comparison was performed for the I^s and I^c observables. For the observable I^c in the proton recoiling case an opposite sign is obtained in the Fix model and experimental data. For the observable I^s in the energy range 970-1200 MeV the calculation of the Fix model shows an amplitude similar to the one in the data but has a different phase. In the energy range 1200-1450 MeV the phase is also different in the Fix model and the amplitude is somewhat larger than in the data. The predictions for both BnGa-PWA solutions show much better agreement with the data. For the observable I^s in the recoiling pion case the calculations with the Fix model in general agree with the data, but there are large differences in the observable I^c, which is in general not the case for the BnGa-PWA predictions. From the overall comparison one can conclude that the data allows to distinguish between the two models and the predictions of BnGa-PWA are in a much better agreement with the data than the calculations of the Fix model. This result can be interpreted as a proof of the importance of the $D_{33}(1700)$ resonance for the reaction $\gamma p \rightarrow p\pi^0\pi^0$ which is predicted with much larger contribution in the BnGa-PWA. However, the predictions given by the BnGa-PWA also have some problems in the description of the data and should be improved. The effects of the data on the BnGa-PWA are presently under investigation. The overall picture showing the latest status of the BnGa-PWA, among other data sets also including CBELSA/TAPS data on the polarization observables I^s and I^c is shown in Table 5.2 [6][ABK+12].

[6]BnGa-PWA includes also resonance decays via higher mass states e.g. in the $D_{13}(1520)\pi$ or $P_{11}(1440)\pi$ modes. The significance of these decay modes is currently under investigation.

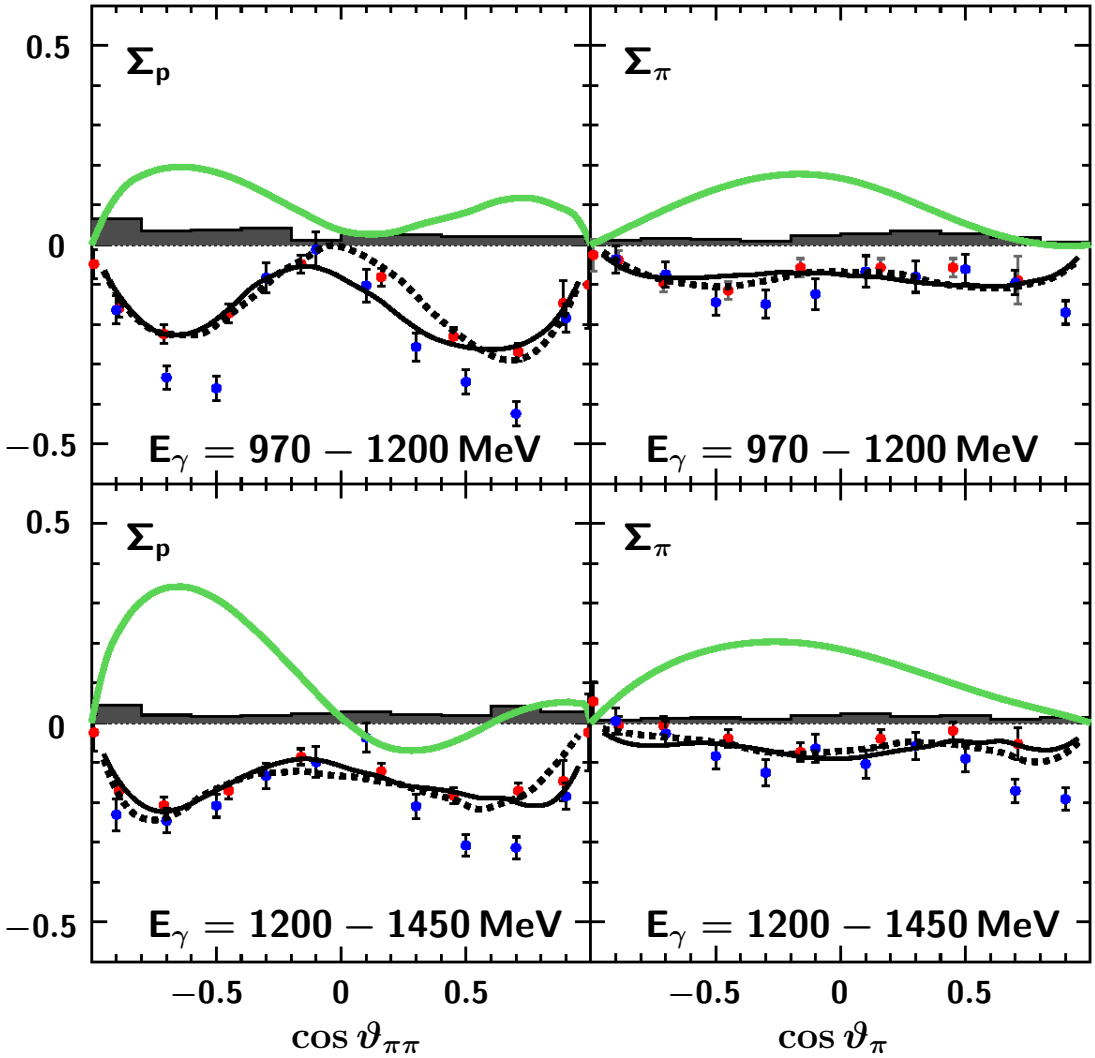

Figure 5.26.: Comparison of experimental data with calculations of the Fix model [Fix05] and BnGa-PWA predictions. Blue: CBELSA/-TAPS data, red: GRAAL data, solid curve: BnGa-PWA solution $D_{33}(1700) \to \Delta\pi$ D-wave dominated, dashed curve: BnGa-PWA solution $D_{33}(1700) \to \Delta\pi$ S-wave dominated, green: calculation of the Fix model. Bars indicate the systematic error.

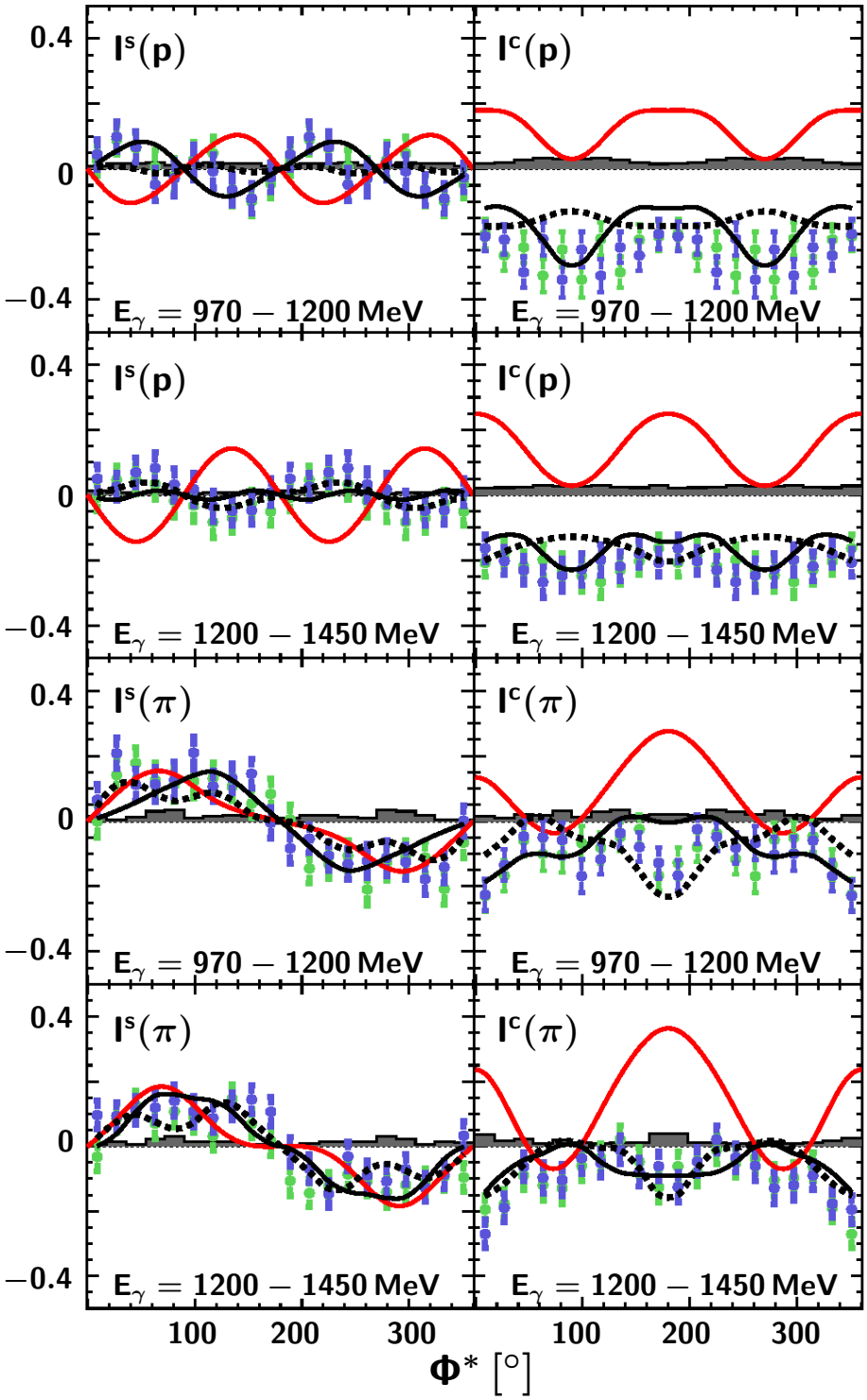

Figure 5.27.: Comparison of experimental data with calculations of the Fix model [Fix05] and BnGa-PWA predictions. Blue circles: I^s and I^c directly extracted out of data, green circles: I^s and I^c after mirror operations, $I^c(\Phi^*) \rightarrow I^c/(2\pi - \Phi^*)$ and $I^s(\Phi^*) \rightarrow -I^s/(2\pi - \Phi^*)$, solid curve: BnGa-PWA solution $D_{33}(1700) \rightarrow \Delta\pi$ D-wave dominated, dashed curve: BnGa-PWA solution $D_{33}(1700) \rightarrow \Delta\pi$ S-wave dominated, red curve: calculation of the Fix model. Bars indicate the systematic error.

Table 5.2.: List of resonances according to the Particle Data Group and BnGa-PWA. Ratings of resonances in the Particle Data Group [N$^+$10] are shown as *, additional stars proposed by the BnGa-PWA are shown by ⋆, (*) corresponds to the stars which have to be removed according to the BnGa-PWA [ABK$^+$12]. The decay modes which can contribute to the reaction $\gamma p \to p\pi^0\pi^0$ are shown in blue.

	all	πN	γN	$N\eta$	ΛK	ΣK	$\Delta\pi$	$N\sigma$
$N(1440)\frac{1}{2}^+$	****	****	***⋆	(*)			***	⋆⋆⋆
$N(1710)\frac{1}{2}^+$	***	***	***	**⋆	⋆⋆⋆	⋆⋆	*(*)	
$N(1880)\frac{1}{2}^+$	⋆⋆	⋆	⋆		⋆⋆	⋆		
$N(1535)\frac{1}{2}^-$	****	****	****	****			*	
$N(1650)\frac{1}{2}^-$	****	****	***	*⋆⋆	***	**	**(*)	
$N(1895)\frac{1}{2}^-$	⋆⋆	⋆	⋆⋆	⋆⋆	⋆⋆	⋆		
$N(1720)\frac{3}{2}^+$	****	****	****	****	**	**	***	
$N(1900)\frac{3}{2}^+$	**⋆	**	⋆⋆⋆	⋆⋆	⋆⋆⋆	⋆⋆	⋆⋆	
$N(1520)\frac{3}{2}^-$	****	****	****	***			****	
$N(1700)\frac{3}{2}^-$	**⋆	**	**	*	*(*)	*	**⋆	
$N(1875)\frac{3}{2}^-$	⋆⋆⋆	⋆	⋆⋆⋆		⋆⋆⋆	⋆⋆		⋆⋆⋆
$N(2150)\frac{3}{2}^-$	⋆⋆	⋆⋆	⋆⋆		⋆⋆		⋆⋆	
$N(1680)\frac{5}{2}^+$	****	****	****	*			**(*)	⋆⋆
$N(1860)\frac{5}{2}^+$	⋆	⋆	⋆					
$N(2000)\frac{5}{2}^+$	*⋆⋆	*(*)	⋆⋆	⋆⋆	⋆⋆	⋆		
$N(1675)\frac{5}{2}^-$	****	****	***(*)	*	*		***(*)	⋆
$N(2060)\frac{5}{2}^-$	⋆⋆⋆	⋆⋆	⋆⋆⋆	⋆		⋆⋆		
$N(1990)\frac{7}{2}^+$	**	*(*)	⋆⋆					
$N(2190)\frac{7}{2}^-$	****	****	*⋆⋆		⋆⋆			
$N(2220)\frac{9}{2}^+$	****	****						
$N(2250)\frac{9}{2}^-$	****	****						
$\Delta(1910)\frac{1}{2}^+$	****	****	**⋆			*⋆	**⋆	
$\Delta(1620)\frac{1}{2}^-$	****	****	***				****	
$\Delta(1900)\frac{1}{2}^-$	**	**	**⋆			*⋆	**⋆	
$\Delta(1232)\frac{3}{2}^+$	****	****	****					
$\Delta(1600)\frac{3}{2}^+$	***	***	**⋆				***	
$\Delta(1920)\frac{3}{2}^+$	***	***	*⋆			*⋆⋆	**	
$\Delta(1700)\frac{3}{2}^-$	***	***	***				**	
$\Delta(1940)\frac{3}{2}^-$	**	⋆⋆					|⋆ from $\Delta\eta$|	
$\Delta(1905)\frac{5}{2}^+$	****	****	****			*⋆⋆	**(**)	
$\Delta(1950)\frac{7}{2}^+$	****	****	***			*⋆⋆	**⋆	

6. Summary

In this work the three-body single polarization observables I^s, I^c and the corresponding two-body observable Σ were measured in the reaction $\gamma p \to p\pi^0\pi^0$ with the CBELSA/TAPS experiment. The selected data set consists of 561,443 events in the energy range $E_\gamma = 970 - 1650\,\mathrm{MeV}$ with a background contamination below 1%. The observables I^s and I^c were measured for the first time in the reaction $\gamma p \to p\pi^0\pi^0$, exposing various structures, particularly pronounced for different invariant mass and angular ranges. Studies of the self-consistency of the data using symmetry and parity conditions showed its high quality and absence of significant systematic effects. The observable Σ being the constant offset of the observable I^c was measured in a quasi-two body approach to the reaction. In comparison to the already existing data, the energy range for Σ was extended from 1450 MeV up to 1650 MeV.

Based on these data and predictions of the Bonn-Gatchina Partial Wave Analysis the question of the dominant mode of the $D_{33}(1700) \to \Delta\pi$ decay was studied and it was shown that the predictions of the Bonn-Gatchina PWA produced either with S- or D-wave dominance describe the experimental data with a similar quality. Even though some of the shapes seen in the data are reproduced none of the two predictions was found to be clearly favored. It is likely that both S- and D-wave modes contribute notably to the $D_{33}(1700) \to \Delta\pi$ decay.

The differences between the Bonn-Gatchina PWA and the Fix isobar model were investigated. These models include similar sets of resonances but the decay modes and the strengths of their contributions in the reaction $\gamma p \to p\pi^0\pi^0$ are different. It was shown that the data allow to clearly distinguish between these predictions in favor of the Bonn-Gatchina PWA. This observation can be interpreted as a confirmation of the significant contribution of the $D_{33}(1700)$ resonance in the reaction $\gamma p \to p\pi^0\pi^0$ predicted by the Bonn-Gatchina PWA, but not by the Fix model. The comparison of the data with the theoretical models showed that the

data provide new constraints for the PWA. Presently the data are included in the Bonn-Gatchina PWA and further studies of resonance properties are on the way.

Additionally, taking the advantage of the high statistics data set, invariant mass distributions and Dalitz plots were investigated in the energy range from 500 MeV to 2500 MeV. Structures indicating contributions of $\Delta(1232)$, $D_{13}(1520)$, $F_{15}(1680)$, $f_0(980)$ and $f_2(1270)$ were observed in the data and confirmed by the Bonn-Gatchina PWA. The latest studies using the Bonn-Gatchina PWA showed that besides the $F_{15}(1680)$ resonance, the $P_{11}(1710)$ resonance also contributes notably in the $p\pi^0$ invariant mass range around 1700 MeV. The data are found to be in excellent agreement with the existing CBELSA data.

A. 5-dimensional acceptance correction

In the following an attempt which was made to correct the inefficiencies of the detector using a model-independent 5-dimensional acceptance correction is discussed. Generated and reconstructed Monte Carlo events (see Section 4.2) have been used in the determination of the acceptance and in the further application of the correction. To achieve an acceptance correction with negligibly low error, an extremely large number of events would be needed, therefore due to statistical limitation the correction was not applied to the data. However, the methods and hints which are shortly described, can be used in the future for the application of the 5-dimensional acceptance correction.

Definition of acceptance

For the determination of the acceptance, generated and reconstructed events have been selected in the energy range $E_\gamma = 970 - 1650\,\mathrm{MeV}$. The same analysis chain used for the data (see Section 4) was applied. The acceptance is determined as a ratio of the number of reconstructed and generated events:

$$A = \frac{\mathrm{N}_{\mathrm{rec}}}{\mathrm{N}_{\mathrm{gen}}}.$$

For the complete reproduction of the detector effects the acceptance has to be determined as function of the set of independent variables describing the reaction while taking into account all correlations between these variables in the phase space. The number of the independent variables for the two-meson final state is calculated as follows. $\gamma\mathrm{p} \rightarrow \mathrm{p}\pi^0\pi^0$ is a reaction with three particles in the final state with known masses and only nine 3-momenta components are needed (3 for each of the particles, 9 in total) for complete description of the reaction.

Three conditions of momentum conservation and the energy conservation law reduce the number of independent variables to $9 - 4 = 5$ variables. Knowledge of these 5 variables allows access to every value of kinematic variables defined in the reaction.

The variables used in the correction

There are various possible choices of the 5 variables describing the phase space. In this work the definitions presented in [Fuc05] were taken. The following variables were chosen: the energy of the incoming photon E_γ, invariant masses of the proton and the first and second pion $m_{p\pi_1}$, $m_{p\pi_2}$ [1] and 2 angles θ_{acc} and φ_{acc}, defined in the CMS frame. In Figure A.1 the angle definition is shown. $\overrightarrow{n_1}$ is a normal to the decay plane and is determined as the vector product of the momenta of the two pions, the angle θ_{acc} is defined as the angle between the normal $\overrightarrow{n_1}$ and the incoming proton. $\overrightarrow{n_2}$ is the vector product of the $\overrightarrow{n_1}$ vector and incoming proton and is defined in the decay plane. The angle φ_{acc} is the angle between $\overrightarrow{n_2}$ and the outgoing proton.

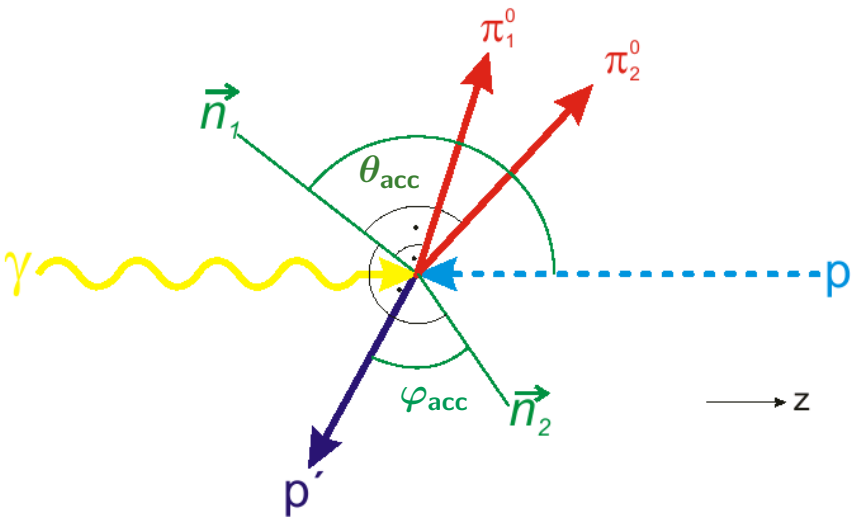

Figure A.1.: Definition of the angles θ_{acc} and φ_{acc} in the CMS frame, taken from [Fuc05].

[1] The invariant masses were calculated symmetrically with two entries for both invariant mass combinations.

The coverage in angles is shown in Figure A.2 where the correlation between $\cos\theta_{acc}$ and ϕ_{acc} is plotted. This distribution is flat for generated events. For

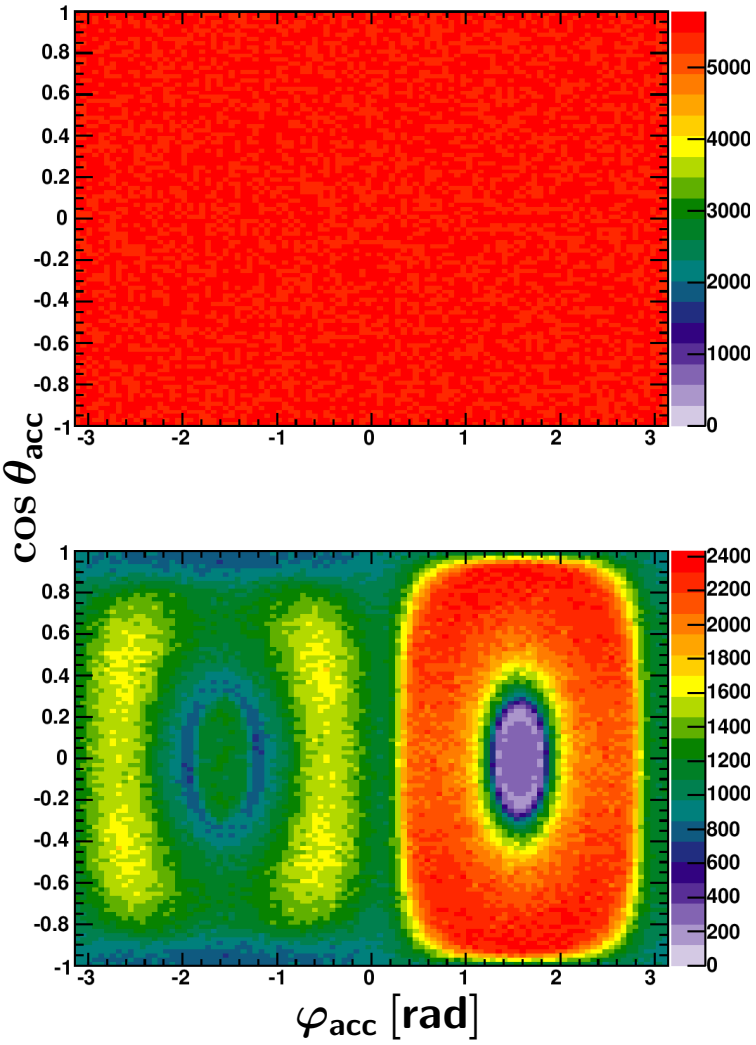

Figure A.2.: Two-dimensional matrix (φ_{acc}, $\cos\theta_{acc}$) for generated (upper) and reconstructed events (lower).

reconstructed events there is an acceptance reduction in certain regions, but no holes are seen in the angular correlation. In comparison to the previous CBELSA experiment [Fuc05] this is achieved by using TAPS covering the forward angular range (see Figure A.2). Already in two dimensions in Figure A.2 one can see that there are correlations which would not be observed by looking only at one-

dimensional projections. A complete description of the 5-dimensional phase space of a three-body final state, is much more complicated since all the correlations between 5 variables have to be taken into account (see next items). The average acceptance in the energy range $E_\gamma = 970 - 1650\,\mathrm{MeV}$ was found to be close to 25%.

Application of the acceptance correction

The information about acceptance determined from Monte Carlo simulation must be stored to be later used in the correction of the experimental data. One way to do it could be the determination of a 5-dimensional function describing the covered phase space. The problem of this method is that the finite statistics is used in the acceptance determination and also it is too complicated to extrapolate/fit the 5-dimensional phase space.

Another way is the discretization of the phase space by introducing a limited number of bins in each of the 5 dimensions used in the correction. In this way a 5-dimensional grid is created and the acceptance factors determined from the ratio of reconstructed and generated events can be stored in the respective bins of that grid. Further, the determined and stored acceptance factors can be used for the correction of the experimental data. The number of events then would be corrected in the following way: events then would be corrected in the following way:

$$N_{corr} = \frac{\mathrm{N_{data}}}{\mathrm{A}}.$$

This method has the advantage to be model-independent, and would allow to take all correlations between variables, occurring in the 5-dimensional phase space, into account. In this analysis 5-dimensional histograms [2] were filled, stored and further used for the acceptance correction. For this one has to identify the location of every data event to be corrected in the 5-dimensional grid. After identification of the bin, the corresponding weighting factor has to be taken from the 5-dimensional acceptance matrix and applied to the data.

[2] TH5F, with implementation of functions required for the correction [vP08].

Selection of the number of bins for the correction

For the acceptance correction described above it is important to have a sufficiently high number of bins to reproduce the complicated shape of the phase space. On the other hand by increasing the number of bins the number of events in these bins is reduced. The division into a higher number of bins increases the error of the correction. Also the number of bins with zero content increases [3]. In this analysis more than 4000 Monte Carlo files, containing 300000 generated events each have been produced for the acceptance determination. An important cross-check for the acceptance correction is the check of reproducibility of any kinematic variable which was not introduced as one of the variables in the acceptance correction. It allows to conclude that the whole phase space is properly reproduced. For that the distributions of kinematic variables for generated and reconstructed events after acceptance correction were compared. The deviation between these two distributions would indicate the errors introduced by the acceptance correction. As a first step the comparison was performed for the 5 dimensions which were introduced in the correction and a good agreement was obtained if the number of events was sufficiently high to populate all the bins in the phase space.

Here and in the next items several examples at already improved and tuned binning, as a result of extensive tests, are shown. The first example shows the case of the acceptance correction with 15 bins in the energy E_γ and 30 bins in the invariant masses $m_{p\pi_1}$ and $m_{p\pi_2}$ and in angular variables $\cos\theta_{acc}$ and φ_{acc}. Figure A.3 shows the spectra of the invariant mass of the $m_{p\pi^0}$, $m_{\pi^0\pi^0}$ and $\cos\vartheta_{\pi^0\pi^0}$ for generated events (black) and for the reconstructed events after acceptance correction (red). The $m_{p\pi^0}$ invariant mass is reproduced with a good quality since that is one of the variables used in the correction and noticeable differences can only occur if there is a significant number of empty or poorly populated bins in the phase space, leading to the overall reduction of the acceptance (see further items). Otherwise this spectrum only allows to conclude that the acceptance correction procedure was applied in the correct order. In the $m_{\pi^0\pi^0}$ invariant spectrum the situation is different, one can see non-negligible deviations particularly at low invariant mases. The error introduced by the acceptance correction for these bins

[3] This effect is more pronounced in the regions where the acceptance is low. The treatment of such cases is described further in the text.

is about 20%. A similar situation is observed in case of $\cos\vartheta_{\pi^0\pi^0}$ (CMS frame) where in some of the bins noticeable deviations are present. These variables are not the ones which carry the information applied in the correction, but anyway as described above, have to be reproduced correctly if the correction is properly applied. Since it is not the case additional studies to improve the correction have been performed.

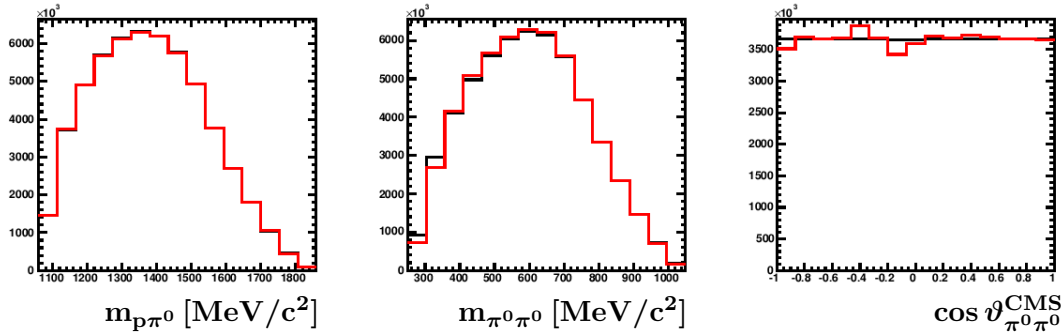

Figure A.3.: Crosscheck of the acceptance correction using 15 bins in energy and 30 bins in the invariant masses and angles. Black: generated events, red: reconstructed events after acceptance correction.

Correlations

One can assume that dependent on the strength of the correlations between different kinematic variables, the number of bins in the variables used in the correction will influence the reproducibility of the particular kinematic variables after application of the correction. For example the invariant masses can vary more with changes of the energy than angular variables, or angular variables influence other angular variables more than the invariant masses [4]. Having the knowledge about these correlations one could find a compromise between the sufficient number of bins to describe the phase space and sufficiently high statistics to fill these bins. In this method more bins were introduced in the variables used for the correction if they are correlated with the variables which have complicated shapes and fine structures in the phase space. For example, it was shown that the quality of correction for $\cos\vartheta^{CMS}_{\pi^0\pi^0}$ and $\cos\vartheta^{CMS}_{\pi^0}$ distributions strongly depends on the number of bins in $\cos\theta_{acc}$ and φ_{acc}. For the correction of the invariant masses $m_{p\pi}$ and

[4] Physical dynamics of the reaction is not considered.

$m_{\pi\pi}$ the change of the number of bins in the variables E_γ, $m_{p\pi_1}$ and $m_{p\pi_2}$ has a big influence. The question of the optimal binning arises and a compromise must be found between the increasing number of bins and the remaining statistics to determine correct acceptance factors with reasonable errors. Examples of correlations between different variables are shown in Figure A.4.

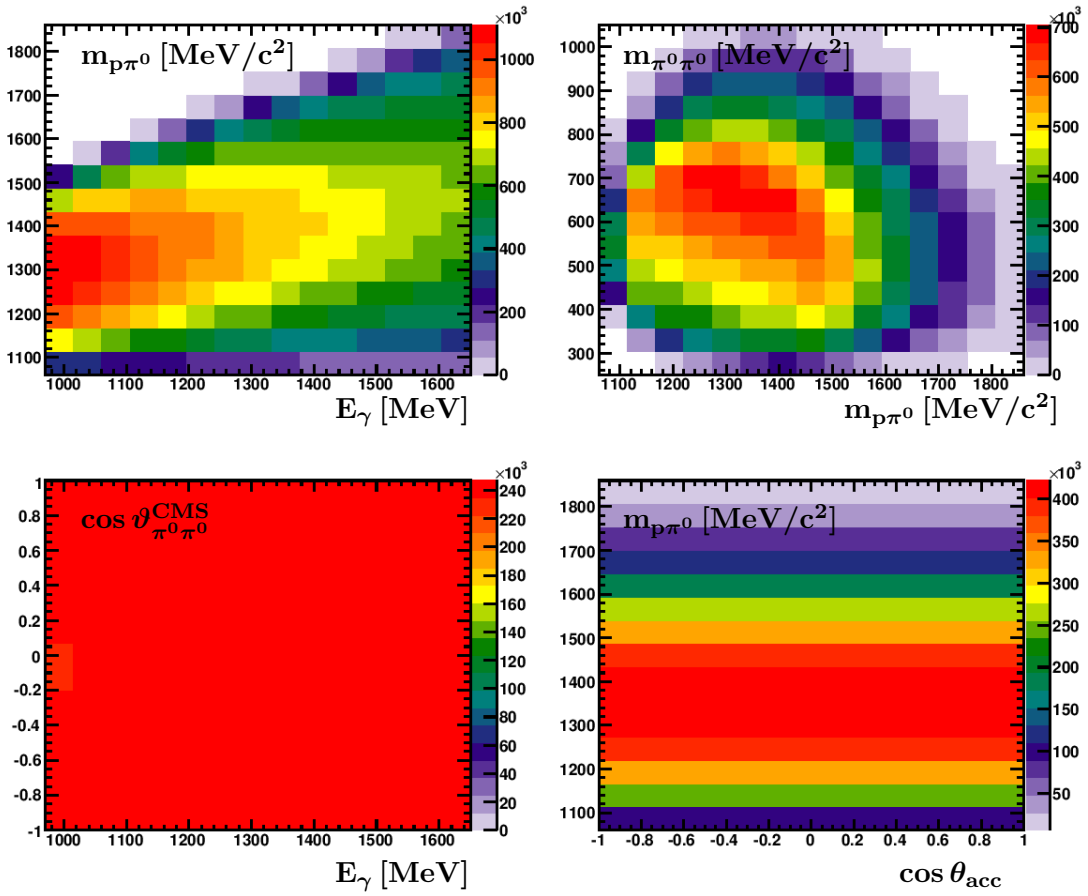

Figure A.4.: Examples of correlations for generated Monte Carlo, upper left: invariant mass $m_{p\pi^0}$ vs. incoming photon energy E_γ, upper right invariant mass $m_{\pi^0\pi^0}$ vs. invariant mass $m_{p\pi^0}$, lower left: $\cos\vartheta^{CMS}_{\pi^0\pi^0}$ vs. E_γ, lower right: invariant mass $m_{p\pi^0}$ vs. $\cos\theta_{acc}$.

In Figure A.3 the spectra after correction using 15 bins in energy and 30 bins in all other variables were shown . Since there is a correlation between angular variables introduced in the correction and angular variables defined in the final state one can expect that the introduction of more bins in the angular variables

improves the reproducibility of the corresponding reference spectra. Indeed (see Figure A.5), using 15 bins in energy and invariant masses and 60 bins in angles the quality of the reconstruction of the variable $\cos\vartheta^{CMS}_{\pi^0\pi^0}$ is improved. In the same time the quality of the reconstruction of the invariant mass $m_{\pi\pi}$ is worse than in Figure A.3. The invariant mass $m_{p\pi}$, however, is reconstructed with good quality. The difference is that $m_{p\pi}$ is included in the correction and has to be reconstructed in any case if there is enough statistics available. To reproduce $m_{\pi\pi}$ the shapes of the phase space have to be sufficiently followed and obviously this is not the case with this binning.

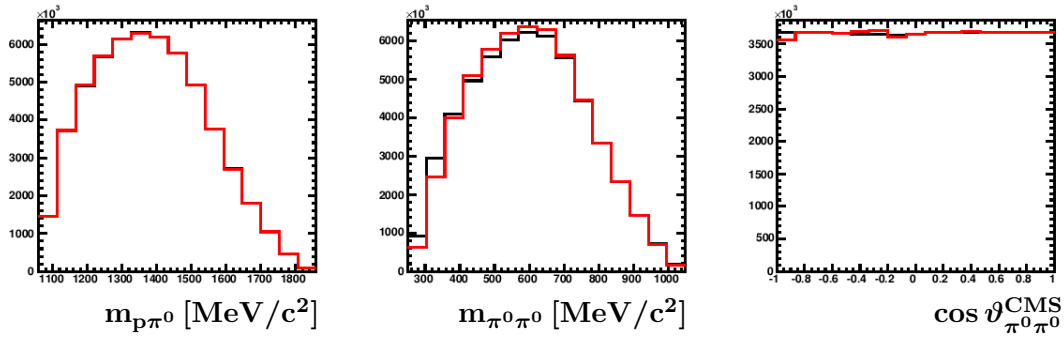

Figure A.5.: Crosscheck of the acceptance correction using 15 bins in energy and invariant masses and 60 in the angles. Black: generated events, red: reconstructed events after acceptance correction.

Now one can do the correction with more bins in the energy and invariant mass to see whether there is an improvement in the respective invariant mass reconstruction. To do that 50 bins were used in energy and invariant masses and 10 bins in both angular variables. The result is shown in Figure A.6. One can see that the variable $m_{\pi\pi}$ is now sufficiently well reproduced, but there is a serious problem in the reproduction of the variable $\cos\vartheta^{CMS}_{\pi^0\pi^0}$ due to a not sufficient number of bins in the angular variables.

To solve the problem one would think that it would be enough to increase the number of bins in all observables. An example of that is shown in Figure A.7 for 30 bins in the energy and invariant masses and 60 bins the angular variables. Here unfortunately, not only the shapes are not reproduced but the integral of the reconstructed events after acceptance correction is reduced significantly. This effect is produced due to the contribution of the bins with no entries at all. If the

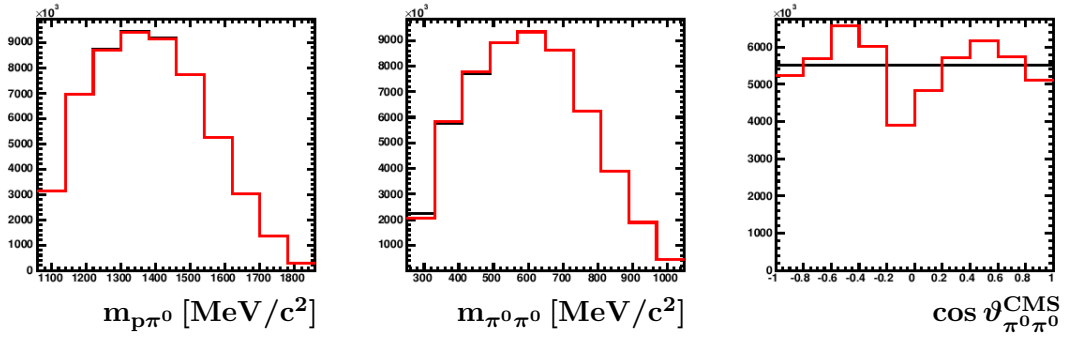

Figure A.6.: Crosscheck of the acceptance correction using 50 bins in energy and invariant masses and 10 in the angles. Black: generated events, red: reconstructed events after acceptance correction.

event in the data falls in one of such bins it be corrected and a factor of zero was attached to it and later used in the correction. One can conclude that it is not possible to go higher in the binning with given statistics.

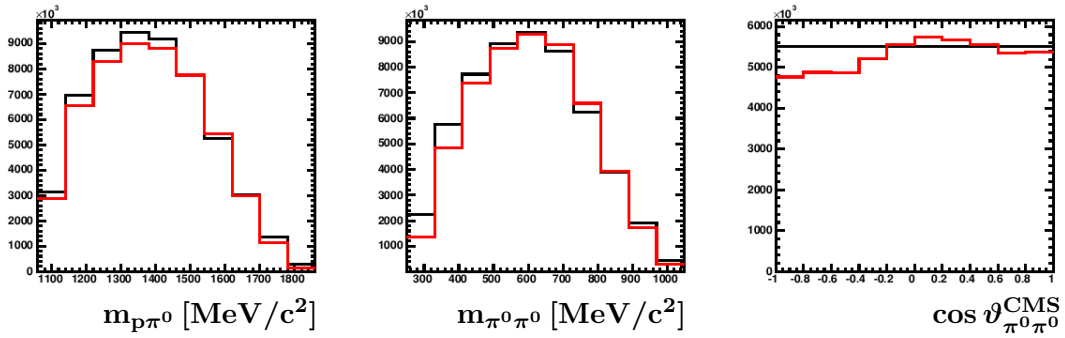

Figure A.7.: Crosscheck of the acceptance correction using 30 bins in energy and invariant masses and 60 in the angles. Black: generated events, red: reconstructed events after acceptance correction.

According to the estimate derived from these and other extensive checks one can conclude that the number of bins for a sufficient correction with the setup used in this work is in order of 50-60 bins in each of the observables. It means that the existing statistics has to be improved with a large factor (roughly about 50), which is not easy to do technically due to time and disk space limitations. Still, there are ways around this which can reduce the amount of work, as discussed in the next item.

Additional methods

If the low acceptance regions are identified it is possible to treat them separately. Optionally, one could create an event generator to fill the existing gaps in the phase space. For example if the acceptance varies strongly with the polar angle one could generate more events in just the regions of low acceptance thus reducing the overall number of events required for the acceptance correction.

For the CBELSA/TAPS setup it was found that the low acceptance due to the the forward hole of TAPS detector and limited acceptance in the overlap region of $28^\circ < \vartheta < 32^\circ$ produce the most problems for the correction. An exclusion of these regions would improve the quality of the correction. However one has to account for the additional acceptance holes produced by this procedure. Further investigations have shown that the largest deviations in case of an insufficient number of bins used in the correction occur due to low acceptance in certain bins in the phase space and also due to large changes in the acceptance between adjacent bins. It means that for the "large" cell in the phase space (which is constructed out of several "small" cells with different acceptance) the factors are averaged over the "large" interval thus producing additional problems for the correction. These effects can be reduced by introduction of more bins in the intervals where the change in acceptance values is large between the neighboring bins. The negative side of this method is the change in statistics and therefore larger error in the divided bins. An additional technique for the solution of this problem is the introduction of a variable binning in the variables used for the correction. For example to reduce the effect of the low statistics on the edges of the invariant mass spectra one can redistribute events (rebin) so that due to different widths of the bins the events are distributed equally in the whole invariant mass range. The drawback of this method is also similar to the problems described above, it averages the acceptance in the region where it changes fast thus leading to a wrong correction.

To summarize, an attempt to do a model-independent acceptance correction was made with application of various methods which can be used in the future. However due to statistical limits the correction was not applied. The tested methods were discussed and the main problem of finding compromise between limited

statistics and good description of the phase space was presented.

B. φ distributions

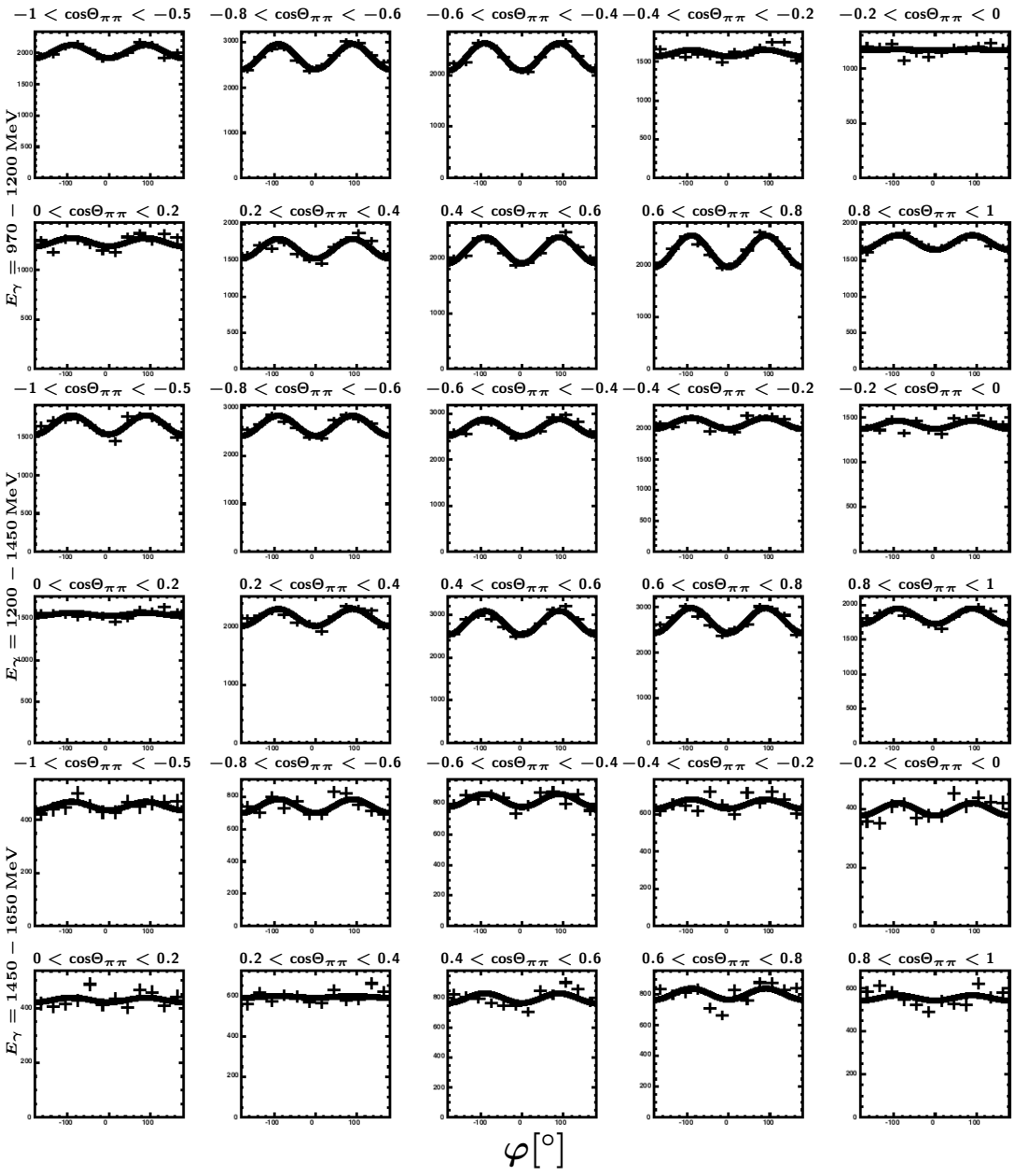

Figure B.1.: φ distributions of the proton binned in $cos\Theta_{\pi\pi}$ (CMS) in the three energy ranges.

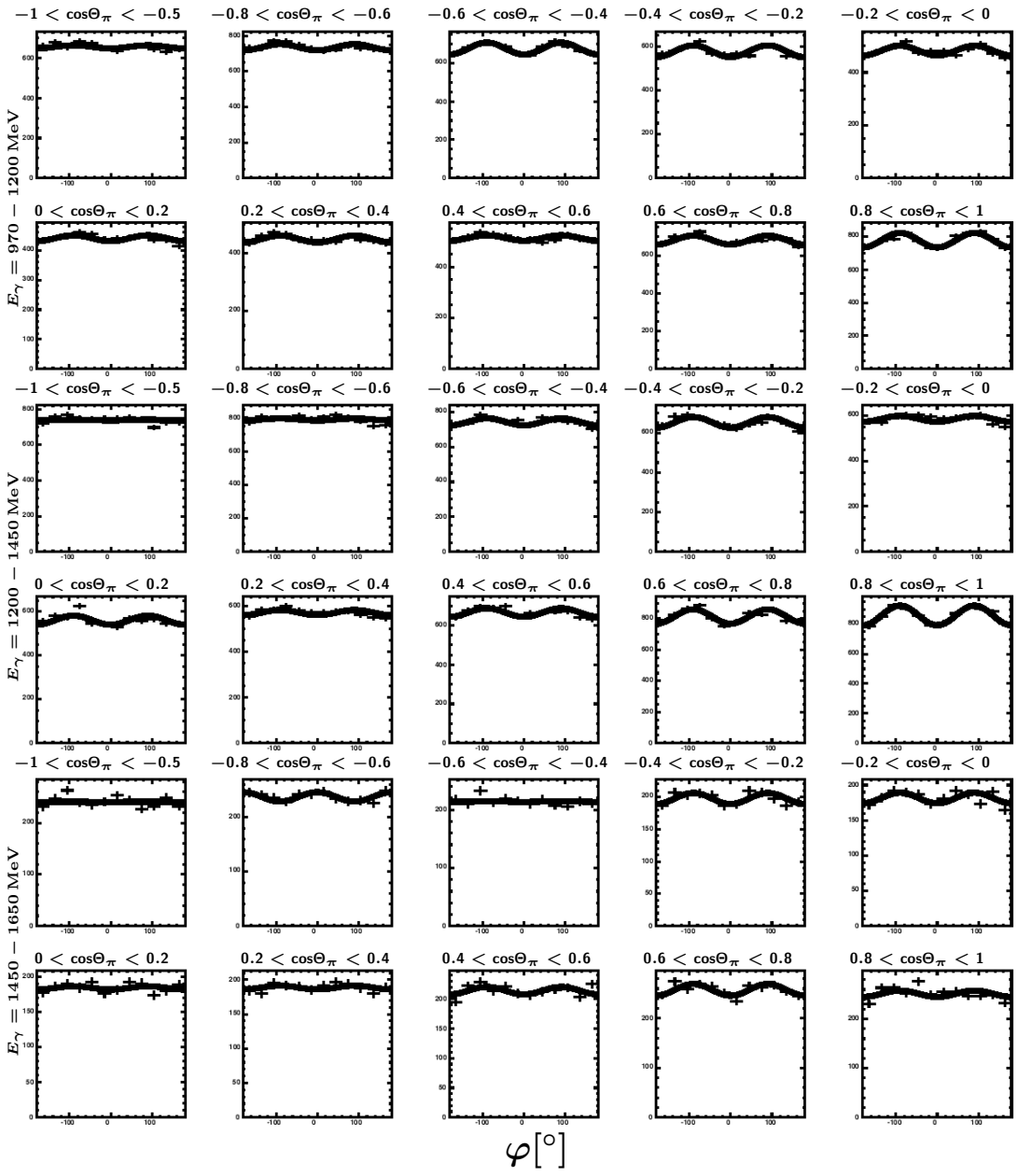

Figure B.2.: φ distributions of the pions binned in $cos\Theta_\pi$ (CMS) in the three energy ranges.

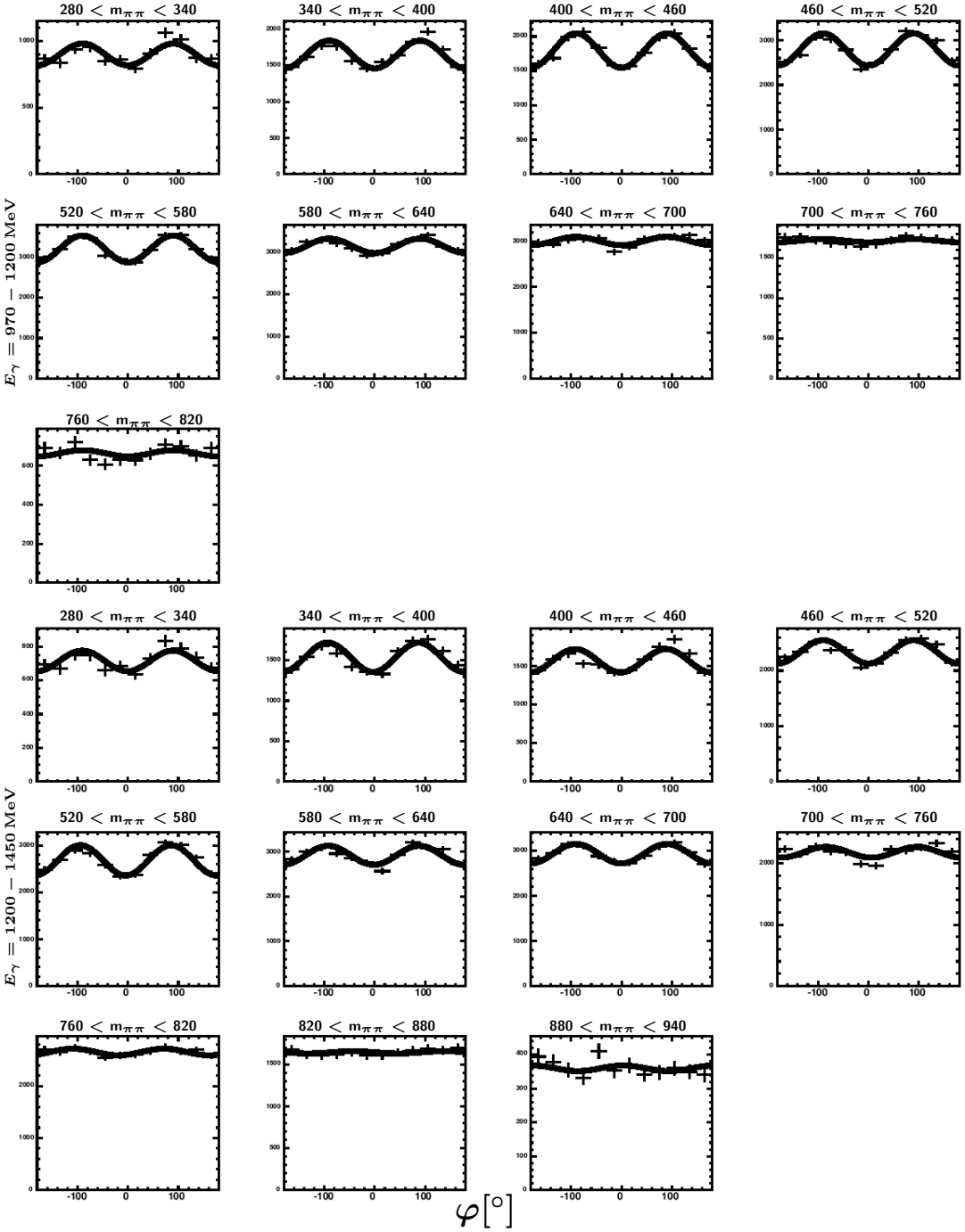

Figure B.3.: φ distributions of the proton binned in the invariant mass $m_{\pi\pi}$ in the energy ranges $E_\gamma = 970 - 1200\,\mathrm{MeV}$ (three upper rows) and $E_\gamma = 1200 - 1450\,\mathrm{MeV}$ (three lower rows).

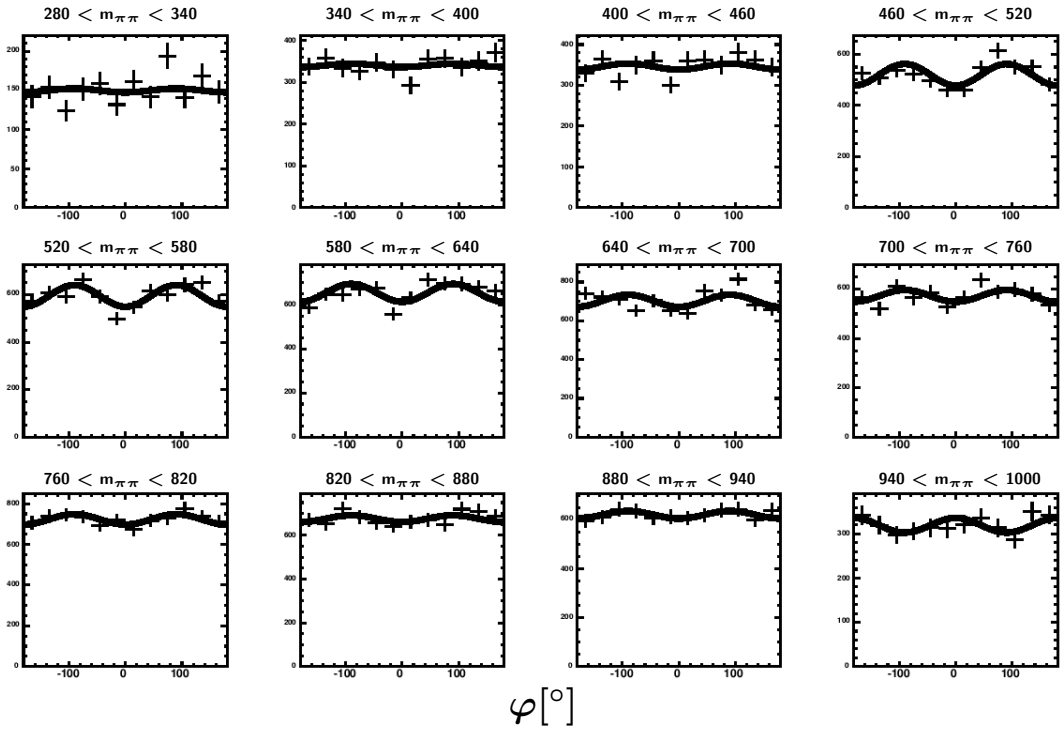

Figure B.4.: φ distributions of the proton binned in $m_{\pi\pi}$ in the energy range $E_\gamma = 1450 - 1650$ MeV.

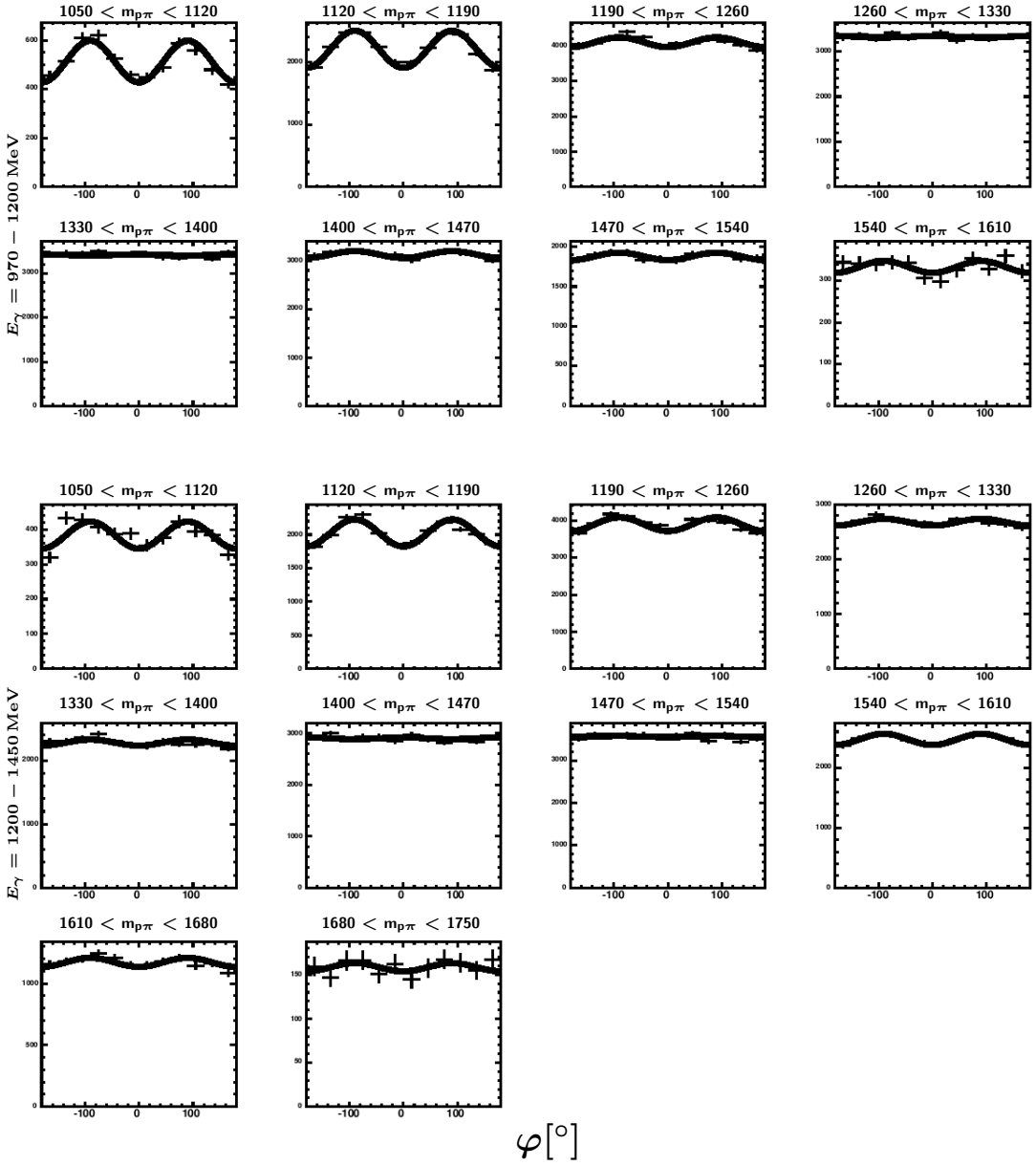

Figure B.5.: φ distributions of the pions binned in $m_{p\pi}$ in the energy range $E_\gamma = 970 - 1200$ MeV (two upper rows) and $E_\gamma = 1200 - 1450$ MeV (three lower rows).

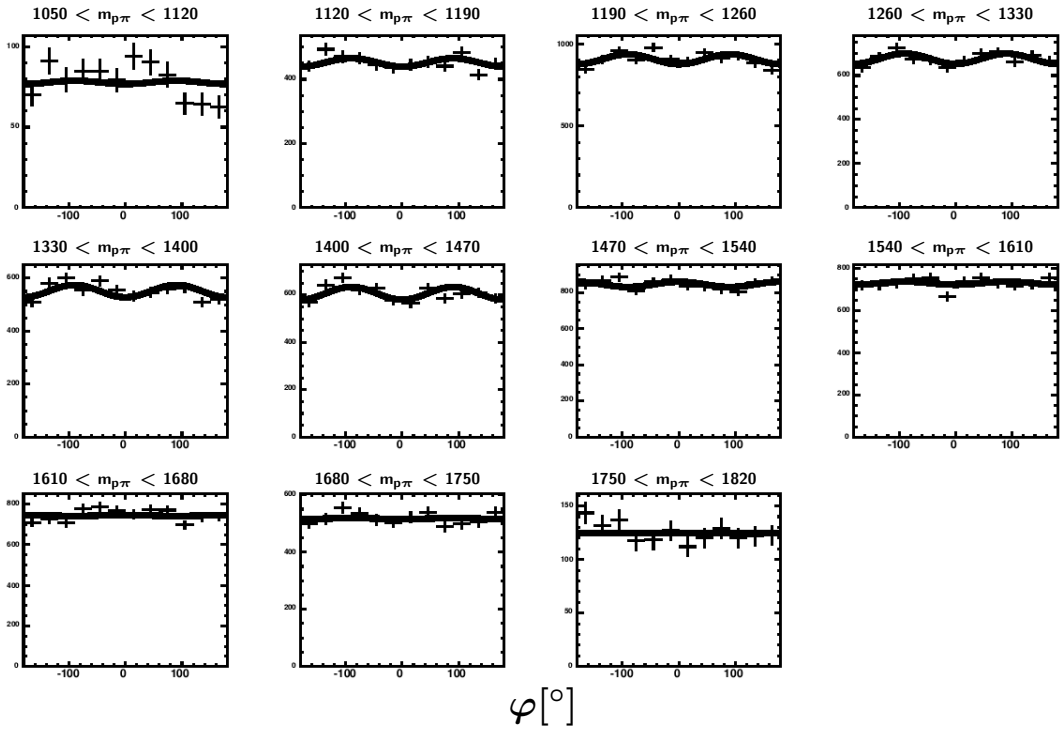

Figure B.6.: φ distributions of the pions binned in $m_{p\pi}$ in the energy range $E_\gamma = 1450 - 1650$ MeV.

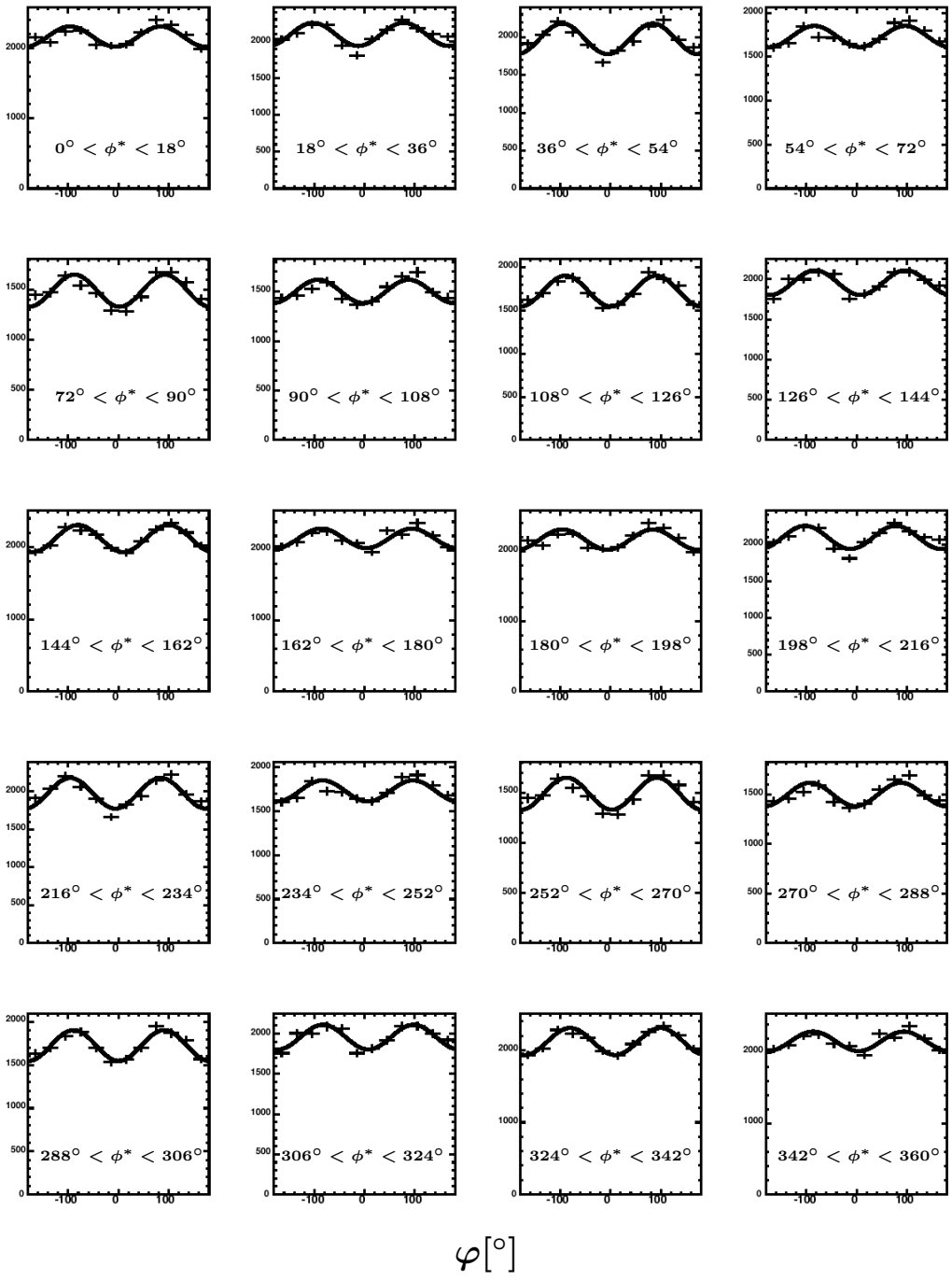

Figure B.7.: φ distributions (proton recoiling) binned in Φ^* in the energy range $E_\gamma = 970 - 1200\,\mathrm{MeV}$.

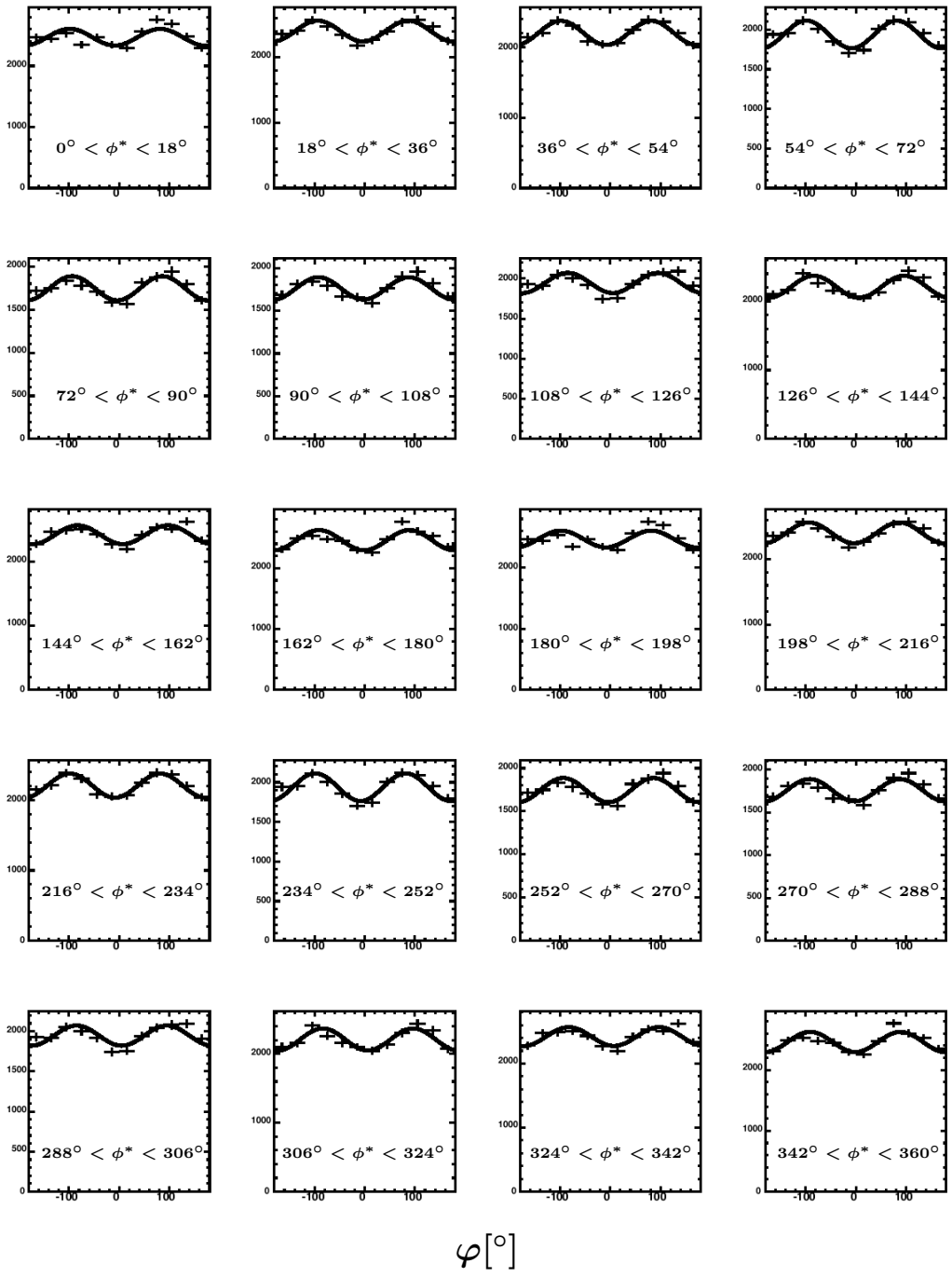

Figure B.8.: φ distributions (proton recoiling) binned in Φ^* in the energy range $E_\gamma = 1200 - 1450\,\mathrm{MeV}$.

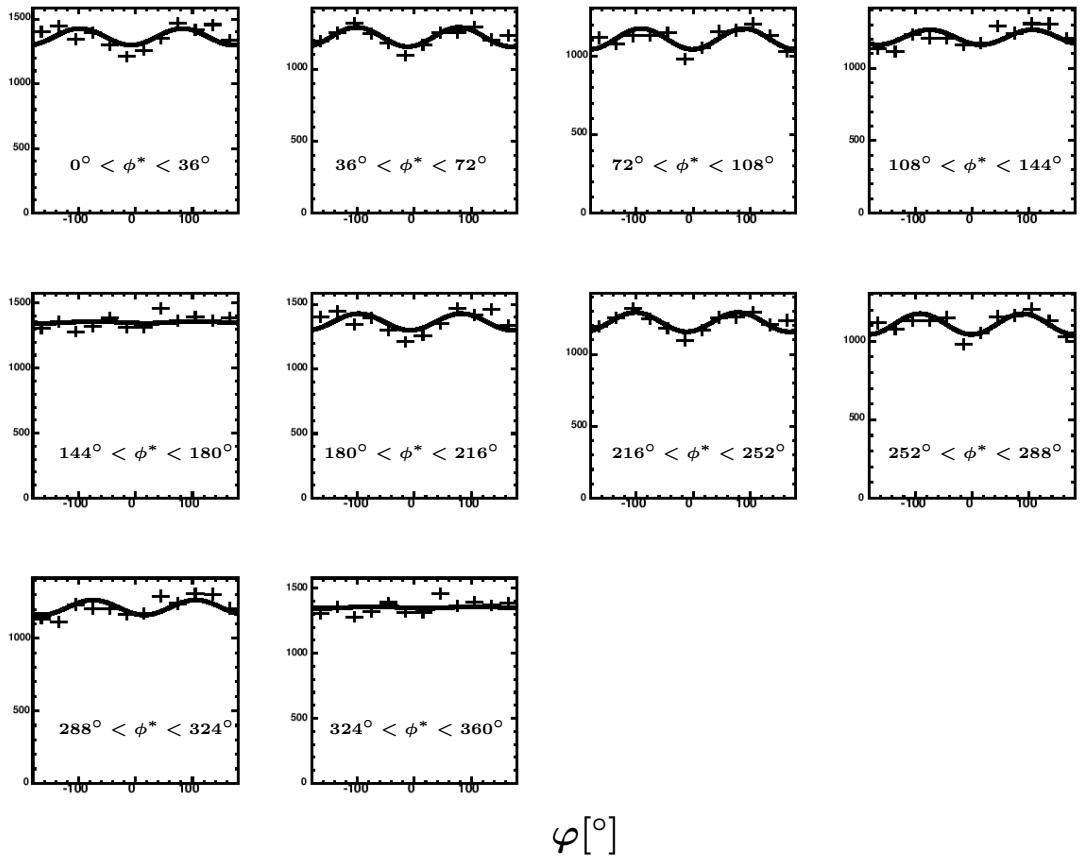

Figure B.9.: φ distributions (proton recoiling) binned in Φ^* in the energy range $E_\gamma = 1450 - 1650\,\mathrm{MeV}$.

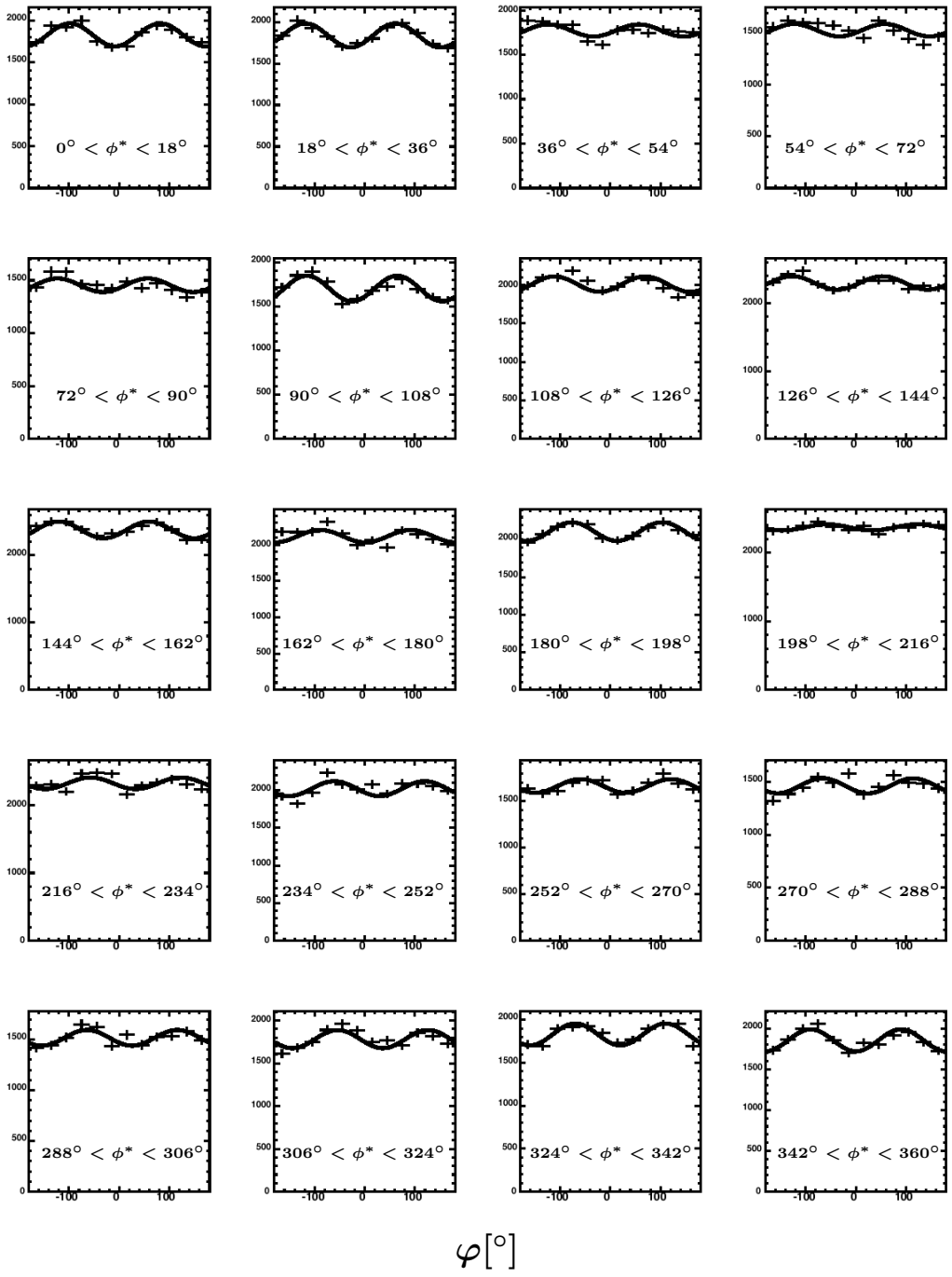

Figure B.10.: φ distributions (pion recoiling) binned in Φ^* in the energy range $E_\gamma = 970 - 1200\,\mathrm{MeV}$.

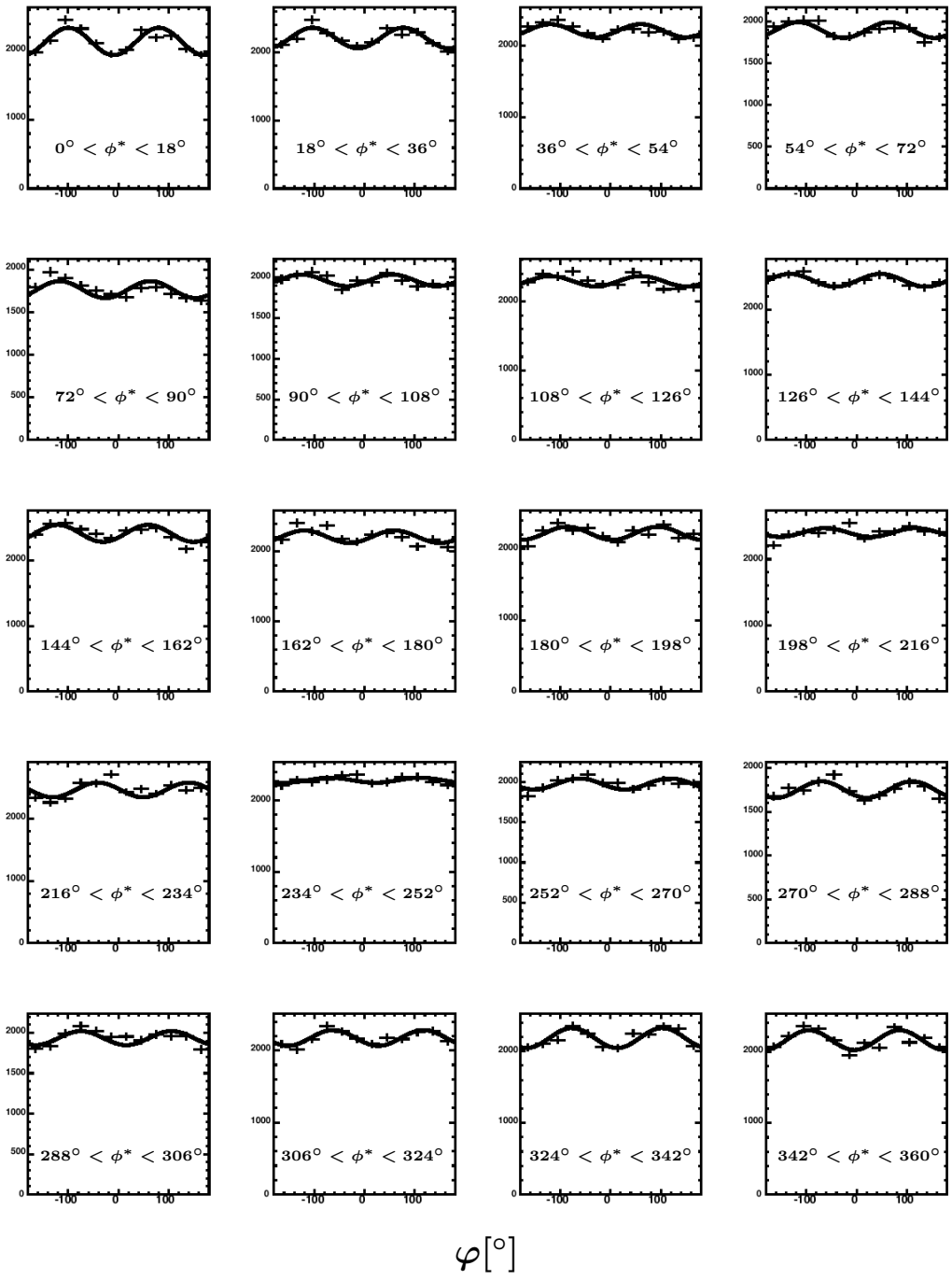

Figure B.11.: φ distributions (pion recoiling) binned in Φ^* in the energy range $E_\gamma = 1200 - 1450\,\mathrm{MeV}$.

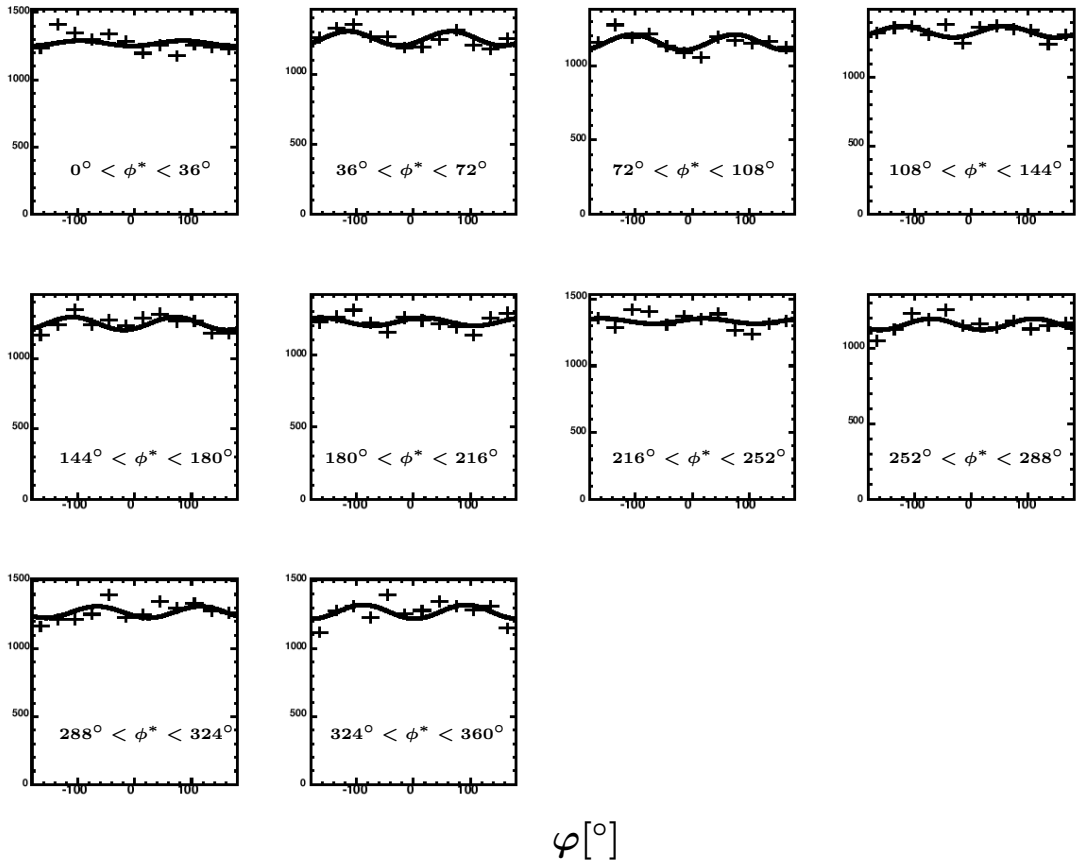

Figure B.12.: φ distributions (pion recoiling) binned in Φ^* in the energy range $E_\gamma = 1450 - 1650\,\mathrm{MeV}$.

C. Dalitz plots

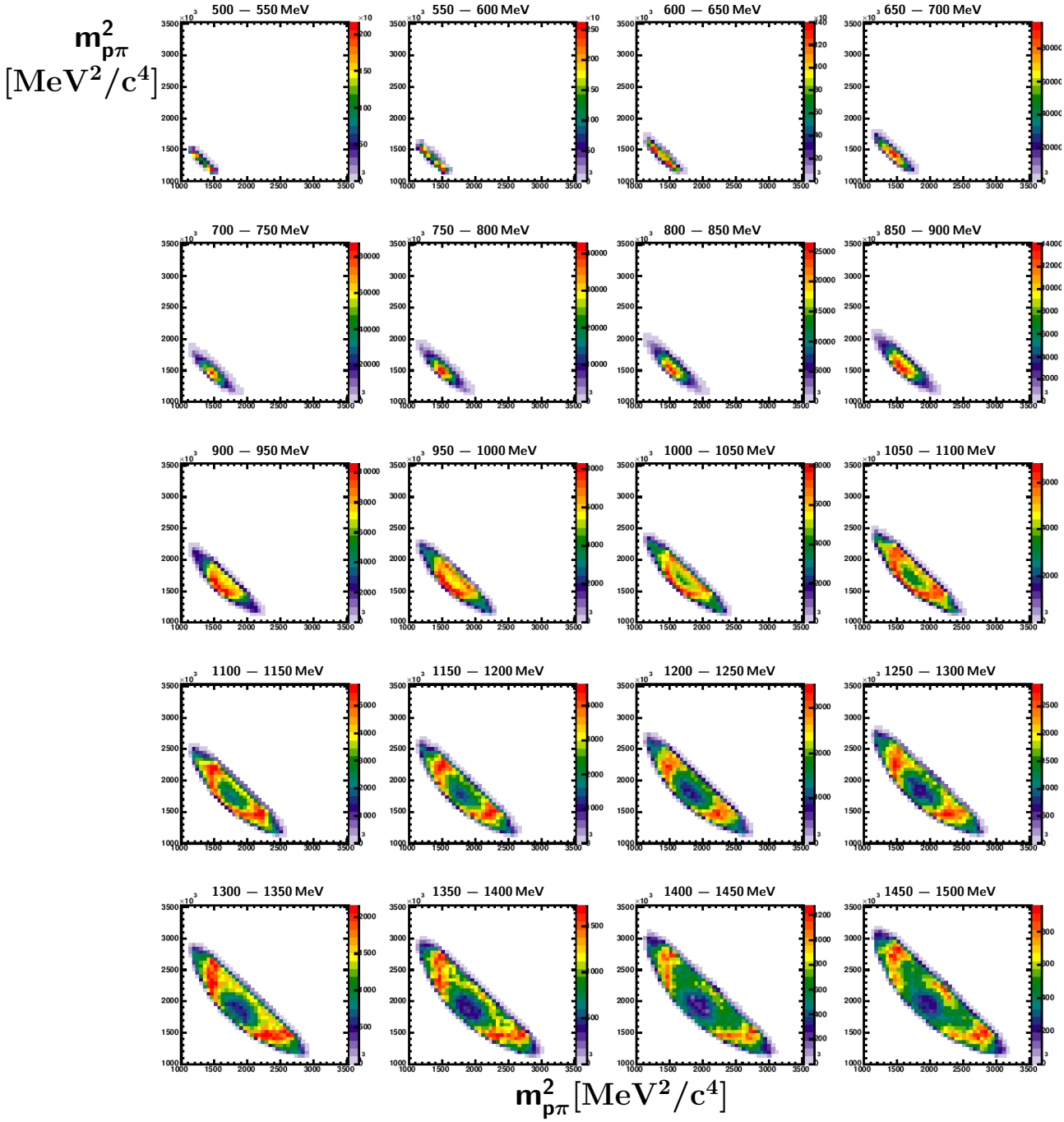

Figure C.1.: Dalitz plots $m^2(p\pi^0)$ vs. $m^2(p\pi^0)$ in the energy range $E_\gamma = 500 - 1500\,\mathrm{MeV}$.

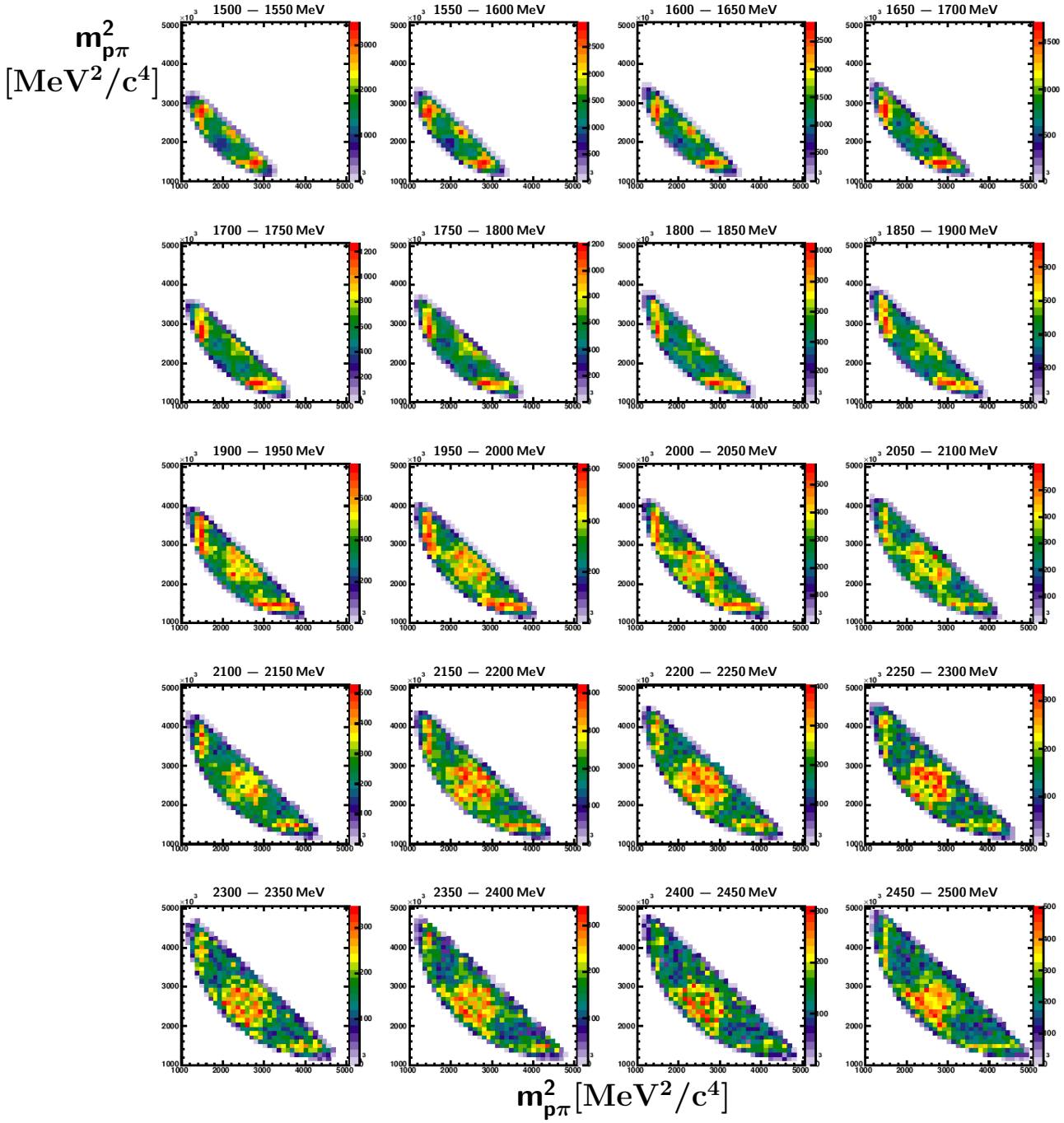

Figure C.2.: Dalitz plots $m^2(p\pi^0)$ vs. $m^2(p\pi^0)$ in the energy range $E_\gamma = 1500 - 2500\,\mathrm{MeV}$.

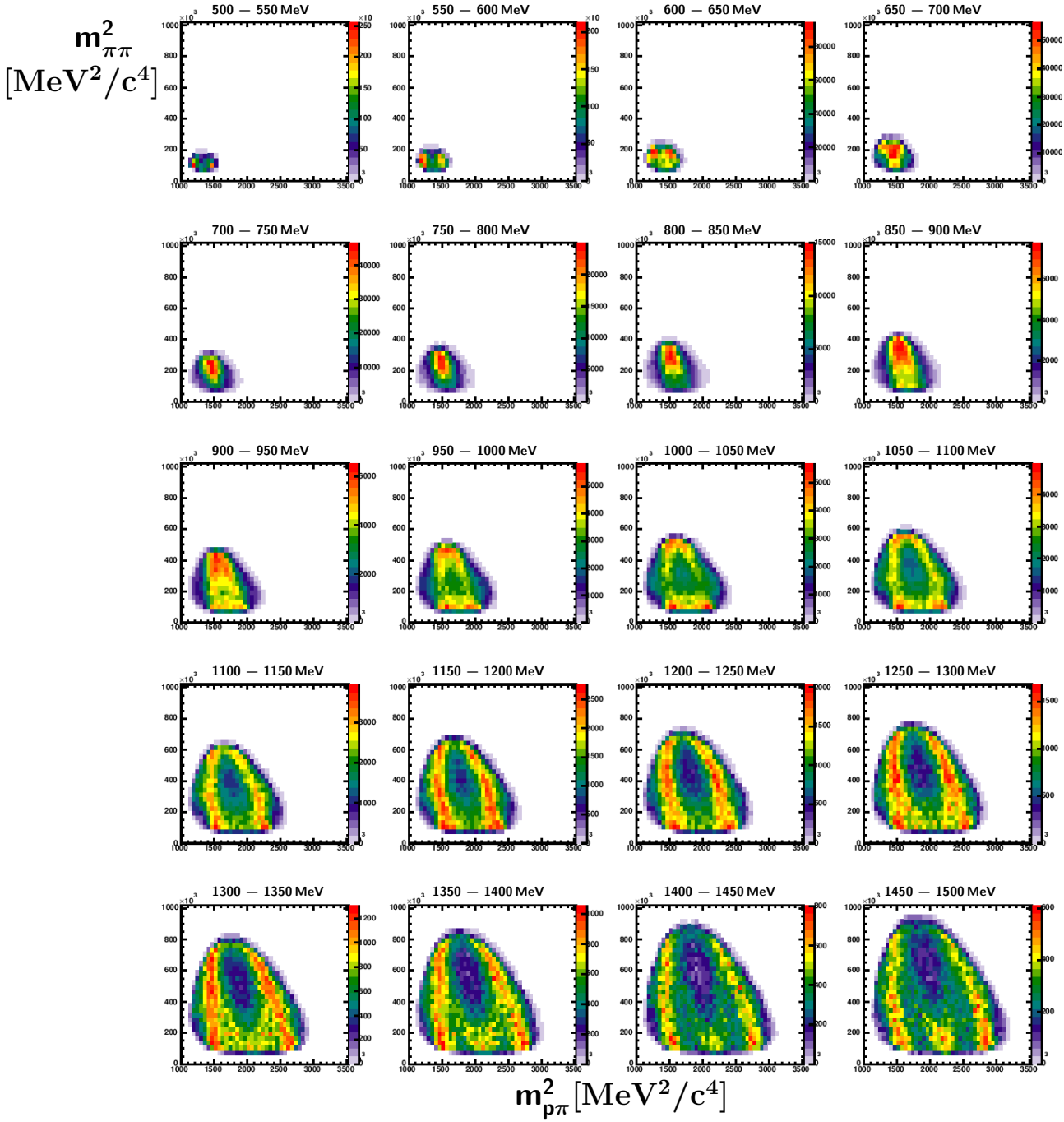

Figure C.3.: Dalitz plots $m^2(\pi^0\pi^0)$ vs. $m^2(p\pi^0)$ in the energy range $E_\gamma = 500 - 1500\,\mathrm{MeV}$.

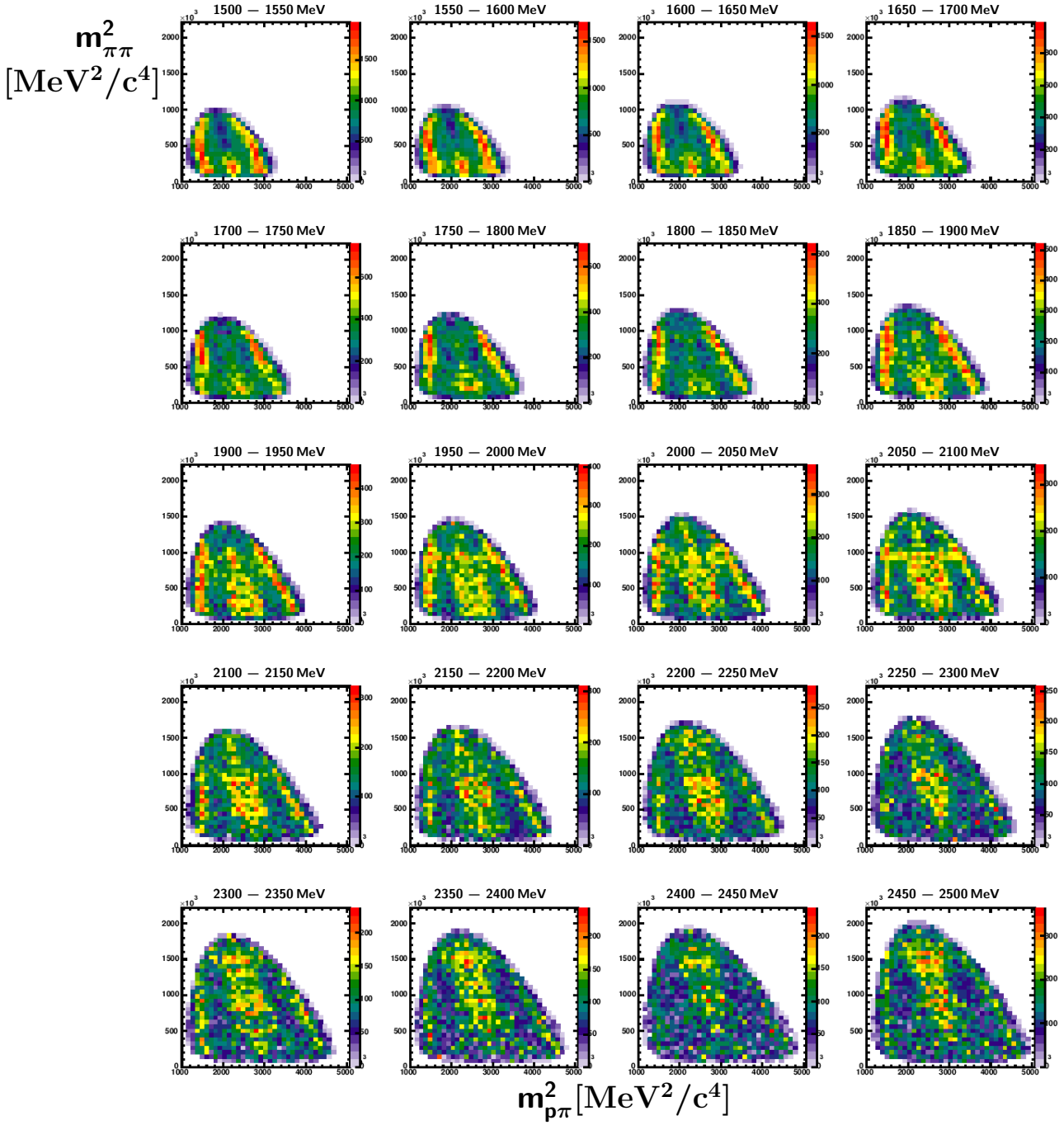

Figure C.4.: Dalitz plots $m^2(\pi^0\pi^0)$ vs. $m^2(p\pi^0)$ in the energy range $E_\gamma = 1500 - 2500\,\mathrm{MeV}$.

List of Figures

List of Tables

Bibliography

[A+92] Aker, E. et al.: *The Crystal Barrel Spectrometer at LEAR.* Nuclear Instruments and Methods in Physics Research, A(321):69–109, 1992.

[A+03] Assafiri, Y. et al.: *Double π^0 photoproduction on the proton at GRAAL.* Physical Review Letters, 90(22):22201, 2003.

[A+05] Ahrens, J. et al.: *Intermediate resonance excitation on the $\gamma p \to p\pi^0\pi^0$ reaction.* Physics Letters, B(624):173–180, 2005.

[ABK+12] Anisovich, A.V., R. Beck, E. Klempt, V.A. Nikonov, A.V. Sarantsev and U. Thoma: *Properties of baryon resonances from a multichannel partial wave analysis.* arXiv:1112.4937v1[hep-ph], 2012.

[AKST05] Anisovich, A.V., E. Klempt, A.V. Sarantsev and U. Thoma: *Partial wave decomposition of pion and photoproduction amplitudes.* European Physical Journal, A(24):111, 2005.

[AS06] Anisovich, A.V. and A.V. Sarantsev: *Partial decay widths of baryons in the spin-momentum operator expansion method.* European Physical Journal, A(30):427, 2006.

[ASB+05] Anisovich, A.V., A.V. Sarantsev, O. Bartholomy, E. Klempt, V.A. Nikonov and U. Thoma: *Photoproduction of baryons decaying into $N\pi$ and $N\eta$.* European Physical Journal, A(25):427, 2005.

[Bar00] Bartholomy, O.: *Test und Modifikation des Lichtpulsersystems für den CB-ELSA-Detektor.* Diploma thesis, Helmholtz-Institut für Strahlen- und Kernphysik, Universität Bonn, 2000.

[BDS75] Barker, I.S., A. Donnachie and J.K. Storrow: *Complete experiments in pseudoscalar photoproduction.* Nuclear Physics, B(95):347–356, 1975.

[Bös06] Böse, S.: *Modifikation und Test des Lichtpulsersystems für den Crystal Barrel Aufbau an ELSA.* Diploma thesis, Helmholtz-Institut für Strahlen- und Kernphysik, Universität Bonn, 2006.

[Cas06] Castelijns, R.: *Photoproduction of strange mesons and hyperons on the proton.* PhD thesis, Rijksuniversiteit Groningen, 2006.

[CR94] Capstick, S. and W. Roberts: *Quasi-two-body decays of nonstrange baryons.* Physical Review, D(49):4570–4586, 1994.

[CR00] Capstick, S. and W. Roberts: *Quark Models of Baryon Masses and Decays.* Progress in Particle and Nuclear Physics, 45:241–331, 2000.

[Cre01] Crede, V.: *CBGEANT 1.08/01.* CB-Note, October 2001.

[E+09] Elsner, D. et al.: *Linearly polarised photon beams at ELSA and measurement of the beam asymmetry in π^0 photoproduction off the proton.* European Physical Journal, A(39):373–381, 2009.

[EDRW11] Edwards, Robert J., Jozef J. Dudek, David G. Richards and Stephen J. Wallace: *Excited state baryon spectroscopy from lattice QCD.* Physical Review D, (84):074508, 2011.

[Els07] Elsner, D.: *Untersuchung kleiner Partialwellenbeitrage in der Nähe dominierender Resonanzbeiträge des Protons mit linear polarisierten Photonen.* PhD thesis, Physikalisches Institut, Universität Bonn, 2007.

[Fix05] Fix, A., Arenhövel H.: *Double pion photoproduction on nucleon and deuteron.* European Physical Journal, A(25):115–135, 2005.

[FN03] F.A. Natter, P. Grabmayr, T. Hehl R.O. Owens S. Wunderlich: *Monte Carlo simulation and analytical calculation of coherent bremsstrahlung and its polarisation.* Nuclear Instruments and Methods in Physics Research, B(211):465–486, 2003.

[Fös01] Fösel, A.: *Entwicklung und Bau des Innendetektors für das Crystal Barrel Experiment an ELSA/Bonn.* PhD thesis, Physikalisches Institut, Universität Erlangen, 2001.

[FP09] Fornet-Ponse, K.: *Die Photonenmarkierungsanlage für das Crystal-Barrel/TAPS-Experiment an ELSA.* PhD thesis, Physikalisches Institut, Universität Bonn, 2009.

[Fro11] Frommberger, F.: *private communication*, 2011.

[Fuc05] Fuchs, M.: *Photoproduktion neutraler Pionpaare mit dem Crystal Barrel Detektor an ELSA.* PhD thesis, Helmholtz-Institut für Strahlen- und Kernphysik, Universität Bonn, 2005.

[G+94] Gabler, A. et al.: *Response of TAPS to monochromatic photons with energies between 45 and 790 MeV.* Nuclear Intruments and Methods in Physics Research, A(346):168–176, 1994.

[Glo00] Glozman, L. Ya.: *Parity doublets and chiral symmetry restoration in baryon spectrum.* Physics Letters, B(475):329–334, 2000.

[Gri08] Griffiths, D.: *Introduction to Elementary Particles.* Wiley, 2nd edition, 2008.

[GSvP+10] Gutz, E., V. Sokhoyan, H. van Pee et al.: *Photoproduction of meson pairs: First measurement of the polarization observable I^s.* Physics Letters, B(687):11–15, 2010.

[Gut10] Gutz, E.: *Measurement of beam asymmetries in the reaction $\gamma p \to p\pi^0\eta$ with the Crystal Barrel/TAPS experiment at ELSA.* PhD thesis, Helmholtz-Institut für Strahlen- und Kernphysik, Universität Bonn, 2010.

[H+97] Härter, F. et al.: *Two neutral pion photoproduction off the proton between threshold and 800 MeV.* Physics Letters, B(401):229–233, 1997.

[Hil06] Hillert, W.: *The Bonn Electron Stretcher Accelerator ELSA: Past and future.* European Physical Journal, A(28):139–148, 2006.

[Hof01] Hoffmann, M.: *Beschleunigung polarisierter Elektronen in der Bonner Elektronen-Beschleunigeranlage ELSA*. PhD thesis, Physikalisches Institut, Universität Bonn, 2001.

[Hor04] Horn, I.: *The decay of the γp system into the $p\pi^0\eta$ final state*. PhD thesis, Helmholtz-Institut für Strahlen- und Kernphysik, Universität Bonn, 2004.

[Jae09] Jaegle, I.: *$\pi^0\pi^0$, η and η' photoproduction off the deutron or The search for missing resonances*. PhD thesis, Universität Basel, 2009.

[Jun00] Junkersfeld, J.: *Kalibration des Crystal-Barrel-ELSA Detektors mit Hilfe der Reaktion $\gamma p \to p\pi^0$*. Diploma thesis, Helmholtz-Institut für Strahlen- und Kernphysik, Universität Bonn, 2000.

[Jun05] Junkersfeld, J.: *Photoproduktion von $\pi^0\omega$ am Proton bei Energien bis zu 3 GeV*. PhD thesis, Helmholtz-Institut für Strahlen- und Kernphysik, Universität Bonn, 2005.

[K+04] Kottulla, M. et al.: *Double π^0 photoproduction off the proton at threshold*. Physics Letters, B(578):63–68, 2004.

[Kle03] Klempt, E.: *Do parity doublets in the baryon spectrum reflect restoration of chiral symmetry*. Physics Letters, B(559):141–152, 2003.

[Kop02] Kopf, B.: *Untersuchung der photoinduzierten Reaktionen $\gamma p \to p\pi^0\pi^0$ und $\gamma p \to p\pi^0\eta$*. PhD thesis, Institut für Kern- und Teilchenphysik, Technische Universität Dresden, 2002.

[Kot04] Kottula, M.: *Recent results from 2 π^0 photoproduction off the proton*. AIP Conference Proceedings, 717:842–847, 2004.

[KZF+09] Krambrich, D., F. Zehr, A. Fix, L. Roca et al.: *Beam-Helicity Asymmetries in Double-Pion Photoproduction off the Proton*. Phys. Rev. Lett., 103(5):052002, 2009.

[Lic69] Lichtenberg, D. B.: *Baryon supermultiplets of SU(6) $\times$ O(3) in a quark-diquark model*. Physical Review, 178(5):2197–2200, 1969.

[LMP01] Löring, U., B.C. Metsch and H.R. Petry: *The light baryon spectrum in a relativistic quark model with instanton-induced quark forces: The non-strange baryon spectrum and ground-states.* European Physical Journal, A(10):395–446, 2001.

[ML95] Murphy, L.Y. and J.M. Laget: *Reaction mechanisms in two pion photoproduction on the proton.* DAPNIA-SPHN, (95-42), 1995.

[MUMP03] Metsch, B., Loring U., D. Merten and H. Petry: *The spectrum and strong decays of baryons in a relativistic quark model.* European Physical Journal, A(18):189–192, 2003.

[N+10] Nakamura, K. et al.: *Review of Particle Physics.* Journal of Physics, G(37), 2010.

[NO02] Nacher, J. C. and E. Oset: *Study of polarization observables in double-pion photoproduction on the proton.* Nuclear Physics, A(697):372–387, 2002.

[Per86] Perkins, D.: *Introduction to High Energy Physics.* Addison-Wesley, 3nd edition, 1986.

[RO05] Roberts, W. and T. Oed: *Polarization Observables for Two-Pion Production off the Nucleon.* Physical Review, C(71):052002, 2005.

[Roc05] Roca, L.: *Helicity asymmetries in double pion photoproduction on the proton.* Nuclear Physics, A(748):192–205, 2005.

[S+05] Suft, G. et al.: *A scintillating fibre detector for the Crystal Barrel experiment at ELSA.* Nuclear Instruments and Methods in Physics Research, A(531):416–424, 2005.

[S+08] Sarantsev, A.V. et al.: *New results on the Roper resonance and the P_{11} partial wave.* Physics Letters, B(659):94–100, 2008.

[San05] Santopinto, E.: *Interacting quark-diquark model of baryons.* Physical Review C, (72):022201, 2005.

[Sar12] Sarantsev, A.: *private communication*, 2012.

[T+08] Thoma, U. et al.: *N $\pi^0\pi^0$ -decays of N^* - and Δ^* -resonances in the second and third resonance region.* Physics Letters, B(659):87–93, 2008.

[Tim69] Timm, U.: *Coherent Bremsstrahlung of Electrons in Crystals.* Fortschritte der Physik, 17:765–808, 1969.

[TO96] Tejedor, J. A. Gomez and E. Oset: *Double pion photoproduction on the nucleon: Study of the isospin channels.* Nuclear Physics, A(600):413–435, 1996.

[Trn06] Trnka, D.: *Investigation of in-medium modifications of the ω meson in photonuclear reactions.* PhD thesis, II. Physikalisches Institut, Universität Giessen, 2006.

[TvPS+05] Thoma, U., H. van Pee, A. Sarantsev et al.: *Measurement of Double Polarisation Observables in $2\pi^0$-Photoproduction with the Crystal Barrel Detector at ELSA.* Proposal to the PAC, August 2005.

[vP03] Pee, H. van: *Untersuchung der Reaktion $\gamma p \to p\pi^0$ für Photonenergien von 0.45 bis 1.3 GeV mit dem Crystal Barrel-Detektor an ELSA.* PhD thesis, Helmholtz-Institut für Strahlen- und Kernphysik, Universität Bonn, 2003.

[vP+07] Pee, H. van et al.: *Photoproduction of π^0-mesons off protons from the $\Delta(1232)$ region to $E_\gamma = 3GeV$.* European Physical Journal, A(31):61, 2007.

[vP08] Pee, H. van: *private communication*, 2008.

[W+00] Wolf, M. et al.: *Photoproduction of neutral pion pairs from the proton.* European Physical Journal, A(9):5–8, 2000.

[Wor72] Worden, R.P.: *Regge models of forward pion and eta photoproduction.* Nuclear Physics, B(37):253–312, 1972.

Aknowledgements

I would like to thank the members of my PhD committee: Prof. Dr. Ulrike Thoma, Prof. Dr. Volker Metag, PD Dr. Bernard Metsch and Prof. Dr. Nikolaus Froitzheim for reading and examining my work. I would like to thank Prof. Dr. Ulrike Thoma for supervising my PhD work, starting from very beginning until the time of defense. I am very grateful for giving me the great opportunity of working within research groups in Bonn and Giessen.

Many thanks to Harald van Pee for his strong support and encouragement at all the steps of the data analysis. Special thanks to Eric Gutz for the work together, many useful discussions and help concerning the work from general view up to minor details. This is a huge impact which is hard to describe within one sentence.

I would like to thank the CBELSA/TAPS group at HISKP (Bonn) for a pleasant working environmnent and work in very different fields together, starting from detector preparation and ending with data analysis and physical interpretation of the obtained results. Also I would like to thank the Bonn-Gatchina PWA group, in particular Andrey Sarantsev and Victor Nikonov for providing their interpretation of the experimentally measured data. Many thanks to Giessen group for the work together. My particular thanks to Karoly Makonyi for many fruitful discussions, his friendship and great support in many cases. Thanks to Russel Jonstone and Tom Jude (PI Bonn) for their suggestions concerning english language in the thesis. I thank everybody who feels that he/she helped me, but I forgot to mention the name.

Many thanks to my friends David, Gia and Gizo in Bonn, they were supporting me in very different circumstances during this work. Thanks to my family and friends in Armenia for their support which I always felt behind my life and work. I thank my wife Kristine Khachatryan for bringing a new light and happiness to my life which was the best support during this work.